UNIVERSIDAD PABLO DE OLAVIDE

DOCTORAL THESIS

Experimental characterization and numerical modeling of ionic and electronic dynamics in nanostructured hybrid materials for photoconversion

---

Author:
Antonio J. Riquelme Expósito

Supervisors:
Prof. Juan Antonio Anta
Prof. Gerko Oskam

Nanostructured Solar Cells Group
Department of Physical, Chemical and Natural Systems

May 12, 2022

Declaration of Authorship

Juan Antonio Anta Montalvo, Catedrático de la Universidad vinculado al Departamento de Sistemas Físicos, Químicos y Naturales de la Universidad Pablo de Olavide y Gerko Oskam, investigador distinguido Beatriz Galindo sénior vinculado al Departamento de Sistemas Físicos, Químicos y Naturales de la Universidad Pablo de Olavide.

Certifican:

Que la presente memoria titulada “Experimental characterization and numerical modeling of ionic and electronic dynamics in nanostructured hybrid materials for photoconversion” presentada por Antonio J. Riquelme Expósitopara la obtención del título de Doctor, ha sido realizada bajo nuestra dirección en el Departamento de Sistemas Físicos, Químicos y Naturales de la Universidad Pablo de Olavide, dentro del programa de doctorado “Medio Ambiente y Sociedad”.

Prof. Juan Antonio Anta
Prof. Gerko Oskam
May 12, 2022

“*Caminante, son tus huellas*
el camino y nada más;
Caminante, no hay camino,
se hace camino al andar.”

Extracto Campos de Castilla (XXIX).
Antonio Machado (1875 - 1939)

Abstract

The development of alternative, low-emission energy sources has gained importance for society as the worldwide energy demand increases while the environmental impact of the accumulated use of fossil fuels becomes more evident, reflected in climate change. As a response to this problem, the scientific community has focused on researching new energy sources. One of the technologies that has been given more attention is photovoltaic technology to directly exploit the vast amount of energy reaching the Earth's surface as sunlight. While silicon-based solar cells have dominated the photovoltaic landscape for many years, the search for alternatives decreasing the need for scarce materials or high energy and cost manufacturing processes has led to the development of third-generation photovoltaics. In this context, dye-sensitized solar cells were a breakthrough in the field as they are made of abundant and cheap materials and comprise relatively simple manufacturing processes.

Furthermore, the adaptability of third-generation photovoltaics and large variety of elements make them very appealing for emerging markets and new applications such as building integrated photovoltaics or indoor applications. Perovskite solar cells rapidly emerged from a particular application of dye-sensitized solar cells to a brand new photovoltaic technology in their own right, reaching outstanding efficiencies thanks to their excellent optoelectronic properties. In addition, the natural abundance of the precursors involved in the synthesis of the material also makes them an up-and-coming technology. However, the lack of stability under environmental conditions, the use of expensive materials as part of the operational device acting as selective layers (spiro-OMeTAD) or the use of gold or silver contacts, along with other technical limitations such as the need for inert environments in the manufacturing process have kept this technology from significant market penetration and widespread implementation. The performance of

this perovskite material is complex related to a significant ionic mobility and the resulting effect on the electrical properties, which drive some of the outstanding optoelectronic properties that makes this material so appealing but held for the problems jeopardizing their up-scaling. For this reason, fundamental knowledge of the electronic and ionic properties behind the positive and negative aspects of these materials is highly needed to help optimize them.

The main aim of this thesis is to understand the ionic and electronic dynamics and the physicochemical processes that determine the photovoltaic performance under operating conditions and the long-term stability of these hybrid nanostructured materials. To accomplish this objective, small-signal perturbation optoelectronic techniques have been used, together with numerical drift-diffusion simulations. The combination of both methods helps to cast light on the electronic and ionic phenomena that determine the functioning of the device as well as the key interplay between them. In this context, the similarities between already understood systems such as dye-sensitized solar cells with the materials studied in this thesis are used to identify and interpret the different signals obtained from small signal perturbation optoelectronic techniques. In addition, combining these experimental techniques with numerical simulations has proven to be, in this thesis, an instrumental approach to understanding the physical meaning of the elements identified in experimental spectra allowing for their interpretation and understanding their role in determining the photovoltaic properties of the device under operation conditions.

Contributions to the Scientific Community

The most relevant publications resulting from this thesis are:

1. *Identification of recombination losses and charge collection efficiency in a perovskite solar cell by comparing impedance response to a drift-diffusion model*
   Antonio J. Riquelme[#],Laurence J. Bennett[#], Nicola E. Courtier, Matthew J. Wolf, Lidia Contreras-Bernal, Alison B. Walker, Giles Richardson and Juan A. Anta. Nanoscale. **2020**, 12, 17385 – 17398.

2. *Internal quantum efficiency and time signals from intensity-modulated photocurrent spectra of perovskite solar cells*
   Antonio J. Riquelme[#], Francisco Enrique Gálvez[#], Lidia Contreras-Bernal, Hernán Míguez and Juan A. Anta. *J. Appl. Phys.* **2020**, 128, 133103.

3. *Characterization of photochromic dye solar cells using small-signal perturbation techniques*
   Antonio J. Riquelme, Valid Mwatati Mwalukuku, Patricia Sánchez-Fernández, Johan Liotier, Renán Escalante, Gerko Oskam, Renaud Demadrille, and Juan A. Anta. *ACS Appl. Energy Mater.* **2021**, 4, 9, 8941 – 8952.

4. *Illumination intensity dependence of the recombination mechanism in mixed perovskite solar cells*
   Alejandra Castro-Chong[#], **Antonio J. Riquelme**[#], Tom Aernouts, Laurence J. Bennett, Giles Richardson, Gerko Oskam and Juan A. Anta. *ChemPlusChem.* **2021**, 86(9), 1347 – 1356.

5. *Understanding equivalent circuits in perovskite solar cells. Insights from drift-diffusion simulation*
   Antonio J. Riquelme, Karen Valadez-Villalobos, Pablo P. Boix, Gerko Oskam, Ivan Mora-Seró and Juan A. Anta *Submitted to Phys. Chem. Chem. Phys.*

6. *Inverted hysteresis in normal and inverted perovskite solar cells*
   Rodrigo García-Rodríguez[#], **Antonio J. Riquelme**[#], Matthew Cowley, Karen Valadez-Villalobos, Gerko Oskam, Laurence J. Bennett, Matthew J. Wolf, Lidia Contreras-Bernal, Juan A. Anta, Petra J. Cameron, Alison B. Walker. *Submitted to SolaRRL.*

Other publications closely related to this thesis are listed below:

1. *A new ideality factor for perovskite solar cells and an analytical theory for their impedance spectroscopy response*
   Laurence J. Bennett, **Antonio J. Riquelme**, Nicola E. Courtier, Juan A. Anta, Giles Richardson. *Submitted to Phys. Rev. Appl.* **Published in arXiv**.

2. *Photochromic naphthopyran dyes incorporating a benzene, thiophene or furan spacer: effect on photochromic, optoelectronic and photovoltaic properties in dye-sensitized solar cells*
   Johan Liotier, Valid Mwatati Mwalukuku, Samuel Fauvel, **Antonio J. Riquelme**, Juan A. Anta, Pascale Maldivi, Renaud Demadrille. *SolaRRL.* **2021**.

3. *Electrochemically assisted growth of $CsPbBr_3$ - based solar cells without selective contacts*
   Daniel Ramírez, Gonzalo Riveros, Patricia Díaz, Javier Verdugo, Gerard Núñez, Susy Lizama, Pamela Lazo, Enrique A. Dalchiele,

Daniel L. Gau, Ricardo E. Marotti, Juan A. Anta, Lidia Contreras-Bernal, **Antonio Riquelme**, Jesús Idígoras. *ChemElectroChem.* **2020**, 7(19), 3961 - 3968.

4. *Photochromic dye-sensitized solar cells with light-driven adjustable optical transmission and power conversion efficiency*
   Quentin Huaulmé, Valid M. Mwalukuku, Damien Joly, Johan Liotier, Yann Kervella, Pascale Maldivi, Stéphanie Narbey, Fréderic Oswald, **Antonio J. Riquelme**, Juan Antonio Anta and Renaud Demadrille. *Nature Energy.* **2020**, 5, 468 - 477.

5. *Dealing with climate parameters in the fabrication of perovskite solar cells under ambient conditions*
   Lidia Contreras-Bernal, **Antonio Riquelme**, Juan Jesús Gallardo, Javier Navas, Jesús Idígoras and Juan A. Anta. *ACS Sustainable Chem. Eng.* **2020**, 8(18), 7132 - 7138.

6. *Intensity-modulated photocurrent spectroscopy and its application to perovskite solar cells*
   Sandheep Ravishankar, **Antonio Riquelme**, Shaibal K. Sarkar, Marisé Garcia-Batlle, Germà Garcia-Belmonte and Juan Bisquert. *J. Phys. Chem. C.* **2019**, 123(41), 24995 - 25014.

7. *Impedance analysis of perovskite solar cells: a case study*
   Lidia Contreras-Bernal, Susana Ramos-Terrón, **Antonio Riquelme**, Pablo P. Boix, Jesús Antonio Idígoras, Iván Mora Seró and Juan A. Anta. *J. Mater. Chem. A.* **2019**, 7, 12191 - 12200.

# Both authors contributed equally to this work

Contents

Chapter 1

Introduction

Abstract

This Chapter provides a general description of the global context surrounding this thesis. It begins with a brief introduction of the current situation and the role of emerging photovoltaic technologies facing global challenges. It continues with a detailed description of the two primary material families studied in this thesis. Finally, the main focus and objectives pursued in this study are presented.

1.1 Global situation and background

It is well-known the anthropogenic impact on climate change, mainly through the emissions of greenhouse effect gases[1–3]. The worldwide energy demand is steadily growing, except for the year 2020, when industrial activity suffered an impasse due to the COVID-19 pandemic and the global confinements[4,5]. The increase in energy demand is caused by both the growth of global population[6] and the growing per capita energy consumption, especially in developing countries[7,8]. Social justice dictates that the countries that are now experiencing economic growth and development have the right to use the energy needed to do so[9]. However, to ensure the availability of energetic resources to supply the increasing demand, renewable energies are needed. As sunlight is a natural resource shared on all the surfaces of the Earth, photovoltaic (PV) energy has a significant role in overcoming this challenge[10].

Although the solar resource is the most democratic energy source, the means to exploit it are not equally distributed. Currently, China is the main manufacturer of silicon materials for PV applications. This fact gives this country a huge role in the renewable energies development of the coming years and a strong position affecting the supply and cost of this material. In addition, the global market of this material is strongly affected by the decisions made towards this industry in this country[11–14]. Apart from sociopolitical considerations, the beginning of the 2020s has already proven beyond doubt how dangerous it is to base a worldwide industry on a few locally distributed suppliers. COVID-19 pandemic produced a temporal collapse of most industrial activity across the world. As China has become the “factory of the world,” this crisis lead to a break in most worldwide supply chains[15]. Among many other industries, the PV sector was also severely affected by this situation[16,17]. In addition, to rely on a few distant supply sources implies inherent risks, such as casual incidents causing bottlenecks in the supply chain[18]. A fine example of what these situations produce is what happened on March 23, 2021, when the Ever Given container ship blocked the Suez Canal for six days. This accident stopped most trade routes between Eastern and Western countries[19,20], including the silicon materials from China used for building PV installations all over the world. Finally, the European Union has faced a new energy crisis during 2021 due to the risk of shortage of gas supply[21,22], which has been worsen due to the conflict in Ukraine. This situation supposes a new example of the hazards of relying on the energy supply of local economies on third-party agents and draws some parallels with the oil crisis in 1973[23] that boosted the modern PV development. This scene, together with the economic aftermath of dealing with COVID-19 pandemics, has led to a so-called new European Green Deal aiming for economic reconstruction, where PV technologies are expected to have a meaningful role[24].

It is important to consider threats and hazards, but also, new market niches have arisen where the properties of silicon-based solar cells lose their competitive edge. The increase of environmental, social awareness and the acceptance of electrical self-consumption opens the building integrated photovoltaics (BIPV) in urban environments. In addition, energy losses across the distribution nets suppose a pressing concern[25]. Thus, the development of decentralized power generation systems is important, especially for supplying rural and isolated areas. For this use, the properties of opacity and rigidity of silicon are not suitable. However, new PV technologies such as dye-sensitized solar cells (DSSC), perovskites solar cells (PSC) or organic photovoltaics (OPV) are currently being studied for these applications[26–28]. The rising of technologies such as home automation and internet of things[29] provide new challenges and opportunities for energy management[30,31]. Power supplying the sensors and circuits involved in smart things requires a major development of batteries or external energy sources. As most of these smart elements are located in rooms, the development of new PV technologies with high efficiencies harvesting the indoor light rather than the direct sunlight has become a hot topic[32–35].

Throughout the XXth and XXIst centuries, the energy landscape in general and PV, in particular, have evolved, and different technologies have risen[36]. Not all of them have established a market footprint with the same depth, and some technologies presented issues beyond the efficiencies reached. Nonetheless, this research paved the understanding of PV and settled the roots of new technologies. In Figure 1.1 the evolution of efficiencies officially reported for the different PV technologies since 1976 is presented.

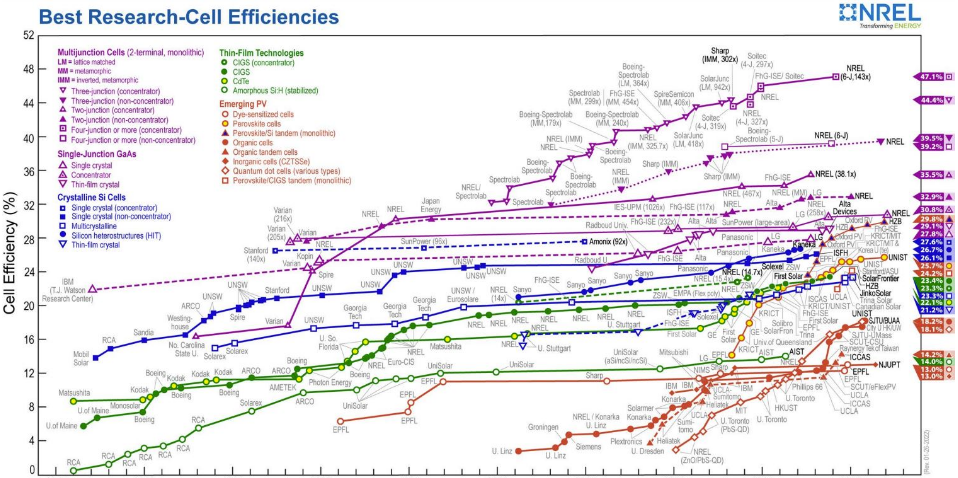

Figure 1.1: Best research-cell efficiency chart with the highest confirmed conversion efficiencies for a range of PV technologies from 1976 to the present by National Renewable Energy Laboratory (NREL)[37] (Consulted the 20th april 2022).

The most widely extended commercial solar cells are based on single and polycrystalline silicon modules. This prominence is due to their high power conversion efficiency (PCE) with records at the moment of writing this thesis of 26.1% and 23.3% respectively[37]. However, the required thickness of these materials (~500 μm) implies high demand for raw materials. This limitation led to the emergence of the second generation of PV technologies[38], focused on reducing the thickness of the devices, reaching the nm – μm range. The technologies included in this generation that reached commercial levels of development were amorphous silicon (a-Si)[39], cadmium telluride (CdTe)[40] and copper indium gallium selenide (CIGS)[41]. Although the general efficiencies remained below the silicon threshold, CdTe and CIGS-based modules reached competitive efficiencies of 22.1% and 23.4%, respectively[37]. However, these high-performance materials rely on scarce raw materials that require high energy demanding manufacturing processes and that in some cases are toxic[42]. The search for new alternatives using raw materials with high availability and low energy demanding manufacturing processes led to the upsurge of the third PV generation[43]. The materials included in this group are based on abundant and cheap materials with limited toxicity and environmental impact such as DSSCs[44], OPV[45], quantum dots (QD)[46] and PSCs[47]. Among these technologies, PSCs present an outstanding record efficiency of 25.7%, although concerns regarding its stability jeopardize its market penetration. DSSCs and OPVs, on the other hand, show more modest performances, with record efficiencies of 13.0% and 18.2%, respectively. However, their higher stability, availability for producing flexible modules, and tunable optoelectronic properties make them very appealing for the new niche applications previously described.

1.2 New generation thin film technologies

In Figure 1.1 the emerging PV technologies stand out for their rapid development in a very short time. A much clearer view is allowed in Figure 1.2

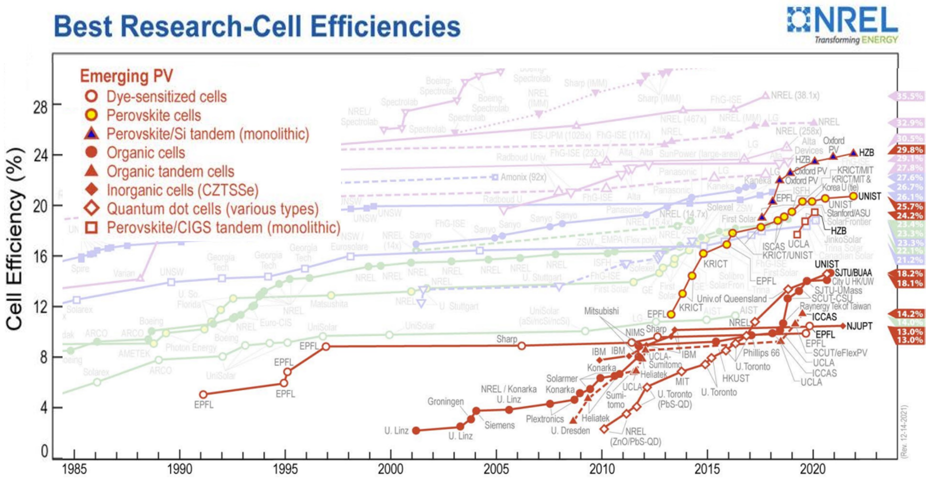

Figure 1.2: Best research-cell efficiency chart with the highest confirmed conversion efficiencies for emerging PV technologies from 1976 to the present by National Renewable Energy Laboratory (NREL)[37] (Consulted the 20^{th} april 2022).

In Figure 1.2, the rapid rise of PSCs is noteworthy. It has almost doubled its efficiency in 7 years, reaching a current record of 25.7%[37]. This rise is the outcome of very fruitful research over the last years since 2009 when Kojima and coworkers[48] reported the fabrication of a DSSC using perovskite as dye sensitizer for the TiO_2 electrode reaching a PCE of 3.8%. As noted from its emergence, PSCs and DSSCs development and understanding are entangled, and both technologies are specific subjects of study in this thesis.

Although DSSCs have not reached such outstanding efficiencies as PSCs, they present other features that appeal to the research community and new market applications. Since the very beginning of the development of DSSCs, by O'Regan and Grätzel, the low cost of manufacturing has been emphasized[44]. In addition, the high versatility of this structure has led to the development of thousands of different dyes[49]. Thus, a huge amount of variables can be researched, understanding the operation of these devices. In addition, the high availability of options increases the possibilities of this technology to adapt to different opportunities, requirements, and uses. Among all these dyes, there is a wide variety of colors, some of them even showing photochromism[50]. These properties enhance the applicability of this technology not only as an energy source but also providing visual attractiveness in their integration with buildings[26,27]. Some other available dyes show outstanding performance harvesting indoor illumination[32–35], opening a second pathway for this technology to reach the market. The customization for these new applications is enhanced by the properties of these devices that allow for making flexible modules[51].

On the other hand, PSCs emerged from a role as dye-sensitizer in DSSCs[48] to develop a new brand technology on their own[47,52,53]. Perovskite materials soon proved not only their efficiency harvesting light as a dye-sensitizer but also behaves as an intrinsic semiconductor that separates the photogenerated charge[54]. This material also shows outstanding optoelectronic properties that have encouraged research and development of this technology seeking higher PCEs, reaching a record efficiency of 25.7% in October 2021[37,55]. Although these high efficiencies are already competing with well-established commercial technologies, some issues are still a drawback for its industrial manufacture[56]. There is a deep concern regarding the stability of the material, which shows chemical and electrical instability that leads to degradation under operation at environmental conditions[57,58] or the toxicity of lead. In addition, further steps towards simplification of the manufacturing methods to suit them to industrial conditions need to be taken[59,60]. Some experimental approaches have been followed to produce PSCs outside the glove box, adapting to environmental conditions in the workplace. This represents a considerable step forward in scaling-up the PSCs manufacturing process to industrial conditions[61–63]. Furthermore, the dual nature of perovskites, the presence of phenomena such as ion migration in the presence of electric fields, etc., presents obscure points in the understanding of the behavior of this kind of material[64] which is a phenomenal scientific intellectual challenge by itself and determine whether perovskites are finally successful in the PV industry or not. Not only there is much effort put on the PV applications of perovskites, but their properties make them very appealing for a whole set of different uses such as light-emitting diodes (LEDs)[65], photoreduction of CO_2 emissions[66] or H_2 and O_2 generation through water splitting[67,68]. This versatility, together with the massive amount of different elements in the perovskite structure or the layers' properties of the device in addition to their dual nature has driven much attention from the research community fueling their curiosity and pushing for unraveling the still unknown properties of this material. In Figure 1.3, it can be observed how, over the last years, both technologies studied in this thesis have gained importance in the development of the PV field.

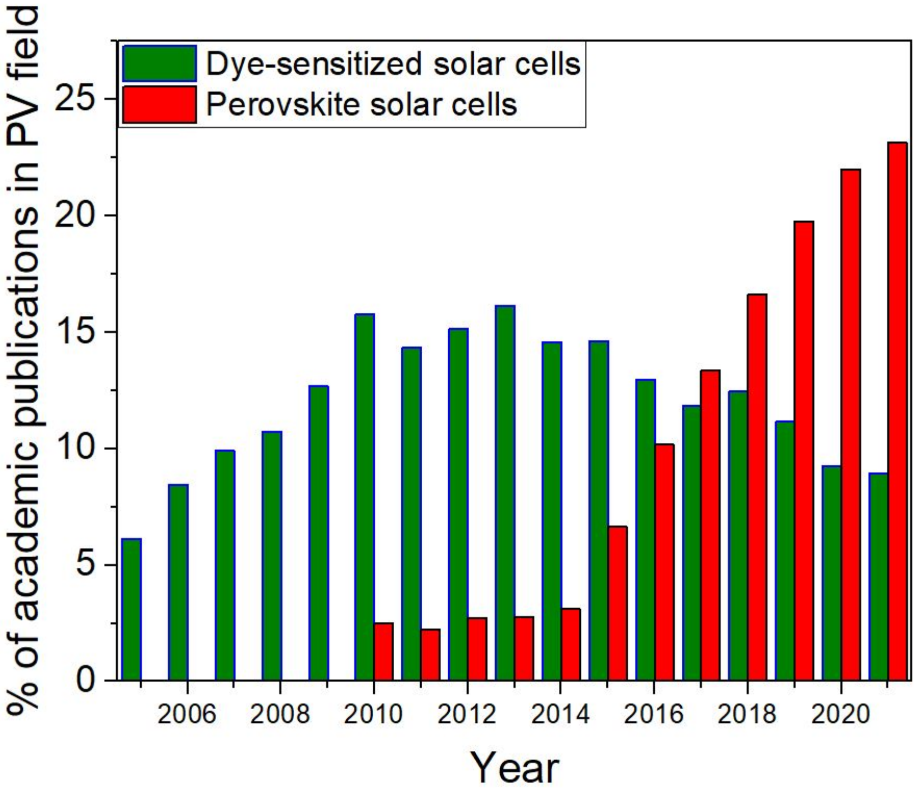

Figure 1.3: Percentage of yearly academic publications (review and research articles) referring to DSSCs (green) and PSCs (red) compared to the total number of publications in the PV field. Yearly data extracted from ScienceDirect website for the 2005-2021 time period.

While DSSCs have attracted steady interest over the last decade, PSCs development has shown strong growth, surpassing DSSCs literary production shortly after its emergence. In addition, the increasing understanding of electrodynamics processes involved in these devices can also be applied to other fields. All this suggests that both DSSCs, PSCs, and other emerging PV technologies will keep showing an upward trend.

1.2.1 Dye-sensitized solar cells

The first reported use of dye-sensitized metal oxide in the presence of electrolyte for energy conversion took place in 1988 by Vlachopoulos and coworkers[69]. However, the DSSC architecture using a mesoporous electrode that is used nowadays was first described by O'Regan and Grätzel in 1991[44]. A DSSC is a photoelectrochemical system. It consists of a transparent electrode coated with a mesoporous layer of metal oxide nanoparticles. The metal oxide is covered by dye molecules, which are the main photoactive element of the system. On the opposite side of the device, a counter-electrode coated with a catalyst for hole extraction closes the circuit. Finally, the whole system is filled with an electrolyte containing a redox mediator. As for the substrates that work as electrodes and counter-electrode, the most commonly used material is glass coated with fluorine-doped tin oxide, known as FTO[49]. A scheme of this device is presented in Figure 1.4.

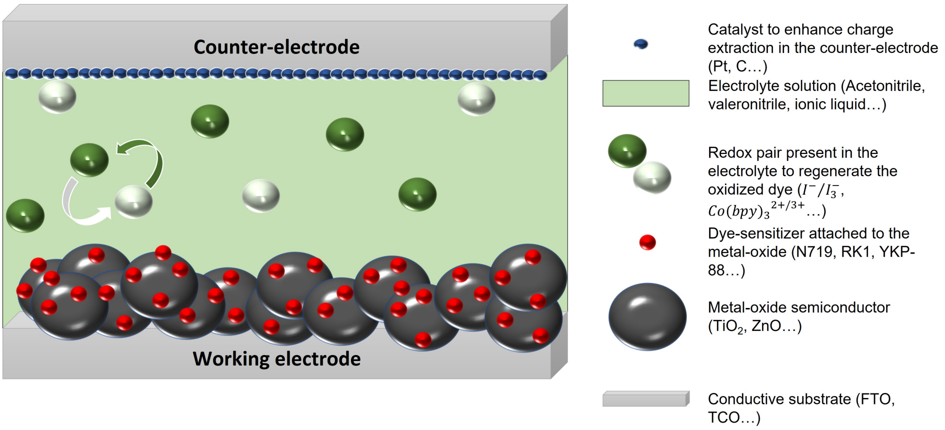

Figure 1.4: Scheme of the architecture of DSSCs.

To be absorbed, the energy of the photons needs to be equal or higher to the difference between the ground (HOMO) and excited (LUMO) energy levels of the dye. When this happens, an electron located in the HOMO level can be excited and reach the LUMO, resulting in an electron-hole pair. If this energy level is above the conduction band (CB) of the metal oxide semiconductor injection of the photogenerated electrons into the CB of the n-type semiconductor is possible. These injected electrons reach the working electrode through diffusion transport mechanisms. The extracted electrons can produce electrical work in the external electrical circuit. As a result of the photogeneration process, the dye molecule is oxidized and remains positively charged. This oxidation is neutralized by a process called regeneration, which can be a limiting aspect for the efficiency of the device[70]. The dye molecule is reduced with a negatively charged redox couple element present in the electrolyte. The now oxidized redox mediator migrates to the counter-electrode, wherein catalyzed chemical reaction is reduced again using the electrons returned to the counter-electrode, so it can participate again in the regeneration process. This way, it can be considered that the electrolyte acts as a hole conductor, equivalent to a p-type material in a traditional n-p junction.

Given that, the system performance is determined by the HOMO and LUMO levels of the dye sensitizer, the Fermi level of the metal oxide semiconductor, and the redox potential of the reactions involving the redox couple[71]. This is a complex system, where the properties of the different components and the interconnections between them determine the optoelectronic and physicochemical properties of the device.

Working electrode

DSSCs studied in this thesis are n-DSSCs, where the metal oxide nanoparticles forming this layer act as an n-type semiconductor, and they work as an electron conductor material. However, p-DSSCs with p-type semiconductors such as NiO are also reported in literature[72,73]. The other central role of this layer is to provide structural support to the dye sensitizer molecules. To account for this dual role, the metal oxide material needs to meet a set of requirements. It is important to have a low enough CB energy to ensure that this selective contact successfully extracts the photogenerated electrons in the dye. On the other hand, the concentration of adhered dye molecules, known as dye loading, depends on the available surface in the metal oxide layer. For this reason, mesoporous structures are used in this type of device. Comparing a mesoporous structure with a flat surface, the available surface for dye absorption with the first option can be several thousand times larger for the same geometric area. Nanostructures with the highest useful surface possible and optimal conducting properties have been widely studied[74,75]. Some examples of this are nanotubes[76,77], nanowires[78–80] or core-shells[81,82]. The properties of the semiconductor can also affect the electron transport and recombination processes inside the device, which are described in detail in *Chapter* 2. In addition to these features, to comply with the philosophy behind the development of DSSC, the material used as a semiconductor needs to be abundant, stable, and non health or environmentally hazardous.

A material that complies with all the requirements described above is TiO_2. It shows mechanical properties that allow for the construction of different mesoporous architectures[83]. This material also presents different crystalline forms working as a semiconductor. Brookite[84] and rutile[85] phases have been used for PV applications, being the second the most thermodynamically stable phase of TiO_2. However, with an energy bandgap (E_g) of 3.2 eV the anatase phase is the most efficient and extended material working as an electrode in DSSCs[86]. Typically, the thickness of this layer is around 10 μm while the nanoparticle diameter is 10 – 30 nm, with a porosity of 50% – 60%[49]. Some alternative materials such as ZnO[87,88] or SnO_2[89] have also been studied but the combination of its optoelectronic properties with low costs makes the anatase TiO_2 films to remain as the most used material for this purpose[75,90,91].

Dye sensitizer

The high E_g of the electrode materials makes them mostly transparent for visible light. For this reason, it is needed to sensitize the electrode with colored molecules able to absorb light in the visible range. For the DSSC to work, the dye molecules need to be anchored to the semiconductor nanoparticles, which is achieved through chemical bonds. Most commercial dyes present for this matter carboxylic acid binding groups[49,92]. It is also important that the anchored dye molecules do not face unfavorable aggregation[49]. For this matter, coadsobers such as chenodeoxycholic acid are usually included to prevent this process[93].

The photogenerated electrons need to be injected into the CB as described before. On the other hand, the excited electrons can also relax and go back to the ground energy level of the dye. Therefore, the excited energy level of the dye needs to be much higher than the CB edge of the semiconductor oxide. For the charge separation to be efficient, the electron injection rate has to be over a hundred times faster than the relaxation of the excited dye[94]. It is needed to account not only for the excited dye energy levels and the semiconductor CB but for the interaction between both elements of the device[91]. On the other hand, for the regeneration process to be also efficient, the oxidized state level of the dye needs to be more positive than the redox potential of the electrolyte[49].

Nowadays there is a vast variety of different dyes, with thousands of different combinations[49]. The most used dyes belong to Ruthenium-complex family (coded N-719, N-3, Z-907...)[95–97]. Alternative molecules have been widely studied by the research community for their interesting optical or electrochemical properties or because their nature made them very appealing for specific applications. Some examples are metal-free organic dyes (coded C-219, RK-1, 6RK-1...)[98–100], or porphyrins (coded LD-14, SM-315...)[101–103], to which belongs SM-315[103], which holds the 13.0% record efficiency for DSSC. In addition, in *Chapter* 4 a new photochromic dye developed by Huaulmé and coworkers[50] is studied.

Electrolyte

The electrolyte in DSSC works as both, hole conductor and as a redox mediator to compensate for the electron injection process between the dye and the metal oxide semiconductor. The electrolyte includes a redox mediator in a solvent and different additives that are not involved in the regeneration process but improve efficiency. These additives usually are Lewis acids and bases, and their major contribution is shifting the electronic band system of the semiconductor[104].

The redox couples move through the solvent between the electrodes by ion diffusion. The reduced species diffuse towards the electrode, regenerating an oxidized dye. The oxidized redox species diffuses back to the counter-electrode, which is reduced by a free electron that reaches the contact from the external circuit. This chemical reaction takes place under the action of a catalyst. These diffusion processes highly depend on the viscosity of the electrolyte solvent and the structural and chemical properties of the redox couple. Therefore, limitations in diffusion transport processes of the ionic species lead to a decrease in the regeneration rate of the dye. In addition, the oxidized ionic species that remains too long in the vicinity of the metal oxide semiconductor surface can behave as electron aceptors, allowing for back recombination of injected electrons. This process is generally considered as one of the most crucial charge loss processes in DSSC[70]. In addition, oxidized dye molecules can recombine with injected electrons in the metal oxide semiconductor. Hence, the dye regeneration kinetics must be much faster than the recombination rate between the oxidized dye and the semiconductor.

The most important element of the electrolyte is the redox couple involved in the dye's regeneration process. I^-/I^{3-} is the classical redox couple used for DSSC[49,71]. However, different redox pairs such as Co^{2+}/Co^{3+}[105], Cu^+/Cu^{2+}[106] or TEMPO/TEMPO$^+$[107] have been explored. As for the solvent, to avoid ionic transport limitations, low viscosity organic solvents such as acetonitrile (ACN)[108] are used. However, these solvents evaporate with time and can suffer leaks, jeopardizing the long-term stability of the device. For this reason, room temperature ionic liquids with high viscosity are also used. These electrolytes present transport limitations, decreasing the efficiency of the cell but enhancing the stability of the device[109].

In addition, solid-state DSSCs combining metal oxide n-type semiconductors with p-type organic semiconductors have also been studied in literature, as they allow for even more stable devices but with very poor efficiencies[110–116].

Counter-electrode

The counter-electrode is needed to close the electrical circuit generated by the DSSC. It consists of a conducting transparent substrate (FTO) coated with a catalyst layer. This element's role is to reduce the redox couple species of the electrolyte that was oxidized during the regeneration process. The action of the catalyst substance accelerates this process. The most used catalyst is platinum[49] but other materials such as graphite[117] or conducting polymers such as PEDOT[118] are being studied to replace the high costs of platinum.

1.2.2 Perovskite solar cells

Perovskite structure owns its name to the mineral with a chemical formula $CaTiO_3$ named after Lev A. Perovski, a Russian mineralogist. The general concept of perovskite relates to minerals with the stoichiometry ABX_3, following the crystalline structure shown in Figure 1.5. Here, A and B are cations, being A larger than B and X is an anion[47].

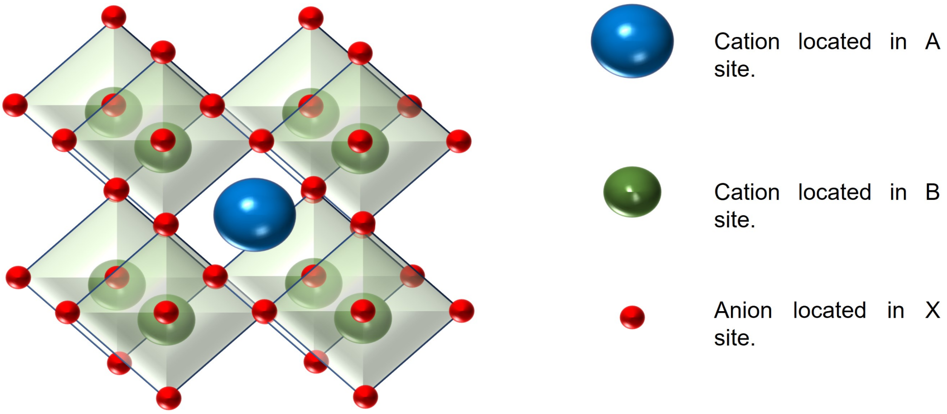

Figure 1.5: Scheme of the perovskite crystalline structure.

Since their discovery, the electrical and optoelectronic characteristics of perovskites have been well studied. These properties have led to the use of this mineral as electronic, magnetic, and refractory materials[119]. For PV applications, the most used perovskite is a synthetic material known as metal halide perovskite (MHP). In this kind of material, the A site is occupied by an inorganic or organic monovalent cation[119]. Many different options have been studied both alone and combining different cations in the so-called multiple cation perovskites[120]. The most common cations that have been studied are methyl-ammonium ($CH_3NH_3^+$), formamidinium ($CH_2(NH_2)_2^+$), rubidium (Rb^+) or cesium (Cs^+)[119,121]. This element of the structure is electronically neutral. However, it can indirectly affect the E_g of the material by changing the crystalline structure[119]. The B site corresponds to a divalent inorganic cation, being lead (Pb^{2+}) the most dominant option[71,119]. The element present in this site determines the lower CB of the material[119]. The toxicity of the lead is one of the most pressing concerns affecting the scaling-up of PSCs. This is the reason why several studies trying to replace this element have been conducted, being tin (Sn^{2+}) one of the most promising options[122–124]. Finally, the X site includes a halide anion such as iodine (I^-), fluorine (F^-), chlorine (Cl^-), or bromide (Br^-). The X site is responsible for the upper valence band (VB) of the perovskite material[119].

The characteristic optoelectronic properties of these materials make them very appealing for PV applications[125,126]. These materials show a very tuneable band gap, from 1.5 to 3.6 eV[119,125], which allows them for optical absorption at a wide range of the solar spectrum, as it will be discussed in detail in *Chapter* 2. This tuneability is possible by changing CB or VB by replacing the B and X sites or altering the crystalline structure with different elements in the A site. In addition, the nature of the bonds of the crystalline structure lead to high charge mobility[127,128] and low non-radiative recombination rate[127]. These properties are related to the strong ionicity of the metal-halide bond[127,128] and the characteristic high defect tolerance[129] of this kind of material, respectively. This high tolerance allows PSCs to reach open-circuit photovoltages (OCP) almost at the thermodynamic limit[129]. These concepts will be discussed in detail in *Chapter* 2. This high diffusion mobility and low recombination rate lead to diffusion lengths in the range of micrometers under solar illumination[130,131]. This diffusion length is much larger than the thickness of perovskite films, which are in the range of hundreds of nanometers. This implies that PSCs show outstanding charge collection efficiencies (CCE), as will be explained in *Chapter* 2.

Perovskite solar cells architecture

To enhance the separation of the photogenerated electron-hole pairs, the perovskite film is sandwiched between an electron transport layer (ETL) and a hole transport layer (HTL). In the most widely used structure, the ETL is coated on a conductive glass (FTO) similar to that used in DSSC. This layer acts as a front electrode. Although this would be enough to ensure a good charge separation, an additional mesoporous layer as a scaffold to the perovskite layer deposition is normally included. This additional element improves the stability and charge extraction of the device, and avoids the direct contact between the perovskite and the front contact, improving the overall efficiency of the device[132–134]. To electrically close the circuit, a metallic material such as gold (Au) or silver (Ag) is evaporated on top of the HTL to act as back contact[71]. As an attempt to decrease the overall costs of these devices, other abundant metals have been explored[135]. A sketch of this regular (n-i-p) structure of PSC is shown in Figure 1.6.

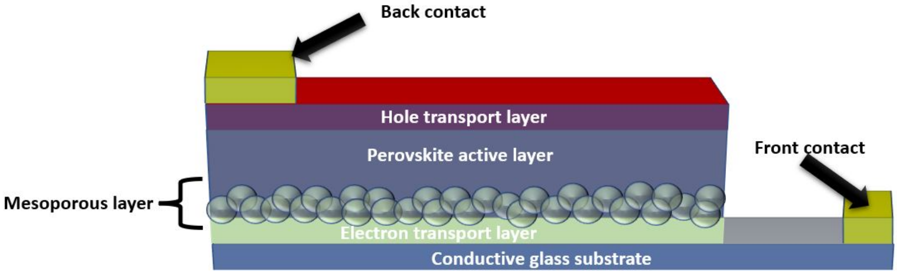

Figure 1.6: Scheme of a regular (n-i-p) PSC structure with mesoporous layer.

In Figure 1.6 the regular (n-i-p) PSC is shown. Nonetheless, this is not the only configuration that has been studied for this kind of devices. The presence or absence of the mesoporous layer distinguish between planar and mesoporous cells. In *Chapters* 5 and 7 the studied PSCs have a mesoporous n-i-p configuration. On the other hand, the simulated PSCs that are included in *Chapters* 6 and 8 correspond to planar (n-i-p) configuration. In addition, if instead of the ETL the layer that is deposited in contact with the conductive glass is the HTL, the architecture is called inverted (p-i-n)[136]. In this thesis, the cells studied in *Chapter* 9 are of this configuration. Although they are beyond the scope of this thesis, several different architectures have been studied in the literature. Tandem solar cells have been widely studied because the possibility of combining materials with different E_g allows for an optimized absorption of light. For this reason, both, silicon/perovskite[137] and perovskite/perovskite[138] tandem cells have been studied. Another configuration that has gained relevance for its stability and its potential industrial scale-up is the triple-stack configuration[139]. The perovskite is infiltrated in all the layers in this kind of device instead of following a sandwiched structure. An ETL of mesoporous TiO_2 is screen printed on a front contact conductive glass coated with compact TiO_2, followed by a mesoporous insulating layer of ZrO_2 or Al_2O_3 and a porous conductive carbon layer acts as the top contact. As mentioned before, the perovskite solution is infiltrated in the three layers where the crystallization process of the perovskite occurs. There is no HTL in this device, but it relies on the perovskite ambipolarity for hole separation.

Electron transport layer

The role of the ETL is similar to the metal oxide nanoparticles described in the DSSCs section, working as a selective material for electrons. Unlike the dye molecules, which are adhered to the metal oxide nanoparticles, perovskite crystallize on top of this layer. As happened with DSSCs, TiO_2 is the most used material for this role, for similar reasons. However, different materials have been studied for this use: Metal oxides such as ZnO[140], SnO_2[141], or sulfides such as CdS[142] and organic materials such as PCBM[143] have been tried to replace TiO_2, which still remains as the most used option[144]. As for scaffold, different selective or insulating metal oxides have been used, such as ZrO_2[145], Al_2O_3[146] or SiO_2[147] and hetero-structures nanoparticles such as Al_2O_3/ZnO, TiO_2/MgO or WO_3/TiO_2 to increase the Fermi level of the ETL[144].

Hole transport layer

Unlike in the typical DSSCs described before, here, the material acting as selective hole contact is not an electrolyte solution but a solid-state layer (similar to the solid-state DSSCs mentioned before). The most widely used material acting as HTL is an organic molecule with the name of spiro-OMeTAD[148,149] and with formula 2,2',7,7'-tetrakis-(N,N-di-4-methoxyphenyl-amino)-9,9' spirobi-fluorene. To rise the mobility of this material, it is normally doped with lithium and cobalt salts[150]. In addition, to improve the homogeneity of this layer, spiro-OMeTAD is also doped with TBP (4-tert-butylpiridine)[148]. However, these additives also increase the hygroscopicity of the material, reducing the stability of the devices under ambient conditions. To counter this damaging effect, a widespread solution is the encapsulation of the devices[151,152]. An alternative approach to solve this problem is the investigation for new dopants that do not induce this increase of hygroscopicity[153,154] or developing alternative deposition processes of spiro-OMeTAD avoiding the presence of additives[155]. Another pressing issue with this material is the high costs of its production due to the high-purity sublimation-grade and complex multi-step synthesis process required for its fabrication. Thus, different materials have been studied to replace spiro-OMeTAD as selective hole contact. Both, inorganic[156–158] and organic[159–162] materials have been studied.

1.3 Motivation and focus of this research

The pursuit of new PV materials has attracted much interest from the research community. To achieve this, several different approaches have been used. Given the massive amount of different variables and interconnections between the different properties of the devices, trial and error strategies are not advisable. There is still much work to do to achieve higher performance devices and solve the issues that still difficult the commercial applications of these materials. It is crucial to gain further comprehension of the electronic and physicochemical processes behind the behavior of PV materials. In addition, the information and knowledge that can be grasped by studying systems so interesting and particular as PSCs are a priceless addition to the

PV research world. This acquired knowledge can be applied to developing new kinds of materials not only in the PV harvesting field. Therefore, this thesis is based on two main objectives:

- To comprehend the fundamental electronic and ionic dynamics involved in generation, transfer, and recombination processes. By learning the role of these critical factors in the performance of the devices, further steps can be taken to develop higher efficiency and stability devices with low toxicity materials.
- To develop advanced characterization protocols that can be of use for any new generation solar cells.

For that purpose, small signal perturbation optoelectronic techniques have been used to determine the electrodynamic behavior of PV devices, focusing on PSCs and both regular and photochromic DSSCs. These techniques also allow for detecting and analyzing individual internal processes, separating pure electronic processes from ionic-driven mechanisms. To gain understanding on these phenomena, the analysis and interpretation of experimental data obtained with these techniques have been combined with drift-diffusion (DD) modeling.

A brief theoretical introduction of the PV devices studied in this thesis, the main small perturbation optoelectronic techniques, and the models are presented in *Chapters* 2 and 3. The main experimental results of this thesis are gathered in *Chapters* 4 and 5 where small perturbation optoelectronic techniques are used to describe the behavior of photochromic DSSC and PSCs, respectively, compared to regular DSSCs. In *Chapters* 6 a novel three-layer DD model is used to gain an understanding of the electronic and ionic dynamics affecting the impedance. *Chapter* 7 focuses on the application of a novel definition of electronic ideality factor[163] to determine the main electronic recombination pathway of PSCs. In *Chapter* 8 the three-layer

DD model is used to compare and gain insight on the physical meaning of two common equivalent circuits (EC) as a tool to interpret impedance spectroscopy of PSCs. Finally, in *Chapter* 9 the same three-layer DD model is applied to address the source behind unusual phenomena such as inverted hysteresis, which is usually related to stability issues of PSCs.

Bibliography

[1] N. Oreskes, "The Scientific Consensus on Climate Change," *Science*, vol. 306, pp. 1686–1686, Dec. 2004. Publisher: American Association for the Advancement of Science Section: Essays on Science and Society.

[2] P. C. Jain, "Greenhouse effect and climate change: scientific basis and overview," *Renewable Energy*, vol. 3, pp. 403–420, June 1993.

[3] G. T. Farmer and J. Cook, *Climate Change Science: A Modern Synthesis*. Dordrecht: Springer Netherlands, 2013.

[4] A. Bahmanyar, A. Estebsari, and D. Ernst, "The impact of different COVID-19 containment measures on electricity consumption in Europe," *Energy Research & Social Science*, vol. 68, p. 101683, Oct. 2020.

[5] E. Buechler, S. Powell, T. Sun, N. Astier, C. Zanocco, J. Bolorinos, J. Flora, H. Boudet, and R. Rajagopal, "Global changes in electricity consumption during COVID-19," *iScience*, vol. 25, p. 103568, Jan. 2022.

[6] "World Population Prospects - Population Division - United Nations - Department of Economic and Social Affairs Population Dynamics *https://population.un.org/wpp/Graphs/Probabilistic/POP/TOT/900* Accessed december, 30th 2021."

[7] S. Bhattacharya and M. Bhattacharya, "Economic growth and Energy consumption nexus in Developing World: The case of China and India," *Journal of Applied Economics and Business Research*, vol. 4, pp. 150–67, Sept. 2014.

[8] B. Muhammad, M. K. Khan, M. I. Khan, and S. Khan, "Impact of foreign direct investment, natural resources, renewable energy consumption, and economic growth on environmental degradation: evidence from BRICS, developing, developed and global countries," *Environmental Science and Pollution Research*, vol. 28, pp. 21789–21798, May 2021.

[9] C. A. Hall and K. Klitgaard, *Energy and the Wealth of Nations*. Cham: Springer International Publishing, 2018.

[10] M. Victoria, N. Haegel, I. M. Peters, R. Sinton, A. Jäger-Waldau, C. del Cañizo, C. Breyer, M. Stocks, and A. Smets, "Solar photovoltaics is ready to power a sustainable future," *Joule*, vol. 5, no. 5, pp. 1041–1056, 2021.

[11] N. K. a. J. Voas, "Where's the Silicon?," *Computer*, vol. 54, no. 08, pp. 11–12, 2021.

[12] S. M. Heidari and A. Anctil, "Material Requirement and Resource Availability for Silicon Photovoltaic Laminate Manufacturing in the Next 10 Years," in *2021 IEEE 48th Photovoltaic Specialists Conference (PVSC)*, pp. 1768–1772, June 2021. ISSN: 0160-8371.

[13] "How China's 'silicon' move has thrown global economic recovery in jeopardy," Oct. 2021. Section: News.

[14] J. Voas, N. Kshetri, and J. F. DeFranco, "Scarcity and Global Insecurity: The Semiconductor Shortage," *IT Professional*, vol. 23, pp. 78–82, Sept. 2021. Conference Name: IT Professional.

[15] X. Li, A. Ghadami, J. M. Drake, P. Rohani, and B. I. Epureanu, "Mathematical model of the feedback between global supply chain disruption and COVID-19 dynamics," *Scientific Reports*, vol. 11, p. 15450, July 2021.

[16] C. Wang, X. Huang, X. Hu, L. Zhao, C. Liu, and P. Ghadimi, "Trade characteristics, competition patterns and COVID-19 related shock propagation in the global solar photovoltaic cell trade," *Applied Energy*, vol. 290, p. 116744, May 2021.

[17] E. Marsillac, "COVID-19 effects on the global PV supply chain," in *2021 IEEE 48th Photovoltaic Specialists Conference (PVSC)*, pp. 2630–2631, June 2021. ISSN: 0160-8371.

[18] D. Ivanov, "Supply Chain Risks, Disruptions, and Ripple Effect," in *Introduction to Supply Chain Resilience: Management, Modelling, Technology* (D. Ivanov, ed.), Classroom Companion: Business, pp. 1–28, Cham: Springer International Publishing, 2021.

[19] I. A. Khan and S. Rahman, "Review and Analysis of Blockage of Suez Canal Region Due to Giant Container Ship," *Marine Technology Society Journal*, vol. 55, pp. 39–43, Sept. 2021.

[20] S. Schiffling and N. V. Kanellos, "How the Ever Given exposed the fragility of global supply chains," *Other*, Apr. 2021.

[21] "The emerging global natural gas market and the energy crisis of 2021-2022," *Foreign Policy*.

[22] D. G. Golea, "The Security Management System from the Perspective of the Global Energy Crisis and the Extended Black Sea Region Escalating Conflict," SSRN Scholarly Paper ID 3845296, Social Science Research Network, Rochester, NY, May 2021.

[23] C. Issawi, "The 1973 Oil Crisis and After," *Journal of Post Keynesian Economics*, vol. 1, pp. 3–26, Dec. 1978. Publisher: Routledge _eprint: https://doi.org/10.1080/01603477.1978.11489099.

[24] I. Kougias, N. Taylor, G. Kakoulaki, and A. Jäger-Waldau, "The role of photovoltaics for the European Green Deal and the recovery plan," *Renewable and Sustainable Energy Reviews*, vol. 144, p. 111017, July 2021.

[25] M. T. Costa-Campi, D. Daví-Arderius, and E. Trujillo-Baute, "The economic impact of electricity losses," *Energy Economics*, vol. 75, pp. 309–322, Sept. 2018.

[26] H. Andreas, "BIPV: Built-in solar energy," *Renewable Energy Focus*, vol. 9, pp. 14–19, Dec. 2008.

[27] M. Pagliaro, R. Ciriminna, and G. Palmisano, "BIPV: merging the photovoltaic with the construction industry," *Progress in Photovoltaics: Research and Applications*, vol. 18, no. 1, pp. 61–72, 2010.

[28] S. Yoon, S. Tak, J. Kim, Y. Jun, K. Kang, and J. Park, "Application of transparent dye-sensitized solar cells to building integrated photovoltaic systems," *Building and Environment*, vol. 46, pp. 1899–1904, 2011.

[29] F. Wortmann and K. Flüchter, "Internet of Things," *Business & Information Systems Engineering*, vol. 57, pp. 221–224, June 2015.

[30] M. A. M. Sadeeq and S. Zeebaree, "Energy Management for Internet of Things via Distributed Systems," *Journal of Applied Science and Technology Trends*, vol. 2, pp. 59–71, Apr. 2021.

[31] A. H. Mohd Aman, N. Shaari, and R. Ibrahim, "Internet of things energy system: Smart applications, technology advancement, and open issues," *International Journal of Energy Research*, vol. 45, no. 6, pp. 8389–8419, 2021. _eprint: https://onlinelibrary.wiley.com/doi/pdf/10.1002/er.6451.

[32] M. Freitag, J. Teuscher, Y. Saygili, X. Zhang, F. Giordano, P. Liska, J. Hua, S. M. Zakeeruddin, J.-E. Moser, M. Grätzel, and A. Hagfeldt, "Dye-sensitized solar cells for efficient power generation under ambient lighting," *Nature Photonics*, vol. 11, pp. 372–378, June 2017.

[33] H. Michaels, M. Rinderle, R. Freitag, I. Benesperi, T. Edvinsson, R. Socher, A. Gagliardi, and M. Freitag, "Dye-sensitized solar cells under ambient light powering machine learning: towards autonomous smart sensors for the internet of things," *Chemical Science*, vol. 11, pp. 2895–2906, Mar. 2020.

[34] S. Biswas and H. Kim, "Solar Cells for Indoor Applications: Progress and Development," *Polymers*, vol. 12, p. 1338, June 2020.

[35] B. Li, B. Hou, and G. A. J. Amaratunga, "Indoor photovoltaics, The Next Big Trend in solution-processed solar cells," *InfoMat*, vol. 3, no. 5, pp. 445–459, 2021. _eprint: https://onlinelibrary.wiley.com/doi/pdf/10.1002/inf2.12180.

[36] T. M. Razykov, C. S. Ferekides, D. Morel, E. Stefanakos, H. S. Ullal, and H. M. Upadhyaya, "Solar photovoltaic electricity: Current status and future prospects," *Solar Energy*, vol. 85, pp. 1580–1608, Aug. 2011. Publisher: Elsevier Limited.

[37] "Best Research-Cell Efficiency Chart – National Renewable Energy Laboratory *https://www.nrel.gov/pv/cell-efficiency.html* Accessed April, 20th 2022."

[38] A. G. Aberle, "Thin-film solar cells," *Thin Solid Films*, vol. 517, pp. 4706–4710, July 2009.

[39] R. Galloni, "Amorphous silicon solar cells," *Renewable Energy*, vol. 8, pp. 400–404, May 1996.

[40] C. S. Ferekides, U. Balasubramanian, R. Mamazza, V. Viswanathan, H. Zhao, and D. L. Morel, "CdTe thin film solar cells: device and technology issues," *Solar Energy*, vol. 77, pp. 823–830, Dec. 2004.

[41] T. Feurer, P. Reinhard, E. Avancini, B. Bissig, J. Löckinger, P. Fuchs, R. Carron, T. P. Weiss, J. Perrenoud, S. Stutterheim, S. Buecheler, and A. N. Tiwari, "Progress in thin film CIGS photovoltaics – Research and development, manufacturing, and applications," *Progress in Photovoltaics: Research and Applications*, vol. 25, no. 7, pp. 645–667, 2017. _eprint: https://onlinelibrary.wiley.com/doi/pdf/10.1002/pip.2811.

[42] T. Dittrich, *Materials Concepts for Solar Cells*. New Jersey: Imperial College Press, Nov. 2014.

[43] M. A. Green, *Third generation photovoltaics: advanced solar energy conversion*. Birkhäuser, 2006.

[44] B. O'Regan and M. Gratzel, "A Low-Cost, High-Efficiency Solar-Cell Based on Dye-Sensitized Colloidal Tio2 Films," *Nature*, vol. 353, no. 6346, pp. 737–740, 1991.

[45] A. M. Bagher, "Introduction to Organic Solar Cells," *Sustainable Energy*, vol. 2, pp. 85–90, Jan. 2014. Number: 3 Publisher: Science and Education Publishing.

[46] I. J. Kramer and E. H. Sargent, "Colloidal Quantum Dot Photovoltaics: A Path Forward," *ACS Nano*, vol. 5, no. 11, pp. 8506–8514, 2011.

[47] M. A. Green, A. Ho-Baillie, and H. J. Snaith, "The emergence of perovskite solar cells," *Nature Photonics*, vol. 8, p. 506, July 2014.

[48] A. Kojima, K. Teshima, Y. Shirai, and T. Miyasaka, “Organometal halide perovskites as visible-light sensitizers for photovoltaic cells,” vol. 131, no. 17, pp. 6050–6051.

[49] A. Hagfeldt, G. Boschloo, L. Sun, L. Kloo, and H. Pettersson, “Dye-Sensitized Solar Cells,” *Chemical Reviews*, vol. 110, pp. 6595–6663, Nov. 2010.

[50] Q. Huaulmé, V. M. Mwalukuku, D. Joly, J. Liotier, Y. Kervella, P. Maldivi, S. Narbey, F. Oswald, A. J. Riquelme, J. A. Anta, and R. Demadrille, “Photochromic dye-sensitized solar cells with light-driven adjustable optical transmission and power conversion efficiency,” *Nature Energy*, pp. 1–10, 2020.

[51] A. Fakharuddin, R. Jose, T. M. Brown, F. Fabregat-Santiago, and J. Bisquert, “A perspective on the production of dye-sensitized solar modules,” *Energy & Environmental Science*, vol. 7, no. 12, pp. 3952–3981, 2014.

[52] B. E. Hardin, H. J. Snaith, and M. D. McGehee, “The renaissance of dye-sensitized solar cells,” vol. 6, no. 3, pp. 162–169.

[53] H. J. Snaith, “Perovskites: The Emergence of a New Era for Low-Cost, High-Efficiency Solar Cells,” *The Journal of Physical Chemistry Letters*, vol. 4, pp. 3623–3630, Nov. 2013.

[54] S. D. Stranks, G. E. Eperon, G. Grancini, C. Menelaou, M. J. P. Alcocer, T. Leijtens, L. M. Herz, A. Petrozza, and H. J. Snaith, “Electron-hole diffusion lengths exceeding 1 micrometer in an organometal trihalide perovskite absorber,” vol. 342, no. 6156, pp. 341–344.

[55] H. Min, D. Y. Lee, J. Kim, G. Kim, K. S. Lee, J. Kim, M. J. Paik, Y. K. Kim, K. S. Kim, M. G. Kim, T. J. Shin, and S. Il Seok, “Perovskite solar cells with atomically coherent interlayers on SnO2 electrodes,” *Nature*, vol. 598, pp. 444–450, Oct. 2021. Bandiera_abtest: a Cg_type: Nature Research Journals Number: 7881 Primary_atype: Research Publisher: Nature Publishing Group Subject_term: Devices for energy harvesting;Solar cells Subject_term_id: devices-for-energy-harvesting;solar-cells.

[56] L. Qiu, L. K. Ono, and Y. Qi, “Advances and challenges to the commercialization of organic–inorganic halide perovskite solar cell technology,” *Materials Today Energy*, vol. 7, pp. 169–189, Mar. 2018.

[57] S. Gholipour and M. Saliba, “From Exceptional Properties to Stability Challenges of Perovskite Solar Cells,” *Small*, vol. 14, no. 46, p. 1802385, 2018. _eprint: https://onlinelibrary.wiley.com/doi/pdf/10.1002/smll.201802385.

[58] I. Mesquita, L. Andrade, and A. Mendes, “Perovskite solar cells: Materials, configurations and stability,” *Renewable and Sustainable Energy Reviews*, Sept. 2017.

[59] H. S. Jung and N.-G. Park, “Perovskite Solar Cells: From Materials to Devices,” *Small*, vol. 11, pp. 10–25, Jan. 2015.

[60] A. Abate, J.-P. Correa-Baena, M. Saliba, M. S. Su’ait, and F. Bella, “Perovskite Solar Cells: From the Laboratory to the Assembly Line,” *Chemistry – A European Journal*, vol. 24, no. 13, pp. 3083–3100, 2018. _eprint: https://onlinelibrary.wiley.com/doi/pdf/10.1002/chem.201704507.

[61] L. Contreras-Bernal, C. Aranda, M. Valles-Pelarda, T. T. Ngo, S. Ramos-Terrón, J. J. Gallardo, J. Navas, A. Guerrero, I. Mora-Seró, J. Idígoras, and J. A. Anta, “Homeopathic Perovskite Solar Cells: Effect of Humidity during Fabrication on the Performance and Stability of the Device,” *The Journal of Physical Chemistry C*, Feb. 2018.

[62] G. Wang, C. Liu, W. Kong, H. Chen, D. Li, A. Amini, B. Xu, and C. Cheng, “Liberating Researchers from the Glovebox: A Universal Thermal Radiation Protocol Toward Efficient Fully Air-Processed Perovskite Solar Cells,” *Solar RRL*, vol. 3, no. 5, p. 1800324, 2019.

[63] L. Contreras-Bernal, A. Riquelme, J. J. Gallardo, J. Navas, J. Idigoras, and J. A. Anta, “Dealing with Climate Parameters in the Fabrication of Perovskite Solar Cells under Ambient Conditions,” *ACS Sustainable Chemistry & Engineering*, Apr. 2020.

[64] Egger David A., Bera Achintya, Cahen David, Hodes Gary, Kirchartz Thomas, Kronik Leeor, Lovrincic Robert, Rappe Andrew M., Reichman David R., and Yaffe Omer, “What remains unexplained about the properties of halide perovskites?,” vol. 0, no. 0, p. 1800691.

[65] X. Zhang, W. Wang, B. Xu, S. Liu, H. Dai, D. Bian, S. Chen, K. Wang, and X. W. Sun, “Thin film perovskite light-emitting diode based on CsPbBr3 powders and interfacial engineering,” *Nano Energy*, vol. 37, pp. 40–45, July 2017.

[66] M. Schreier, L. Curvat, F. Giordano, L. Steier, A. Abate, S. M. Zakeeruddin, J. Luo, M. T. Mayer, and M. Grätzel, “Efficient photosynthesis of carbon monoxide from CO2 using perovskite photovoltaics,” *Nature Communications*, vol. 6, p. 7326, June 2015. Bandiera_abtest: a Cc_license_type: cc_by Cg_type: Nature Research Journals Number: 1 Primary_atype: Research Publisher: Nature Publishing Group Subject_term: Materials for energy and catalysis;Solar energy and photovoltaic technology Subject_term_id: materials-for-energy-and-catalysis;solar-energy-and-photovoltaic-technology.

[67] Y.-S. Chen, J. S. Manser, and P. V. Kamat, “All Solution-Processed Lead Halide Perovskite-BiVO4 Tandem Assembly for Photolytic Solar Fuels Production,” *Journal of the American Chemical Society*, vol. 137, pp. 974–981, Jan. 2015.

[68] M. Moniruddin, B. Ilyassov, X. Zhao, E. Smith, T. Serikov, N. Ibrayev, R. Asmatulu, and N. Nuraje, “Recent progress on perovskite materials in photovoltaic and water splitting applications,” *Materials Today Energy*, vol. 7, pp. 246–259, Mar. 2018.

[69] N. Vlachopoulos, P. Liska, J. Augustynski, and M. Graetzel, “Very efficient visible light energy harvesting and conversion by spectral sensitization of high surface area polycrystalline titanium dioxide films,” *Journal of the American Chemical Society*, vol. 110, pp. 1216–1220, Feb. 1988. Publisher: American Chemical Society.

[70] J. R. Jennings, Y. Liu, and Q. Wang, “Efficiency Limitations in Dye-Sensitized Solar Cells Caused by Inefficient Sensitizer Regeneration,” *J. Phys. Chem. C*, vol. 115, no. 30, pp. 15109–15120, 2011.

[71] A. Smets, K. Jäger, O. Isabella, R. van Swaaij, and M. Zeman, *Solar Energy: The physics and engineering of photovoltaic conversion, technologies and systems*. Cambridge: UIT Cambridge Limited, 2016.

[72] P. Qin, M. Linder, T. Brinck, G. Boschloo, A. Hagfeldt, and L. Sun, “High Incident Photon-to-Current Conversion Efficiency of p-Type Dye-Sensitized Solar Cells Based on NiO and Organic Chromophores,” *Advanced Materials*, vol. 21, pp. 2993–2996, Aug. 2009.

[73] S. Powar, T. Daeneke, M. T. Ma, D. Fu, N. W. Duffy, G. Götz, M. Weidelener, A. Mishra, P. Bäuerle, L. Spiccia, and U. Bach, “Highly Efficient p-Type Dye-Sensitized Solar Cells based on Tris(1,2-diaminoethane)Cobalt(II)/(III) Electrolytes,” *Angewandte Chemie*, vol. 125, no. 2, pp. 630–633, 2013.

[74] Q. Zhang and G. Cao, “Nanostructured photoelectrodes for dye-sensitized solar cells,” *Nano Today*, vol. 6, pp. 91–109, Feb. 2011.

[75] J. Idígoras, J. Sobuś, M. Jancelewicz, E. Azaceta, R. Tena-Zaera, J. A. Anta, and M. Ziółek, “Effect of different photoanode nanostructures on the initial charge separation and electron injection process in dye sensitized solar cells: A photophysical study with indoline dyes,” *Materials Chemistry and Physics*, vol. 170, pp. 218–228, Feb. 2016.

[76] K. Zhu, N. R. Neale, A. Miedaner, and A. J. Frank, “Enhanced charge-collection efficiencies and light scattering in dye-sensitized solar cells using oriented TiO2 nanotubes arrays,” *Nano Letters*, vol. 7, no. 1, pp. 69–74, 2007.

[77] J. R. Jennings, A. Ghicov, L. M. Peter, P. Schmuki, and A. B. Walker, “Dye-sensitized solar cells based on oriented TiO2 nanotube arrays: Transport, trapping, and transfer of electrons,” *Journal of the American Ceramic Society*, vol. 130, pp. 13364–13372, Oct. 2008.

[78] J. B. Baxter and E. S. Aydil, “Dye-sensitized solar cells based on semiconductor morphologies with ZnO nanowires,” *Solar Energy Materials and Solar Cells*, vol. 90, pp. 607–622, Mar. 2006.

[79] M. Law, L. E. Greene, J. C. Johnson, R. Saykally, and P. Yang, “Nanowire dye-sensitized solar cells,” *Nature Materials*, vol. 4, p. 455, June 2005.

[80] J. Fan, Y. Hao, A. Cabot, E. M. J. Johansson, G. Boschloo, and A. Hagfeldt, “Cobalt(II/III) Redox Electrolyte in ZnO Nanowire-Based Dye-Sensitized Solar Cells,” *ACS Applied Materials & Interfaces*, 2013.

[81] A. Kay and M. Grätzel, “Dye-Sensitized Core-Shell Nanocrystals: Improved Efficiency of Mesoporous Tin Oxide Electrodes Coated with a Thin Layer of an Insulating Oxide,” *Chemistry of Materials*, vol. 14, pp. 2930–2935, July 2002.

[82] M. Law, L. E. Greene, A. Radenovic, T. Kuykendall, J. Liphardt, and P. Yang, “ZnO-Al2O3 and ZnO-TiO2 Core-Shell Nanowire Dye-Sensitized Solar Cells,” *The Journal of Physical Chemistry B*, vol. 110, pp. 22652–22663, Nov. 2006.

[83] M. Jankulovska, T. Berger, S. S. Wong, R. Gómez, and T. Lana-Villarreal, “Trap States in TiO2 Films Made of Nanowires, Nanotubes or Nanoparticles: An Electrochemical Study,” *ChemPhysChem*, pp. n/a–n/a, 2012.

[84] D. Pourjafari, D. Reyes-Coronado, A. Vega-Poot, R. Escalante, D. Kirkconnell-Reyes, R. García-Rodríguez, J. A. Anta, and G. Oskam, “Brookite-Based Dye-Sensitized Solar Cells: Influence of Morphology and Surface Chemistry on Cell Performance,” *The Journal of Physical Chemistry C*, vol. 122, pp. 14277–14288, July 2018.

[85] N. G. Park, J. v. d. Lagemaat, and A. J. Frank, “Comparison of dye-sensitized rutile- and anatase-based TiO2 solar cells,” *Journal of Physical Chemistry B*, vol. 104, no. 38, pp. 8989–8994, 2000.

[86] W. Shao, F. Gu, C. Li, and M. Lu, “Highly Efficient Dye-Sensitized Solar Cells by Using a Mesostructured Anatase TiO2 Electrode with High Dye Loading Capacity,” *Ind. Eng. Chem. Res.*, vol. 49, no. 19, pp. 9111–9116, 2010.

[87] L. Y. Zeng, S. Y. Dai, W. W. Xu, and K. J. Wang, “Dye-sensitized solar cells based on ZnO films,” *Plasma Science & Technology*, vol. 8, no. 2, pp. 172–175, 2006.

[88] J. A. Anta, E. Guillén, and R. Tena-Zaera, “ZnO-Based Dye-Sensitized Solar Cells,” *J. Phys. Chem. C*, 2012.

[89] B. V. Bergeron, A. Marton, G. Oskam, and G. J. Meyer, “Dye-Sensitized SnO2 Electrodes with Iodide and Pseudohalide Redox Mediators,” *The Journal of Physical Chemistry B*, vol. 109, pp. 937–943, Jan. 2005.

[90] P. Tiwana, P. Docampo, M. B. Johnston, H. J. Snaith, and L. M. Herz, “Electron Mobility and Injection Dynamics in Mesoporous ZnO, SnO2, and TiO2 Films Used in Dye-Sensitized Solar Cells,” *ACS Nano*, vol. 5, no. 6, pp. 5158–5166, 2011.

[91] J. Sobuś, G. Burdziński, J. Karolczak, J. Idígoras, J. A. Anta, and M. Ziółek, “Comparison of TiO2 and ZnO Solar Cells Sensitized with an Indoline Dye: Time-Resolved Laser Spectroscopy Studies of Partial Charge Separation Processes,” *Langmuir*, vol. 30, pp. 2505–2512, Mar. 2014.

[92] A. Hagfeldt and M. Graetzel, “Light-Induced Redox Reactions in Nanocrystalline Systems,” *Chemical Reviews*, vol. 95, pp. 49–68, Jan. 1995. Publisher: American Chemical Society.

[93] S. Ito, H. Miura, S. Uchida, M. Takata, K. Sumioka, P. Liska, P. Comte, P. Pechy, and M. Graetzel, “High-conversion-efficiency organic dye-sensitized solar cells with a novel indoline dye,” *Chemical Communications*, no. 41, pp. 5194–5196, 2008.

[94] S. E. Koops, B. C. O’Regan, P. R. F. Barnes, and J. R. Durrant, “Parameters Influencing the Efficiency of Electron Injection in Dye-Sensitized Solar Cells,” *Journal of the American Chemical Society*, vol. 131, pp. 4808–4818, Apr. 2009.

[95] Y. V. Zubavichus, Y. L. Slovokhotov, M. K. Nazeeruddin, S. M. Zakeeruddin, M. Grätzel, and V. Shklover, “Structural Characterization of Solar Cell Prototypes Based on Nanocrystalline TiO2 Anatase Sensitized with Ru Complexes. X-ray Diffraction, XPS, and XAFS Spectroscopy Study,” *Chemistry of Materials*, vol. 14, pp. 3556–3563, Aug. 2002.

[96] O. A. Blackburn, B. J. Coe, M. Helliwell, Y. T. Ta, L. M. Peter, H. Wang, J. A. Anta, and E. Guillén, “Ruthenium (II) dichloro or dithiocyanato complexes with 4, 4: 2, 2: 4, 4-quaterpyridinium ligands: towards photosensitizers with enhanced low-energy absorption properties,” *Polyhedron*, 2012.

[97] J. Warnan, V.-M. Guerin, F. B. Anne, Y. Pellegrin, E. Blart, D. Jacquemin, T. Pauporté, and F. Odobel, “Ruthenium Sensitizer Functionalized by Acetylacetone Anchoring Groups for Dye-Sensitized Solar Cells,” *The Journal of Physical Chemistry C*, vol. 117, pp. 8652–8660, May 2013.

[98] D. Shi, Y. M. Cao, N. Pootrakulchote, Z. H. Yi, M. F. Xu, S. M. Zakeeruddin, M. Graetzel, and P. Wang, “New Organic Sensitizer for Stable Dye-Sensitized Solar Cells with Solvent-Free Ionic Liquid Electrolytes,” *Journal of Physical Chemistry C*, vol. 112, no. 44, pp. 17478–17485, 2008.

[99] W. D. Zeng, Y. M. Cao, Y. Bai, Y. H. Wang, Y. S. Shi, M. Zhang, F. F. Wang, C. Y. Pan, and P. Wang, “Efficient Dye-Sensitized Solar Cells with an Organic Photosensitizer Featuring Orderly Conjugated Ethylenedioxythiophene and Dithienosilole Blocks,” *Chemistry of Materials*, vol. 22, no. 5, pp. 1915–1925, 2010.

[100] D. Joly, L. Pellejà, S. Narbey, F. Oswald, T. Meyer, Y. Kervella, P. Maldivi, J. N. Clifford, E. Palomares, and R. Demadrille, “Metal-free organic sensitizers with narrow absorption in the visible for solar cells exceeding 10% efficiency,” *Energy & Environmental Science*, vol. 8, no. 7, pp. 2010–2018, 2015.

[101] W. M. Campbell, K. W. Jolley, P. Wagner, K. Wagner, P. J. Walsh, K. C. Gordon, L. Schmidt-Mende, M. K. Nazeeruddin, Q. Wang, M. Gratzel, and D. L. Officer, “Highly Efficient Porphyrin Sensitizers for Dye-Sensitized Solar Cells,” *The Journal of Physical Chemistry C*, vol. 111, no. 32, pp. 11760–11762, 2007.

[102] A. Yella, H.-W. Lee, H. N. Tsao, C. Yi, A. K. Chandiran, M. Nazeeruddin, E. W.-G. Diau, C.-Y. Yeh, S. M. Zakeeruddin, and M. Grätzel, “Porphyrin-Sensitized Solar Cells with Cobalt (II/III)–Based Redox Electrolyte Exceed 12 Percent Efficiency,” *Science*, vol. 334, pp. 629 –634, Nov. 2011.

[103] S. Mathew, A. Yella, P. Gao, R. Humphry-Baker, B. F. E. Curchod, N. Ashari-Astani, I. Tavernelli, U. Rothlisberger, M. K. Nazeeruddin, and M. Grätzel, “Dye-sensitized solar cells with 13% efficiency achieved through the molecular engineering of porphyrin sensitizers,” *Nature Chemistry*, vol. 6, pp. 242–247, Mar. 2014.

[104] J. Halme, P. Vahermaa, K. Miettunen, and P. Lund, “Device Physics of Dye Solar Cells,” *Advanced Materials*, vol. 22, pp. E210–E234, Sept. 2010.

[105] L. Spiccia, “Aqueous dye-sensitized solar cell electrolytes based on the cobalt(II)/(III) tris(bipyridine) redox couple,” *Energy & Environmental Science*, Oct. 2012.

[106] K. Kannankutty, C.-C. Chen, V. S. Nguyen, Y.-C. Lin, H.-H. Chou, C.-Y. Yeh, and T.-C. Wei, “tert-Butylpyridine Coordination with [Cu(dmp)2]2+/+ Redox Couple and Its Connection to the Stability of the Dye-Sensitized Solar Cell,” *ACS Applied Materials & Interfaces*, vol. 12, pp. 5812–5819, Feb. 2020. Publisher: American Chemical Society.

[107] W. Yang, M. Söderberg, A. I. K. Eriksson, and G. Boschloo, “Efficient aqueous dye-sensitized solar cell electrolytes based on a TEMPO/TEMPO+ redox couple,” *RSC Advances*, vol. 5, pp. 26706–26709, Mar. 2015. Publisher: The Royal Society of Chemistry.

[108] H. Fang, J. Ma, M. J. Wilhelm, B. G. DeLacy, and H.-L. Dai, “Influence of Solvent on Dye-Sensitized Solar Cell Efficiency: What is so Special About Acetonitrile?,” *Particle & Particle Systems Characterization*, vol. 38, no. 5, p. 2000220, 2021. _eprint: https://onlinelibrary.wiley.com/doi/pdf/10.1002/ppsc.202000220.

[109] D. B. Kuang, C. Klein, Z. P. Zhang, S. Ito, J. E. Moser, S. M. Zakeeruddin, and M. Gratzel, “Stable, high-efficiency ionic-liquid-based mesoscopic dye-sensitized solar cells,” *Small*, vol. 3, no. 12, pp. 2094–2102, 2007.

[110] F. Fabregat-Santiago, J. Bisquert, L. Cevey, P. Chen, M. Wang, S. M. Zakeeruddin, and M. Grätzel, “Electron Transport and Recombination in Solid-State Dye Solar Cell with Spiro-OMeTAD as Hole Conductor,” *Journal of the American Chemical Society*, vol. 131, pp. 558–562, Jan. 2009.

[111] P. Chen, J. H. Yum, F. D. Angelis, E. Mosconi, S. Fantacci, S. J. Moon, R. H. Baker, J. Ko, M. K. Nazeeruddin, and M. Gratzel, “High Open-Circuit Voltage Solid-State Dye-Sensitized Solar Cells with Organic Dye,” *NANO LETTERS*, vol. 9, pp. 2487–2492, June 2009.

[112] D. Hwang, S. M. Jo, D. Y. Kim, V. Armel, D. R. MacFarlane, and S.-Y. Jang, “High-Efficiency, Solid-State, Dye-Sensitized Solar Cells Using Hierarchically Structured TiO2 Nanofibers,” *ACS Applied Materials & Interfaces*, vol. 3, no. 5, pp. 1521–1527, 2011.

[113] J. Kim, J. K. Koh, B. Kim, S. H. Ahn, H. Ahn, D. Y. Ryu, J. H. Kim, and E. Kim, “Enhanced Performance of I2-Free Solid-State Dye-Sensitized Solar Cells with Conductive Polymer up to 6.8%,” *Advanced Functional Materials*, vol. 21, pp. 4633–4639, Dec. 2011.

[114] I. Chung, B. Lee, J. He, R. P. H. Chang, and M. G. Kanatzidis, “All-solid-state dye-sensitized solar cells with high efficiency,” *Nature*, vol. 485, pp. 486–489, May 2012.

[115] B. Liu, X. Li, M. Liu, Z. Ning, Q. Zhang, C. Li, K. Müllen, and W. Zhu, “Photovoltaic performance of solid-state DSSCs sensitized with organic isophorone dyes: Effect of dye-loaded amount and dipole moment,” *Dyes and Pigments*, vol. 94, no. 1, pp. 23–27, 2012.

[116] E. M. J. Johansson, L. Yang, E. Gabrielsson, P. W. Lohse, G. Boschloo, L. Sun, and A. Hagfeldt, “Combining a Small Hole-Conductor Molecule for Efficient Dye Regeneration and a Hole-Conducting Polymer in a Solid-State Dye-Sensitized Solar Cell,” *The Journal of Physical Chemistry C*, vol. 116, pp. 18070–18078, Aug. 2012.

[117] W. J. Lee, E. Ramasamy, D. Y. Lee, and J. S. Song, “Efficient Dye-Sensitized Solar Cells with Catalytic Multiwall Carbon Nanotube Counter Electrodes,” *ACS Applied Materials & Interfaces*, vol. 0, no. 0.

[118] J. Idígoras, E. Guillén, F. J. Ramos, J. A. Anta, M. K. Nazeeruddin, and S. Ahmad, “Highly efficient flexible cathodes for dye sensitized solar cells to complement Pt@TCO coatings,” *Journal of Materials Chemistry A*, vol. 2, no. 9, pp. 3175–3181, 2014.

[119] N.-G. Park, M. Grätzel, and T. Miyasaka, eds., *Organic-Inorganic Halide Perovskite Photovoltaics*. Cham: Springer International Publishing, 2016.

[120] B. Philippe, M. Saliba, J.-P. Correa-Baena, U. B. Cappel, S.-H. Turren-Cruz, M. Grätzel, A. Hagfeldt, and H. Rensmo, “Chemical Distribution of Multiple Cation (Rb+, Cs+, MA+, and FA+) Perovskite Materials by Photoelectron Spectroscopy,” *Chemistry of Materials*, vol. 29, pp. 3589–3596, Apr. 2017.

[121] P. P. Boix, S. Agarwala, T. M. Koh, N. Mathews, and S. G. Mhaisalkar, “Perovskite Solar Cells: Beyond Methylammonium Lead Iodide,” *The Journal of Physical Chemistry Letters*, vol. 6, pp. 898–907, Mar. 2015.

[122] P. Umari, E. Mosconi, and F. De Angelis, “Relativistic GW calculations on CH3NH3PbI3 and CH3NH3SnI3 perovskites for solar cell applications,” *Scientific Reports*, vol. 4, p. 4467, Mar. 2014.

[123] M. Roknuzzaman, K. K. Ostrikov, H. Wang, A. Du, and T. Tesfamichael, “Towards lead-free perovskite photovoltaics and optoelectronics by ab-initio simulations,” *Scientific Reports*, vol. 7, pp. 1–8, Oct. 2017.

[124] J. Sanchez-Diaz, R. S. Sánchez, S. Masi, M. Kreĉmarová, A. O. Alvarez, E. M. Barea, J. Rodriguez-Romero, V. S. Chirvony, J. F. Sánchez-Royo, J. P. Martinez-Pastor, and I. Mora-Seró, “Tin perovskite solar cells with >1,300 h of operational stability in N2 through a synergistic chemical engineering approach,” *Joule*, Mar. 2022.

[125] J. S. Manser, J. A. Christians, and P. V. Kamat, “Intriguing Optoelectronic Properties of Metal Halide Perovskites,” *Chemical Reviews*, vol. 116, pp. 12956–13008, June 2016.

[126] J. Ling, P. K. K. Kizhakkedath, T. M. Watson, I. Mora-Seró, L. Schmidt-Mende, T. M. Brown, and R. Jose, “A Perspective on the Commercial Viability of Perovskite Solar Cells,” *Solar RRL*, vol. 5, no. 11, p. 2100401, 2021.

[127] C. S. Ponseca, T. J. Savenije, M. Abdellah, K. Zheng, A. Yartsev, T. Pascher, T. Harlang, P. Chabera, T. Pullerits, A. Stepanov, J.-P. Wolf, and V. Sundström, "Organometal Halide Perovskite Solar Cell Materials Rationalized: Ultrafast Charge Generation, High and Microsecond-Long Balanced Mobilities, and Slow Recombination," *Journal of the American Chemical Society*, vol. 136, pp. 5189–5192, Apr. 2014. Publisher: American Chemical Society.

[128] L. M. Herz, "Charge-Carrier Mobilities in Metal Halide Perovskites: Fundamental Mechanisms and Limits," *ACS Energy Letters*, vol. 2, pp. 1539–1548, July 2017. Publisher: American Chemical Society.

[129] W. Tress, "Perovskite Solar Cells on the Way to Their Radiative Efficiency Limit – Insights Into a Success Story of High Open-Circuit Voltage and Low Recombination," *Advanced Energy Materials*, vol. 7, p. 1602358, July 2017.

[130] G. Xing, N. Mathews, S. Sun, S. S. Lim, Y. M. Lam, M. Grätzel, S. Mhaisalkar, and T. C. Sum, "Long-range balanced electron- and hole-transport lengths in organic-inorganic CH3nh3pbi3," vol. 342, no. 6156, pp. 344–347.

[131] M. B. Johnston and L. M. Herz, "Hybrid Perovskites for Photovoltaics: Charge-Carrier Recombination, Diffusion, and Radiative Efficiencies," *Accounts of Chemical Research*, vol. 49, pp. 146–154, Jan. 2016. Publisher: American Chemical Society.

[132] B. C. O'Regan, P. R. F. Barnes, X. Li, C. Law, E. Palomares, and J. M. Marin-Beloqui, "Optoelectronic Studies of Methylammonium Lead Iodide Perovskite Solar Cells with Mesoporous TiO2: Separation of Electronic and Chemical Charge Storage, Understanding Two Recombination Lifetimes, and the Evolution of Band Offsets during J–V Hysteresis," *Journal of the American Chemical Society*, vol. 137, pp. 5087–5099, Apr. 2015.

[133] A. Listorti, E. J. Juarez-Perez, C. Frontera, V. Roiati, L. Garcia-Andrade, S. Colella, A. Rizzo, P. Ortiz, and I. Mora-Sero, "Effect of Mesostructured Layer upon Crystalline Properties and Device Performance on Perovskite Solar Cells," *The Journal of Physical Chemistry Letters*, vol. 6, pp. 1628–1637, May 2015.

[134] A. M. Adams, J. M. Marin-Beloqui, G. Stoica, and E. Palomares, "The influence of the mesoporous TiO2 scaffold on the performance of methyl ammonium lead iodide (MAPI) perovskite solar cells: charge injection, charge recombination and solar cell efficiency relationship," *Journal of Materials Chemistry A*, vol. 3, pp. 22154–22161, Nov. 2015.

[135] L. Wang, G.-R. Li, Q. Zhao, and X.-P. Gao, "Non-precious transition metals as counter electrode of perovskite solar cells," *Energy Storage Materials*, vol. 7, pp. 40–47, Apr. 2017.

[136] M. Saliba, J.-P. Correa-Baena, C. M. Wolff, M. Stolterfoht, N. Phung, S. Albrecht, D. Neher, and A. Abate, "How to Make over 20% Efficient Perovskite Solar Cells in Regular (n–i–p) and Inverted (p–i–n) Architectures," *Chemistry of Materials*, vol. 30, pp. 4193–4201, July 2018.

[137] S. Altazin, L. Stepanova, J. Werner, B. Niesen, C. Ballif, and B. Ruhstaller, "Design of perovskite/crystalline-silicon monolithic tandem solar cells," *Optics Express*, vol. 26, pp. A579–A590, May 2018.

[138] G. E. Eperon, T. Leijtens, K. A. Bush, R. Prasanna, T. Green, J. T.-W. Wang, D. P. McMeekin, G. Volonakis, R. L. Milot, R. May, A. Palmstrom, D. J. Slotcavage, R. A. Belisle, J. B. Patel, E. S. Parrott, R. J. Sutton, W. Ma, F. Moghadam, B. Conings, A. Babayigit, H.-G. Boyen, S. Bent, F. Giustino, L. M. Herz, M. B. Johnston, M. D. McGehee, and H. J. Snaith, "Perovskite-perovskite tandem photovoltaics with optimized band gaps," *Science*, vol. 354, pp. 861–865, Nov. 2016.

[139] S. M. P. Meroni, C. Worsley, D. Raptis, and T. M. Watson, "Triple-Mesoscopic Carbon Perovskite Solar Cells: Materials, Processing and Applications," *Energies*, vol. 14, p. 386, Jan. 2021. Number: 2 Publisher: Multidisciplinary Digital Publishing Institute.

[140] J. Zhang and T. Pauporté, "Effects of Oxide Contact Layer on the Preparation and Properties of CH3NH3PbI3 for Perovskite Solar Cell Application," *The Journal of Physical Chemistry C*, vol. 119, no. 27, pp. 14919–14928, 2015.

[141] B. Roose and R. H. Friend, "Extrinsic Electron Concentration in SnO2 Electron Extracting Contact in Lead Halide Perovskite Solar Cells," *Advanced Materials Interfaces*, vol. 0, no. 0, p. 1801788.

[142] E. J. Juarez-Perez, M. Wuler, F. Fabregat-Santiago, K. Lakus-Wollny, E. Mankel, T. Mayer, W. Jaegermann, and I. Mora-Sero, "Role of the Selective Contacts in the Performance of Lead Halide Perovskite Solar Cells," *The Journal of Physical Chemistry Letters*, vol. 5, no. 4, pp. 680–685, 2014.

[143] S. S. Kim, S. Bae, and W. H. Jo, "Performance enhancement of planar heterojunction perovskite solar cells by n-doping of electron transporting layer," *Chemical Communications*, 2015.

[144] K. Mahmood, S. Sarwar, and M. T. Mehran, "Current status of electron transport layers in perovskite solar cells: materials and properties," *RSC Advances*, vol. 7, pp. 17044–17062, Mar. 2017. Publisher: The Royal Society of Chemistry.

[145] H. Lakhiani, T. Dunlop, F. D. Rossi, S. Dimitrov, R. Kerremans, C. Charbonneau, T. Watson, J. Barbé, and W. C. Tsoi, "Variations of Infiltration and Electronic Contact in Mesoscopic Perovskite Solar Cells Revealed by High-Resolution Multi-Mapping Techniques," *Advanced Functional Materials*, vol. 29, no. 25, p. 1900885, 2019.

[146] P. Calado, D. Burkitt, J. Yao, J. Troughton, T. M. Watson, M. J. Carnie, A. M. Telford, B. C. O'Regan, J. Nelson, and P. R. Barnes, "Identifying Dominant Recombination Mechanisms in Perovskite Solar Cells by Measuring the Transient Ideality Factor," *Physical Review Applied*, vol. 11, p. 044005, Apr. 2019.

[147] M. Anaya, W. Zhang, B. C. Hames, Y. Li, F. Fabregat-Santiago, M. E. Calvo, H. J. Snaith, H. Míguez, and I. Mora-Seró, "Electron injection and scaffold effects in perovskite solar cells," *Journal of Materials Chemistry C*, vol. 5, no. 3, pp. 634–644, 2017.

[148] E. J. Juarez-Perez, M. R. Leyden, S. Wang, L. K. Ono, Z. Hawash, and Y. Qi, "Role of the Dopants on the Morphological and Transport Properties of Spiro-MeOTAD Hole Transport Layer," *Chemistry of Materials*, vol. 28, pp. 5702–5709, Aug. 2016. Publisher: American Chemical Society.

[149] Z. Hawash, L. K. Ono, and Y. Qi, "Recent Advances in Spiro-MeOTAD Hole Transport Material and Its Applications in Organic–Inorganic Halide Perovskite Solar Cells," *Advanced Materials Interfaces*, vol. 5, p. 1700623, Jan. 2018.

[150] A. Abate, T. Leijtens, S. Pathak, J. Teuscher, R. Avolio, M. E. Errico, J. Kirkpatrik, J. M. Ball, P. Docampo, I. McPherson, and H. J. Snaith, "Lithium salts as "redox active" p-type dopants for organic semiconductors and their impact in solid-state dye-sensitized solar cells," *Physical Chemistry Chemical Physics*, vol. 15, pp. 2572–2579, Jan. 2013.

[151] J. Idígoras, F. J. Aparicio, L. Contreras-Bernal, S. Ramos-Terrón, M. Alcaire, J. R. Sánchez-Valencia, A. Borras, Barranco, and J. A. Anta, "Enhancing Moisture and Water Resistance in Perovskite Solar Cells by Encapsulation with Ultrathin Plasma Polymers," *ACS Applied Materials & Interfaces*, vol. 10, pp. 11587–11594, Mar. 2018.

[152] R. Cheacharoen, N. Rolston, D. Harwood, K. A. Bush, R. H. Dauskardt, and M. D. McGehee, "Design and understanding of encapsulated perovskite solar cells to withstand temperature cycling," *Energy & Environmental Science*, vol. 11, pp. 144–150, Jan. 2018.

[153] L. Caliò, M. Salado, S. Kazim, and S. Ahmad, "A Generic Route of Hydrophobic Doping in Hole Transporting Material to Increase Longevity of Perovskite Solar Cells," *Joule*, vol. 2, pp. 1800–1815, Sept. 2018.

[154] G. Ren, W. Han, Y. Deng, W. Wu, Z. Li, J. Guo, H. Bao, C. Liu, and W. Guo, "Strategies of modifying spiro-OMeTAD materials for perovskite solar cells: a review," *Journal of Materials Chemistry A*, vol. 9, pp. 4589–4625, Mar. 2021. Publisher: The Royal Society of Chemistry.

[155] A. Barranco, M. C. Lopez-Santos, J. Idigoras, F. J. Aparicio, J. Obrero-Perez, V. Lopez-Flores, L. Contreras-Bernal, V. Rico, J. Ferrer, J. P. Espinos, A. Borras, J. A. Anta, and J. R. Sanchez-Valencia, "Enhanced Stability of Perovskite Solar Cells Incorporating Dopant-Free Crystalline Spiro-OMeTAD Layers by Vacuum Sublimation," *Advanced Energy Materials*, vol. 0, no. 0, p. 1901524.

[156] J. You, L. Meng, T.-B. Song, T.-F. Guo, Y. M. Yang, W.-H. Chang, Z. Hong, H. Chen, H. Zhou, Q. Chen, Y. Liu, N. De Marco, and Y. Yang, "Improved air stability of perovskite solar cells via solution-processed metal oxide transport layers," *Nature Nanotechnology*, vol. advance online publication, 2015.

[157] C. Zuo and L. Ding, "Solution-Processed Cu2O and CuO as Hole Transport Materials for Efficient Perovskite Solar Cells," *Small*, vol. 11, pp. 5528–5532, Nov. 2015.

[158] C. C. Boyd, R. C. Shallcross, T. Moot, R. Kerner, L. Bertoluzzi, A. Onno, S. Kavadiya, C. Chosy, E. J. Wolf, J. Werner, J. A. Raiford, C. de Paula, A. F. Palmstrom, Z. J. Yu, J. J. Berry, S. F. Bent, Z. C. Holman, J. M. Luther, E. L. Ratcliff, N. R. Armstrong, and M. D. McGehee, "Overcoming Redox Reactions at Perovskite-Nickel Oxide Interfaces to Boost Voltages in Perovskite Solar Cells," *Joule*, July 2020.

[159] D. Bi, L. Yang, G. Boschloo, A. Hagfeldt, and E. M. J. Johansson, "Effect of Different Hole Transport Materials on Recombination in CH3NH3PbI3 Perovskite-Sensitized Mesoscopic Solar Cells," *The Journal of Physical Chemistry Letters*, vol. 4, pp. 1532–1536, May 2013.

[160] S. N. Habisreutinger, T. Leijtens, G. E. Eperon, S. D. Stranks, R. J. Nicholas, and H. J. Snaith, "Carbon Nanotube/Polymer Composites as a Highly Stable Hole Collection Layer in Perovskite Solar Cells," *Nano Letters*, vol. 14, pp. 5561–5568, Oct. 2014.

[161] O. Malinkiewicz, C. Roldán-Carmona, A. Soriano, E. Bandiello, L. Camacho, M. K. Nazeeruddin, and H. J. Bolink, "Metal-Oxide-Free Methylammonium Lead Iodide Perovskite-Based Solar Cells: the Influence of Organic Charge Transport Layers," *Advanced Energy Materials*, vol. 4, p. 1400345, Oct. 2014.

[162] M. Saliba, S. Orlandi, T. Matsui, S. Aghazada, M. Cavazzini, J.-P. Correa-Baena, P. Gao, R. Scopelliti, E. Mosconi, K.-H. Dahmen, F. De Angelis, A. Abate, A. Hagfeldt, G. Pozzi, M. Graetzel, and M. K. Nazeeruddin, "A molecularly engineered hole-transporting material for efficient perovskite solar cells," *Nature Energy*, p. 15017, 2016.

[163] L. J. Bennett, A. J. Riquelme, N. E. Courtier, J. A. Anta, and G. Richardson, “A new ideality factor for perovskite solar cells and an analytical theory for their impedance spectroscopy response,” *arXiv:2105.11226 [cond-mat, physics:physics]*, May 2021. arXiv: 2105.11226.

Chapter 2

Theoretical Background

Abstract

This Chapter presents the physical and chemical fundamentals to understand the working principles of solar cells in general and the particularities of DSSCs and PSCs.

2.1 Solar irradiation

The Sun produces $3.8{\cdot}10^{14}$ TW of power[1] due to the hydrogen fusion to helium that occurs in its inside. This energy source makes planet Earth habitable and sustains the biosphere by ensuring the photosynthesis of plants that will feed other living beings like animals, whose biomass will ultimately form the hydrocarbons we burn nowadays for energy. Sunpower is also the driving force of the wind in our planet and the water cycle that feeds hydroelectric power. In other words, almost all the electricity generated on our planet comes directly or indirectly from the Sun.

Fusion reactions that feed the Sun produce one He core, two neutrinos, electromagnetic radiation, and two positrons, which are annihilated with electrons, producing additional radiation, according to Einstein's equation[2].

$$E = mc_0^2 \tag{2.1}$$

where E is the radiation energy released during the annihilation, m is the mass of the positrons and electrons involved, and c_0 is the speed of light in the vacuum.

As it was described by Planck[3] and Einstein[4] among others in the emergence of quantum physics[5], the radiation emitted by the Sun is discretised in photons. Each photon has a characteristic energy given by Planck's equation[3]

$$E = hf \tag{2.2}$$

being E the characteristic energy of the quant, h the Planck constant and f the frequency of the radiation emitted, and it relates to the wavelength (λ)

of the radiation as follows:

$$\lambda = \frac{c_0}{f} \tag{2.3}$$

The emissions from the Sun are not homogeneous in the entire electromagnetic spectrum. It presents a behavior similar to a black body of 5670 K, which is the temperature at its surface[1,6]. The total irradiance reaching the Earth's atmosphere at the mean Sun-Earth distance is 1.361 $\mathrm{W \cdot m^{-2}}$, known as the solar constant. However, before reaching the surface of the Earth, the solar radiation is affected by the atmospheric conditions, changing its intensity and distribution[7]. The irradiation reaching the surface depends on the angle at which it crosses the atmosphere because the longer the path length, the higher the attenuation that will suffer. This attenuation is determined by the Air Mass (AM) parameter that is defined as

$$AM = \frac{1}{\cos(\Phi_{sun})} \tag{2.4}$$

where Φ_{sun} is the angle of elevation of the Sun. The irradiation reaching the atmosphere before crossing the atmosphere is known as AM0. The standard spectral distribution considered for PV applications is AM1.5G, corresponding to a Φ_{sun} of 48.2°[7,8]. This atmosphere thickness implies an attenuation of the solar radiation that makes the mean irradiance in the surface be 900 $\mathrm{W/m^2}$. However, for consensus, this standard spectrum is normalized, so the integrated irradiance of this spectrum is 1000 $\mathrm{W/m^2}$, which is known as one sun illumination[6]. The effects of the attenuation caused by the atmosphere can be observed in Figure 2.1

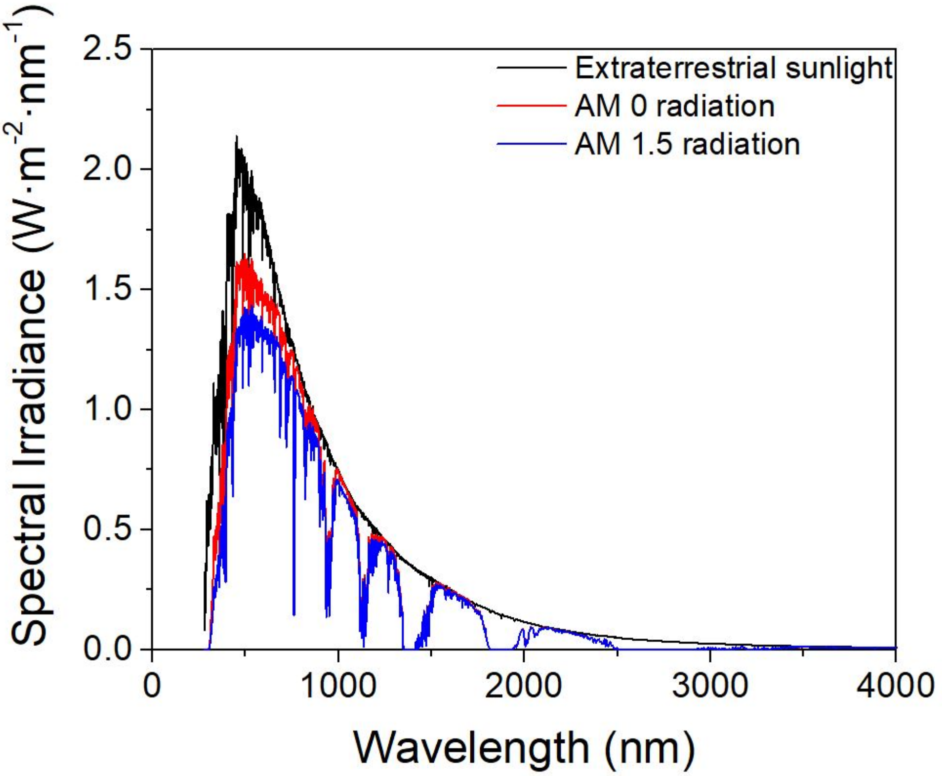

Figure 2.1: Spectra of light exiting the Sun (Extraterrestrial sunlight), reaching the top of Earth's atmosphere (AM0) and after crossing the atmosphere (AM1.5G).

Although there are stational and local variations, the AM1.5G is established as a standard by convention. Attending to the spectral emission observed in Figure 2.1, the region of the spectrum with the highest irradiance corresponds to the visible light. Thus, an optimal PV material will harvest as much radiation at this wavelength range as possible.

2.2 Photovoltaic solar cells

Solar PV energy conversion is the most direct way of harvesting energy from the Sun. It is a one-step process that transforms incident photons into usable electricity. This technique relies on the photoelectric effect, described in the early XX Century thanks to the works of Max Planck[3] and Albert Einstein[4].

The materials used for this kind of application are generally semiconductors capable of absorbing the energy of the photons by exciting the valence electrons to higher energy levels where they can freely move towards an external electric circuit.

The empty state produced by this excitation of the electron is known as a hole, which has the same electrical charge that an electron but is opposite. These electrons and holes show a potential difference, which creates the need for an electric field that ensures the separation of the charge carriers[9].

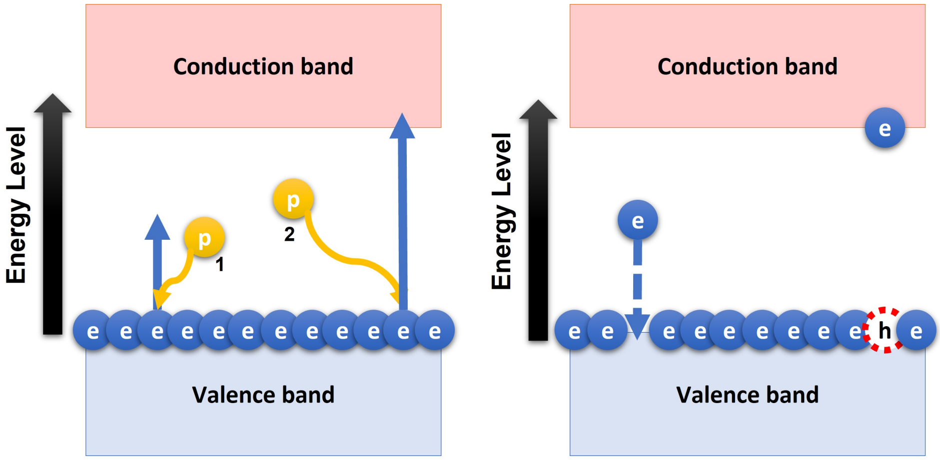

Figure 2.2: Basic schema of the different causalities that can happen when photons of different energies reach the PV material.

Due to the Pauli Exclusion Principle applied to crystals[10], electrons' energy levels may exist as free electrons are limited. The intermediate energy levels between the VB where the non-excited electrons remain and the CB where the excited electrons can exist are known as forbidden bands, and the difference in the energy levels between the VB and the CB is E_g, which is one of the main parameters used to assess the PV performance of a particular material[11].

As can be observed in Figure 2.2, photon number 1 energy is not enough for the excited electron to reach the CB, so since it can not cross the forbidden gap, it can not be absorbed and the material can be considered transparent for that wavelength. Photon 2 energy, on the other hand, allows the excited electron to reach the CB.

This indicates that a material of a certain E_g will only absorb photons of a specific wavelength range of the radiation spectrum.

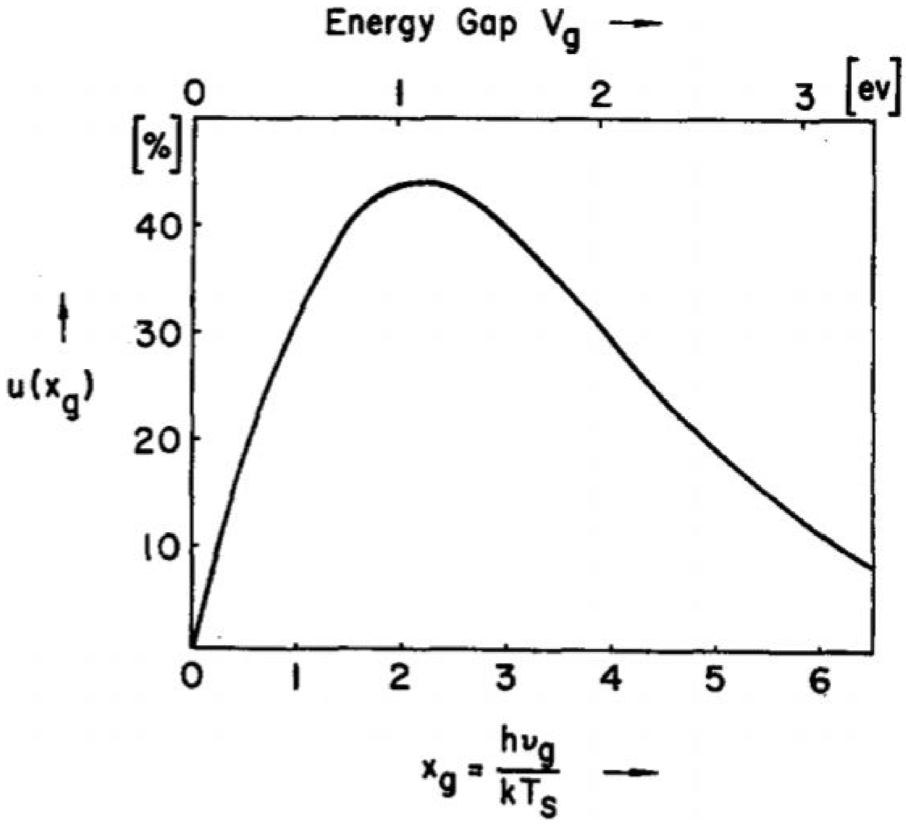

Figure 2.3: Dependence of the maximum theoretical efficiency upon the E_g of the semiconductor (Figure 3 of the work by William Shockley and Hans J. Queisser).[12]

In 1961, William Shockley and Hans J. Queisser[12] calculated the theoretical maximum efficiency (30% at 1.1 eV E_g) for a single p-n junction solar cell where the only source of loss of collected power is radiative recombination. As can be appreciated in the currently reported efficiency records of Figure 1.1, there is still room for improvement to reach the theoretical limit of efficiency presented in Figure 2.3. These calculations were made considering a 6000 K black body spectrum. However, in 2016 S. Rühle repeated the calculations considering the AM1.5G measured global spectra, correcting this theoretical maximum efficiency to 33.7% with a E_g of 1.34 eV.[13]

As a summary, to show a good PV performance, these semiconductor materials need to meet some fundamental requirements[14]:

- The material's E_g should be equal or lower than the energy of the majority of incident photons in the material.
- There has to be an electric field or any other microscopic mechanism that ensures an asymmetry that allows for the separation of the free electron and hole carriers so the device's electrodes can successfully collect them.
- It needs to include conductive selective materials that allows the separation of electron and hole carriers to produce a usable electric potential.

2.3 Basic semiconductor physics concepts

Depending on its ability to conduct electricity, materials are classified as insulating (if electrons can not flow at all) or conductors (when the electrons can move freely). Semiconductor materials are an intermediate case, where they can act as conductors or insulators depending on the conditions: Presence of an electromagnetic field, the temperature, or the incident radiation.

A more complex way of defining these different materials is through the magnitude of the E_g, where a material is considered an insulator when $E_g >$ 3 eV, for conductor materials $E_g = 0$ eV, and in semiconductors, E_g can have values between 0.5 eV and 3 eV.

There are some key aspects of the semiconductors that determine the characteristics and performance of the PV device[1]:

- The E_g of the material that determines the wavelength range of radiation that can be absorbed.
- The concentration of donor and acceptor atoms as dopants and their effect on the properties of the doped materials.
- The diffusion coefficient of the photogenerated charge carriers and its impact on the drift and diffusion charge transport processes.
- The recombination processes as source of charge loss in the device and their impact in the diffusion length of the excess charge carriers.

2.3.1 Energy bandgap and electronic states

As explained before, the E_g indicates the minimum energy that a photon needs to have to permit the excited electron to move from the VB to the CB. Thus, the E_g characterizes the absorption properties of the semiconductor and its thermal and electrical conductivity. The gap between bands is necessary for PV applications, as the extra potential energy absorbed by the electrons from the photons to reach the CB is extracted from the system as electrical energy[6]. In addition, this E_g avoids the excited electrons' decay back down to their ground state before they can be extracted to the circuit.

Unlike molecular systems with discrete molecular orbital energy levels, solid materials present broad energy bands where the electric charge can be delocalized. Thus, to determine the energy levels of these bands at a given temperature, it is necessary to determine the occupation probability of electronic states by electrons. This statistics are driven by the Fermi-Dirac distribution function[6,9]

$$f(E) = \frac{1}{1+\exp(\frac{E_C-E_F}{k_BT})} \tag{2.5}$$

being E$_C$ the lower energy edge of the CB, E$_F$ the Fermi level, k_B the Boltzmann constant, and T the absolute temperature. The Fermi level corresponds to the chemical potential (μ) of the electrons in a solid material[9]. This approximation is valid when the difference between E$_F$ and E$_C$ is of the same range as k_BT. For the case of non-degenerate semiconductors (E$_C$ - E$_F$ $\gg k_BT$), the Fermi-Dirac distribution can be approximated using Boltzmann distribution to describe the occupation of the CB. Therefore, the total electron density (n_c) in the *CB* is given by[6]

$$n_c = \int_{E_C}^{\infty} N_c(E) f(E) dE \approx N_c \exp\left(-\frac{E_C - E_F}{k_B T}\right) \tag{2.6}$$

where N_c is the density of states (DoS) at the CB edge. Thus, it is possible to relate the Fermi level in Eq. 2.5 to the total electron density in Eq. 2.6 through

$$n_c = N_c \exp\left(-\frac{E_C - E_F}{k_B T}\right) \tag{2.7}$$

Following this line of thought, the concentration of holes (p_v) in the VB edge can be estimated using

$$p_v = N_v \exp\left(-\frac{E_V - E_F}{k_B T}\right) \tag{2.8}$$

being N_v the DoS of holes in the VB and E$_V$ the upper energy edge of this band. For an intrinsic semiconductor, in the abscence of light $n_c = p_v$. Thus, the intrinsic concentration of charge carriers (n_i) can be calculated as follows

$$n_i^2 = n_c p_v = N_c N_v \exp\left(\frac{E_V - E_C}{k_B T}\right) = N_c N_v \left(-\frac{E_g}{k_B T}\right) \tag{2.9}$$

Intrinsic semiconductors have a relatively small conductivity because the Fermi level (at 0 K) is in the middle of the energy gap. Thus, to increase the conductivity of the material, impurities levels, known as dopants, can be introduced within the E$_g$. In that case, the equivalence $n_i = n_c = p_v$ does not hold and there is a majority charge carrier. Therefore, the Fermi level is shifted from the middle of the E_g and moves towards the CB or the VB as shown in Figure 2.4.

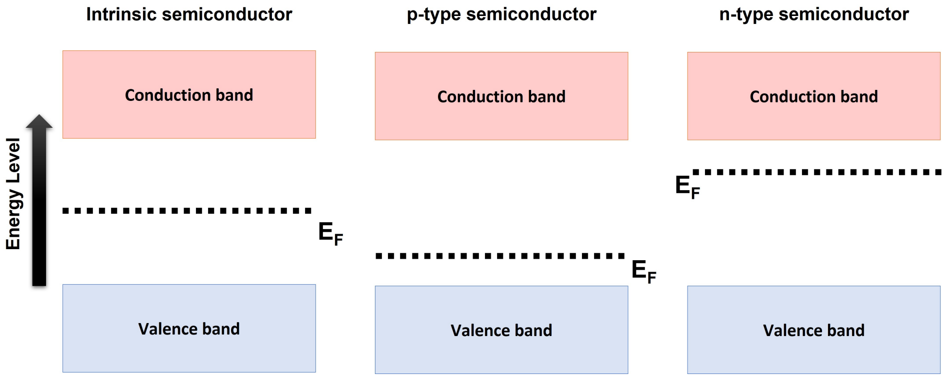

Figure 2.4: Schema of electronic band structure of different types of semiconductors with E_F being the Fermi level.

When the doping occurs by adding donor atoms (N_D), the majority charge carriers are the electrons, and the Fermi level is raised, producing a n-type semiconductor. On the other hand, when acceptor atoms (N_A) are introduced, the majority charge carriers are holes, lowering the Fermi level and leading to a p-type material[1].

The density of carriers can be adjusted by modifying the density of dopants. For n-doped materials, at room temperature and when $N_D \gg n_i$, the electron density can be approximated to the dopant density and the hole density can be expressed as[6]

$$p = \frac{n_i^2}{N_D} \tag{2.10}$$

Similarly, for p-doped materials, at room temperature and when $N_A \gg n_i$, the hole density is equivalent to the dopant density and the electron density is determined by

$$n = \frac{n_i^2}{N_A} \tag{2.11}$$

The impact of changing the electron and hole density on the calculation of the Fermi level can be observed in Eqs. 2.7 and 2.8. Thus, the effect of doping is to shift the Fermi level toward the CB or the VB for *n* and *p* doping, respectively, as can be observed in Figure 2.4. Therefore, doping materials is a mechanism for improving the conductivity of the semiconductor at equilibrium without adding energy to the system[6].

2.3.2 Classical description of a photovoltaic solar cel: p-n junction

For a device to harvest the light, an asymmetry needs to be built to ensure that electrons and holes are driven in different directions. Slight variations in the work function of the materials lead to large electric fields that are very useful for this purpose[6]. Thus, many PV technologies use a combination of n-type and p-type semiconductors that enhance the charge separation of the photogenerated electron-hole pairs. This is known as *p-n* junctions, and it is called homojunction when the *p* and *n* doped material is the same, or heterojunction when the materials acting as n-type and p-type semiconductors are different. When these materials are isolated, electroneutrality is kept. In n-type materials, the excess free electrons are compensated by positively ionized donor atoms, while in p-type materials, the excess free holes are compensated by negatively ionized acceptor atoms[1]. At a p-n junction, there is a potential barrier that blocks the majority carrier flow, providing the asymmetric resistances required to ensure charge separation[6].

When both materials are put together, the excess free electrons in n-type semiconductor diffuse to the p-type material, while excess free holes in the p-type material diffuse in the opposite direction, leading to a depletion of mobile charge carriers in the vicinity of the junction. However, the ionized atoms that compensated the free electrons and holes in *n* and *p* materials remain in this area, resulting in an electric field and a space charge area. This electric field is responsible for the generation of a voltage at the junction, which receives the name of built-in potential(V_{bi}), which under equilibrium is negative in the p-type region compared to the n-type region[1]. The resulting energy band diagram of this junction is shown in Figure 2.5.

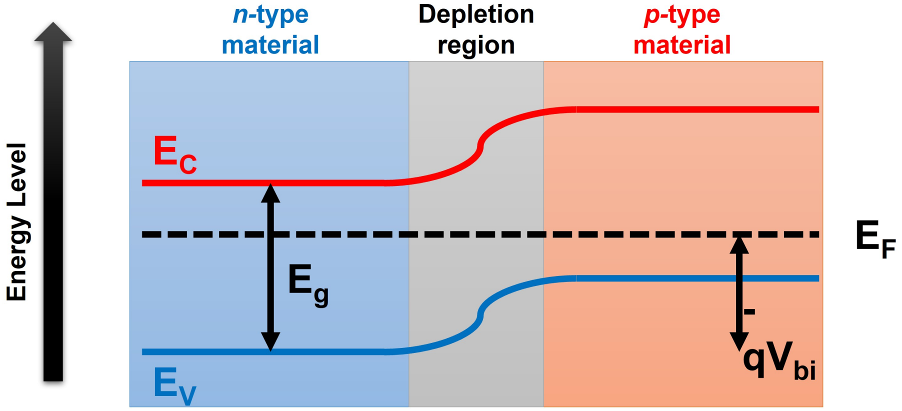

Figure 2.5: Energy band diagram of a p-n junction under equilibrium.

As the Fermi level is determined by the probability of occupation of a certain energy level by an electron[9], it remains constant across the junction. At the junction between both semiconductors, the exchange of carriers produce a potential step, that is represented by bending the bands[6].The internal electric field generated in the depletion region of the p-n junction produces the mentioned electrostatic potential difference (V_{bi}), which is determined as follows[1]:

$$qV_{bi} = E_g - k_B T \ln\left(\frac{N_V}{N_A}\right) - k_B T \ln\left(\frac{N_C}{N_D}\right) = E_g - k_B T \ln\left(\frac{N_V N_C}{N_A N_D}\right) \quad (2.12)$$

being q the elementary charge. Combining this expression with Eq. 2.9, the V_{bi} can be calculated as

$$V_{bi} = \frac{k_B T}{q} \ln\left(\frac{N_A N_D}{n_i^2}\right) \tag{2.13}$$

Although this relation holds under equilibrium, when an external bias potential (V) is applied, the Fermi level rises on one side with respect to the other, modifying the drop of potential across the junction. A negative bias under dark conditions in the p region increases the depletion in the space charge region as it withdraws carriers from the junction, while a positive bias produces the opposite effect, reducing the depletion. On the other hand, when the semiconductor is under illumination, photogenerated electrons and holes are built up in the n and p regions, respectively, producing a shift of the Fermi level similar to the observed under a positive bias[6].

The electric field produced in the classical p-n junction makes the devices behave like a two-terminal system that conducts like a diode under dark conditions and generates photovoltage under illumination[6].

2.3.3 Diode equation

When V is positive regarding the potential in the p-type material, decreasing the potential difference across the junction, the system is under forward-bias voltage. The reduction of this electric field barrier increases the minority carriers' concentration at the edges of the depletion region. This process receives the name of the minority-carrier injection. These minority carriers diffuse to the bulk of the quasi-neutral region and recombine with the majority carriers in bulk. This process is compensated by the drift of minority carriers[1].

This current produced by minority-carrier injection that flows in the opposite direction to the photocurrent receives the name of the dark current

(J_{dark}) and depends on the externally applied voltage (V). Most solar devices behave like diodes under dark conditions, admitting much more current under forward bias than reverse bias. For an ideal diode, this relation is given by[6]

$$J_{dark}(V) = J_0 \left[\exp\left(\frac{qV}{k_B T} \right) - 1 \right] \tag{2.14}$$

where J_0 is the dark saturation current, which can be calculated as follows[1]

$$J_0 = q n_i^2 \left(\frac{D_n}{L_n N_A} + \frac{D_p}{L_p N_D} \right) \tag{2.15}$$

being D_n and D_p the diffusion coefficient of electrons and holes, respectively, and L_n and L_p the diffusion lengths of electrons and holes.

When a device is put under illumination, electron-hole pairs are photogenerated, increasing the concentration of minority carriers, leading to a current flow across the depletion region. This produces a photogeneration current density (J)[1]. When an external potential is applied under illumination, the photogenerated electrons and holes are collected by the n-type and p-type materials due to the potential difference between semiconductors. Thus, the charge transfer processes in the p-n junction depend on the externally applied potential and the Fermi level under illumination.

The maximum generated photocurrent is reached when J_{dark} is null, which happens when the applied voltage is 0 V. This is called the short-circuit photocurrent (J_{SC}). The current-voltage response of the cell is determined by the sum of J_{SC} and J_{dark} according to the superposition approximation[6]. Thus, the photocurrent at each value of applied voltage can be described as

$$J(V) = J_{SC} - J_{dark}(V) \tag{2.16}$$

which, for an ideal diode is[6]

$$J = J_{SC} - J_0 \left[\exp\left(\frac{qV}{k_B T} \right) - 1 \right] \tag{2.17}$$

When the solar cell is under illumination, electrons and holes move to opposite directions due to the junction's electric field and accumulate at the extremes. The maximum charge separation determines the photovoltage and depends on the externally applied potential and the Fermi level under illumination[6].

The maximum potential difference is reached at the OC and is known as OC voltage (V_{OC}). This occurs when the contacts of the cell are isolated and is equivalent to the condition when the J_{dark} and J_{SC} cancel out. For an ideal diode, this voltage can be extracted from Eq. 2.17 as[6]

$$V_{OC} = \frac{k_B T}{q} \ln\left(\frac{J_{SC}}{J_0} + 1 \right) \tag{2.18}$$

However, most solar devices do not behave exactly like ideal diodes. Usually, the dark current dependence on the bias voltage is weaker than described for ideal diodes. The real dependence on the applied voltage modifies Eq. 2.17 as[6]

$$J = J_{SC} - J_0 \left[\exp\left(\frac{qV}{n_{ID} k_B T} \right) - 1 \right] \tag{2.19}$$

and, consequently, the OC voltage is determined by

$$V_{OC} = \frac{n_{ID} k_B T}{q} \ln\left(\frac{J_{SC}}{J_0} + 1 \right) \tag{2.20}$$

where n_{ID} is the so-called ideality factor, which quantifies the junction's quality compared to an ideal diode, and has typical values between 1 and 2. This parameter also gives information about the main recombination mechanisms driving the behavior of the solar cell[1].

2.3.4 Recombination mechanisms

The term “recombination” that has already been mentioned refers to any removal mechanism that leads to the loss of free mobile electrons and holes. This happens through the decay of an excited electron to a lower energy state[6]. The different mechanisms that may be present in PV devices are radiative recombination, Auger recombination, trap-assisted Shockley-Read-Hall (SRH) recombination, and surface recombination[6]. They will be described later in detail, and a simple schematic of these mechanisms can be observed in Figure 2.6

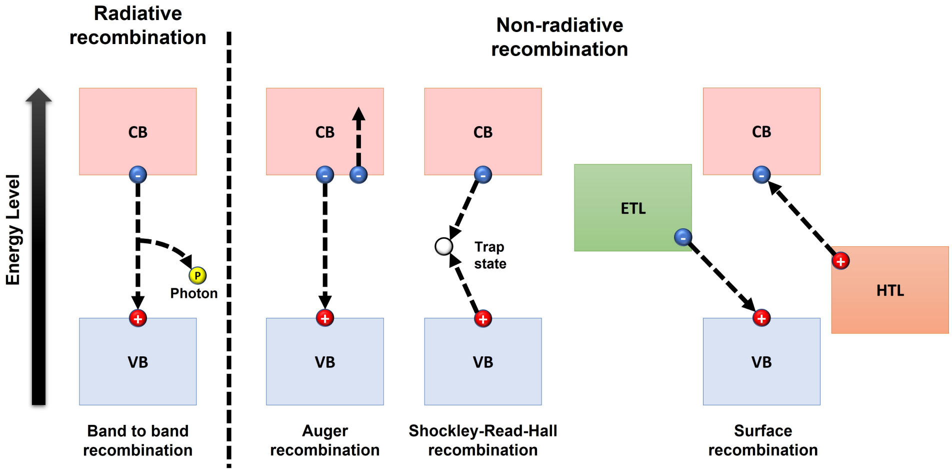

Figure 2.6: Schematic of different recombination mechanisms.

Under illumination and at open-circuit (OC) voltage, according to the diode behavior, all the photogenerated carriers (G_n) are recombined. From classical kinetics, the recombination rate (U_n) at the equilibrium can be expressed using the following empirical model[15]

$$U_n = k_{rec} n^{\gamma} \tag{2.21}$$

being k_{rec} a recombination constant and γ the reaction order in the sub-linear recombination kinetics. This is proportional to the densities of electronic carriers involved in each recombination mechanism. As it will be described later, in radiative and surface recombination, an electron-hole pair is involved, so $\gamma = 2$, while three carriers are involved in Auger recombination giving $\gamma = 3$. In SRH recombination, on the other hand, a charge carrier interacts with recombination centers or trap states. Thus, $\gamma = 1$[16].

The presence of recombination mechanisms affects the carriers density that was calculated in the equilibrium through Eq. 2.9. In addition, at high-injection conditions, the photogenerated carrier densities are much larger than the intrinsic and majority carriers at the CB and VB[1,6]. Assuming the equivalence $n_c = p_v$ for intrinsic semiconductors, this equation can be rewritten as

$$n = (N_c N_v)^{\frac{1}{2}} \exp\left(-\frac{E_g - qV}{2k_B T}\right) \tag{2.22}$$

Under OC conditions described in Eq. 2.20 and combining Eqs. 2.21 and 2.22, n_{ID} and γ are connected through[17]

$$n_{ID} = \frac{2}{\gamma} \tag{2.23}$$

Thus, given the reaction orders mentioned for the different recombination mechanisms, the expected n_{ID} for radiative and surface recombination is 1, for SRH recombination is 2, and for Auger recombination 2/3[18].

As it was mentioned before, J_{dark} described in Eq. 2.14 opposes the photogeneration current, acting as a recombination curent (J_{rec}). As this current depends on the potential, it can be used to connect the J_{rec} with the photopotential of the cell through[17]

$$J_{rec} = qdU_n = J_{00} \exp\left(-\gamma \frac{E_g - qV}{2k_B T}\right) \tag{2.24}$$

Here, d is the active layer thickness and J_{00} is a constant that determines the recombination rate[15,17]. From the reciprocal of the derivative of the voltage included in Eq. 2.24 it is possible to calculate the recombination resistance at a given voltage as[15,17,19–21]

$$R_{rec} = \left(\frac{\delta J_{rec}}{\delta V} \right)^{-1} = R_{00} \exp\left(-\frac{\beta q V}{k_B T} \right) \tag{2.25}$$

being R_{00} a numerical parameter that indicates the recombination resistance at short-circuit (SC) conditions and β is the transfer or recombination parameter, related to the n_{ID} by

$$n_{ID} = \frac{1}{\beta} \tag{2.26}$$

As it will be detailed discussed in Chapter 3, the most used tool to determine the recombination properties of a fully working PV device is electrical impedance spectroscopy (EIS).

Although the process to calculate the recombination rate, current and resistance are similar for the different types of recombination, the mechanisms presented in Figure 2.6 have some particularities that are discussed below.

Radiative recombination

The term radiative refers to the emission of a photon when electron-hole pairs recombine directly with an energy similar to E_g[1]. This process is known as band-to-band recombination, and it occurs when an electron goes back from the CB to interact with a hole in the VB. Thus, the new photons can be reabsorbed and recycled. The possibility of recovering as photons the energy released during the recombination process makes that cells where this is the dominant recombination process have very high efficiencies[22].

This phenomenon is also responsible for the photoluminescence observed in semiconductors used for PV applications.

The source of this mechanism is that when the temperature is higher than 0 K, the vibration of the crystal lattice breaks bonds, generating electron-hole pairs in a process called thermal generation (G_{th}). To hold the equilibrium, thermal recombination (R_{th}) takes place at the same rate as G_{th}. This rate is proportional to the concentration of electrons in the CB (n_0)and the concentration of holes (p_0) in the VB[9]

$$R_{th} = \beta_{rad} n_0 p_0 \tag{2.27}$$

where β_{rad} is a material and process dependent constant. Under illumination, the recombination rate increase as the electron and hole concentrations rise

$$R_d = \beta_{rad}(np - n_i^2) \tag{2.28}$$

Under high-injection conditions, the radiative recombination rate depends on the densities of both carriers. For this reason, it also receives the name of bimolecular recombination, and its rate can be calculated as

$$R_d = \beta_{rad} np \tag{2.29}$$

The thermodynamic limit that was shown before in Figure 2.3 implies that radiative recombination is the only recombination process in the device[12]. Thus, the more dominant this recombination process is in a PV material, the more it will approach its theoretical efficiency limit. The thermodynamic limit of the V_{OC} in the case of 100% radiative recombination is given by[23]

$$V_{OC,rad} = \frac{k_B T}{q} \ln\left(\frac{J_{SC}}{q\Phi_{em,0}} + 1\right) \tag{2.30}$$

being $\Phi_{em,0}$ the emission spectrum given by

$$\Phi_{em,0} = \int \alpha_{abs}(E)\varphi_{BB}(E)dE \tag{2.31}$$

where φ_{BB} represents the infrared black body spectrum.

Auger recombination

This recombination mechanism was discovered and reported by Lisa Meitner in 1922[24] and by Pierre Victor Auger in 1923[25]. This process involves three electronic carriers, and it is of particular importance in indirect semiconductors[1]. Here, the collision of two carriers of the same polarity produces the excitation of one of the carriers to higher kinetic energy, while the other recombines across the E_g with a carrier of opposite charge. Thus, instead of producing a photon, the energy released in the recombination process is transferred as kinetic energy to the third carrier, and it will be ultimately lost as heat when the carrier relaxes back to the band edge[6]. For direct E_g materials like the studied in this thesis, the recombination rate of this process is much lower than for all the other recombination processes[26]. Thus, it is not considered to have a significant contribution.

Shockley-Read-Hall recombination

SRH recombination involves defect or traps states in the band gap, and it is the most important recombination mechanism in most semiconductors with PV applications[6]. This process receives the name of the three scientists who described this process: W. Shockley, W.T. Read[27] and R.N. Hall[28]. The trap states or recombination centers introduce allowed energy levels within the forbidden gap. These levels, unlike the free carriers, are spatially localized. A free electron can be trapped by one of these defects, attracting a hole with which it recombines, and a free hole can recombine with a trapped electron[1]. The trapped carriers can also be released by thermal activation. The SRH expression for recombination through a single trap state is given by[6]

$$R_{SRH} = \frac{np - n_i^2}{\tau_n(p + p_t) + \tau_p(n + n_t)} \tag{2.32}$$

where p_t and n_t are the hole and electron density in traps, respectively, when the Fermi level is equal to the trap level, and τ_n and τ_p are the lifetimes for electron and hole capture by the trap. For electrons, this lifetime can be calculated as

$$\tau_n = \frac{1}{B_n N_t} \tag{2.33}$$

where N_t is the trap density and B_n can be expressed as

$$B_n = v_n \sigma_n \tag{2.34}$$

being v_n the thermal velocity of the electron and σ_n the capture cross section. Similarly, for holes the lifetime is determined by

$$\tau_p = \frac{1}{B_p N_t} \tag{2.35}$$

Here, the coefficient B_p for holes is given by

$$B_p = v_p \sigma_p \tag{2.36}$$

where v_p is the thermal velocity of the hole and σ_p its capture cross section.

For doped materials, Eq. 2.32 is significantly simplified, as R_{SRH} becomes proportional to the excess carrier density. For n type materials, SRH recombination can be expressed as

$$R_{SRH} \approx \frac{p - p_0}{\tau_p} \tag{2.37}$$

while for p type materials, the expression is

$$R_{SRH} \approx \frac{n - n_0}{\tau_n} \tag{2.38}$$

This recombination mechanism is maximized when n and p are of similar magnitude. Finally, for most semiconductors, the most significant contribution to this recombination comes from trap states located close to the center of the E_g. Thus, for bulk material with a uniform density of traps, like PSC[29], it is possible to make the approximation that recombination through one particular trap level is dominant given in Eq. 2.32[6].

Surface recombination

Spatial variations in the nature or density of the dominant trap can lead to important rises in the recombination rate. In real devices, this typically happens at the interfaces between different crystal regions in a multicrystalline material or the vicinity of the interface between selective contacts and the active layer[6]. If these selective materials have a low charge extraction efficiency or charge conductivity, it can lead to charge accumulation at interfaces, resulting in dangling bonds that act as additional defects[1]. Considering the spatial dimension of this type of recombination, the surface recombination flux per unit area can be calculated as[6]

$$R_{surf}\delta x = \frac{n_s p_s n_i^2}{\frac{1}{S_n}(p_s + p_t) + \frac{1}{S_p}(n_s + n_t)} \tag{2.39}$$

where n_s and p_s are the electron and hole densities at the surface, respectively and S_n is the surface recombination velocity for electrons towards the surface from the bulk, that can be expressed as

$$S_n = B_n N_t \tag{2.40}$$

On the other hand, S_p is the surface recombination for holes and can be calculated by

$$S_p = B_p N_t \tag{2.41}$$

For doped materials, Eq. 2.39 is much simplified. For n type materials, it is reduced to

$$R_{surf}\delta x = S_p(p_s - p_0) \tag{2.42}$$

while for p type materials it can be expressed as

$$R_{surf}\delta x = S_n(n_s - n_0) \tag{2.43}$$

This is particulary important in devices like PSCs where the perovskite active layer is sandwiched between a p type material and a n type material acting as ETL and HTL, as it was described in Figure 1.6.

Lifetime and Diffusion length

In order to produce a current density (J) that the system can collect, the photogenerated carriers need to reach the selective contacts before they are affected by any of the recombination processes described above. To this matter, the concepts of charge carriers lifetime (τ_n and τ_p) and diffusion length (L_n and L_p) are of vital importance. The lifetime is the average time a carrier remains in an excited state before suffering recombination, while the diffusion length is the average length these carriers move between their generation and recombination. The diffusion length of electronic carriers depends on the recombination lifetime of the carriers and its diffusion coefficient as[1]

$$L_n = \sqrt{D_n \tau_n} \tag{2.44}$$

for electrons and

$$L_p = \sqrt{D_p \tau_p} \tag{2.45}$$

for holes.

Thus, the determination of the diffusion length depends on how long it takes the carriers to recombine and how fast they move in the device. The charge transport properties give information about this second element.

2.3.5 Drift and diffusion

As mentioned before, in PV, the two mechanisms involved in charge transport are drift and diffusion. Drift corresponds to a charged carrier's motion in response to an electric field ($\vec{\zeta}$). This force accelerates the positive holes in the direction of the field and the negative electrons in the opposite. The resulting movement of charges can be described as average drift velocities $\vec{v}_{dn}$ and $\vec{v}_{dp}$ for electrons and holes, respectively. For low electric fields, these velocities are directly proportional to the electric field and can be calculated by[1].

$$\vec{v}_{dn} = -\mu_n \vec{\zeta} \tag{2.46}$$

for electrons, while for holes it is expressed as

$$\vec{v}_{dp} = \mu_p \vec{\zeta} \tag{2.47}$$

where μ_n and μ_p are the mobility of electrons and holes, respectively, which measures the capacity of the charge carriers to move through the semiconductor material. The resulting electron drift current is given by

$$\vec{J}_{n,drift} = -qn\vec{v}_{dn} = qn\mu_n \vec{\zeta} \tag{2.48}$$

while the hole drift current is determined by

$$\vec{J}_{p,drift} = qp\vec{v}_{dp} = qp\mu_p \vec{\zeta} \tag{2.49}$$

Thus, the resulting total drift current from the combination of Eqs. 2.48 and 2.49 is given by

$$\vec{J}_{drift} = q(p\mu_p + n\mu_n)\vec{\zeta} \tag{2.50}$$

The second mechanism involved in charge transport is diffusion. This process is produced by the tendency of the carriers to spread out from regions of high carrier density into others with lower concentrations by random thermal motion. Hence, the resulting diffusion current is proportional to the gradient in carrier concentration. For electrons, this current is given by

$$\vec{J}_{n,diff} = qD_n\vec{\nabla}n \tag{2.51}$$

while for holes, it is determined by

$$\vec{J}_{p,diff} = qD_p\vec{\nabla}p \tag{2.52}$$

Combining both equations, the resulting total diffusion current can be expressed as

$$\vec{J}_{diff} = q(D_n\vec{\nabla}n - D_p\vec{\nabla}p) \tag{2.53}$$

The connection between charge mobility and the electronic diffusion coefficients also appears in Eqs. 2.57 and 2.45 through the so-called Einstein relations, derived from Brownian motion kinetics and reached independently by W. Sutherland[30], A. Einstein[31] and M. Smoluchowski[32]. For the diffusion of charged particles, the most common expression for this relation is[6]

$$\mu_{mob} = \frac{qD}{k_B T} \tag{2.54}$$

Thus, through combining Eqs. 2.50 and 2.53, the total current can be calculated by

$$\vec{J} = \vec{J}_{drift} + \vec{J}_{diff} = q(p\mu_p + n\mu_n)\vec{\zeta} + q(D_n\vec{\nabla}n - D_p\vec{\nabla}p) \tag{2.55}$$

Eq. 2.55 is valid under the following assumptions[6]:

- Electron and hole densities form a quasi thermal equilibrium with a characteristic Fermi level and temperature.
- Electron and hole temperatures are equal to the lattice temperature.
- The relaxation time approximation holds. This means that changes in state occupancy are more likely to happen due to scattering collisions than to generation, recombination, or trapping events removing a carrier from that band.
- Electron and hole states can be described by a quantum number. This is true for crystalline materials.
- The Boltzmann approximation is valid. This happens for non-degenerate semiconductors where E_C - $E_{f_n} \gg k_B T$ and E_{f_p} - $E_V \gg k_B T$.
- The composition of the semiconductor material remains constant. This implies no local variations in the electron affinity, E_g, or effective mass.

2.4 Dye-sensitized solar cells particulars

In *Chapter* 1, the working principles of DSSC were briefly described to introduce the structure of the device. This section provides a more detailed overview of the different processes involved in the operation of these devices. The mechanisms determining the behavior of DSSCs after the photoexcitation of the dye molecule can be separated into seven different reactions that interact with each other[33]:

1. Excited state decay.

2. Electron injection.
3. Regeneration of the oxidized dyes.
4. Electron transport through the semiconductor film.
5. Recombination of electrons in the semiconductor with oxidized dyes.
6. Recombination of electrons in the semiconductor with oxidized electrolyte species.
7. Reduction of electron acceptors in the electrolyte at the counter electrode.

Reactions 1, 5, and 6 are recombination processes responsible for charge losses of the system. On the other hand, reactions 2, 3, 4, and 7 correspond to electron transfer processes. These mechanisms occur at a different timescale, and frequency-dependent optoelectronic characterization techniques can give additional individual information about these mechanisms. These techniques will be described in detail in *Chapter* 3.

Excited state decay and electron injection

These two processes compete directly, as the photoexcited electrons can be injected into the semiconductor or decay to their ground state. The excited state decay is nothing but the already described direct band-to-band recombination. The typical lifetime considered for the most extended dyes (Ru-complexes[33]) is in the time range of tens of nanoseconds[34]. More recent studies suggest that the lifetime of this state in fully working devices can be in the time range of picoseconds[35]. In contrast to this, for Ru-complexes directly attached to an metal oxide surface produce ultrafast electron injection in the femtosecond time range[36–38]. Nonetheless, for complete DSSC devices, the reported injection kinetics are much slower, making it possible the kinetic competition between both processes[39–41]. This kinetic depends on the difference between the CB of the semiconductor and the excited state of the dye[42] and on the interaction between the metal oxide and the dye[43]. In general, for the most used metal oxide (TiO_2), injection is swift and is not a limiting factor. However, other metal oxides like ZnO present much slower injection kinetics, which reduces their performance[35,43,44].

To determine the electron injection efficiency (φ_{inj}), it is necessary to consider the electron injection and the excited state decay rates. It can be calculated by[33]

$$\varphi_{inj} = \frac{k_{inj}}{k_{inj} + k_{dec}} \tag{2.56}$$

where k_{inj} is the rate constant for electron injection and k_{dec} for the excited state decay. To consider that the injection is efficient, the normal criterium[33,45] is that k_{inj} should be about 100 times larger than k_{dec}.

Regeneration of the oxidized dyes

After the electron injection from the excited dye to the CB of the metal oxide, the oxidized dye molecule needs to be reduced by an electron donor present in the electrolyte for regeneration. This mechanism is mainly limited by the diffusion kinetics of the donor species in the electrolyte. For nonviscous electrolytes like ACN, the diffusion range constant is around $10^9 - 10^{10} M^{-1} s^{-1}$.[33]. The other main aspect of the electrolyte properties involved in the regeneration process is the concentration of the electron donor. To avoid the recombination of the oxidized dyes and ensure an efficient charge separation, the regeneration rate needs to be much faster than the electron recombination between from the metal oxide to the oxidized dye[46,47]. This is ensured through a high concentration of electron donors in the electrolyte. However, while an insufficient regeneration of the dye decreases the lifespan of the device and its overall performance[48], an excess of this concentration can lead to poor photovoltages[49]. For iodine-based electrolytes, which are the most used in the field, concentrations of the range 0.1M - 0.5M are normally used[33,50,51].

The regeneration charge transfer from the electron donor in the electrolyte to the oxidized dye depends on the free energy difference between the dye's ground state and the electrolyte's redox potential. Although for most Ru-based dyes and some organic dyes, this free energy difference is 0.5 V[52], the nature and concentration of different cations and additives in the electrolyte can modify its redox potential[46,53].

Electronic transport in the semiconductor

The small particle size of the nanostructured metal oxide[54] and the low doping level[55], together with the presence of the electrolyte, whose ionic strength screens the electric fields, results in the absence of the formation of a depletion region. This means that drift transport processes can be neglected and the charge carriers transport in the metal oxide takes place mainly by diffusion[56–59]. Thus, it is the gradient in electron concentration the main driving force for electronic transport in this kind of device, as it was explained before for diffusion charge transport resulting in Eq. 2.53 for electrons in n-type DSSCs.

The electronic diffusion coefficient in DSSCs is found to be dependent on the photogenerated electron concentration and Fermi level in the metal oxide[33]. This can be experimentally observed through the increase of the diffusion coefficient at higher light intensities[60,61]. This is usually explained using a multiple trapping (MT) model, where electrons are considered to be mostly trapped in localized states below the CB, and they are released by thermal activation[61–65]. Thus, the chemical electron diffusion coefficient (D_μ)can be approximated from the MT model by the following expression[66–69]

$$D_{\mu} = D_0 \exp\left(\frac{(1-\alpha)({}_{n}E_F - E_{F,redox})}{k_B T}\right) \tag{2.57}$$

being D_0 is the diffusion coefficient in the dark, α is the trap parameter (with values usually in the range of 0.15 - 0.35 for most DSSC[66,70–72]), ${}_{n}\mathrm{E}_F$ is the quasi Fermi level resulting on the shifting caused by the filling of the trap distribution and $\mathrm{E}_{F,redox}$ is the Fermi level at the redox potential. As it will be shown in *Chapter* 3, this chemical electron diffusion coefficient can also be extracted from small-perturbation optoelectronic techniques.

The energy of the traps across the electronic structure of the semiconductor material is defined by the energy trap distribution or density of states g_E, which depends on the α parameter as shown below[73–76]

$$g_E = \frac{\alpha N_t}{k_B T} \exp\left(-\frac{\alpha(E_C - E)}{k_B T}\right) \tag{2.58}$$

The α parameter quantifies the mean trap energy in the distribution. As the filling of traps depends on the potential (induced through an external voltage or by illumination), a chemical capacitance (C_{μ}) of electron accumulation can be defined[72,77]. This capacitance corresponds to the average energy distribution of trap states below the transport level. This parameter is a thermodynamic measure of the capability of the PV system to accept or release additional carriers as a consequence of a change in the applied potential or light intensity. This voltage dependence can be expressed as

$$C_{\mu} = C_0 \exp\left(-\frac{\alpha q V}{k_B T}\right) \tag{2.59}$$

Here, C_0 is a constant that depends on the trap density, the temperature and the E$_C$ energy level and it can be calculated by[78,79]

$$C_0 = d(1-\phi_{por})\alpha\frac{q^2N_t}{k_BT}exp\left(\alpha\frac{E_{redox}-E_C}{k_BT}\right) \tag{2.60}$$

where ϕ_{por} is the porosity of the nanostructured material, and E$_{redox}$ is the redox potential of the electrolyte. In *Chapter* 3 the use of EIS to determine and analyze the chemical capacitance considering different shifts in the Fermi level caused by variations in the filling of traps is discussed. For instance, a typical shift of the E$_C$ level, detected by a linear displacement of the C_μ vs V plot, is produced by the presence of certain additives in the electrolyte[15,66,78].

Recombination of electrons in the semiconductor

The slow diffusion transport of the photogenerated carriers through the metal oxide competes with recombination processes. In DSSC, the transported electrons can recombine with oxidized dye molecules that have not been regenerated yet and with the oxidized electron acceptors in the electrolyte[33]. It is commonly accepted that the main pathway for recombination in DSSC is between the metal oxide and the oxidized electrolyte elements[15]. In this case, according to classical chemical kinetics, the rate for this recombination process or back reaction (U_n) can be expressed as

$$U_n = k_{rec}n^{\nu_n}[acceptor^+]^{\nu_{acceptor^+}} \tag{2.61}$$

where $[acceptor^+]$ is the concentration of electrons and oxidized electrolyte electron acceptors, respectively, and their power exponents the partial reaction orders for each element. As the concentration of electron donor can be considered much larger than the electron density[33], the last element of this reaction can also be considered a constant. In addition, evidence for non-linearity (reaction order different than 1) in the recombination process has been widely reported[58,80,81]. Thus, considering that electrons can be transferred only from the CB, the recombination rate above can be rewritten as

$$U_n = k_r n^{\beta} \tag{2.62}$$

being k_r the product of the constant rate k_0 and the oxidized electrolyte electron donor density and β the reaction order for recombination (recombination parameter). For DSSCβ usually presents values within the range 0.5 - 0.8[66,70–72].

In *Chapter* 3 it will be explained how to determine the recombination resistance of the device using small-perturbation optoelectronic techniques.

Reduction of electron acceptors in the electrolyte

The oxidized electron acceptors resulting from the regeneration process of the dye are reduced at the counter-electrode so they can be newly involved in the regeneration[82]. The redox mediator is transported between the working electrode and the counter electrode by diffusion, resulting in a diffusion impedance acting as a series resistance in the DSSC. This resistance depends on the diffusion coefficient and concentration of the redox pair and the distance between electrodes[33,83]. The determination of this resistance by EIS and its interpretation will be discussed in *Chapter* 3. After reaching the counter electrode, the charge transfer reaction to reduce the electron acceptors requires an overpotential (ν) at a certain J, producing a charge transfer resistance ($R_{CT_{ce}}$) given by[33]

$$R_{CT_{ce}} = \frac{RT}{n_{reac} F J_{ex}} \tag{2.63}$$

where R is the ideal gas constant, n_{reac} the number of electrons involved in the reduction reaction of each electron acceptor molecule, F the Faraday's constant and J_{ex} is the current exchange density. For most state-of-the-art devices, this reaction is not considered a limiting aspect of the cell's performance. On the other hand, the diffusion of the redox mediator in the electrolyte can limit the efficiency of the device when using viscous electrolytes like ionic liquids[84–86].

2.5 Perovskite solar cells specifics

As was mentioned in *Chapter* 1, PSCs are based on an asymmetric sandwich configuration, where the active absorbing layer is within two selective materials. A simple schema of the most common basic configuration of this kind of device can be seen in Figure 1.6. Compared to the doping levels of the n-type and p-type doped electron and hole transport materials, the perovskite layer can be considered an intrinsic material. Thus, it is normally accepted that the regular PSCs behave as a n-i-p junction[87–91] (or p-i-n for inverted architecture devices).

However, the electronic nature of perovskite PV materials is under debate[92–94]. The doping properties of the perovskite material depend on the most abundant type of chemical defect in the crystalline structure[95,96]. In this regard, the presence of mobile anion vacancies can play a significant role locally altering the doping levels in the perovskite layer, leading to a p-type material[97,98]. In addition, the directed inclusion of defects in the crystalline structure[99–101] or changing the preparation conditions[102] can make the perovskite to act as n-type or p-type material. This property has been studied to develop *p-n* perovskite homojunctions[103,104] or to delete one of the selective materials[105–107].

Considering the simple p-i-n band structure of PSC, the photovoltage of these heterojunction devices is determined by the Fermi level difference between the ETL and the HTL[108]

$$qV = E_F^p - E_F^n \tag{2.64}$$

where E_F^p and E_F^n are the Fermi levels of the p-type and n-type selective materials. Eqs. 2.7 and 2.8 that determine the electron and hole density, respectively, in the active layer, can also be expressed as

$$n_c = N_c \exp\left(-\frac{E_C - E_F^n}{k_B T}\right) \tag{2.65}$$

$$p_v = N_v \exp\left(-\frac{E_V - E_F^p}{k_B T}\right) \tag{2.66}$$

The structure of a perovskite bulk sandwiched between two selective materials also affect the recombination properties of the material. These devices present a complex situation where different recombination mechanisms shown in Figure 2.6 coexist. It is accepted SRH recombination in the bulk of the perovskite and surface recombination at the interfaces between the perovskite layer and the selective contacts are the dominant processes in PSCs[17–19,109–114]. In the bulk of the perovskite, the presence of defects can be originated by impurities, grain boundaries or additional crystalline/amorphous phases[115,116]. The SRH lifetime described for electrons and holes in Eqs. 2.33 and 2.35 depends on the density and capture rate of the recombination centers. This second parameter is inversely proportional to the dielectric constant of the material (ε), which determines the ability of the material to screen charge, reaching values as high as 70 for $MAPbI_3$ perovskites[117,118]. Most point defects in PSCs with low formation energies only create shallow level states rather than deep traps, leading to these materials to show much longer SRH lifetimes than other semiconductors[116] and impressively long carriers diffusion lengths[92,115,119]. The dielectric contribution of the perovskite material produces a capacitive effect known as geometric capacitance (C_{geo}) that can be expressed as[120]

$$C_{geo} = \frac{A\varepsilon_p\varepsilon_0}{d} \tag{2.67}$$

where A is the area of the device, ε_p is the relative permittivity of the perovskite material compared to the permittivity of vacuum (ε_0). This capacitance can be extracted from EIS measurements, as will be discussed in *Chapter* 3.

PSCs are also peculiar as they show mixed ionic-electronic properties due to the high mobility of ionic vacancies in their crystalline structure[121,122]. This property means that in addition to electron and hole charge carriers moving, in PSCs, there is an additional mobile species, which are charged ions[115]. For $MAPbI_3$ perovskites, this motion corresponds to the migration of iodine ions as the I^- ions in the edge of the PbI_6 octahedron have the shortest distance and lowest activation barrier with its nearest neighbors, compared to the MA^+ and Pb^{2+} ions[121]. The understanding of the relation between the recombination mechanisms in different types of PSCs and the role of the ionic motion in these processes[123–125] is subject of intense debate in the literature and is one of the main topics of this thesis. A deeper look into the effects of this ion migration in the performance of PSCs producing *JV* hysteresis and its implications in the determination of the recombination mechanism through n_{ID} obtained from Eq. 2.20 is provided in the subsections below.

2.5.1 Ion migration and hysteresis

The I^- ions require only a minimal electrical field to migrate in the crystalline perovskite structure compared to the build-in electrical field of PSCs[96,115]. These moving charged ions can attract carriers of opposite charge from the electrodes to maintain electroneutrality, causing local chemical doping in the perovskite films. The depletion regions resulting from this process receive the name of Debye or space-charge layers[126–129], with a ionic Debye length of[120]

$$L_D = \sqrt{\frac{\varepsilon_p \varepsilon_0 k_B T}{q^2 N_0}} \tag{2.68}$$

being N_0 the total density of mobile ions forming the interfacial space charge of the diffuse layer. These Debye layers respond to the V_{bi} in the perovskite layer, screening its electric field. Depending on the nature of the contact work functions, which determine the V_{bi}, and the applied potential, the ions can accumulate in the vicinity of the HTL or the ETL, as can be observed in Figure 2.7.

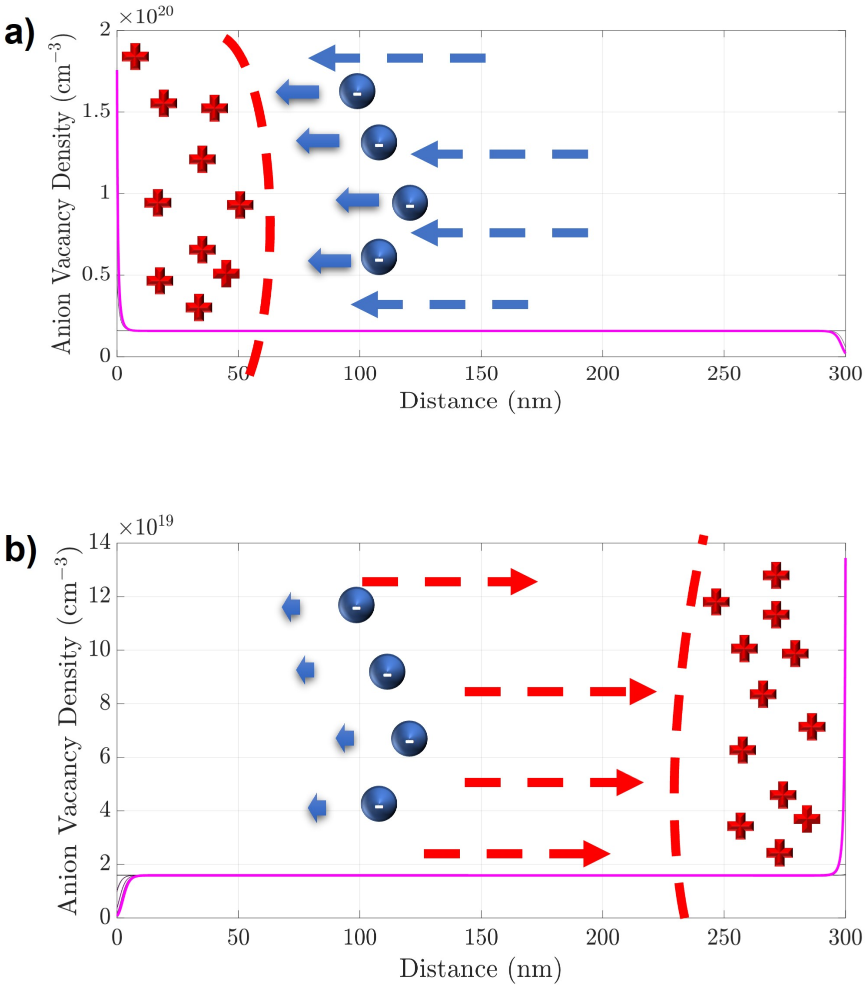

Figure 2.7: Schematic of the formation of Debye layers in a PSCs under conditions leading to anion vacancy accumulation in the vicinity of the ETL (a) and the HTL (b) and the effect of the resulting electric field on the electronic charge extraction. The ionic distribution corresponds to the result of simulations done using the drift-diffusion model *IonMonger*, described in *Chapter* 3.

As a result of the ionic distribution in the perovskite layer, in Figure 2.7 it is shown that depending on the transport layer vicinity where the mobile anion vacancies accumulate, the resulting electric field can work for or against the electronic transport towards the selective contacts. The slow ionic migration makes these layers' formation as a response to the applied voltage a time-dependent process. This ion movement is accountable for another phenomena observed in PSCs, which is the hysteresis in the *JV* curves[130–135]. Hysteresis is a dynamic effect resulting from the slow response of PSCs to a change in the external voltage. The observable outcome is the variation in the *JV* curves with scan rate, scan direction, temperature, the crystallinity of the material, and nature of the contacts[136,137]. Different mechanisms and processes within the PSCs can impact this phenomenon. It is well known that the accumulation of the mobile ionic species at the perovskite/selective contact interfaces can modify the internal electric field driving charge carriers to the ETL and HTL, which can cause hysteresis[127,135,138–143]. The alteration of charge carrier injection or extraction at the transport layer interfaces can lead to charge carrier accumulation, which can also be linked to the occurrence of hysteresis[133,144,145] To analyze the hysteresis, *JV* curves for a forward scan (from J_{SC} to V_{OC}) are usually compared to *JV* curves for reverse scan (V_{OC} to J_{SC}) as is shown in Figure 2.8.

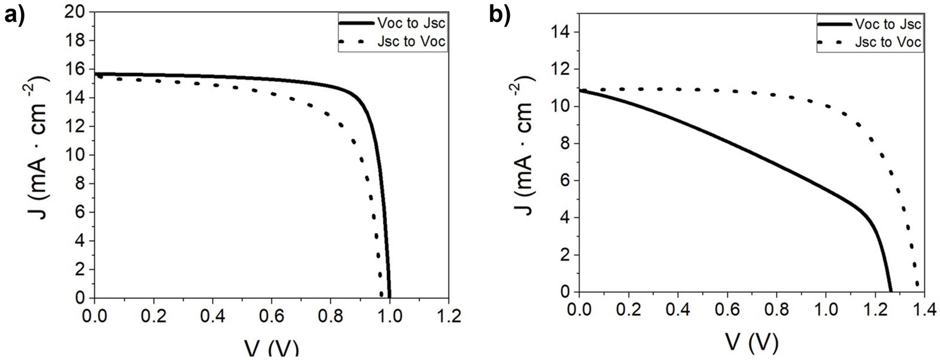

Figure 2.8: Examples of a *JV* curve showing regular (a) and inverted (b) hysteresis. The *JV* curves are the result of simulations done using the DD model *IonMonger*, described in *Chapter* 3.

In Figure 2.8a it is shown the most common hysteresis phenomena, known as regular hysteresis, where the efficiency obtained for the V_{OC} to J_{SC} scan exceeds the achieved by the J_{SC} to V_{OC} scan direction. This is known as regular hysteresis, while in Figure 2.8b, the opposite situation is presented in a result that receives the name of inverted hysteresis. To quantify the hysteresis and determine if it is regular or inverted, the degree of hysteresis (DoH) can be used. This is defined by[139,143]

$$DoH = 100\frac{A_{rev} - A_{for}}{Max.(A_{rev}, A_{for})}\% \tag{2.69}$$

being A_{rev} the area under the JV curve for V_{OC} to J_{SC} scan and A_{for} the area under the J_{SC} to V_{OC} JV curve. When the obtained DoH value is positive, the hysteresis can be considered normal or regular, while when the value is negative, the hysteresis is considered inverted. Regular hysteresis can be explained[127,139] by the slow reorganization of the mobile ions at the transport layer interfaces when the external voltage changes. This ionic distribution causes a favorable internal electric field for charge collection in the reverse scan and unfavorable in the forward. In addition, depending on the diffusion coefficient of the mobile ions in the perovskite layer, the scan rate where this DoH is maximum changes[143]. Inverted hysteresis is a less common phenomena, and its source is still under debate[135,145–147]. Differences between regular and inverted hysteresis and the mechanisms that can be behind the latter are discussed in more detail in *Chapter* 9.

2.5.2 Electronic ideality factor

During the development of this thesis, a novel idea concerning the determination of n_{ID} via Eqs. 2.19 and 2.20 in PSCs has arisen[148,149]. As previously explained, the determination of the n_{ID} factor provides information about the recombination mechanism driving the performance of a PV device. However, for PSCs, values outside the typical range of values (1-2)[19,150] and non-integer values between 1 and 2[17,112,151,152] have been reported, hampering its interpretation using the classical diode theory. The classical approach to the determination of n_{ID} in PV devices considers the transport and recombination mechanisms involving electronic carriers (electrons and holes). However, as mentioned before, in PSCs, a high density of mobile ionic charge coexist with the aforementioned electronic carriers. Thus, the distribution of these ionic species controls the internal electric field in the perovskite layer, as mentioned above, evolving on a slower timescale than the charge-carrier dynamics[18,139,153]. As a result of this distribution, the electric potential across the perovskite film rapidly changes across the previously described Debye layers[133,154,155]. The potential difference caused by the Debye layers depends on the permittivity and the mean density of the ionic species forming the Debye layers[139]. An example of the sudden change in the electrical potential caused by the Debye layers can be observed in Figure 2.9.

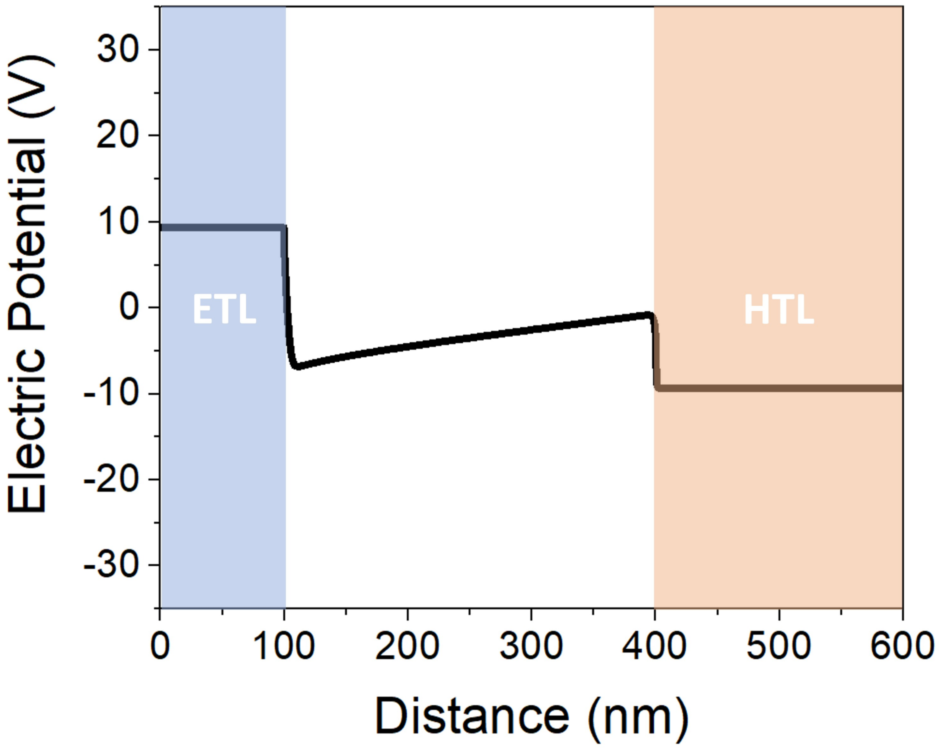

Figure 2.9: Example of the electric potential distribution at V_{OC} of drift-diffusion simulated JV curve of a PSC. The electric potential distribution is the result of simulations done using the drift-diffusion model Ion Monger, described in *Chapter* 3.

To help to explain the non-integer and voltage-dependent n_{ID}, Courtier[148] derived a modified ectypal diode model relating J and V for steady-state measurements, including the effects of ionic charge accumulation at the interfaces. This model considers that recombination losses are controlled by the electric potential distribution, which, as mentioned before, depends on the ionic distribution. By applying this model, Courtier[148] found that the observed voltage dependence of n_{ID} is the result of the nonlinear capacitance associated with the accumulation of charge in the Debye layers[139,153]. This ectypal factor can be measured by the light intensity vs V_{OC} comparison that, as will be shown in *Chapter* 3, is used to determine the traditional n_{ID}. The voltage-dependent ectypal ideality factor (n_{EC}) can be calculated using Eq. 2.70

$$\frac{q}{k_B T}\frac{\delta V_{OC}}{\delta \ln F_{ph}} = n_{EC}\left(1 - \frac{V_{OC} - V_{bi}}{n_{EC}}\frac{dn_{EC}}{dV_{OC}}\right)^{-1} \tag{2.70}$$

being F_{ph} the photonic flux. This n_{EC} intends to replace the classical n_{ID} by a voltage-dependent value that captures the dependence of the dominant recombination mechanism on the electric field across the perovskite layer. In her work, Courtier[148] also determines n_{EC} for steady-state conditions

$$n_{EC} = \frac{V_{bi} - V_{DC}}{F_i(V_1, V_2, V_3, V_4)} \tag{2.71}$$

where $F(V)$ refers to different combinations of the voltage differences (V_1, V_2, V_3 and V_4 in Figure 2.10).

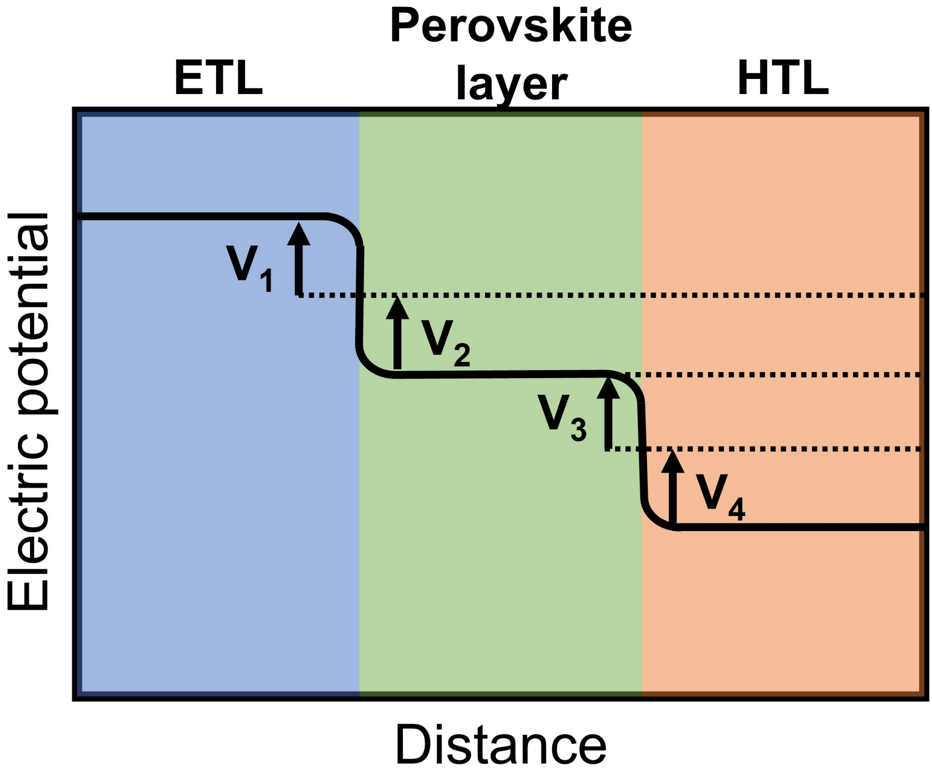

Figure 2.10: Sketch illustrating the potential distribution at steady-state across a PSC, including the four potential drops caused by ionic accumulation that can be involved in the determination of $F(V)$. Figure modified from the left panel of Figure 2 of Courtier's article introducing the ectypal factor concept[148].

Depending on the dominant voltage drops included in Figure 2.10 in Eq. 2.71 the value of n_{EC} for different recombination mechanisms can be estimated[148]. For hole-limited SRH recombination in the bulk of the perovskite, n_{EC} is determined by

$$n_{EC} = \frac{V_{bi} - V}{V_{bi} - V - V_1 - V_2} \tag{2.72}$$

while for the electron-limited recombination, this value is given by

$$n_{EC} = \frac{V_{bi} - V}{V_{bi} - V - V_3 - V_4} \tag{2.73}$$

As for SRH recombination in the interface between the perovskite layer and the selective contacts, for the interface with the ETL, n_{EC} is given by

$$n_{EC} = \frac{V_{bi} - V}{V_{bi} - V - V_1} \tag{2.74}$$

and for the interface with the HTL, this value can be calculated as

$$n_{EC} = \frac{V_{bi} - V}{Vbi - V - V_4} \tag{2.75}$$

Following this line of thought, where the ionic motion inside the PSC is also taken into account when applying the diode model, Bennett *et al.*[149] extended the determination of n_{EC} using EIS measurements. EIS have been widely used to determine the traditional n_{ID} by analyzing the voltage dependence of the high frequency resistance of EIS[17,21], as it will be described in *Chapter* 3. The voltage-dependent n_{EC} can be determined from EIS measurements as

$$n_{EC} = \frac{q}{k_B T} R(\omega \to 0) \left(J_{DC} \Big|_{V=V_0} - J_{DC} \Big|_{V=0} \right) \tag{2.76}$$

where $R(\omega \to 0)$ is the low-frequency (LF) limit resistance from the EIS measurement, and J_{DC} is the current density at the DC voltage of the EIS measurement ($V = V_0$) and SC ($V = 0$) respectively. Due to the mentioned voltage dependence of the classical n_{ID} for PSCs caused by the ion motion, its application to this kind of device is disputed and can be considered as an "apparent" ideality factor (n_{AP}). For this reason, Bennett *et al.*[149] identify an alternative dimensionless constant receiving the name of electronic ideality factor (n_{EL}). This factor allows obtaining the information provided by the traditional ideality factor in conventional PV semiconductors. For this reason, n_{EL} can be used as a tool to identify the dominant recombination mechanism taking place in a PSC. This dimensionless value can be calculated from the results of an EIS measurement at a given DC voltage (V_{DC}) by[149]

$$n_{EL} = \frac{R_{HF}(V_{DC})J_{rec}(V_{DC})}{V_T} \tag{2.77}$$

where R_{HF} is the high-frequency (HF) resistance extracted from the EIS measurement, as it will be explained in *Chapter* 3 and J_{rec} is the recombination current, which can be estimated from

$$J_{rec}(V_{DC}) = J_{gen} - J(V_{DC}) \tag{2.78}$$

where J_{gen} is assumed to be J_{SC} and $J(V_{DC})$ is the steady-state current output of the cell at DC voltage of the EIS measurement. Combining Eqs. 2.77 and 2.78 n_{EL} can be extracted from a EIS measurement by

$$n_{EL} = \frac{q}{k_B T} R_{HF} \left(J_{DC}\bigg|_{V=V_0} - J_{DC}\bigg|_{V=0} \right) \tag{2.79}$$

where R_{HF} is the high frequency resistance, as it will be described in *Chapter* 3. At high frequencies, the sinusoidal voltage perturbation of EIS is applied to the steady-state ionic configuration, so the ions are effectively immobile as they are too slow to respond to the voltage oscillations. Thus, the HF EIS allows for probing the electronic properties of PSCs at a steady state. For this reason, n_{EL} is not voltage-dependent, and it is a purely electronic parameter without the influence of the physical behavior of the ions in the perovskite layer. More information about the EIS technique and the determination of the resistive and capacitive elements can be found in *Chapter* 3. In addition, the determination of n_{EC} and n_{EL} are used in *Chapters* 7 and 8.

Bibliography

[1] A. Smets, K. Jäger, O. Isabella, R. van Swaaij, and M. Zeman, *Solar Energy: The physics and engineering of photovoltaic conversion, technologies and systems*. Cambridge: UIT Cambridge Limited, 2016.

[2] A. Einstein, "Ist die Trägheit eines Körpers von seinem Energieinhalt abhängig?," *Annalen der Physik*, vol. 323, no. 13, pp. 639–641, 1905. _eprint: https://onlinelibrary.wiley.com/doi/pdf/10.1002/andp.19053231314.

[3] M. Planck, "Ueber das Gesetz der Energieverteilung im Normalspectrum," *Annalen der Physik*, vol. 309, no. 3, pp. 553–563, 1901. _eprint: https://onlinelibrary.wiley.com/doi/pdf/10.1002/andp.19013090310.

[4] A. Einstein, "Über einen die Erzeugung und Verwandlung des Lichtes betreffenden heuristischen Gesichtspunkt," *Annalen der Physik*, vol. 322, no. 6, pp. 132–148, 1905. _eprint: https://onlinelibrary.wiley.com/doi/pdf/10.1002/andp.19053220607.

[5] M. J. Klein, "Max Planck and the beginnings of the quantum theory," *Archive for History of Exact Sciences*, vol. 1, pp. 459–479, Oct. 1961.

[6] J. Nelson, *The Physics of Solar Cells*. Imperial College Press, 1 ed., Sept. 2003.

[7] "Reference Air Mass 1.5 Spectra."

[8] G03 Committee, "Tables for Reference Solar Spectral Irradiances: Direct Normal and Hemispherical on 37 Tilted Surface," tech. rep., ASTM International.

[9] S. M. Sze and K. K. Ng, *Physics of Semiconductor Devices*. John Wiley & Sons, Nov. 2006.

[10] W. Pauli, "Über den Zusammenhang des Abschlusses der Elektronengruppen im Atom mit der Komplexstruktur der Spektren," *Zeitschrift für Physik*, vol. 31, pp. 765–783, Feb. 1925.

[11] E. E. Michaelides, *Alternative Energy Sources*. Green Energy and Technology, Berlin, Heidelberg: Springer Berlin Heidelberg, 2012.

[12] W. Shockley and H. J. Queisser, "Detailed balance limit of efficiency of p-n junction solar cells," *Journal of Applied Physics*, vol. 32, no. 3, pp. 510–&, 1961.

[13] S. Rühle, "Tabulated values of the shockley–queisser limit for single junction solar cells," vol. 130, pp. 139–147.

[14] T. Dittrich, *Materials Concepts for Solar Cells*. New Jersey: Imperial College Press, Nov. 2014.

[15] F. Fabregat-Santiago, G. Garcia-Belmonte, I. Mora-Seró, and J. Bisquert, "Characterization of nanostructured hybrid and organic solar cells by impedance spectroscopy," *Physical Chemistry Chemical Physics*, vol. 13, no. 20, pp. 9083–9118, 2011.

[16] C.-t. Sah, R. N. Noyce, and W. Shockley, "Carrier Generation and Recombination in P-N Junctions and P-N Junction Characteristics," *Proceedings of the IRE*, vol. 45, pp. 1228–1243, Sept. 1957. Conference Name: Proceedings of the IRE.

[17] L. Contreras-Bernal, M. Salado, A. Todinova, L. Calio, S. Ahmad, J. Idígoras, and J. A. Anta, "Origin and Whereabouts of Recombination in Perovskite Solar Cells," *The Journal of Physical Chemistry C*, vol. 121, no. 18, pp. 9705–9713, 2017.

[18] P. Calado, D. Burkitt, J. Yao, J. Troughton, T. M. Watson, M. J. Carnie, A. M. Telford, B. C. O'Regan, J. Nelson, and P. R. Barnes, "Identifying Dominant Recombination Mechanisms in Perovskite Solar Cells by Measuring the Transient Ideality Factor," *Physical Review Applied*, vol. 11, p. 044005, Apr. 2019.

[19] J.-P. Correa-Baena, S.-H. Turren-Cruz, W. Tress, A. Hagfeldt, C. Aranda, L. Shooshtari, J. Bisquert, and A. Guerrero, "Changes from Bulk to Surface Recombination Mechanisms between Pristine and Cycled Perovskite Solar Cells," *ACS Energy Letters*, vol. 2, no. 3, pp. 681–688, 2017.

[20] O. Almora, K. T. Cho, S. Aghazada, I. Zimmermann, G. J. Matt, C. J. Brabec, M. K. Nazeeruddin, and G. Garcia-Belmonte, "Discerning recombination mechanisms and ideality factors through impedance analysis of high-efficiency perovskite solar cells," *Nano Energy*, vol. 48, pp. 63–72, 2018.

[21] L. Contreras-Bernal, S. Ramos-Terrón, A. Riquelme, P. P. Boix, J. Idígoras, I. Mora-Seró, and J. A. Anta, "Impedance analysis of perovskite solar cells: a case study," *Journal of Materials Chemistry A*, vol. 7, pp. 12191–12200, May 2019.

[22] T. Kirchartz and U. Rau, "What Makes a Good Solar Cell?," *Advanced Energy Materials*, vol. 0, no. 0, p. 1703385.

[23] W. Tress, "Perovskite Solar Cells on the Way to Their Radiative Efficiency Limit – Insights Into a Success Story of High Open-Circuit Voltage and Low Recombination," *Advanced Energy Materials*, vol. 7, p. 1602358, July 2017.

[24] L. Meitner, “Über die Entstehung der -Strahl-Spektren radioaktiver Substanzen,” *Zeitschrift für Physik*, vol. 9, pp. 131–144, Dec. 1922.

[25] P. Auger, “Sur les rayons secondaires produits dans un gaz par des rayons X.,” *CR Acad. Sci. (F)*, vol. 177, p. 169, 1923.

[26] M. B. Johnston and L. M. Herz, “Hybrid Perovskites for Photovoltaics: Charge-Carrier Recombination, Diffusion, and Radiative Efficiencies,” *Accounts of Chemical Research*, vol. 49, pp. 146–154, Jan. 2016.

[27] W. Shockley and W. T. Read, “Statistics of the Recombinations of Holes and Electrons,” *Physical Review*, vol. 87, pp. 835–842, Sept. 1952.

[28] R. N. Hall, “Electron-Hole Recombination in Germanium,” *Physical Review*, vol. 87, pp. 387–387, July 1952. Publisher: American Physical Society.

[29] Y. Dang, Y. Liu, Y. Sun, D. Yuan, X. Liu, W. Lu, G. Liu, H. Xia, and X. Tao, “Bulk crystal growth of hybrid perovskite material CH3NH3PbI3,” *Crystengcomm*, vol. 17, no. 3, pp. 665–670, 2015.

[30] W. Sutherland, “LXXV. A dynamical theory of diffusion for non-electrolytes and the molecular mass of albumin,” *The London, Edinburgh, and Dublin Philosophical Magazine and Journal of Science*, vol. 9, pp. 781–785, June 1905. Publisher: Taylor & Francis _eprint: https://doi.org/10.1080/14786440509463331.

[31] A. Einstein, “Über die von der molekularkinetischen Theorie der Wärme geforderte Bewegung von in ruhenden Flüssigkeiten suspendierten Teilchen,” *Annalen der Physik*, vol. vol. 4, t. 17, 1905.

[32] M. von Smoluchowski, “Zur kinetischen Theorie der Brownschen Molekularbewegung und der Suspensionen,” Jan. 1906.

[33] A. Hagfeldt, G. Boschloo, L. Sun, L. Kloo, and H. Pettersson, “Dye-Sensitized Solar Cells,” *Chemical Reviews*, vol. 110, pp. 6595–6663, Nov. 2010.

[34] A. Hagfeldt and M. Grätzel, “Molecular Photovoltaics,” *Accounts of Chemical Research*, vol. 33, pp. 269–277, May 2000. Publisher: American Chemical Society.

[35] J. Idígoras, J. Sobuś, M. Jancelewicz, E. Azaceta, R. Tena-Zaera, J. A. Anta, and M. Ziółek, “Effect of different photoanode nanostructures on the initial charge separation and electron injection process in dye sensitized solar cells: A photophysical study with indoline dyes,” *Materials Chemistry and Physics*, vol. 170, pp. 218–228, Feb. 2016.

[36] J. B. Asbury, Y. Wang, and T. Lian, “Multiple-Exponential Electron Injection in Ru(dcbpy)2(SCN)2 Sensitized ZnO Nanocrystalline Thin Films,” *J. Phys. Chem. B*, vol. 103, no. 32, pp. 6643–6647, 1999.

[37] R. Katoh, A. Furube, A. V. Barzykin, H. Arakawa, and M. Tachiya, “Kinetics and mechanism of electron injection and charge recombination in dye-sensitized nanocrystalline semiconductors,” *Coordination Chemistry Reviews*, vol. 248, pp. 1195–1213, July 2004.

[38] A. Furube, R. Katoh, K. Hara, S. Murata, H. Arakawa, and M. Tachiya, “Ultrafast Stepwise Electron Injection from Photoexcited Ru-Complex into Nanocrystalline ZnO Film via Intermediates at the Surface,” *J. Phys. Chem. B*, vol. 107, no. 17, pp. 4162–4166, 2003.

[39] S. A. Haque, Y. Tachibana, R. L. Willis, J. E. Moser, M. Gratzel, D. R. Klug, and J. R. Durrant, “Parameters influencing charge recombination kinetics in dye-sensitized nanocrystalline titanium dioxide films,” *Journal of Physical Chemistry B*, vol. 104, no. 3, pp. 538–547, 2000.

[40] J. Halme, G. Boschloo, A. Hagfeldt, and P. Lund, “Spectral Characteristics of Light Harvesting, Electron Injection, and Steady-State Charge Collection in Pressed TiO2 Dye Solar Cells,” *The Journal of Physical Chemistry C*, vol. 112, pp. 5623–5637, Apr. 2008.

[41] P. R. F. Barnes, A. Y. Anderson, S. E. Koops, J. R. Durrant, and B. C. O’Regan, “Electron Injection Efficiency and Diffusion Length in Dye-Sensitised Solar Cells Derived from Incident Photon Conversion Efficiency Measurements.,” *The Journal of Physical Chemistry C*, vol. 113, p. 12615, July 2009.

[42] R. Katoh, A. Furube, K. Hara, S. Murata, H. Sugihara, H. Arakawa, and M. Tachiya, “Efficiencies of Electron Injection from Excited Sensitizer Dyes to Nanocrystalline ZnO Films as Studied by Near-IR Optical Absorption of Injected Electrons,” *The Journal of Physical Chemistry B*, vol. 106, pp. 12957–12964, Dec. 2002. Publisher: American Chemical Society.

[43] J. Sobuś, G. Burdziński, J. Karolczak, J. Idígoras, J. A. Anta, and M. Ziółek, “Comparison of TiO2 and ZnO Solar Cells Sensitized with an Indoline Dye: Time-Resolved Laser Spectroscopy Studies of Partial Charge Separation Processes,” *Langmuir*, vol. 30, pp. 2505–2512, Mar. 2014.

[44] J. A. Anta, E. Guillén, and R. Tena-Zaera, “ZnO-based dye-sensitized solar cells,” *The Journal of Physical Chemistry C*, vol. 116, no. 21, pp. 11413–11425, 2012.

[45] S. E. Koops, B. C. O’Regan, P. R. F. Barnes, and J. R. Durrant, “Parameters Influencing the Efficiency of Electron Injection in Dye-Sensitized Solar Cells,” *Journal of the American Chemical Society*, vol. 131, pp. 4808–4818, Apr. 2009.

[46] S. Pelet, J.-E. Moser, and M. Grätzel, “Cooperative Effect of Adsorbed Cations and Iodide on the Interception of Back Electron Transfer in the Dye Sensitization of Nanocrystalline TiO2,” *The Journal of Physical Chemistry B*, vol. 104, pp. 1791–1795, Mar. 2000.

[47] S. A. Haque, Y. Tachibana, D. R. Klug, and J. R. Durrant, “Charge Recombination Kinetics in Dye-Sensitized Nanocrystalline Titanium Dioxide Films under Externally Applied Bias,” *The Journal of Physical Chemistry B*, vol. 102, pp. 1745–1749, Mar. 1998. Publisher: American Chemical Society.

[48] J. R. Jennings, Y. Liu, and Q. Wang, “Efficiency Limitations in Dye-Sensitized Solar Cells Caused by Inefficient Sensitizer Regeneration,” *J. Phys. Chem. C*, vol. 115, no. 30, pp. 15109–15120, 2011.

[49] A. Mathew, V. Anand, G. M. Rao, and N. Munichandraiah, “Effect of iodine concentration on the photovoltaic properties of dye sensitized solar cells for various I2/LiI ratios,” *Electrochimica Acta*, vol. 87, pp. 92–96, Jan. 2013.

[50] J. M. Vicent-Luna, J. Idígoras, S. Hamad, S. Calero, and J. A. Anta, “Ion Transport in Electrolytes for Dye-Sensitized Solar Cells: A Combined Experimental and Theoretical Study,” *The Journal of Physical Chemistry C*, vol. 118, no. 49, pp. 28448–28455, 2014.

[51] J. Idígoras, L. Pellejà, E. Palomares, and J. A. Anta, “The Redox Pair Chemical Environment Influence on the Recombination Loss in Dye-Sensitized Solar Cells,” *The Journal of Physical Chemistry C*, vol. 118, no. 8, pp. 3878–3889, 2014.

[52] I. Montanari, J. Nelson, and J. R. Durrant, “Iodide electron transfer kinetics in dye-sensitized nanocrystalline TiO2 films,” *Journal of Physical Chemistry B*, vol. 106, no. 47, pp. 12203–12210, 2002.

[53] H. Wang and L. M. Peter, “Influence of Electrolyte Cations on Electron Transport and Electron Transfer in Dye-Sensitized Solar Cells,” *The Journal of Physical Chemistry C*, vol. 116, pp. 10468–10475, May 2012.

[54] J. J. Kelly and D. Vanmaekelbergh, “Charge carrier dynamics in nanoporous photoelectrodes,” *Electrochimica Acta*, vol. 43, pp. 2773–2780, June 1998.

[55] G. K. Boschloo, A. Goossens, and J. Schoonman, “Photoelectrochemical Study of Thin Anatase TiO2 Films Prepared by Metallorganic Chemical Vapor Deposition,” *Journal of The Electrochemical Society*, vol. 144, p. 1311, Apr. 1997. Publisher: IOP Publishing.

[56] A. Petrozza, C. Groves, and H. J. Snaith, “Electron transport and recombination in dye-sensitized mesoporous TiO2 probed by photoinduced charge-conductivity modulation spectroscopy with Monte Carlo modeling,” *Journal of the American Chemical Society*, vol. 130, no. 39, pp. 12912–12920, 2008.

[57] M. Wang, P. Chen, R. Humphry-Baker, S. M. Zakeeruddin, and M. Gratzel, “The Influence of Charge Transport and Recombination on the Performance of Dye-Sensitized Solar Cells,” *CHEMPHYSCHEM*, vol. 10, pp. 290–299, Jan. 2009.

[58] J. Villanueva-Cab, H. Wang, G. Oskam, and L. M. Peter, “Electron Diffusion and Back Reaction in Dye-Sensitized Solar Cells: The Effect of Nonlinear Recombination Kinetics,” *The Journal of Physical Chemistry Letters*, vol. 1, no. 4, pp. 748–751, 2010.

[59] J. Navas, E. Guillén, R. Alcántara, C. Fernández-Lorenzo, J. Martín-Calleja, G. Oskam, J. Idígoras, T. Berger, and J. A. Anta, “Direct Estimation of the Electron Diffusion Length in Dye-Sensitized Solar Cells,” *The Journal of Physical Chemistry Letters*, vol. 0, no. 0, pp. 1045–1050, 2011.

[60] F. Cao, G. Oskam, G. J. Meyer, and P. C. Searson, “Electron transport in porous nanocrystalline TiO2 photoelectrochemical cells,” *Journal of Physical Chemistry*, vol. 100, no. 42, pp. 17021–17027, 1996.

[61] L. Dloczik, O. Ileperuma, I. Lauermann, L. M. Peter, E. A. Ponomarev, G. Redmond, N. J. Shaw, and I. Uhlendorf, “Dynamic Response of Dye-Sensitized Nanocrystalline Solar Cells: Characterization by Intensity-Modulated Photocurrent Spectroscopy,” *The Journal of Physical Chemistry B*, vol. 101, no. 49, pp. 10281–10289, 1997.

[62] J. van de Lagemaat and A. J. Frank, “Effect of the Surface-State Distribution on Electron Transport in Dye-Sensitized TiO2 Solar Cells: Nonlinear Electron-Transport Kinetics,” *The Journal of Physical Chemistry B*, vol. 104, pp. 4292–4294, May 2000.

[63] J. Bisquert and V. S. Vikhrenko, “Interpretation of the time constants measured by kinetic techniques in nanostructured semiconductor electrodes and dye-sensitized solar cells,” *Journal of Physical Chemistry B*, vol. 108, no. 7, pp. 2313–2322, 2004.

[64] A. C. Fisher, L. M. Peter, E. A. Ponomarev, A. B. Walker, and K. G. U. Wijayantha, “Intensity dependence of the back reaction and transport of electrons in dye-sensitized nanocrystalline TiO solar cells,” *Journal of Physical Chemistry B*, vol. 104, no. 5, pp. 949–958, 2000.

[65] J. Bisquert, “Chemical diffusion coefficient of electrons in nanostructured semiconductor electrodes and dye-sensitized solar cells,” *Journal of Physical Chemistry B*, vol. 108, no. 7, pp. 2323–2332, 2004.

[66] E. Guillén, L. M. Peter, and J. A. Anta, “Electron Transport and Recombination in ZnO-Based Dye-Sensitized Solar Cells,” *J. Phys. Chem. C*, vol. 115, no. 45, pp. 22622–22632, 2011.

[67] J. A. Anta, I. Mora-Sero, T. Dittrich, and J. Bisquert, “Interpretation of diffusion coefficients in nanostructured materials from random walk numerical simulation,” *Physical Chemistry Chemical Physics*, vol. 10, no. 30, pp. 4478–4485, 2008.

[68] S. Ito, S. M. Zakeeruddin, R. Humphry-Baker, P. Liska, R. Charvet, P. Comte, M. K. Nazeeruddin, P. Pechy, M. Takata, H. Miura, S. Uchida, and M. Gratzel, “High-efficiency organic-dye-sensitized solar cells controlled by nanocrystalline-TiO2 electrode thickness,” *Advanced Materials*, vol. 18, pp. 1202–1205, May 2006.

[69] J. Bisquert, “Theory of the Impedance of Electron Diffusion and Recombination in a Thin Layer,” *The Journal of Physical Chemistry B*, vol. 106, no. 2, pp. 325–333, 2002.

[70] J. Bisquert, A. Zaban, and P. Salvador, “Analysis of the mechanisms of electron recombination in nanoporous TiO dye-sensitized solar cells. Nonequilibrium steady-state statistics and interfacial electron transfer via surface states,” *Journal of Physical Chemistry B*, vol. 106, no. 34, pp. 8774–8782, 2002.

[71] J. Bisquert and I. Mora-Seró, “Simulation of Steady-State Characteristics of Dye-Sensitized Solar Cells and the Interpretation of the Diffusion Length,” *The Journal of Physical Chemistry Letters*, vol. 1, no. 1, pp. 450–456, 2010.

[72] J. Bisquert, “Chemical capacitance of nanostructured semiconductors: its origin and significance for nanocomposite solar cells,” *Physical Chemistry Chemical Physics*, vol. 5, no. 24, pp. 5360–5364, 2003.

[73] J. A. Anta and V. Morales-Florez, “Combined effect of energetic and spatial disorder on the trap-limited electron diffusion coefficient of metal-oxide nanostructures,” *Journal of Physical Chemistry C*, vol. 112, no. 27, pp. 10287–10293, 2008. Times Cited: 0 Cited Reference Count: 48 English Article J PHYS CHEM C 321VT.

[74] J. A. Anta, I. Mora-Sero, T. Dittrich, and J. Bisquert, “Dynamics of charge separation and trap-limited electron transport in TiO2 nanostructures,” *Journal of Physical Chemistry C*, vol. 111, no. 37, pp. 13997–14000, 2007.

[75] J. v. d. Lagemaat and A. J. Frank, “Effect of the surface-state distribution on electron transport in dye-sensitized TiO2 solar cells: Nonlinear electron-transport kinetics,” *Journal of Physical Chemistry B*, vol. 104, no. 18, pp. 4292–4294, 2000. Times Cited: 77 Cited Reference Count: 16 English Letter J PHYS CHEM B 313MM.

[76] J. Bisquert, F. Fabregat-Santiago, I. Mora-Sero, G. Garcia-Belmonte, E. M. Barea, and E. Palomares, “A review of recent results on electrochemical determination of the density of electronic states of nanostructured metal-oxide semiconductors and organic hole conductors,” *Inorganica Chimica Acta*, vol. 361, no. 3, pp. 684–698, 2008. Times Cited: 4 Cited Reference Count: 92 English Review INORG CHIM ACTA 280KV.

[77] F. Fabregat-Santiago, H. Randriamahazaka, A. Zaban, J. Garcia-Canadas, G. Garcia-Belmonte, and J. Bisquert, “Chemical capacitance of nanoporous-nanocrystalline TiO2 in a room temperature ionic liquid,” *Physical Chemistry Chemical Physics*, vol. 8, no. 15, pp. 1827–1833, 2006.

[78] S. R. Raga, E. M. Barea, and F. Fabregat-Santiago, “Analysis of the Origin of Open Circuit Voltage in Dye Solar Cells,” *The Journal of Physical Chemistry Letters*, vol. 3, no. 12, pp. 1629–1634, 2012.

[79] D. Pourjafari, D. Reyes-Coronado, A. Vega-Poot, R. Escalante, D. Kirkconnell-Reyes, R. García-Rodríguez, J. A. Anta, and G. Oskam, “Brookite-Based Dye-Sensitized Solar Cells: Influence of Morphology and Surface Chemistry on Cell Performance,” *The Journal of Physical Chemistry C*, vol. 122, pp. 14277–14288, July 2018.

[80] J. P. Gonzalez-Vazquez, G. Oskam, and J. A. Anta, “Origin of Nonlinear Recombination in Dye-Sensitized Solar Cells: Interplay between Charge Transport and Charge Transfer,” *The Journal of Physical Chemistry C*, Oct. 2012.

[81] M. Ansari-Rad, Y. Abdi, and E. Arzi, “Reaction Order and Ideality Factor in Dye-Sensitized Nanocrystalline Solar Cells: A Theoretical Investigation,” *J. Phys. Chem. C*, vol. 116, no. 20, pp. 10867–10872, 2012.

[82] K. Sharma, V. Sharma, and S. S. Sharma, “Dye-Sensitized Solar Cells: Fundamentals and Current Status,” *Nanoscale Research Letters*, vol. 13, p. 381, Nov. 2018.

[83] A. Hauch and A. Georg, “Diffusion in the electrolyte and charge-transfer reaction at the platinum electrode in dye-sensitized solar cells,” *Electrochimica Acta*, vol. 46, pp. 3457–3466, Aug. 2001.

[84] D. Shi, N. Pootrakulchote, R. Z. Li, J. Guo, Y. Wang, S. M. Zakeeruddin, M. Gratzel, and P. Wang, “New Efficiency Records for Stable Dye-Sensitized Solar Cells with Low-Volatility and Ionic Liquid Electrolytes,” *Journal of Physical Chemistry C*, vol. 112, no. 44, pp. 17046–17050, 2008.

[85] Y. Cao, J. Zhang, Y. Bai, R. Li, S. M. Zakeeruddin, M. Grätzel, and P. Wang, “Dye-Sensitized Solar Cells with Solvent-Free Ionic Liquid Electrolytes,” *The Journal of Physical Chemistry C*, vol. 112, pp. 13775–13781, Sept. 2008.

[86] L. González-García, J. Idígoras, A. R. González-Elipe, A. Barranco, and J. A. Anta, "Charge collection properties of dye-sensitized solar cells based on 1-dimensional TiO2 porous nanostructures and ionic-liquid electrolytes," *Journal of Photochemistry and Photobiology A: Chemistry*, vol. 241, pp. 58–66, 2012.

[87] K. Miyano, N. Tripathi, M. Yanagida, and Y. Shirai, "Lead Halide Perovskite Photovoltaic as a Model p–i–n Diode," *Accounts of Chemical Research*, 2016.

[88] C. Momblona, L. Gil-Escrig, E. Bandiello, E. M. Hutter, M. Sessolo, K. Lederer, J. Blochwitz-Nimoth, and H. J. Bolink, "Efficient vacuum deposited p-i-n and n-i-p perovskite solar cells employing doped charge transport layers," *Energy & Environmental Science*, vol. 9, pp. 3456–3463, Nov. 2016.

[89] J. Diekmann, P. Caprioglio, M. H. Futscher, V. M. Le Corre, S. Reichert, F. Jaiser, M. Arvind, L. P. Toro, E. Gutierrez-Partida, F. Peña-Camargo, C. Deibel, B. Ehrler, T. Unold, T. Kirchartz, D. Neher, and M. Stolterfoht, "Pathways toward 30% Efficient Single-Junction Perovskite Solar Cells and the Role of Mobile Ions," *Solar RRL*, vol. 5, no. 8, p. 2100219, 2021. _eprint: https://onlinelibrary.wiley.com/doi/pdf/10.1002/solr.202100219.

[90] N.-G. Park, "Perovskite solar cells: an emerging photovoltaic technology," *Materials Today*, vol. 18, pp. 65–72, Mar. 2015.

[91] E. C. Smith, C. L. C. Ellis, H. Javaid, L. A. Renna, Y. Liu, T. P. Russell, M. Bag, and D. Venkataraman, "Interplay between Ion Transport, Applied Bias, and Degradation under Illumination in Hybrid Perovskite p-i-n Devices," *The Journal of Physical Chemistry C*, 2018.

[92] S. D. Stranks, G. E. Eperon, G. Grancini, C. Menelaou, M. J. P. Alcocer, T. Leijtens, L. M. Herz, A. Petrozza, and H. J. Snaith, "Electron-Hole Diffusion Lengths Exceeding 1 Micrometer in an Organometal Trihalide Perovskite Absorber," *Science*, vol. 342, no. 6156, pp. 341–344, 2013.

[93] A. Guerrero, E. J. Juarez-Perez, J. Bisquert, I. Mora-Sero, and G. Garcia-Belmonte, "Electrical field profile and doping in planar lead halide perovskite solar cells," *Applied Physics Letters*, vol. 105, p. 133902, Sept. 2014.

[94] J. Kim, S.-H. Lee, J. H. Lee, and K.-H. Hong, "The Role of Intrinsic Defects in Methylammonium Lead Iodide Perovskite," *The Journal of Physical Chemistry Letters*, vol. 5, pp. 1312–1317, Apr. 2014. Publisher: American Chemical Society.

[95] L. A. Frolova, N. N. Dremova, and P. A. Troshin, "The chemical origin of the p-type and n-type doping effects in the hybrid methylammonium–lead iodide (MAPbI3) perovskite solar cells," *Chemical Communications*, vol. 51, pp. 14917–14920, Sept. 2015.

[96] Y. Yuan, J. Chae, Y. Shao, Q. Wang, Z. Xiao, A. Centrone, and J. Huang, "Photovoltaic Switching Mechanism in Lateral Structure Hybrid Perovskite Solar Cells," *Advanced Energy Materials*, vol. 5, no. 15, p. 1500615.

[97] A. Zohar, I. Levine, S. Gupta, O. Davidson, D. Azulay, O. Millo, I. Balberg, G. Hodes, and D. Cahen, "What Is the Mechanism of MAPbI3 p-Doping by I2? Insights from Optoelectronic Properties," *ACS Energy Letters*, vol. 2, pp. 2408–2414, Oct. 2017.

[98] M. García-Batlle, O. Baussens, S. Amari, J. Zaccaro, E. Gros-Daillon, J.-M. Verilhac, A. Guerrero, and G. Garcia-Belmonte, "Moving Ions Vary Electronic Conductivity in Lead Bromide Perovskite Single Crystals through Dynamic Doping," *Advanced Electronic Materials*, vol. n/a, no. n/a, p. 2000485.

[99] S. Colella, E. Mosconi, P. Fedeli, A. Listorti, F. Gazza, F. Orlandi, P. Ferro, T. Besagni, A. Rizzo, G. Calestani, G. Gigli, F. De Angelis, and R. Mosca, "MAPbI3-xClx Mixed Halide Perovskite for Hybrid Solar Cells: The Role of Chloride as Dopant on the Transport and Structural Properties," *Chemistry of Materials*, vol. 25, pp. 4613–4618, Nov. 2013.

[100] M. Fischer, K. Tvingstedt, A. Baumann, and V. Dyakonov, "Doping Profile in Planar Hybrid Perovskite Solar Cells Identifying Mobile Ions," *ACS Applied Energy Materials*, vol. 1, pp. 5129–5134, Oct. 2018.

[101] X. Ma, L. Yang, K. Lei, S. Zheng, C. Chen, and H. Song, "Doping in inorganic perovskite for photovoltaic application," *Nano Energy*, vol. 78, p. 105354, Dec. 2020.

[102] D. Song, P. Cui, T. Wang, D. Wei, M. Li, F. Cao, X. Yue, P. Fu, Y. Li, Y. He, B. Jiang, and M. Trevor, "Managing Carrier Lifetime and Doping Property of Lead Halide Perovskite by Postannealing Processes for Highly Efficient Perovskite Solar Cells," *The Journal of Physical Chemistry C*, vol. 119, no. 40, pp. 22812–22819, 2015.

[103] B. Dänekamp, C. Müller, M. Sendner, P. P. Boix, M. Sessolo, R. Lovrincic, and H. J. Bolink, "Perovskite–Perovskite Homojunctions via Compositional Doping," *The Journal of Physical Chemistry Letters*, vol. 9, pp. 2770–2775, June 2018. Publisher: American Chemical Society.

[104] P. Cui, D. Wei, J. Ji, H. Huang, E. Jia, S. Dou, T. Wang, W. Wang, and M. Li, "Planar p–n homojunction perovskite solar cells with efficiency exceeding 21.3%," *Nature Energy*, vol. 4, pp. 150–159, Feb. 2019. Number: 2 Publisher: Nature Publishing Group.

[105] A. Mei, X. Li, L. Liu, Z. Ku, T. Liu, Y. Rong, M. Xu, M. Hu, J. Chen, Y. Yang, M. Grätzel, and H. Han, “A hole-conductor–free, fully printable mesoscopic perovskite solar cell with high stability,” *Science*, vol. 345, pp. 295–298, July 2014.

[106] D. Liu, J. Yang, and T. L. Kelly, “Compact Layer Free Perovskite Solar Cells with 13.5% Efficiency,” *Journal of the American Chemical Society*, vol. 136, pp. 17116–17122, Dec. 2014.

[107] E. Edri, S. Kirmayer, A. Henning, S. Mukhopadhyay, K. Gartsman, Y. Rosenwaks, G. Hodes, and D. Cahen, “Why Lead Methylammonium Tri-Iodide Perovskite-Based Solar Cells Require a Mesoporous Electron Transporting Scaffold (but Not Necessarily a Hole Conductor),” *Nano Letters*, vol. 14, no. 2, pp. 1000–1004, 2014.

[108] C. Xiong and Y. Ruo-He, “Photovoltage analysis of a heterojunction solar cell,” *Chinese Physics B*, vol. 20, pp. 57302–057302, May 2011.

[109] E. Guillén, F. J. Ramos, J. A. Anta, and S. Ahmad, “Elucidating Transport-Recombination Mechanisms in Perovskite Solar Cells by Small-Perturbation Techniques,” *The Journal of Physical Chemistry C*, vol. 118, pp. 22913–22922, Oct. 2014.

[110] P. Yadav, S. H. Turren Cruz, D. Prochowicz, M. M. Tavakoli, K. Pandey, S. M. Zakeeruddin, M. Grätzel, A. Hagfeldt, and M. Saliba, “Elucidation of Charge Recombination and Accumulation Mechanism in Mixed Perovskite Solar Cells,” *The Journal of Physical Chemistry C*, 2018.

[111] I. Zarazua, G. Han, P. P. Boix, S. Mhaisalkar, F. Fabregat-Santiago, I. Mora-Seró, J. Bisquert, and G. Garcia-Belmonte, “Surface Recombination and Collection Efficiency in Perovskite Solar Cells from Impedance Analysis,” *The Journal of Physical Chemistry Letters*, vol. 7, pp. 5105–5113, Dec. 2016.

[112] M. Stolterfoht, P. Caprioglio, C. M. Wolff, J. A. Márquez, J. Nordmann, S. Zhang, D. Rothhardt, U. Hörmann, Y. Amir, A. Redinger, L. Kegelmann, F. Zu, S. Albrecht, N. Koch, T. Kirchartz, M. Saliba, T. Unold, and D. Neher, “The impact of energy alignment and interfacial recombination on the internal and external open-circuit voltage of perovskite solar cells,” *Energy & Environmental Science*, vol. 12, pp. 2778–2788, Sept. 2019.

[113] J. Idígoras, L. Contreras-Bernal, J. M. Cave, N. E. Courtier, Barranco, A. Borras, J. R. Sánchez-Valencia, J. A. Anta, and A. B. Walker, “The Role of Surface Recombination on the Performance of Perovskite Solar Cells: Effect of Morphology and Crystalline Phase of TiO2 Contact,” *Advanced Materials Interfaces*, vol. 5, p. 1801076, Nov. 2018.

[114] C. M. Wolff, P. Caprioglio, M. Stolterfoht, and D. Neher, “Nonradiative Recombination in Perovskite Solar Cells: The Role of Interfaces,” *Advanced Materials*, vol. 0, no. 0, p. 1902762.

[115] N.-G. Park, M. Grätzel, and T. Miyasaka, eds., *Organic-Inorganic Halide Perovskite Photovoltaics*. Cham: Springer International Publishing, 2016.

[116] G. O. Odunmbaku, S. Chen, B. Guo, Y. Zhou, N. A. N. Ouedraogo, Y. Zheng, J. Li, M. Li, and K. Sun, “Recombination Pathways in Perovskite Solar Cells,” *Advanced Materials Interfaces*, vol. n/a, no. n/a, p. 2102137. _eprint: https://onlinelibrary.wiley.com/doi/pdf/10.1002/admi.202102137.

[117] R. E. Brandt, V. Stevanović, D. S. Ginley, and T. Buonassisi, “Identifying defect-tolerant semiconductors with high minority-carrier lifetimes: beyond hybrid lead halide perovskites,” *MRS Communications*, vol. 5, pp. 265–275, June 2015. Publisher: Cambridge University Press.

[118] Q. Lin, A. Armin, R. C. R. Nagiri, P. L. Burn, and P. Meredith, “Electro-optics of perovskite solar cells,” *Nature Photonics*, vol. 9, pp. 106–112, Feb. 2015.

[119] G. Xing, N. Mathews, S. Sun, S. S. Lim, Y. M. Lam, M. Grätzel, S. Mhaisalkar, and T. C. Sum, “Long-Range Balanced Electron- and Hole-Transport Lengths in Organic-Inorganic CH3NH3PbI3,” *Science*, vol. 342, no. 6156, pp. 344–347, 2013.

[120] P. Lopez-Varo, J. A. Jiménez-Tejada, M. García-Rosell, S. Ravishankar, G. Garcia-Belmonte, J. Bisquert, and O. Almora, “Device Physics of Hybrid Perovskite Solar cells: Theory and Experiment,” *Advanced Energy Materials*, vol. 8, no. 14, p. 1702772, 2018.

[121] C. Eames, J. M. Frost, P. R. F. Barnes, B. C. O’Regan, A. Walsh, and M. S. Islam, “Ionic transport in hybrid lead iodide perovskite solar cells,” *Nature Communications*, vol. 6, p. 7497, June 2015.

[122] A. Walsh, D. O. Scanlon, S. Chen, X. G. Gong, and S.-H. Wei, “Self-Regulation Mechanism for Charged Point Defects in Hybrid Halide Perovskites,” *Angewandte Chemie (International Ed. in English)*, vol. 54, pp. 1791–1794, Feb. 2015.

[123] S. T. Birkhold, J. T. Precht, H. Liu, R. Giridharagopal, G. E. Eperon, L. Schmidt-Mende, X. Li, and D. S. Ginger, “Interplay of Mobile Ions and Injected Carriers Creates Recombination Centers in Metal Halide Perovskites under Bias,” *ACS Energy Letters*, pp. 1279–1286, May 2018.

[124] A. Pockett and M. J. Carnie, “Ionic Influences on Recombination in Perovskite Solar Cells,” *ACS Energy Letters*, vol. 2, pp. 1683–1689, July 2017.

[125] F. Ebadi, M. Aryanpour, R. Mohammadpour, and N. Taghavinia, “Coupled Ionic-Electronic Equivalent Circuit to Describe Asymmetric Rise and Decay of Photovoltage Profile in Perovskite Solar Cells,” *Scientific Reports*, vol. 9, pp. 1–9, Aug. 2019.

[126] S. E. J. O’Kane, G. Richardson, A. Pockett, R. G. Niemann, J. M. Cave, N. Sakai, G. E. Eperon, H. J. Snaith, J. M. Foster, P. J. Cameron, and A. B. Walker, “Measurement and modelling of dark current decay transients in perovskite solar cells,” *Journal of Materials Chemistry C*, vol. 5, no. 2, pp. 452–462, 2017. Publisher: Royal Society of Chemistry.

[127] G. Richardson, S. E. J. O’Kane, R. G. Niemann, T. A. Peltola, J. M. Foster, P. J. Cameron, and A. B. Walker, “Can slow-moving ions explain hysteresis in the current–voltage curves of perovskite solar cells?,” *Energy & Environmental Science*, vol. 9, pp. 1476–1485, Feb. 2016.

[128] J. M. Foster, H. J. Snaith, T. Leijtens, and G. Richardson, “A Model for the Operation of Perovskite Based Hybrid Solar Cells: Formulation, Analysis, and Comparison to Experiment,” *SIAM Journal on Applied Mathematics*, vol. 74, pp. 1935–1966, Jan. 2014. Publisher: Society for Industrial and Applied Mathematics.

[129] O. Almora, A. Guerrero, and G. Garcia-Belmonte, “Ionic charging by local imbalance at interfaces in hybrid lead halide perovskites,” *Applied Physics Letters*, vol. 108, no. 4, p. 043903, 2016.

[130] H. J. Snaith, A. Abate, J. M. Ball, G. E. Eperon, T. Leijtens, N. K. Noel, S. D. Stranks, J. T.-W. Wang, K. Wojciechowski, and W. Zhang, “Anomalous Hysteresis in Perovskite Solar Cells,” *The Journal of Physical Chemistry Letters*, vol. 5, pp. 1511–1515, May 2014.

[131] H.-S. Kim, I.-H. Jang, N. Ahn, M. Choi, A. Guerrero, J. Bisquert, and N.-G. Park, “Control of I–V Hysteresis in CH3NH3PbI3 Perovskite Solar Cell,” *The Journal of Physical Chemistry Letters*, vol. 6, pp. 4633–4639, Nov. 2015.

[132] B. Chen, M. Yang, S. Priya, and K. Zhu, “Origin of J–V Hysteresis in Perovskite Solar Cells,” *The Journal of Physical Chemistry Letters*, vol. 7, no. 5, pp. 905–917, 2016.

[133] S. A. L. Weber, I. M. Hermes, S.-H. Turren-Cruz, C. Gort, V. W. Bergmann, L. Gilson, A. Hagfeldt, M. Graetzel, W. Tress, and R. Berger, “How the formation of interfacial charge causes hysteresis in perovskite solar cells,” *Energy & Environmental Science*, vol. 11, pp. 2404–2413, 2018.

[134] L. Cojocaru, S. Uchida, K. Tamaki, P. V. V. Jayaweera, S. Kaneko, J. Nakazaki, T. Kubo, and H. Segawa, “Determination of unique power conversion efficiency of solar cell showing hysteresis in the I-V curve under various light intensities,” *Scientific Reports*, vol. 7, p. 11790, Sept. 2017.

[135] D. A. Jacobs, Y. Wu, H. Shen, C. Barugkin, F. J. Beck, T. P. White, K. Weber, and K. R. Catchpole, “Hysteresis phenomena in perovskite solar cells: the many and varied effects of ionic accumulation,” *Physical Chemistry Chemical Physics*, vol. 19, pp. 3094–3103, Jan. 2017. Publisher: The Royal Society of Chemistry.

[136] S. N. Habisreutinger, N. K. Noel, and H. J. Snaith, “Hysteresis Index: A Figure without Merit for Quantifying Hysteresis in Perovskite Solar Cells,” *ACS Energy Letters*, vol. 3, pp. 2472–2476, Oct. 2018.

[137] L. Contreras, J. Idígoras, A. Todinova, M. Salado, S. Kazim, S. Ahmad, and J. A. Anta, “Specific cation interactions as the cause of slow dynamics and hysteresis in dye and perovskite solar cells: a small-perturbation study,” *Physical Chemistry Chemical Physics*, vol. 18, pp. 31033–31042, Nov. 2016.

[138] S. Ravishankar, O. Almora, C. Echeverría-Arrondo, E. Ghahremanirad, C. Aranda, A. Guerrero, F. Fabregat-Santiago, A. Zaban, G. Garcia-Belmonte, and J. Bisquert, “Surface Polarization Model for the Dynamic Hysteresis of Perovskite Solar Cells,” *The Journal of Physical Chemistry Letters*, vol. 8, pp. 915–921, Mar. 2017.

[139] N. E. Courtier, J. M. Cave, J. M. Foster, A. B. Walker, and G. Richardson, “How transport layer properties affect perovskite solar cell performance: insights from a coupled charge transport/ion migration model,” *Energy & Environmental Science*, vol. 12, pp. 396–409, Dec. 2018.

[140] D. A. Jacobs, H. Shen, F. Pfeffer, J. Peng, T. P. White, F. J. Beck, and K. R. Catchpole, “The two faces of capacitance: New interpretations for electrical impedance measurements of perovskite solar cells and their relation to hysteresis,” *Journal of Applied Physics*, vol. 124, p. 225702, Dec. 2018.

[141] F. Ebadi, N. Taghavinia, R. Mohammadpour, A. Hagfeldt, and W. Tress, “Origin of apparent light-enhanced and negative capacitance in perovskite solar cells,” *Nature Communications*, vol. 10, p. 1574, Apr. 2019.

[142] M. T. Neukom, A. Schiller, S. Züfle, E. Knapp, J. Ávila, D. Pérez-del Rey, C. Dreessen, K. P. Zanoni, M. Sessolo, H. J. Bolink, and B. Ruhstaller, “Consistent Device Simulation Model Describing Perovskite Solar Cells in Steady-State, Transient, and Frequency Domain,” *ACS Applied Materials & Interfaces*, vol. 11, pp. 23320–23328, July 2019.

[143] J. M. Cave, N. E. Courtier, I. A. Blakborn, T. W. Jones, D. Ghosh, K. F. Anderson, L. Lin, A. A. Dijkhoff, G. J. Wilson, K. Feron, M. Saiful Islam, J. M. Foster, G. Richardson, and A. B. Walker, "Deducing transport properties of mobile vacancies from perovskite solar cell characteristics," *Journal of Applied Physics*, vol. 128, p. 184501, Nov. 2020. Publisher: American Institute of Physics.

[144] M. D. Bastiani, G. Dell'Erba, M. Gandini, V. D'Innocenzo, S. Neutzner, A. R. S. Kandada, G. Grancini, M. Binda, M. Prato, J. M. Ball, M. Caironi, and A. Petrozza, "Ion Migration and the Role of Preconditioning Cycles in the Stabilization of the J–V Characteristics of Inverted Hybrid Perovskite Solar Cells," *Advanced Energy Materials*, vol. 6, no. 2, p. 1501453, 2016.

[145] W. Tress, J. P. Correa Baena, M. Saliba, A. Abate, and M. Graetzel, "Inverted Current–Voltage Hysteresis in Mixed Perovskite Solar Cells: Polarization, Energy Barriers, and Defect Recombination," *Advanced Energy Materials*, pp. n/a–n/a, July 2016.

[146] H. Shen, D. A. Jacobs, Y. Wu, T. Duong, J. Peng, X. Wen, X. Fu, S. K. Karuturi, T. P. White, K. Weber, and K. R. Catchpole, "Inverted Hysteresis in CH3NH3PbI3 Solar Cells: Role of Stoichiometry and Band Alignment," *The Journal of Physical Chemistry Letters*, vol. 8, pp. 2672–2680, June 2017.

[147] A. O. Alvarez, R. Arcas, C. A. Aranda, L. Bethencourt, E. Mas-Marzá, M. Saliba, and F. Fabregat-Santiago, "Negative Capacitance and Inverted Hysteresis: Matching Features in Perovskite Solar Cells," *The Journal of Physical Chemistry Letters*, pp. 8417–8423, Sept. 2020.

[148] N. Courtier, "Interpreting Ideality Factors for Planar Perovskite Solar Cells: Ectypal Diode Theory for Steady-State Operation," *Physical Review Applied*, vol. 14, p. 024031, Aug. 2020. Publisher: American Physical Society.

[149] L. J. Bennett, A. J. Riquelme, N. E. Courtier, J. A. Anta, and G. Richardson, "A new ideality factor for perovskite solar cells and an analytical theory for their impedance spectroscopy response," *arXiv:2105.11226 [cond-mat, physics:physics]*, May 2021. arXiv: 2105.11226.

[150] A. Pockett, G. E. Eperon, T. Peltola, H. J. Snaith, A. Walker, L. M. Peter, and P. J. Cameron, "Characterization of Planar Lead Halide Perovskite Solar Cells by Impedance Spectroscopy, Open-Circuit Photovoltage Decay, and Intensity-Modulated Photovoltage/Photocurrent Spectroscopy," *The Journal of Physical Chemistry C*, vol. 119, pp. 3456–3465, Feb. 2015.

[151] H. Tan, A. Jain, O. Voznyy, X. Lan, F. P. G. d. Arquer, J. Z. Fan, R. Quintero-Bermudez, M. Yuan, B. Zhang, Y. Zhao, F. Fan, P. Li, L. N. Quan, Y. Zhao, Z.-H. Lu, Z. Yang, S. Hoogland, and E. H. Sargent, "Efficient and stable solution-processed planar perovskite solar cells via contact passivation," *Science*, vol. 355, pp. 722–726, Feb. 2017.

[152] P. Caprioglio, C. M. Wolff, O. J. Sandberg, A. Armin, B. Rech, S. Albrecht, D. Neher, and M. Stolterfoht, "On the Origin of the Ideality Factor in Perovskite Solar Cells," *Advanced Energy Materials*, vol. 10, no. 27, p. 2000502, 2020.

[153] N. E. Courtier, J. M. Foster, S. E. J. O'kane, A. B. Walker, and G. Richardson, "Systematic derivation of a surface polarisation model for planar perovskite solar cells," *European Journal of Applied Mathematics*, vol. 30, pp. 427–457, June 2019. Publisher: Cambridge University Press.

[154] I. M. Hermes, Y. Hou, V. W. Bergmann, C. J. Brabec, and S. A. L. Weber, "The Interplay of Contact Layers: How the Electron Transport Layer Influences Interfacial Recombination and Hole Extraction in Perovskite Solar Cells," *The Journal of Physical Chemistry Letters*, vol. 9, pp. 6249–6256, Nov. 2018.

[155] M. Cai, N. Ishida, X. Li, X. Yang, T. Noda, Y. Wu, F. Xie, H. Naito, D. Fujita, and L. Han, "Control of Electrical Potential Distribution for High-Performance Perovskite Solar Cells," *Joule*, vol. 2, pp. 296–306, Feb. 2018.

Chapter 3

Materials and Methods

Abstract

This Chapter describes the characterization techniques applied in the studies included in this thesis. A fundamental description of the small perturbation optoelectronic techniques is provided too. Good practices and particularities of using these characterization tools to the materials studied in this thesis are also brought. Finally, a detailed description of the two numerical models used in this work is included.

3.1 Characterization techniques

3.1.1 Intensity current-voltage (JV) curve

The most important characteristic of a solar cell and the most used figure of merit to determine the overall performance of a PV device is the current-voltage (JV) curve. To obtain this, the photocurrent density (J) is recorded while a linear variable external potential (V) is applied[1,2]. The shape of this curve responds to the diode equation described in *Chapter* 2 and is presented in Figure 3.1 where the main PV parameters that can be extracted from the JV curve are also indicated

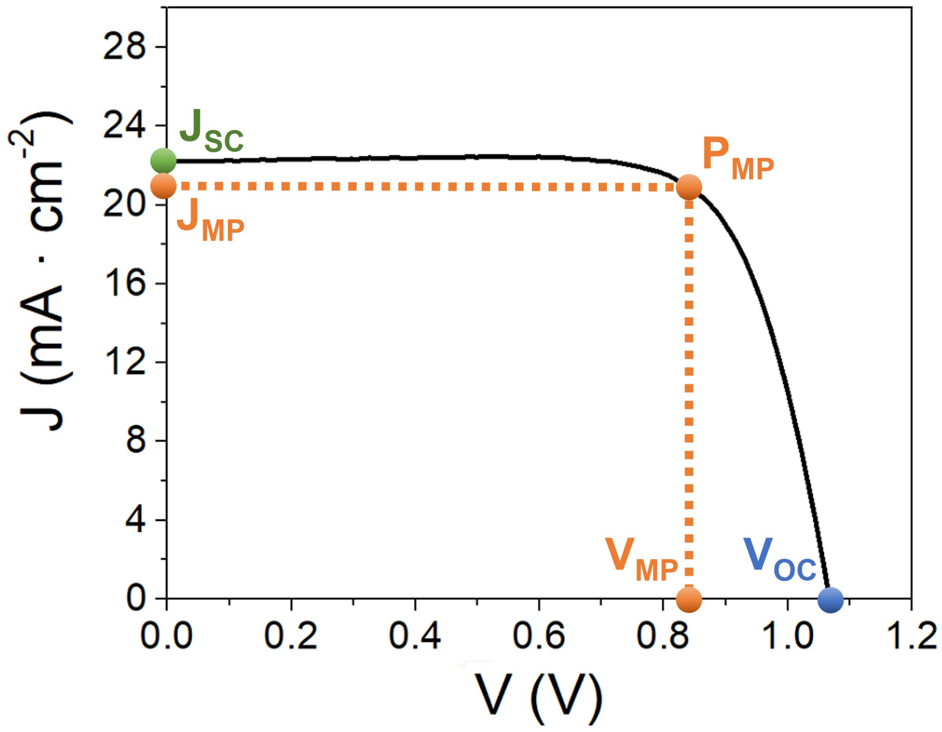

Figure 3.1: Example of the JV curve of a PSC obtained under illumination in a solar simulator. In the Figure, the main PV parameters are indicated: V_{OC} open-circuit voltage, J_{SC} short circuit current density, P_{MP} maximum power point, V_{mp} voltage at P_{MP} and J_{MP} current density at P_{MP}.

From the JV curve in Figure 3.1 V_{OC} and J_{SC} parameters, described in *Chapter* 2 are easily extracted by recording the voltage and photocurrent values at the Y-axis and X-axis origin, respectively. The V_{OC} is the point where J is zero. At this point, the resistance is infinite. Another critical value to determine the performance of a PV device is the maximum output power of the device per unit area. The maximum power point (P_{MP}) is given by the square under the IV curve with the largest area. This point corresponds to the largest value of the product $V \cdot J$. The voltage reached at this maximum power point is indicated as V_{MP} while the current is J_{MP}. Finally, when the external potential and the resistance are zero, the cell is under short-circuit conditions, and its photocurrent density is maximum J_{SC}.

The overall efficiency of the PV device is given by the power conversion efficiency (PCE), which is calculated as

$$PCE = \frac{J_{SC} \cdot V_{OC} \cdot FF}{P_{incident}} \tag{3.1}$$

where $P_{incident}$ is the power density of the incident light and FF is the fill factor, a parameter that quantifies how close to a rectangle the JV curve is. It is defined as

$$FF = \frac{J_{MP} \cdot V_{MP}}{J_{SC} V_{OC}} \tag{3.2}$$

The FF can be affected by the ideality factor, which was described in *Chapter* 2, and by parasitic resistances. These loss sources can be series resistance (R_S) that accounts for the opposition of the cell material to the current flow, or shunt resistance (R_{SH}), which reflects the leakage of currents through the device, near the edge of the device and between contacts of different polarity.

For the experiments included in this thesis, two different light sources were utilized (see Figure 3.2) and two pieces of equipment to apply the external potential and record the photocurrent response were used. In addition, a mask was employed to define the active area of the studied PV devices.

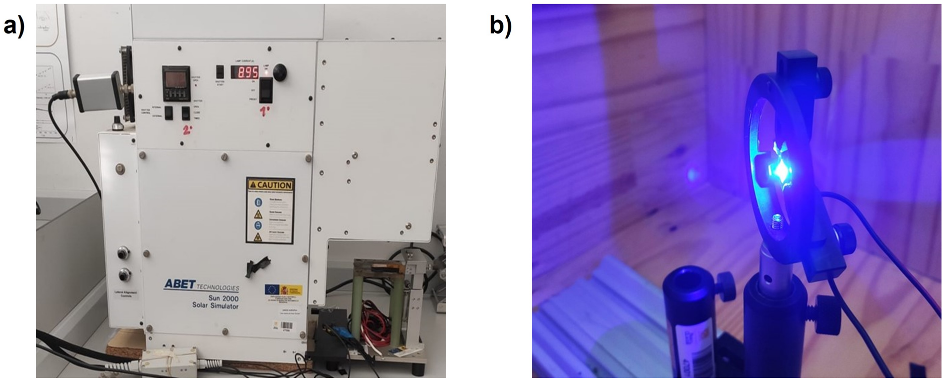

Figure 3.2: External illumination sources used in this thesis. Solar simulator *ABET Technologies Sun 2000* (a), and 465 nm monochromatic LED *Osram Golden Dragon Plus* (b).

In Figure 3.2a, a solar simulator used as the standard light source for basic characterization during this thesis is shown. This source consists of a xenon lamp of 150W and a set of filters for the correct simulation of the AM1.5G solar spectrum (see *Chapter* 2). The irradiance was calibrated to the standard value of 1 sun (1000 $W \cdot \mathrm{m}^{-2}$) using a reference monocrystalline silicon solar cell (*Oriel, 91150*). The current-voltage response under this illumination source was typically registered using a *Keithley model 2400* picoamperimeter using a scan rate of 100 $\mathrm{mV} \cdot \mathrm{s}^{-1}$ and a sweep delay of 20 s. Additional *JV* curves using this solar simulator were recorded using an *Autolab/PGSTAT302N* potentiostat combining forward and reverse scans (see *Chapter* 2) at a wide variety of scan rates. This potentiostat can also be coupled to an LED using a LED Driver. More information about this coupling is provided in the Section referring to small-perturbation optoelectronic techniques.

Two sets of LEDs have been used in this thesis. In Figure 3.2b, a 465 nm monochromatic *Osram Golden Dragon Plus* is shown. In addition to this, similar LEDs of the same producer emitting white light and 630 nm monochromatic light have been used in this work. As it has been said before, these LEDs are controlled by coupling them to a *Autolab/PGSTAT302N* potentiostat through an LED Driver using the NOVA software. The calibration of these light sources is done using a *Thorlabs FDS100* silicon photodiode.

3.1.2 UV-Visible spectroscopy

The light absorbed by the perovskite materials and dyes used in this thesis was determined using ultraviolet-visible (UV-Vis) spectroscopy. This technique can measure the different interactions of the light with the sample, where absorption, transmission, and reflection of the incident light have to be considered. In this technique, a light beam passes through a sample or is reflected from a film surface, and its attenuation is measured. In this thesis, the UV-visible absorption spectra have been measured using a *Cary 100* UV-vis spectrophotometer (*Agilent*) in the range of 200-800 nm. Typically obtained absorbance spectra for PSCs and DSSCs are shown in Figure 3.3.

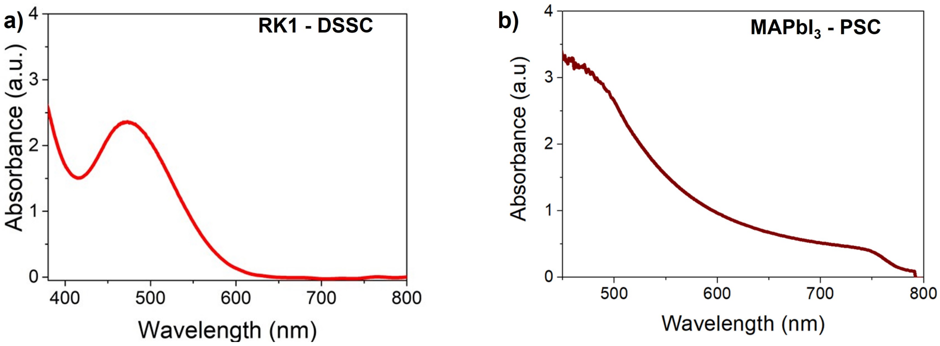

Figure 3.3: Examples of absorbance spectra of an RK1-based DSSC (a) and a MAPbI$_3$ PSC (b).

The concentration of the absorbing compound (c) can be linearly related to the measured absorbance (A_{abs}) using the Beer-Lambert law

$$A_{abs} = -\log T_{tr} = \log \frac{I_{inc}}{I_{tr}} = \varepsilon \cdot d \cdot c \tag{3.3}$$

where Ttr is the transmittance, I_{inc} and I_{tr} the incident and transmitted intensity, respectively, and ε_{mol} the molar absorption coefficient[3]. Additionally, the absorption coefficient α_{abs} of the sample can be calculated as

$$\alpha_{abs} = \frac{1}{d} \frac{\ln(1 - R_{ref})^2}{T_{tr}} \tag{3.4}$$

being R_{ref} the reflectance of the sample. The relative intensities of absorbance, reflectance and transmittance are connected by

$$A_{abs} + T_{tr} + R_{rf} = 1 \tag{3.5}$$

UV-Vis spectra also allow to estimate the optical bandgap of the active absorbing material using a Tauc plot[4]. For a direct bandgap, it can be calculated by

$$(hf\varepsilon_{mol})^{\frac{1}{2}} = A_{tauc}(hf - E_g) \tag{3.6}$$

where A_{tauc} is a proportionality constant.

3.1.3 Incident Photon to Current Efficiency (IPCE)

The External Quantum Efficiency (EQE) or Incident Photon to Current Efficiency (IPCE), is defined as the number of electrons delivered to the external circuit from the PV device compared to the number of incident photons for a given wavelength[2,5–7].

$$\mathrm{EQE}(\lambda) = \frac{h \cdot c \cdot J_{SC}(\lambda)}{q \cdot \lambda \cdot P_{light}(\lambda)} \tag{3.7}$$

This technique is a valuable tool to assess the device's performance by converting the incident photons with different wavelengths into electrons. In general, the EQE is determined by the combination of three different processes[2]:

- The absorption coefficient of the active material.
- The efficiency of charge separation, driven by the interfacial charge transfer processes.
- The efficiency of charge collection at the contact, that depends on the charge recombination.

For DSSCs, as was described in *Chapter* 2, some additional aspects need to be considered when assessing the performance of the solar device. One of the main parameters affecting the IPCE is the dye loading, which accounts for the number of dye molecules that the semiconductor can adsorb. In addition, the ratio between the electron injection and the regeneration of the oxidized dye plays a crucial role in determining this IPCE[8]. Two examples of IPCE spectra obtained and its integrated short-circuit photocurrent for the primary PV materials (DSSCs and PSCs) analyzed in this thesis can be found in Figure 3.4

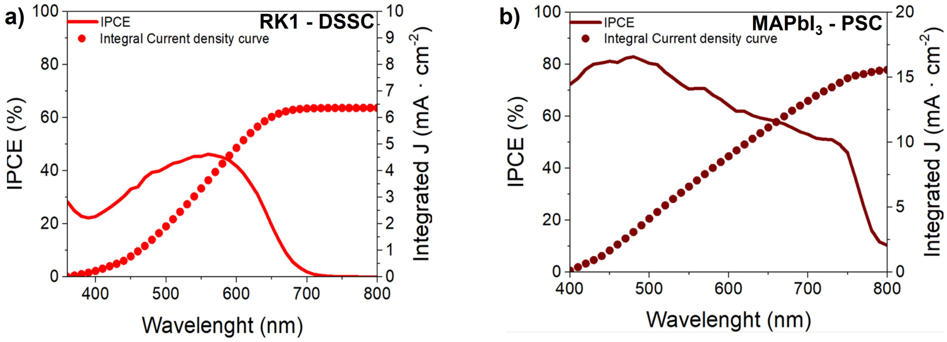

Figure 3.4: Examples of IPCE spectra and integrated photocurrent of an RK1-based DSSC (a) and a MAPbI$_3$ PSC (b).

The integrated photocurrent shown in Figure 3.4 can be calculated by overlapping the IPCE results with the spectral photon flux of the incident irradiation[8]

$$J_{SC(int)} = q \int_{\lambda_{min}}^{\lambda_{max}} I_{inc}(\lambda) \cdot IPCE(\lambda) \cdot d\lambda \tag{3.8}$$

when comparing this integrated photocurrent to the actual J_{SC} obtained under the solar simulator, a range of up to 20% mismatch between the values is usually accepted[9,10]. Combining the EQE or IPCE in Figure 3.4 with the absorptive properties extracted from Figure 3.3, it is possible to determine the internal quantum efficiency (IQE) by

$$\mathrm{IQE} = \mathrm{EQE} \cdot T_{tr} \tag{3.9}$$

IQE accounts for the fraction of absorbed photons converted into electron-hole pairs in the solar cell. This information makes the IQE the most direct and unambiguous theoretical figure of merit for charge separation in a solar cell at any voltage that generates current away from OC conditions. Thus, it allows gaining meaningful information about the efficiency of charge separation and collection[11]. In this thesis, IPCE was measured using an *high-efficiency spectral illuminator*. This equipment consists of a 300W Xe arc lamp attached to a *McPherson 789A-3* monochromator, which produces a monochromatic light beam with a selected wavelength. IPCE measurements in this thesis were done in the wavelength range of 350-800 nm with a step of 10 nm. The photocurrent generated by the sample for each wavelength is recorded by a *Keithley 6485* picoamperimeter. To determine the EQE, the illumination power at each wavelength is calibrated using a *Thorlabs FDS100* silicon photodiode and a mask of a smaller size than the active area of the PV device and the photodiode[5,12,13].

In addition to this "steady-state" IPCE, the EQE of PSCs can be measured at different frequencies[14] and, as it will be shown in the next section and discussed in detail in *Chapter* 5, EQE values can be extracted from IMPS measurements.

3.1.4 Small-perturbation optoelectronic techniques

Small-perturbation optoelectronic techniques, also known as "small-wave" or "small-signal" techniques, are critical characterization tools to extract information about the transport and recombination processes described in *Chapter* 2 taking place in the PV devices at different time scales[15–25]. These techniques consist of the application of a sinusoidal modulation in voltage or light intensity superimposed to the direct current (DC) bias applied voltage or illumination, respectively. The phase and magnitude of the sinusoidal photocurrent or photovoltage response of the PV device is recorded, as shown in Figure 3.5. The relation between the frequency dependent signal ($\mathrm{S}(\omega)$) and perturbation ($\mathrm{P}(\omega)$) in small-perturbation techniques can be quantified by a transfer function ($\mathrm{Z}_{tr}(\omega)$):

$$\mathrm{Z}_{tr}(\omega) = \frac{\mathrm{S}(\omega)}{\mathrm{P}(\omega)} \tag{3.10}$$

In these small-perturbation measurements, the perturbation is applied at a wide range of frequencies (typically 0.01 - 10^5 Hz). This range corresponds to the timescales for relevant electronic and ionic processes occurring in the solar cells. This frequency range is also restrained by the technical limitations of the potentiostat and the technique itself[23,26].

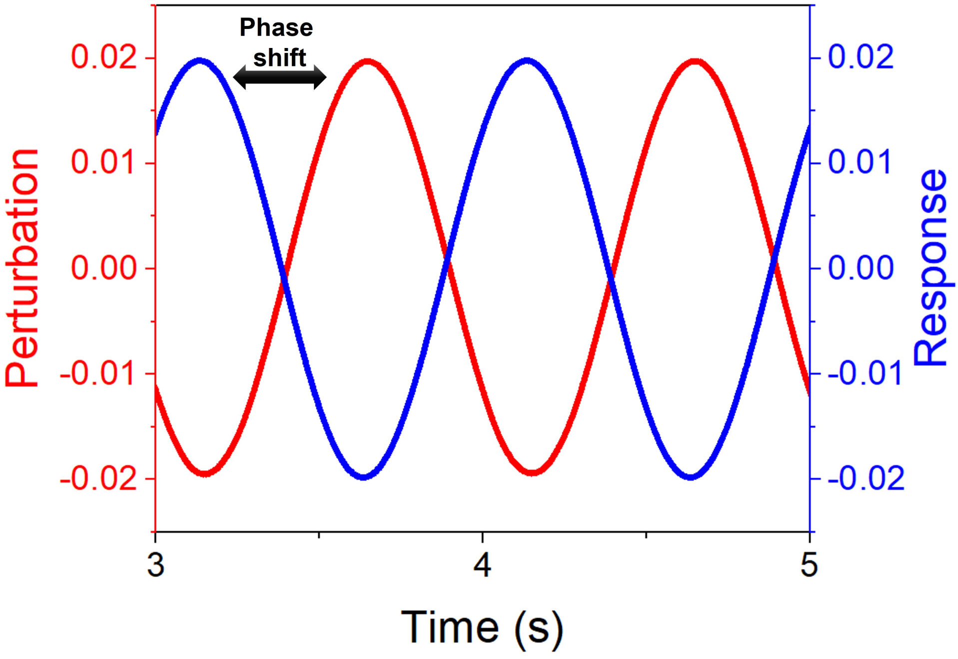

Figure 3.5: Sinusoidal response in a linear system to a sinusoidal perturbation in the time domain.

For the information resulting from these techniques to be meaningful and reliable, it is necessary to meet experimental requirements in terms of stability of the system[27]. In addition, the amplitude of the perturbation needs to be small enough to ensure a linear response of the PV device, but still, to be large enough to produce a response (causality)[26,28]. To ensure that the characterization technique is done on a stable PV device, as a standard procedure, prior to the beginning of the measurement, the solar cell is held under the same DC bias illumination that will be applied during the characterization process until V_{OC} of the device is stabilized. In addition, to check that the solar cell has not suffered from degradation during the process, *JV* curves at the same light intensity are done before and after each measurement are done, to confirm that the main photovoltaic parameters of the PV device have not been altered. In addition, to characterize PV devices especially sensible to degradation under ambient conditions, a sealed chamber with a nitrogen atmosphere and with a quartz window to allow the illumination of the sample has also been used.

To confirm the linearity between the response of the PV device and the alternate current (AC) perturbation introduced in the system, the applied AC perturbation is compared to the amplitude of the perturbation to the response. It is possible to assess the linearity of the response via a so-called Lissajous curve[26] as it is shown in Figure 3.6. A linear response produces straight lines or symmetric curves, while nonlinearity causes the formation of asymmetric curves.

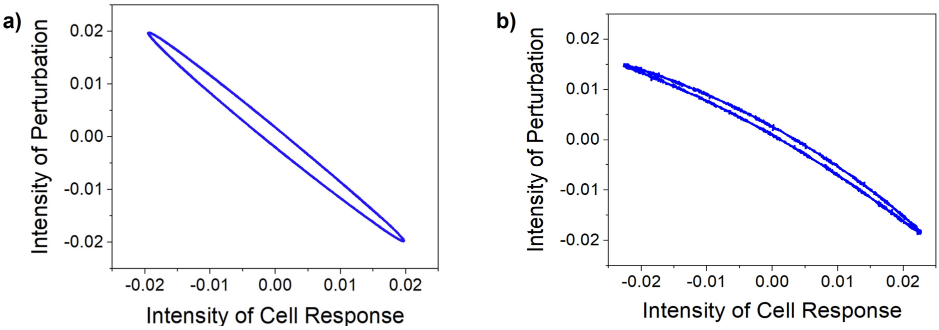

Figure 3.6: Examples of Lissajous curves of a linear (a) and a nonlinear (b) response.

The small-perturbation techniques used in this thesis are electrical impedance spectroscopy (EIS), intensity-modulated photocurrent spectroscopy (IMPS), and intensity-modulated photovoltage spectroscopy (IMVS). These measurements were done using the potentiostat and LED driver system, and the two LED sets mentioned in the *JV* curve section, using the controling software NOVA 2.1.1.

Electrical impedance spectroscopy (EIS)

In EIS, the voltage of the PV device is perturbed by a small perturbation, recording the current response as shown in Figure 3.5, as a function of the modulation frequency[26]. The measured impedance is linked to an AC circuit's electrical resistance (R). This resistance refers to the property of a circuit element to oppose the flow of an electrical current. For a DC circuit, the potential (V) and current (I), which are signal and response in EIS, respectively, are connected through Ohm's law

$$R = \frac{V}{J} \tag{3.11}$$

This relation holds for an ideal resistor, while the impedance (Z) includes the relative amplitudes of the voltage perturbation and the current response and the phase shift between them. The voltage and current are usually described as a vector rotating with a constant angular frequency (ω)[26,28]. Thus, the voltage perturbation in the frequency domain ($V(\omega)$) can be expressed as

$$V(\omega) = V_0 \cos \omega t \tag{3.12}$$

where V_0 is the amplitude of the voltage perturbation and ω is related to the linear frequency (f) by

$$\omega = 2\pi f \tag{3.13}$$

The current response also presents an angular frequency, which can be shifted with respect to the applied potential perturbation and is given by

$$I(\omega) = I_0 \cos(\omega t + \phi) \tag{3.14}$$

being I_0 the amplitude of the current response and ϕ the phase shift. This shift refers to the delay of the current response to the voltage. Given this, the Ohm's law in Eq. 3.11 can be adapted to calculate the impedance of an electrochemical system and express it as a transfer function

$$Z(\omega) = \frac{V(\omega)}{I(\omega)} = \frac{V_0 \cos \omega t}{I_0 \cos(\omega t + \phi)} \tag{3.15}$$

A common approach to express the impedance is using complex numbers, which simplifies the representation of the relative magnitude and phase of the perturbation and response signals[26]. Complex numbers can be expressed using Euler's equation

$$e^{j\theta} = \cos\theta + j\sin\theta \tag{3.16}$$

Thus, the perturbation and the response as a function of ω can be written as

$$V(\omega) = V_0 \cdot e^{j\omega t} \qquad\qquad I(\omega) = I_0 \cdot e^{j(\omega t + \phi)} \tag{3.17}$$

Thus, the impedance in Eq. 3.15 can be simplified as

$$Z = \frac{V_0}{I_0} e^{-j\phi} = Z_0 e^{-j\phi} \tag{3.18}$$

Applying Euler's relation in Eq. 3.16, the impedance can also be expressed as

$$Z_0 e^{j\phi} = Z_0 \cos(\phi) - Z_0 j \sin(\phi) \tag{3.19}$$

Applying basic concepts of complex numbers, this expression means that the impedance can be separated into a real (Z') and an imaginary (Z'') part, including information on the phase shift ϕ. As this shift depends on each frequency probed in the measurement process, the impedance response of a

PV device can be written as

$$Z(\omega) = Z'(\omega) + jZ''(\omega) \tag{3.20}$$

As it is shown in Figure 3.7, the information extracted from impedance measurements can be plotted in three different ways:

1. Nyquist plot: The real part of the impedance in the X-axis and the imaginary part in the Y-axis.
2. Bode plot: A double-Y plot with the frequency as common X-axis and the magnitude ($|Z|$) and the phase shift (ϕ) in the Y-axis.
3. Cole-Cole plot: The frequency of the perturbation in the X-axis and the imaginary part in the Y-axis.

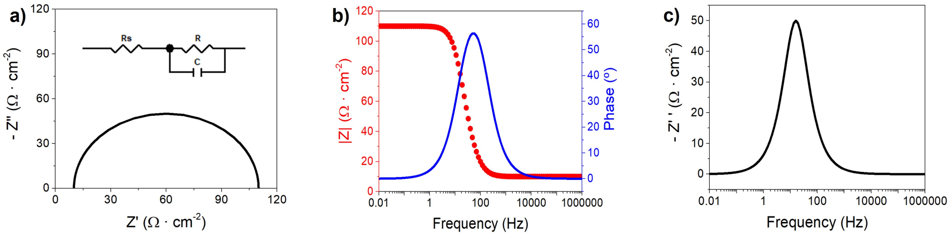

Figure 3.7: Example of an impedance spectrum using three different plots: Nyquist (a), Bode (b), and Cole-Cole (c). The impedance was simulated using the EC in the inset of (a), setting a R_S of 10 $\Omega \cdot cm^{-2}$, a R of 100 Ω·cm^{-2} and a C of 0.0001 F.

Figure 3.7 was obtained by simulating an EC consisting of a series resistance and an RC element (a resistance and a capacitance in parallel to each other). A more detailed description of the different circuit elements used to reproduce and fit EIS is provided in a later section of this *Chapter*. Most impedance responses for the PV systems studied in this thesis produce a signal in the first quadrant (negative imaginary part values). This signal means a delay between the applied voltage perturbation and the current response due to the system capacitance. However, for some particular devices, the spectra crossing to the second quadrant, corresponding to a negative capacitance, have been reported[29–34]. This phenomena is also observed and discussed in *Chapters* 6 and 9. Each RC element reproduces a semicircle in the Nyquist plot, which can be related to a transport or recombination process within the PV device. The equivalent feature to these semicircles in the Cole-Cole and Bode plots is the peak observed at a certain frequency. The product of R and C values produces a time constant that defines the frequency where these peaks can be observed

$$\tau_{EIS} = R \cdot C \tag{3.21}$$

Note that as in the Cole-Cole plot, what is being represented is the imaginary part of the vector, the frequency where the peak appears is the linear frequency f, while the phase shift represented in the Bode plot depends on the angular frequency (ω) of the vector. Thus, there is a shift of 2π between the peak frequency in the Cole-Cole plot and the Bode plot.

Intensity-modulated spectroscopy (IMPS and IMVS)

Intensity-modulated spectroscopy relies on a small sinusoidal modulation of the photon flux reaching the PV device[35,36]. In IMPS, the recorded response of the PV device is the photocurrent, and these measurements are done under potentiostatic conditions, while in IMVS, the photovoltage response is measured, keeping the solar cell under galvanostatic conditions. In this thesis, the IMPS measurements were done at SC while IMVS was performed at the V_{OC}. As explained before for EIS, the ratio between the signal perturbation and the response of the PV system can be expressed as a transfer function using a complex number. For IMPS, this transfer function

($Y(\omega)$) is defined as

$$Y(\omega) = \frac{J(\omega)}{I_{inc}(\omega)} = \frac{J_0 \sin(\omega t + \phi)}{I_{0(inc)} \sin \omega t} \tag{3.22}$$

being $J(\omega)$ the frequency-dependent photocurrent response and $I_{inc}(\omega)$ the frequency-modulated light intensity. This transfer function can also be expressed as a complex number

$$Y(\omega) = Y_0 \cos \phi + Y_0 j \sin \phi \tag{3.23}$$

Like EIS, the resulting IMPS response for each frequency probed during the characterization can be represented using Nyquist, Bode, and Cole-Cole plots. However, in this thesis, the two main plots used to represent IMPS are Nyquist and Cole-Cole, as shown in Figure 3.8.

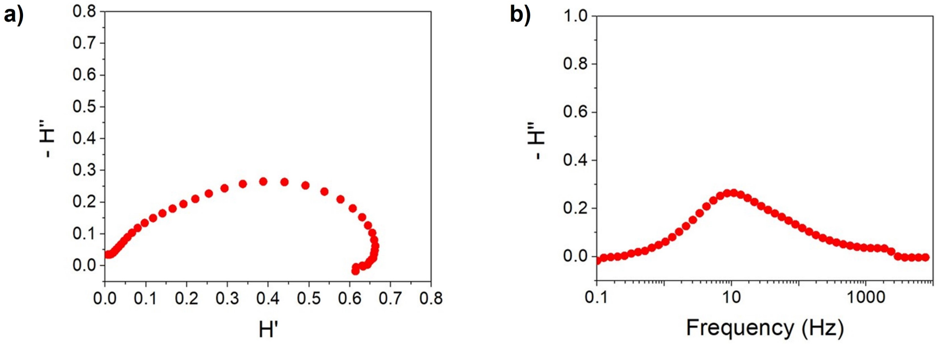

Figure 3.8: Example of an IMPS spectrum using two different plots: Nyquist (a) and Cole-Cole (b). The IMPS was measured on an RK1-based DSSC with a monochromatic (630 nm) LED as the illumination source.

In Figure 3.8 it can be observed an example of an IMPS measured on a DSSC. The description and interpretation of this type of spectra for PSC are commented on in detail in *Chapter* 5. The H' and $-H''$ values were normalized in terms of IQE. The reason for this normalization being possible is that the transfer function in IMPS can also be expressed as a differential quantum efficiency at a given wavelength and modulation frequency[14,25,36–39]. This can be deduced from Eq. 3.22, as the result of dividing the photocurrent generated by the PV system by the input photon flux is the definition of the EQE. Thus, by converting I_{inc} in Eq. 3.22 in an photon flux (Φ), it is possible to normalize the measured IMPS in terms of frequency-dependent quantum efficiency[14] via dimensionless ratios

$$\mathrm{EQE}(\lambda,\omega) = \frac{J(\lambda,\omega)}{\Phi_0(\lambda,\omega)} \tag{3.24}$$

$$\mathrm{IQE}(\lambda,\omega) = \frac{J(\lambda,\omega)}{\Phi_a(\lambda,\omega)} \tag{3.25}$$

where Φ_0 and Φ_a are the wavelength and frequency-dependent incident and absorbed photon flux, respectively. Bearing this in mind, the transfer function in IMPS can also be expressed as a differential internal quantum efficiency at a given wavelength and modulation frequency[14,25,36–39]

$$dl\ \mathrm{IQE}(\lambda,\omega) = \frac{\delta J(\lambda,\omega)}{\delta \Phi_a(\lambda,\omega)} \tag{3.26}$$

which represents the ratio of excess collected electrons relative to a slight excess of photogenerated electrons over a stationary DC baseline. In addition, to estimate the steady-state IQE in DSSCs and related devices the following expressions can be used[40]

$$\mathrm{IQE} = 1 - \frac{\tau_t}{\tau_{rec}} \tag{3.27}$$

$$\mathrm{IQE} = 1 - \left(\frac{d}{L_n}\right)^2 \tag{3.28}$$

being τ_t and τ_{rec} the electron transport and recombination lifetimes, respectively. These expressions represent mathematically the intuitive fact that in any solar cell, the IQE becomes larger when the transport is faster, and the recombination is slower. In the low-frequency limit, the IMPS crosses the X-axis at a value that corresponds to the steady-state EQE. Additionally, by determining the optical properties of the active PV material at the wavelength of the light source, it is possible to convert the EQE into IQE through Eq. 3.9. All IMPS results included in this thesis are reported normalized as IQE. To make this conversion possible, it is paramount to accurately determine the DC bias light intensity during the measurement and the exact amplitude of the perturbation. The LED used for this characterization is connected to the potentiostat through an LED driver and controlled via NOVA software. However, the input data is given as the electric current sent to the LED. Thus, an equivalence between this input current and the resulting light intensity must be done.

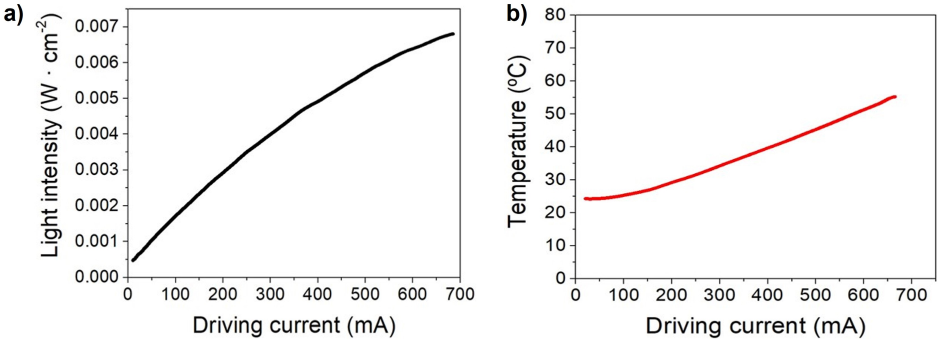

Figure 3.9: Driving current to light intensity conversion curve (a) (Figure 42 in LED Driver User Manual) and surface temperature of the LED cover as a function of the driving current (b) (Figure 10 in LED Driver User Manual). Figures extracted from Metrohm Autolab B.V. LED Driver User Manual[41]

As can be observed in Figure 3.9a, the relation between the driving current in the LED and the resulting light intensity is not linear. Thus, to accurately determine the light intensity perturbation's amplitude, the conversion between the input amplitude of the LED driving current, and the real light intensity modulation needs to be done. It is important to say that this calibration is a procedure that has been ignored or overlooked largely in the specialized literature. In addition, attending to Figure 3.9b, the operation of the LED implies a rise in its temperature, eventually leading to an inevitable loss of performance[42–44] and a decrease in the output light intensity during the IMPS measurement, which also needs to be taken into account. Thus, in this thesis, after each IMPS characterization, a similar procedure was followed on the *Thorlabs FDS100* silicon photodiode. As in the case of EIS, each semicircle observed in the Nyquist plot has an equivalent peak in the Cole-Cole plot at a specific frequency. The resulting time constant depends on recombination and transport processes[40]. However, when IMPS is performed under SC conditions, it can be assumed that transport processes dominate the performance of the device[45]. Thus, a diffusion coefficient can be extracted from the IMPS time constant. In the case of DSSCs, as can be observed in Figure 3.8, IMPS produces a semicircle, which time constant can be related to the effective electron diffusion coefficient by[15,46,47]

$$\tau_{IMPS} = \frac{d^2}{\gamma_{IMPS} D_n} \tag{3.29}$$

where γ_{IMPS} is a numerical factor, which depends on d, absorption coefficient, and illumination direction. Its value can be approximated to 2.5[15].

In PSCs 2-3 semicircles are usually observed[17,18,22,24,25,48] and the interpretation of these main signals is detailed discussed in *Chapter* 5.

In the case of IMVS, the perturbation is also an optical modulation, similar to IMPS. However, in this technique, the recorded response of the PV system is the photovoltage, and it is performed under galvanostatic conditions (usually at V_{OC}). Thus, the transfer function for IMVS can be expressed as

$$Y_{PV}(\omega) = \frac{V(\omega)}{I_{inc}(\omega)} = \frac{V_0 \sin(\omega t + \phi)}{I_{0(inc)} \sin \omega t} \tag{3.30}$$

Again, this transfer function can also be expressed as a complex number

$$Y_{PV}(\omega) = Y_{PV_0} \cos\phi + Y_{PV_0} j \sin\phi \tag{3.31}$$

As in the previously described small-perturbation optoelectronic techniques, IMVS results can be plotted in Nyquist, and Cole-Cole plots, where each semicircle observed in the first plot has an equivalent peak in the second, with a specific time constant (τ_{IMVS}). In this case, as the measurement is done at V_{OC}, this time constant corresponds to the effective electron lifetime[49,50].

Combining this recombination lifetime with the electron diffusion coefficient extracted from IMPS, it is possible to approximate the small-signal perturbation charge carrier diffusion length by[49]

$$L_n = \sqrt{D_n \cdot \tau_{IMVS}} \tag{3.32}$$

provided that both parameters are measured at the same quasi-Fermi level position[51–54]. As explained in the following section, the recombination lifetime can also be extracted from EIS measurements. In both cases, at the same light intensity, the position of the quasi-Fermi level in IMVS and EIS is different from the position in IMPS because they are done at OC and SC, respectively. To estimate this shift, a voltage correction needs to be performed[15,24,55,56]. It is easy to show by compbination of Eqs. 3.20, 3.22 and 3.30 that the transfer functions of the three small-perturbation techniques described are related via the equation:

$$Z(\omega) = \frac{Z_{PV}(\omega)}{Y(\omega)} \tag{3.33}$$

3.2 Theoretical and numerical tools

3.2.1 Equivalent circuits

The impedance response (Eq. 3.20) represented in Figure 3.7 can be expressed using Kirchoff's circuit laws[28] as

$$Z(\omega) = R_S + \left(\frac{1}{R} + j\omega C\right)^{-1} \tag{3.34}$$

which produces a semicircle in the first quadrant with its origin on the real-part axis value given by R_S. For real systems such as DSSCs and PSCs, an ideal capacitor C fails to reproduce the observed experimental results completely. Although the reason for this nonideal behavior is still under debate, it is commonly associated with chemical reactions involving several steps or with porosity and roughness of the working electrode. For this reason, constant phase elements (CPE) are usually considered instead of ideal capacitors. These elements reproduce nonideal capacitors, taking into consideration that for solid electrodes, this element is not purely capacitive but includes a resistive component[26]. These parameters consist of two frequency-independent parameters, T, a pseudocapacitance value, and P, a numerical parameter taking values between 0 and 1. When $P = 0$, the CPE becomes a resistor, and when $P = 1$, it is an ideal capacitor. It is generally accepted that if $P \geq 0.8$, the CPE element can be considered a capacitor whose capacitance can be calculated as[57]

$$C = \frac{(R \cdot T_{CPE})^{1/P_{CPE}}}{R} \tag{3.35}$$

In this thesis, the software used to fit and reproduce both experimental and drift-diffusion (DD) simulated impedance spectra was *Scribner ZView* 2. This software allows for building ECs with different elements that account for the features observed in EIS as semicircles in the Nyquist plot and peaks in the Bode and Cole-Cole plots. A general introduction to the most common ECs used for DSSCs and PSCs and the primary information extracted from EIS spectra is provided below. In addition, in *Chapter* 9 a detailed discussion about the physical meaning of the circuit elements of two widely used ECs in PSCs is provided.

Use and interpretation in DSSCs

EIS response of DSSCs depends on aspects like the nature and structure of the semiconductor, the viscosity, and the composition of the electrolyte or the DC voltage applied during the measurements or the illumination conditions. In spite of this complexity, a representative example of a typical EIS Nyquist plot is described in Figure 3.10.

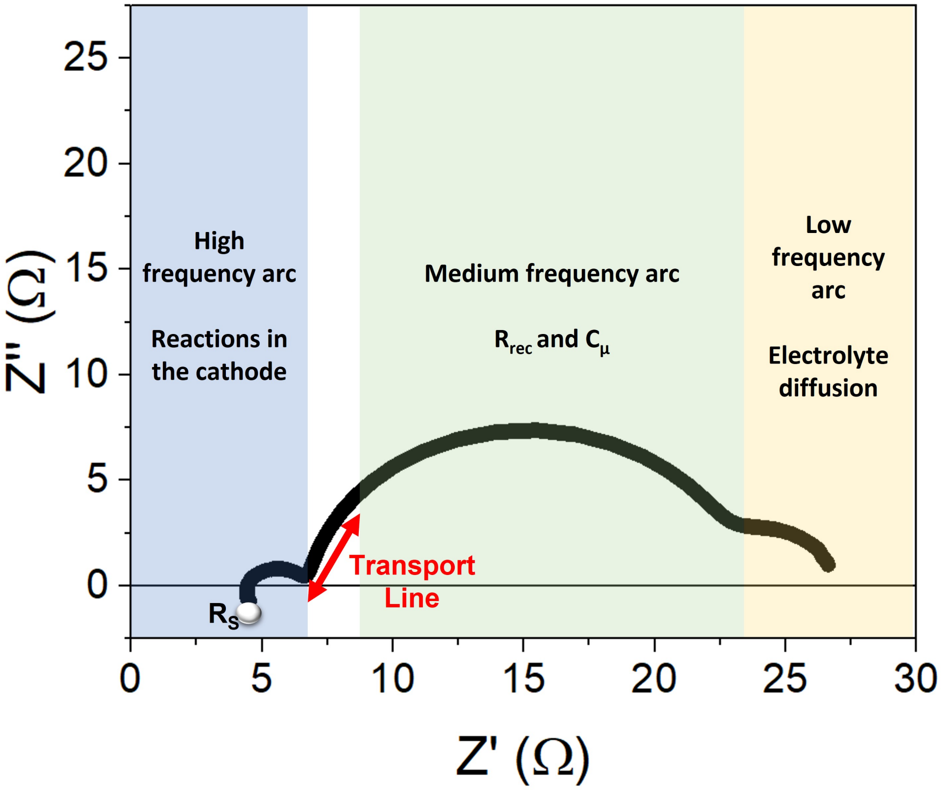

Figure 3.10: Nyquist plot of the impedance response of an RK1-based DSSC using TiO_2 as semiconductor, iodine-based ACN electrolyte and a Pt cathode with an active area of 0.25 cm^2.

In Figure 3.10 the contribution of the different components involved in the functioning of DSSCs can be observed. The first point of the EIS, or in other words, the resulting impedance for the highest frequency probed in the experiment, corresponds to the R_S. This resistance includes parasitic resistance losses caused by the device, such as the resistance of the conducting glass, the connections used during the measurement, etc[23]. The first semicircle observed in Figure3.10 is the result of a cathodic impedance due to the platinised electrode[58,59], produced by the combination of the double-layer capacitance (C_{pt}) and the charge transfer resistance of the reduction of the electron acceptors shown in Eq. 2.63[45]. This semicircle is ideally followed by a 45° Warburg-line diffusion element[60], which for DSSCs is related to the electron transport resistance in the metal oxide[61]. The medium frequency feature, which is usually the biggest in size of the semicircles in EIS of DSSCs, corresponds to the parallel combination of the charge transfer or recombination resistance (R_{rec}) and the chemical capacitance in the semiconductor film (C_{μ})[61–65]. Finally, at low frequencies, sometimes a last feature is visible. It can take the form of a Warburg element or a semicircle. This signal accounts for the redox species diffusion in the electrolyte and gets more evident with the use of high viscosity ionic liquids[66,67].

To reproduce the contributions mentioned above, the most used EC in Figure 3.11 devised to extract the information about recombination and electronic transport processes taking place within the DSSC was proposed by Bisquert and coworkers[16,61]. In the *ZView* software used in this thesis to fit EIS, this diffusion-recombination transmission line model is included as an extended element coded DX1.

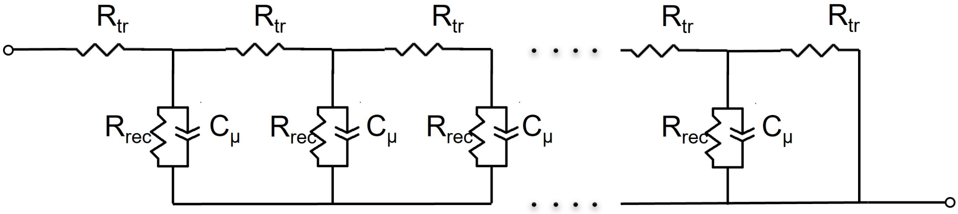

Figure 3.11: Transmission line model for DSSC proposed by Bisquert and coworkers[16,61].

As it can be inferred from Eq. 2.59, by analyzing the voltage dependence of C_{μ} extracted from Figure 3.11, it is possible to determine the value of α of the analyzed solar cell. As for R_{rec}, it generally also shows an exponential voltage dependence that can be mathematically described as[68]

$$R_{rec} = R_{00} \exp\left(-\frac{\beta q V}{k_B T}\right) \tag{3.36}$$

As it was described in *Chapter* 2, knowing the values of α and β can provide with valuable information regarding the distribution of localized states in the oxide[69] and the recombination reaction order for the free electrons in Eq. 2.61[70], respectively. In addition, from the specific time constant of the medium frequency arc, the effective electron lifetime (τ_n) can be determined[50] as follows

$$\tau_n = C_\mu \cdot R_{rec} \tag{3.37}$$

Finally, when the transmission line is clearly observed in the spectrum, and the transport resistance can be extracted using the EC in Figure 3.11, the small-perturbation diffusion length can be calculated as[16]

$$\frac{L_n}{d} = \sqrt{\frac{R_{rec}}{R_t}} \tag{3.38}$$

However, when this element is not visible in the impedance spectrum, this way of calculation can not be used, and it is necessary to use the approach described in Eq. 3.32, either using a lifetime extracted from IMVS or from the mid-frequency time constant of EIS[15].

Use and interpretation in PSCs

The typical EIS of PSC comprises two well-distinguishable semicircles in the first quadrant in the Nyquist plot (Figure 3.12) correlated with their corresponding peaks in the Bode and Cole-Cole plots[19,20,24,71].

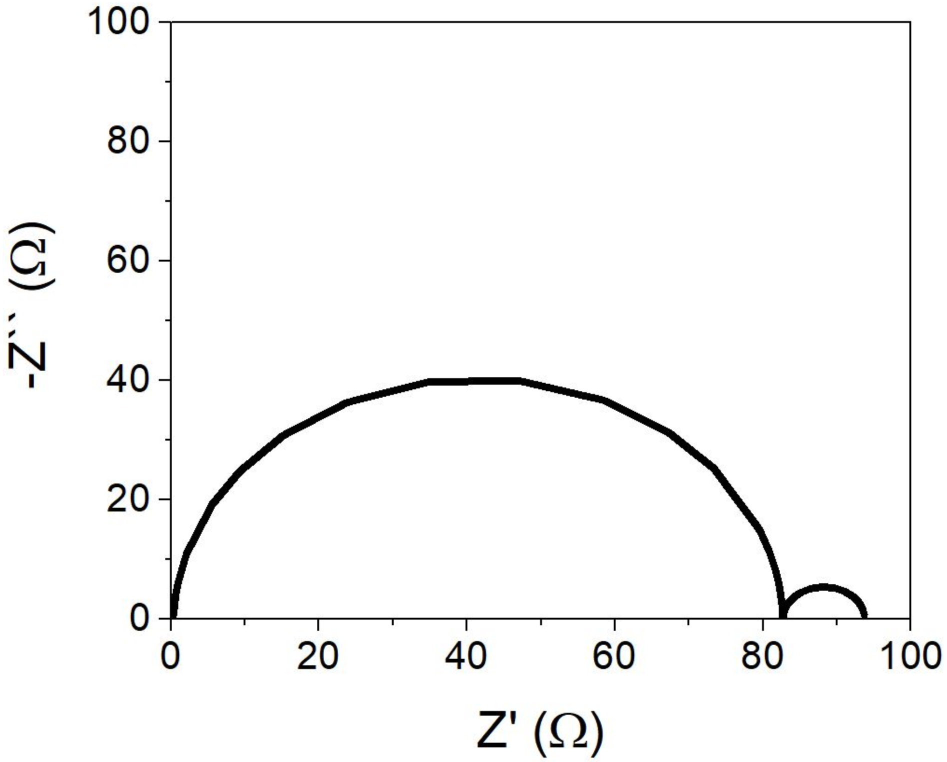

Figure 3.12: Nyquist plot of an EIS of a $MAPbI_3$ PSC simulated using the DD model *IonMonger* considering an active area of 0.33 cm^2.

The HF arc is usually attributed to electronic transport and recombination processes in the bulk of the active layer or the selective materials[16,24,72]. The low frequency signal is connected to the diffusion of ions and charge accumulation at interfaces[71,73]. To fit these spectra, a variety of ECs can be found in the literature[23,74,75]. To reproduce the simple spectra shown in Figure 3.12, basic circuits combining at least two resistors and two capacitors in various arrangements are used[19–21,76]. This EC, depicted in Figure 3.13, referred to as the "series equivalent circuit" (SEC), has been applied to most of the EIS measurements in PSC done in this thesis.

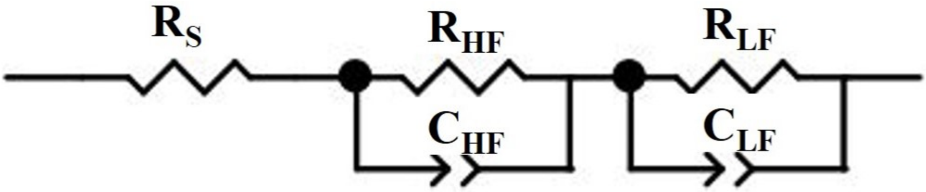

Figure 3.13: Series equivalent circuit typically used to fit EIS of PSCs.

By fitting the typical spectra in Figure 3.12 using SEC (3.13), it is commonly observed[20] that the characteristic time constant of the LF signal does not depend on the DC voltage, while the time constant of the HF arc increases exponentially as the DC voltage gets higher. As for the resistances of both arcs, they decrease exponentially with DC voltage. However, only the slope of the logarithm of R_{HF} coincides with the slope of the V_{OC} light intensity dependence used to determine n_{AP} (2.20). C_{HF} is close to being independent of the DC voltage, with a tendency to increase at sufficiently high voltages. The value at the flat region can be approximated to the value of the geometric capacitance in Eq. 2.67, considering a roughness factor, which takes the value of 4 for flat devices[17] or 100 for a mesoporous device[77]. C_{LF} shows an exponential increase with DC voltage, with the same slope that the decrease of R_{LF} with DC voltage, resulting in a voltage-independent time constant.

Additionally, in *Chapter* 8 a second EC[19,75,78], referred to as “parallel equivalent circuit” (PEC) is compared with the classic SEC, in order to gain further insight on the physical meaning of the different circuit elements used to fit DD simulated EIS of PSCs. This model, in Figure 3.14, is inspired by the aforementioned EC used to analyze DSSC[16,79,80].

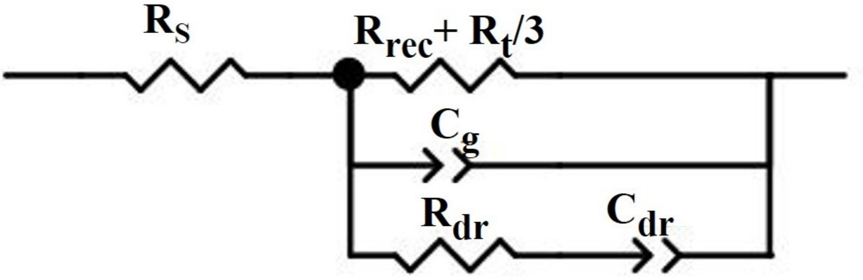

Figure 3.14: Parallel equivalent circuit used to fit EIS of PSCs in *Chapter* 9.

This circuit includes a geometrical capacitance C_g, accounting for the dielectric behavior of the active layer component of the device. The resistor in parallel, $R_{rec}+R_t/3$, where R_{rec} represents the recombination resistance and R_t the transport resistance, encompasses both arcs and thus reproduces the DC resistance of the device. The model infers that most high-performance PSCs are not limited by transport processes but by recombination. Thus, the $R_{rec}+R_t/3$ element can be reduced just to R_{rec} considering the transport resistance negligible for state-of-the-art cells. The PEC includes an additional branch formed by a resistor and a capacitor (R_{dr} and C_{dr}) similar to the one used for dielectric relaxation-like processes, which accounts for the LF processes like ion migration or carrier accumulation at the interfaces, that cannot follow the HF variations like electronic transport and recombination processes. Although this process cannot be considered a pure dielectric relaxation, its behavior in terms of EC elements is similar, and due to that, it is called a dielectric relaxation-like process. This additional branch comprising R_{dr} and C_{dr} splits the spectra into two parts analogous to the two arcs in the SEC, which can be defined by R_{HF} and R_{LF} resistances. It is important to highlight that elements from PEC and vice versa can yield the elements of the SEC. In the case of the resistor, the relation is[81]:

$$R_{HF} = \frac{(R_{rec} + R_t/3) \cdot R_{dr}}{(R_{rec} + R_t/3) + R_{dr}} \tag{3.39}$$

$$R_{LF} = (R_{rec} + R_t/3) - R_{HF} \tag{3.40}$$

Finally, from this circuit elements, it is possible to calculate the DC resistance (R_{DC})

$$R_{DC} = R_S + R_{rec} + R_t/3 \tag{3.41}$$

This EC aims to adequately separate the DC resistive components of the solar cell (via Eq.3.41) from the indirect effect of the dielectric relaxation-like element contained in the R_{dr}/C_{dr} branch. However, the exact physical/molecular meaning of R_{dr} and C_{dr} parameters remain unclear. The comparison between both ECs described in this section and the study of their physical meaning attending to the impact of different parameters controlled through DD simulation is made in *Chapter* 8.

3.2.2 Drift-diffusion modelling

DD modeling consists of numerical solvers that allow for the calculation of the differential equations that reproduces the mechanisms of transport and recombination described in *Chapter* 2. In this thesis, two different time-dependent DD models are used. The first one, called the “single layer DD model,” only contains explicitly electronic processes in the active perovskite layer. The impact of the ionic distribution is reproduced through an external screening of the electric field. This model can be used to reproduce *JV* curves and transients. The second, the “Three layers DD model,” includes the ETL and HTL, the active perovskite layer, and a mobile ionic species restrained to the active perovskite layer. This DD model can reproduce *JV* curves and EIS spectra, as it will be shown in the following *Chapters*.

Single layer drift-diffusion model

The DD model used in *Chapter* 5 differs from the classical models used in DSSC[38,46,68] in the explicit consideration of electrons and holes in the active perovskite layer. A web-based version of this single-layer DD model can be found in `https://solarsoft.upo.es` The differential equations to be solved are[68,82]

$$\frac{\delta c_i}{\delta t} = D_i \frac{\delta}{\delta x}\left(\frac{q c_i}{k_B T}\frac{\delta \phi}{\delta x} + \frac{\delta c_i}{\delta x}\right) + G - R_{rec}; \qquad \frac{\delta^2 \phi}{\delta x^2} = -\frac{\rho}{\varepsilon_p \varepsilon_0}, \tag{3.42}$$

being c_i $(i = n, p)$ the electron/hole density, D_i the electron/hole diffusion coefficients, ρ the net charge density, G the photogeneration term and Rec the recombination rate. The generation term is computed via a Lambert-Beer expression:

$$G = \Phi_0 \alpha_{abs}(\lambda)\exp(-\alpha_{abs}(\lambda)d) \tag{3.43}$$

where $\alpha_{abs}(\lambda)$ is the absorption coefficient at a given wavelength. The recombination mechanism in this model is assumed to be a bulk SRH recombination[21,83], described in *Chapter* 2 and with a recombination rate given by 2.32.

To numerically solve Eq. 3.42 for electrons and holes, a discretized scheme and the forward time central space method[68] is used. The following boundary conditions were considered[82].

$$n(x=0,t)=n_0(V);p(x=0,t)=p_0(V) \tag{3.44}$$

$$n(x,t=0)=n_0(V);p(x,t=0)=p_0(V) \tag{3.45}$$

$$\left(\frac{dn(x,t)}{dx}\right)_{x=d}=0; \qquad \left(\frac{dp(x,t)}{dx}\right)_{x=0}=0 \tag{3.46}$$

These boundary conditions imply that the electron and hole densities are fixed by the applied voltage, whereas the transfer of electrons is blocked at the HTL ($x=d$) and the transfer of holes is blocked at the ETL interface ($x=0$). In addition to these boundary conditions involving the electronic carriers, an additional boundary condition is included for the electric field:

$$\zeta(x=0)=\zeta(x=d)=0 \tag{3.47}$$

which implies that the screening effect of the ions acts by canceling the field within the active layers[84]. Finally, the initial values of the electron/holes densities are calculated using

$$n_0(x=0,V)=N_c\exp\left(-\frac{E_c-E_{f(n)}}{k_BT}\right) \tag{3.48}$$

$$p_0(x=d,V)=N_v\exp\left(-\frac{E_v-E_{f(p)}}{k_BT}\right) \tag{3.49}$$

These equations are equivalent to the boundary condition

$$n_0(x=0)p_0(x=d)=N_vN_c\exp\left(-\frac{E_g-V}{k_BT}\right) \tag{3.50}$$

Once the equation is solved, the photocurrent density for a given value of V is obtained from the stationary density profile at the contacts

$$J = \left(\frac{dn(x,t)}{dx}\right)_{x=0} = \left(\frac{dp(x,t)}{dx}\right)_{x=d} \tag{3.51}$$

By solving the equations for different values of V, the entire JV curve can be obtained, and the IQE can be extracted by dividing the photocurrent by the photogeneration in Eq.3.43.

Three layers ionic-electronic drift-diffusion model

The DD model used in *Chapters* 6, 7, 8 and 9 is the numerical model *IonMonger*[84–87], a fully-coupled one-dimensional DD model that accounts for the motion of electrons, holes and positive anion vacancies in a planar PSC. The cell is modelled as a three-layer structure in which a perovskite absorber layer is sandwiched between doped electron and hole transport layers, as illustrated in Figure 3.15.

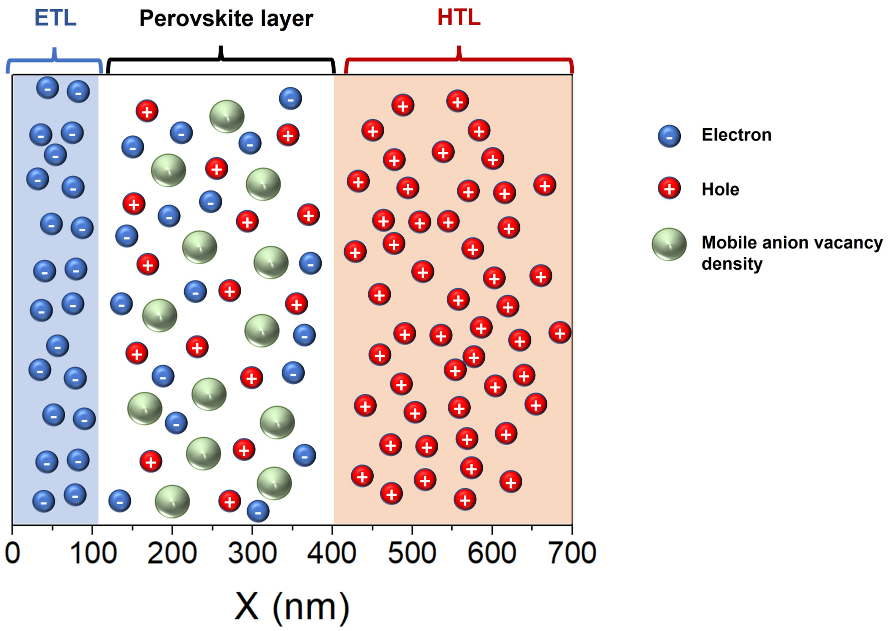

Figure 3.15: Schematic of the three layers simulated device reproduced by *IonMonger*, including the three mobile species (electrons, holes, and anion vacancies). Thickness of the ETL (b_E) is 100 nm, while the active layer d is 300 nm thick and the HTL thickness (b_H) is 300 nm.

Within the perovskite layer, all three charged species are present whilst, within the ETL, the ion and hole densities are not considered. The same happens in the HTL for the ion and electron densities. Since both holes and electrons are only present in appreciable numbers in the perovskite layer, significant charge carrier recombination only occurs within this layer or at its interfaces with the ETL and HTL. In the perovskite layer, the recombination is driven by a combination of the bimolecular and SRH recombination mechanisms (see *Chapter* 2) while on the interfaces with the selective materials, only SRH recombination is assumed to occur, consistent with the assumption that the free minority carrier density is negligible in the ETL and the HTL. In the perovskite layer ($0 < x <$ b), n and p are driven in time, t, and one spatial dimension, x, via the continuity equations

$$\frac{\delta n}{\delta t} - \frac{1}{q}\frac{\delta J_n}{\delta x} = G - R_{rec}, \qquad J_n = qD_n\left(\frac{\delta n}{\delta x} - \frac{n}{k_B T}\frac{\delta \phi}{\delta x}\right), \tag{3.52}$$

$$\frac{\delta p}{\delta t} + \frac{1}{q}\frac{\delta J_p}{\delta x} = G - Rec, \qquad J_p = -qD_p\left(\frac{\delta p}{\delta x} + \frac{p}{k_B T}\frac{\delta \phi}{\delta x}\right), \tag{3.53}$$

In addition, the migration of the anion vacancies (N_0) is governed by the following equation

$$\frac{\delta N_0}{\delta t} + \frac{\delta F_P}{\delta x} = 0, \qquad F_P = -D_{ion}\left(\frac{\delta N_0}{\delta x} + \frac{P}{k_B T}\frac{\delta \phi}{\delta x}\right), \tag{3.54}$$

where F_P is the ionic flux and D_{ion} is the anion vacancy diffusion coefficient. Equations (3.52 -3.54) are coupled to Poisson's equation for the electric potential

$$\frac{\delta^2 \phi}{\delta x^2} = \frac{q}{\varepsilon_p}(N_{cat} - N_0 + n - p) \tag{3.55}$$

Here, N_{cat} is the uniform immobile cation vacancy density, which is equivalent to the mean anion vacancy density in order to ensure the electrical charge neutrality. Electrons and holes are generated in the perovskite layer according to the Beer-Lambert profile for a single wavelength of light like in the previous DD model, following Eq. 3.43

Recombination happening in the bulk of the perovskite is calculated using a combination of bimolecular and trap-assisted SRH processes (see *Chapter* 2), given by

$$R(n,p) = (np - n_i^2) + \frac{(np - n_i^2)}{\tau_n p + \tau_p n + k_3} \tag{3.56}$$

Here, τ_n and τ_p are the SRH pseudo-lifetimes for electrons and holes and k_3 is a constant from the deep trap approximation used by Courtier et al[86] and n_i can be determined, as shown in *Chapter* 2 by Eq. 2.9

As for the SRH surface recombination between the perovskite layer and the selective contacts, this is determined at the ETL/perovskite interface by

$$R_l(n,p) = \frac{n|_{x=0^-} p|_{x=0^+} - n_i^2}{p|_{x=0^+}/v_{nE} + n|_{x=0^-}/v_{pE} + k_1} \tag{3.57}$$

In this case, v_{nE} and v_{pE} are the electron and hole recombination velocities across the ETL/perovskite interface, and k_1 is a constant from the deep trap approximation at the ETL/perovskite interface. The electron concentration at the interface of the ETL and the hole concentration at the interface of the perovskite are given by $n|_{x=0^-}$ and $p|_{x=0^+}$, respectively. In the same way, the recombination at the perovskite/HTL interface is defined by

$$R_r(n,p) = \frac{n|_{x=d^-} p|_{x=d^+} - n_i^2}{p|_{x=d^+}/v_{nH} + n|_{x=d^-}/v_{pH} + k_2} \tag{3.58}$$

where v_{nH} and v_{pH} are the electron and hole recombination velocities at the perovskite/HTL interface and k_2 is a constant from the deep trap approximation at the perovskite/HTL interface. The electron concentration at the interface of the perovskite is denoted by $n|_{x=b^-}$ while the hole concentration at the HTL interface is given by $p|_{x=b^+}$.

Vacancy anion migration, generation, and bulk recombination are restrained to the perovskite layer. Thus, the conservation equations for electrons in the ETL $(-b_E < x < 0)$ are given by

$$\frac{\delta n}{\delta t}-\frac{1}{q}\frac{\delta J_n}{\delta x}=0, \qquad J_n=qD_E\left(\frac{\delta n}{\delta x}-\frac{n}{k_BT}\frac{\delta \phi}{\delta x}\right) \tag{3.59}$$

with

$$\frac{\delta^2 \phi}{\delta x^2}=\frac{q}{\varepsilon_E}(n-d_E) \tag{3.60}$$

Here, D_E is the electronic diffusion coefficient in the ETL, and ε_E and d_E are the permittivity and effective doping density of the ETL. The conservation equations for holes in the HTL $(d < x < d+b_H)$ are given by

$$\frac{\delta p}{\delta t}+\frac{1}{q}\frac{\delta J_p}{\delta x}=0, \qquad J_p=-qD_H\left(\frac{\delta p}{\delta x}+\frac{p}{k_BT}\frac{\delta \phi}{\delta x}\right) \tag{3.61}$$

with

$$\frac{\delta^2 \phi}{\delta x^2}=\frac{q}{\varepsilon_H}(d_H-p) \tag{3.62}$$

where D_H is the hole diffusion coefficient in the HTL and ε_H and d_H are the HTL permittivity and effective doping density respectively.

To simulate the physics behind a perovskite solar cell operation, a set of boundary conditions are applied to all the previously described equations. To model metal contacts at the ETL and HTL edges, the following conditions are applied

$$\begin{gathered}\phi|_{x=-b_E}=0, \qquad n|_{x=-b_E}=d_E, \\ \phi|_{x=d+b_H}=V-V_{bi}, \qquad p|_{x=d+b_H}=d_H\end{gathered} \tag{3.63}$$

At the ETL/MAPbI$_3$ interface

$$\phi|_{x=0^-} = \phi|_{x=0^+}, \qquad \varepsilon_E \frac{\delta\phi}{\delta x}|_{x=d^-} = \varepsilon_H \frac{\delta\phi}{\delta x}|_{x=d^+},$$

$$p|_{x=d^-} = k_H p|_{x=d^+}, \qquad J_n|_{x=d} = -qR_{l_r}, \qquad F_p|_{x=0} = 0 \tag{3.64}$$

At the MAPbI$_3$/HTL interface

$$\phi|_{x=d^-} = \phi|_{x=d^+}, \qquad \varepsilon_p \frac{\delta\phi}{\delta x}|_{x=d^-} = \varepsilon_H \frac{\delta\phi}{\delta x}|_{x=d^+}, \qquad p|_{x=d^-} = k_H p|_{x=d^+},$$

$$J_n|_{x=b} = -qR_{l_r}, \qquad F_P|_{x=0} = 0 \tag{3.65}$$

where k_E and k_H accounts for the ratio of the carrier densities at either side of the perovskite and transport layer interface. This is determined by

$$k_E = \frac{g_c}{g_{c,E}} \exp\left(-\frac{E_c - E_{c,E}}{qk_BT}\right), \qquad k_H = \frac{g_v}{g_{v,H}} \exp\left(-\frac{E_v - E_{v,H}}{qk_BT}\right) \tag{3.66}$$

Here, $g_{c,E}$ and $g_{v,H}$ are the density of states of the ETL conduction band and HTL valence band, respectively, E_C and E_V are the energies of the conduction and valence bands of the perovskite layer, while $E_{C,E}$ and $E_{V,H}$ are the energies of the conduction and valence bands of the ETL and HTL. In this thesis, it is assumed that the density of states of the selective transport layers is equal to the effective doping densities in those layers. This means $g_{c,E} = d_E$ and $g_{v,H} = d_H$. As a result of this, the band edges $E_{c,E}$ and $E_{v,H}$ are equal to the Fermi levels in the ETL and HTL, denoted by E_{FE} and E_{FH}. Considering this, the built-in voltage is determined by

$$V_{bi} = \frac{1}{q}(E_{FE} - E_{FH}) = \frac{1}{q}(E_{C,E} - E_{V,H}) \tag{3.67}$$

By solving these equations for a specific applied potential ($V(t)$), which appears in the form of a boundary condition, the solution can be used to determine the output current density ($J(t)$) on the cell contacts. Impedance spectra are simulated by applying a sinusoidal voltage perturbation, as previously described for experimental EIS. The current response is analyzed using a Fourier transform to extract its phase and amplitude for each frequency. This enables the impedance to be calculated and a spectrum constructed over a wide frequency range.

Bibliography

[1] A. Smets, K. Jäger, O. Isabella, R. van Swaaij, and M. Zeman, *Solar Energy: The physics and engineering of photovoltaic conversion, technologies and systems*. Cambridge: UIT Cambridge Limited, 2016.

[2] J. Nelson, *The Physics of Solar Cells*. Imperial College Press, 1 ed., Sept. 2003.

[3] D. F. Swinehart, “The Beer-Lambert Law,” *Journal of Chemical Education*, vol. 39, p. 333, July 1962. Publisher: American Chemical Society.

[4] J. Tauc, R. Grigorovici, and A. Vancu, “Optical Properties and Electronic Structure of Amorphous Germanium,” *physica status solidi (b)*, vol. 15, no. 2, pp. 627–637, 1966. _eprint: https://onlinelibrary.wiley.com/doi/pdf/10.1002/pssb.19660150224.

[5] W. Ananda, “External quantum efficiency measurement of solar cell,” in *2017 15th International Conference on Quality in Research (QiR) : International Symposium on Electrical and Computer Engineering*, pp. 450–456, July 2017.

[6] A. Riquelme, F. E. Gálvez, L. Contreras-Bernal, H. Míguez, and J. A. Anta, “Internal quantum efficiency and time signals from intensity-modulated photocurrent spectra of perovskite solar cells,” *Journal of Applied Physics*, vol. 128, no. 13, p. 133103, 2020.

[7] P. Hierrezuelo-Cardet, A. F. Palechor-Ocampo, J. Caram, F. Ventosinos, D. Pérez-del Rey, H. J. Bolink, and J. A. Schmidt, “External quantum efficiency measurements used to study the stability of differently deposited perovskite solar cells,” *Journal of Applied Physics*, vol. 127, p. 235501, June 2020.

[8] J. Halme, P. Vahermaa, K. Miettunen, and P. Lund, “Device Physics of Dye Solar Cells,” *Advanced Materials*, vol. 22, pp. E210–E234, Sept. 2010.

[9] J. A. Christians, J. S. Manser, and P. V. Kamat, “Best Practices in Perovskite Solar Cell Efficiency Measurements. Avoiding the Error of Making Bad Cells Look Good,” *The Journal of Physical Chemistry Letters*, vol. 6, pp. 852–857, Mar. 2015.

[10] E. Zimmermann, P. Ehrenreich, T. Pfadler, J. A. Dorman, J. Weickert, and L. Schmidt-Mende, “Erroneous efficiency reports harm organic solar cell research,” *Nature Photonics*, vol. 8, pp. 669–672, Sept. 2014. Number: 9 Publisher: Nature Publishing Group.

[11] G. F. Burkhard, E. T. Hoke, and M. D. McGehee, “Accounting for Interference, Scattering, and Electrode Absorption to Make Accurate Internal Quantum Efficiency Measurements in Organic and Other Thin Solar Cells,” *Advanced Materials*, vol. 22, no. 30, pp. 3293–3297, 2010. _eprint: https://onlinelibrary.wiley.com/doi/pdf/10.1002/adma.201000883.

[12] E44 Committee, “Test Method for Spectral Responsivity Measurements of Photovoltaic Devices,” tech. rep., ASTM International.

[13] M. Bliss, A. Smith, T. R. Betts, J. Baker, F. De Rossi, S. Bai, T. Watson, H. Snaith, and R. Gottschalg, “Spectral Response Measurements of Perovskite Solar Cells,” *IEEE Journal of Photovoltaics*, vol. 9, pp. 220–226, Jan. 2019.

[14] S. Ravishankar, C. Aranda, P. P. Boix, J. A. Anta, J. Bisquert, and G. Garcia-Belmonte, “Effects of Frequency Dependence of the External Quantum Efficiency of Perovskite Solar Cells,” *The Journal of Physical Chemistry Letters*, vol. 9, no. 11, pp. 3099–3104, 2018.

[15] E. Guillén, L. M. Peter, and J. A. Anta, “Electron Transport and Recombination in ZnO-Based Dye-Sensitized Solar Cells,” *J. Phys. Chem. C*, vol. 115, no. 45, pp. 22622–22632, 2011.

[16] F. Fabregat-Santiago, G. Garcia-Belmonte, I. Mora-Seró, and J. Bisquert, “Characterization of nanostructured hybrid and organic solar cells by impedance spectroscopy,” *Physical Chemistry Chemical Physics*, vol. 13, no. 20, pp. 9083–9118, 2011.

[17] A. Pockett, G. E. Eperon, T. Peltola, H. J. Snaith, A. Walker, L. M. Peter, and P. J. Cameron, “Characterization of Planar Lead Halide Perovskite Solar Cells by Impedance Spectroscopy, Open-Circuit Photovoltage Decay, and Intensity-Modulated Photovoltage/Photocurrent Spectroscopy,” *The Journal of Physical Chemistry C*, vol. 119, pp. 3456–3465, Feb. 2015.

[18] M. Neukom, S. Züfle, S. Jenatsch, and B. Ruhstaller, “Opto-electronic characterization of third-generation solar cells,” *Science and Technology of Advanced Materials*, vol. 19, pp. 291–316, Dec. 2018.

[19] A. R. Pascoe, N. W. Duffy, A. D. Scully, F. Huang, and Y.-B. Cheng, “Insights into Planar CH3NH3PbI3 Perovskite Solar Cells Using Impedance Spectroscopy,” *The Journal of Physical Chemistry C*, vol. 119, pp. 4444–4453, Mar. 2015. Publisher: American Chemical Society.

[20] L. Contreras-Bernal, S. Ramos-Terrón, A. Riquelme, P. P. Boix, J. Idígoras, I. Mora-Seró, and J. A. Anta, “Impedance analysis of perovskite solar cells: a case study,” *Journal of Materials Chemistry A*, vol. 7, pp. 12191–12200, May 2019.

[21] L. Contreras-Bernal, M. Salado, A. Todinova, L. Calio, S. Ahmad, J. Idígoras, and J. A. Anta, “Origin and Whereabouts of Recombination in Perovskite Solar Cells,” *The Journal of Physical Chemistry C*, vol. 121, no. 18, pp. 9705–9713, 2017.

[22] S. Ravishankar, C. Aranda, S. Sanchez, J. Bisquert, M. Saliba, and G. Garcia-Belmonte, “Perovskite Solar Cell Modeling Using Light- and Voltage-Modulated Techniques,” *The Journal of Physical Chemistry C*, vol. 123, pp. 6444–6449, Mar. 2019.

[23] E. v. Hauff and D. Klotz, “Impedance spectroscopy for perovskite solar cells: characterisation, analysis, and diagnosis,” *Journal of Materials Chemistry C*, vol. 10, pp. 742–761, Jan. 2022. Publisher: The Royal Society of Chemistry.

[24] E. Guillén, F. J. Ramos, J. A. Anta, and S. Ahmad, “Elucidating Transport-Recombination Mechanisms in Perovskite Solar Cells by Small-Perturbation Techniques,” *The Journal of Physical Chemistry C*, vol. 118, pp. 22913–22922, Oct. 2014.

[25] S. Ravishankar, A. Riquelme, S. K. Sarkar, M. Garcia-Batlle, G. Garcia-Belmonte, and J. Bisquert, “Intensity-Modulated Photocurrent Spectroscopy and Its Application to Perovskite Solar Cells,” *The Journal of Physical Chemistry C*, vol. 123, no. 41, pp. 24995–25014, 2019.

[26] A. Lasia, *Electrochemical Impedance Spectroscopy and its Applications*. New York, NY: Springer New York, 2014.

[27] S. Ravishankar, M. Garcia-Batlle, J. Bisquert, G. Garcia-Belmonte, J. Odrobina, and C.-A. Schiller, “Removing Instability-Caused Low-Frequency Features in Small Perturbation Spectra of Perovskite Solar Cells,” *The Journal of Physical Chemistry C*, vol. 124, pp. 15793–15799, July 2020.

[28] E. Barsoukov and J. R. Macdonald, eds., *Impedance Spectroscopy: Theory, Experiment, and Applications*. Hoboken, N.J: Wiley-Interscience, 2 edition ed., 2005.

[29] I. Mora-Sero, J. Bisquert, F. Fabregat-Santiago, G. Garcia-Belmonte, G. Zoppi, K. Durose, Y. Proskuryakov, I. Oja, A. Belaidi, T. Dittrich, R. Tena-Zaera, A. Katty, C. Levy-Clement, V. Barrioz, and S. J. C. Irvine, “Implications of the Negative Capacitance Observed at Forward Bias in Nanocomposite and Polycrystalline Solar Cells,” *Nano Letters*, vol. 6, pp. 640–650, Apr. 2006.

[30] E. Ghahremanirad, A. Bou, S. Olyaee, and J. Bisquert, “Inductive Loop in the Impedance Response of Perovskite Solar Cells Explained by Surface Polarization Model,” *The Journal of Physical Chemistry Letters*, vol. 8, pp. 1402–1406, Apr. 2017.

[31] F. Fabregat-Santiago, M. Kulbak, A. Zohar, M. Vallés-Pelarda, G. Hodes, D. Cahen, and I. Mora-Seró, “Deleterious Effect of Negative Capacitance on the Performance of Halide Perovskite Solar Cells,” *ACS Energy Letters*, vol. 2, pp. 2007–2013, Sept. 2017.

[32] D. Klotz, “Negative capacitance or inductive loop? – A general assessment of a common low frequency impedance feature,” *Electrochemistry Communications*, vol. 98, pp. 58–62, Jan. 2019.

[33] F. Ebadi, N. Taghavinia, R. Mohammadpour, A. Hagfeldt, and W. Tress, “Origin of apparent light-enhanced and negative capacitance in perovskite solar cells,” *Nature Communications*, vol. 10, p. 1574, Apr. 2019.

[34] A. O. Alvarez, R. Arcas, C. A. Aranda, L. Bethencourt, E. Mas-Marzá, M. Saliba, and F. Fabregat-Santiago, “Negative Capacitance and Inverted Hysteresis: Matching Features in Perovskite Solar Cells,” *The Journal of Physical Chemistry Letters*, pp. 8417–8423, Sept. 2020.

[35] L. M. Peter, “Dynamic aspects of semiconductor photoelectrochemistry,” *Chemical Reviews*, vol. 90, pp. 753–769, 1990.

[36] E. A. Ponomarev and L. M. Peter, “A generalized theory of intensity modulated photocurrent spectroscopy (IMPS),” *Journal of Electroanalytical Chemistry*, vol. 396, no. 1, pp. 219–226, 1995.

[37] O. Almora, D. Miravet, G. J. Matt, G. Garcia-Belmonte, and C. J. Brabec, “Analytical model for light modulating impedance spectroscopy (LIMIS) in all-solid-state p-n junction solar cells at open-circuit,” *Applied Physics Letters*, vol. 116, no. 1, p. 013901, 2020.

[38] J. Halme, “Linking optical and electrical small amplitude perturbation techniques for dynamic performance characterization of dye solar cells,” *Physical Chemistry Chemical Physics*, vol. 13, no. 27, p. 12435, 2011.

[39] L. Bertoluzzi and J. Bisquert, “Investigating the Consistency of Models for Water Splitting Systems by Light and Voltage Modulated Techniques,” *The Journal of Physical Chemistry Letters*, vol. 8, no. 1, pp. 172–180, 2017.

[40] G. Schlichthorl, N. G. Park, and A. J. Frank, “Evaluation of the charge-collection efficiency of dye-sensitized nanocrystalline TiO2 solar cells,” *Journal of Physical Chemistry B*, vol. 103, no. 5, pp. 782–791, 1999.

[41] “Metrohm Autolab B.V. LED Driver. User manual,” 2012.

[42] O. Heikkilä, J. Oksanen, and J. Tulkki, “Ultimate limit and temperature dependency of light-emitting diode efficiency,” *Journal of Applied Physics*, vol. 105, p. 093119, May 2009. Publisher: American Institute of Physics.

[43] P. Dalapati, N. B. Manik, and A. N. Basu, “Effect of temperature on the intensity and carrier lifetime of an AlGaAs based red light emitting diode,” *Journal of Semiconductors*, vol. 34, p. 092001, Sept. 2013. Publisher: IOP Publishing.

[44] J. Park and Y. Kawakami, “Temperature-Dependent Dynamic Behaviors of Organic Light-Emitting Diode,” *Journal of Display Technology*, vol. 2, pp. 333–340, Dec. 2006. Publisher: IEEE.

[45] A. Hagfeldt, G. Boschloo, L. Sun, L. Kloo, and H. Pettersson, “Dye-Sensitized Solar Cells,” *Chemical Reviews*, vol. 110, pp. 6595–6663, Nov. 2010.

[46] L. Dloczik, O. Ileperuma, I. Lauermann, L. M. Peter, E. A. Ponomarev, G. Redmond, N. J. Shaw, and I. Uhlendorf, “Dynamic Response of Dye-Sensitized Nanocrystalline Solar Cells: Characterization by Intensity-Modulated Photocurrent Spectroscopy,” *The Journal of Physical Chemistry B*, vol. 101, no. 49, pp. 10281–10289, 1997.

[47] A. J. Frank, N. Kopidakis, and J. v. d. Lagemaat, “Electrons in nanostructured TiO2 solar cells: transport, recombination and photovoltaic properties,” *Coordination Chemistry Reviews*, vol. 248, no. 13, pp. 1165–1179, 2004.

[48] J. Bisquert and M. Janssen, “From Frequency Domain to Time Transient Methods for Halide Perovskite Solar Cells: The Connections of IMPS, IMVS, TPC, and TPV,” *The Journal of Physical Chemistry Letters*, vol. 12, pp. 7964–7971, Aug. 2021. Publisher: American Chemical Society.

[49] J. Bisquert and V. S. Vikhrenko, “Interpretation of the time constants measured by kinetic techniques in nanostructured semiconductor electrodes and dye-sensitized solar cells,” *Journal of Physical Chemistry B*, vol. 108, no. 7, pp. 2313–2322, 2004.

[50] J. Bisquert, F. Fabregat-Santiago, I. Mora-Seró, G. Garcia-Belmonte, and S. Giménez, “Electron Lifetime in Dye-Sensitized Solar Cells: Theory and Interpretation of Measurements,” *The Journal of Physical Chemistry C*, vol. 113, no. 40, pp. 17278–17290, 2009.

[51] A. C. Fisher, L. M. Peter, E. A. Ponomarev, A. B. Walker, and K. G. U. Wijayantha, “Intensity dependence of the back reaction and transport of electrons in dye-sensitized nanocrystalline TiO solar cells,” *Journal of Physical Chemistry B*, vol. 104, no. 5, pp. 949–958, 2000.

[52] A. B. Walker, L. M. Peter, K. Lobato, and P. J. Cameron, “Analysis of photovoltage decay transients in dye-sensitized solar cells,” *Journal of Physical Chemistry B*, vol. 110, no. 50, pp. 25504–25507, 2006.

[53] J. Villanueva-Cab, H. Wang, G. Oskam, and L. M. Peter, “Electron Diffusion and Back Reaction in Dye-Sensitized Solar Cells: The Effect of Nonlinear Recombination Kinetics,” *The Journal of Physical Chemistry Letters*, vol. 1, no. 4, pp. 748–751, 2010.

[54] J. R. Jennings, F. Li, and Q. Wang, “Reliable Determination of Electron Diffusion Length and Charge Separation Efficiency in Dye-Sensitized Solar Cells,” *The Journal of Physical Chemistry C*, vol. 114, no. 34, pp. 14665–14674, 2010.

[55] G. Boschloo and A. Hagfeldt, “Activation energy of electron transport in dye-sensitized TiO2 solar cells,” *Journal of Physical Chemistry B*, vol. 109, no. 24, pp. 12093–12098, 2005.

[56] L. M. Peter, “Characterization and modeling of dye-sensitized solar cells,” *Journal of Physical Chemistry C*, vol. 111, no. 18, pp. 6601–6612, 2007.

[57] L. Kavan, M. Zukalova, O. Vik, and D. Havlicek, “Sol–Gel Titanium Dioxide Blocking Layers for Dye-Sensitized Solar Cells: Electrochemical Characterization,” *ChemPhysChem*, vol. 15, no. 6, pp. 1056–1061, 2014. _eprint: https://onlinelibrary.wiley.com/doi/pdf/10.1002/cphc.201400026.

[58] A. Hauch and A. Georg, “Diffusion in the electrolyte and charge-transfer reaction at the platinum electrode in dye-sensitized solar cells,” *Electrochimica Acta*, vol. 46, pp. 3457–3466, Aug. 2001.

[59] J. Idígoras, E. Guillén, F. J. Ramos, J. A. Anta, M. K. Nazeeruddin, and S. Ahmad, “Highly efficient flexible cathodes for dye sensitized solar cells to complement Pt@TCO coatings,” *Journal of Materials Chemistry A*, vol. 2, no. 9, pp. 3175–3181, 2014.

[60] S. R. Taylor and E. Gileadi, “Physical Interpretation of the Warburg Impedance,” *CORROSION*, vol. 51, pp. 664–671, Sept. 1995.

[61] J. Bisquert, “Theory of the Impedance of Electron Diffusion and Recombination in a Thin Layer,” *The Journal of Physical Chemistry B*, vol. 106, no. 2, pp. 325–333, 2002.

[62] Q. Wang, J.-E. Moser, and M. Grätzel, “Electrochemical Impedance Spectroscopic Analysis of Dye-Sensitized Solar Cells,” *The Journal of Physical Chemistry B*, vol. 109, no. 31, pp. 14945–14953, 2005.

[63] F. Fabregat-Santiagoa, J. Bisquert, E. Palomares, S. A. Haque, and J. R. Durrant, “Impedance spectroscopy study of dye-sensitized solar cells with undoped spiro-OMeTAD as hole conductor,” *Journal of Applied Physics*, vol. 100, no. 3, pp. 034510–034517, 2006.

[64] F. Fabregat-Santiago, J. Bisquert, L. Cevey, P. Chen, M. Wang, S. M. Zakeeruddin, and M. Grätzel, “Electron Transport and Recombination in Solid-State Dye Solar Cell with Spiro-OMeTAD as Hole Conductor,” *Journal of the American Chemical Society*, vol. 131, pp. 558–562, Jan. 2009.

[65] J. Bisquert, I. Mora-Sero, and F. Fabregat-Santiago, “Diffusion–Recombination Impedance Model for Solar Cells with Disorder and Nonlinear Recombination,” *ChemElectroChem*, pp. n/a–n/a, 2013.

[66] T. Hoshikawa, T. Ikebe, R. Kikuchi, and K. Eguchi, “Effects of electrolyte in dye-sensitized solar cells and evaluation by impedance spectroscopy,” *Electrochimica Acta*, vol. 51, no. 25, pp. 5286–5294, 2006.

[67] Y. Xie, P. Joshi, S. B. Darling, Q. Chen, T. Zhang, D. Galipeau, and Q. Qiao, “Electrolyte Effects on Electron Transport and Recombination at ZnO Nanorods for Dye-Sensitized Solar Cells,” *J. Phys. Chem. C*, vol. 114, no. 41, pp. 17880–17888, 2010.

[68] J. A. Anta, J. Idígoras, E. Guillén, J. Villanueva-Cab, H. J. Mandujano-Ramírez, G. Oskam, L. Pellejà, and E. Palomares, “A continuity equation for the simulation of the current–voltage curve and the time-dependent properties of dye-sensitized solar cells,” *Physical Chemistry Chemical Physics*, vol. 14, no. 29, pp. 10285–10299, 2012.

[69] J. Bisquert, “Chemical capacitance of nanostructured semiconductors: its origin and significance for nanocomposite solar cells,” *Physical Chemistry Chemical Physics*, vol. 5, no. 24, pp. 5360–5364, 2003.

[70] J. Bisquert and I. Mora-Seró, “Simulation of Steady-State Characteristics of Dye-Sensitized Solar Cells and the Interpretation of the Diffusion Length,” *The Journal of Physical Chemistry Letters*, vol. 1, no. 1, pp. 450–456, 2010.

[71] M. Bag, L. A. Renna, R. Y. Adhikari, S. Karak, F. Liu, P. M. Lahti, T. P. Russell, M. T. Tuominen, and D. Venkataraman, “Kinetics of Ion Transport in Perovskite Active Layers and Its Implications for Active Layer Stability,” *Journal of the American Chemical Society*, vol. 137, no. 40, pp. 13130–13137, 2015.

[72] I. Zarazua, G. Han, P. P. Boix, S. Mhaisalkar, F. Fabregat-Santiago, I. Mora-Seró, J. Bisquert, and G. Garcia-Belmonte, “Surface Recombination and Collection Efficiency in Perovskite Solar Cells from Impedance Analysis,” *The Journal of Physical Chemistry Letters*, vol. 7, pp. 5105–5113, Dec. 2016.

[73] A. Guerrero, G. Garcia-Belmonte, I. Mora-Sero, J. Bisquert, Y. S. Kang, T. J. Jacobsson, J.-P. Correa-Baena, and A. Hagfeldt, “Properties of Contact and Bulk Impedances in Hybrid Lead Halide Perovskite Solar Cells Including Inductive Loop Elements,” *The Journal of Physical Chemistry C*, vol. 120, pp. 8023–8032, Apr. 2016.

[74] A. Todinova, L. Contreras-Bernal, M. Salado, S. Ahmad, N. Morillo, J. Idígoras, and J. A. Anta, “Towards universal approach to the analysis of impedance spectra of perovskite solar cells. Equivalent circuits and empirical analysis.,” *ChemElectroChem*.

[75] S.-M. Yoo, S. J. Yoon, J. A. Anta, H. J. Lee, P. P. Boix, and I. Mora-Seró, “An Equivalent Circuit for Perovskite Solar Cell Bridging Sensitized to Thin Film Architectures,” *Joule*, Aug. 2019.

[76] A. Pockett and M. J. Carnie, “Ionic Influences on Recombination in Perovskite Solar Cells,” *ACS Energy Letters*, vol. 2, pp. 1683–1689, July 2017.

[77] A. Todinova, J. Idígoras, M. Salado, S. Kazim, and J. A. Anta, “Universal Features of Electron Dynamics in Solar Cells with TiO Contact: From Dye Solar Cells to Perovskite Solar Cells,” *The Journal of Physical Chemistry Letters*, vol. 6, no. 19, pp. 3923–3930, 2015.

[78] D. Moia, I. Gelmetti, P. Calado, W. Fisher, M. Stringer, O. Game, Y. Hu, P. Docampo, D. Lidzey, E. Palomares, J. Nelson, and P. R. F. Barnes, “Ionic-to-electronic current amplification in hybrid perovskite solar cells: ionically gated transistor-interface circuit model explains hysteresis and impedance of mixed conducting devices,” *Energy & Environmental Science*, vol. 12, no. 4, pp. 1296–1308, 2019.

[79] J. Bisquert, A. Zaban, and P. Salvador, “Analysis of the mechanisms of electron recombination in nanoporous TiO dye-sensitized solar cells. Nonequilibrium steady-state statistics and interfacial electron transfer via surface states,” *Journal of Physical Chemistry B*, vol. 106, no. 34, pp. 8774–8782, 2002.

[80] F. Fabregat-Santiago, J. Bisquert, G. Garcia-Belmonte, G. Boschloo, and A. Hagfeldt, “Influence of electrolyte in transport and recombination in dye-sensitized solar cells studied by impedance spectroscopy,” *Solar Energy Materials and Solar Cells*, vol. 87, no. 1, pp. 117–131, 2005.

[81] J. Bisquert, L. Bertoluzzi, I. Mora-Sero, and G. Garcia-Belmonte, “Theory of Impedance and Capacitance Spectroscopy of Solar Cells with Dielectric Relaxation, Drift-Diffusion Transport, and Recombination,” *The Journal of Physical Chemistry C*, vol. 118, pp. 18983–18991, Aug. 2014.

[82] Y. Zhou and A. Gray-Weale, “A numerical model for charge transport and energy conversion of perovskite solar cells,” *Physical Chemistry Chemical Physics*, vol. 18, pp. 4476–4486, Feb. 2016.

[83] W. Tress, M. Yavari, K. Domanski, P. Yadav, B. Niesen, J. P. C. Baena, A. Hagfeldt, and M. Graetzel, “Interpretation and evolution of open-circuit voltage, recombination, ideality factor and subgap defect states during reversible light-soaking and irreversible degradation of perovskite solar cells,” *Energy & Environmental Science*, vol. 11, pp. 151–165, 2018.

[84] G. Richardson, S. E. J. O'Kane, R. G. Niemann, T. A. Peltola, J. M. Foster, P. J. Cameron, and A. B. Walker, "Can slow-moving ions explain hysteresis in the current–voltage curves of perovskite solar cells?," *Energy & Environmental Science*, vol. 9, pp. 1476–1485, Feb. 2016.

[85] N. E. Courtier, G. Richardson, and J. M. Foster, "A fast and robust numerical scheme for solving models of charge carrier transport and ion vacancy motion in perovskite solar cells," *Applied Mathematical Modelling*, vol. 63, pp. 329–348, July 2018.

[86] N. E. Courtier, J. M. Cave, J. M. Foster, A. B. Walker, and G. Richardson, "How transport layer properties affect perovskite solar cell performance: insights from a coupled charge transport/ion migration model," *Energy & Environmental Science*, vol. 12, pp. 396–409, Dec. 2018.

[87] N. E. Courtier, J. M. Cave, A. B. Walker, G. Richardson, and J. M. Foster, "IonMonger: a free and fast planar perovskite solar cell simulator with coupled ion vacancy and charge carrier dynamics," *Journal of Computational Electronics*, vol. 12, pp. 396–409, Sept. 2019.

Chapter 4

Characterization of photochromic dye-sensitized solar cells using small-signal perturbation techniques.

Abstract

Photochromic DSSCs are novel semitransparent PV devices that self-adjust their optical properties to the irradiation conditions. This feature makes them especially suitable for BIPV. These novel solar cells have already achieved efficiencies above 4%, and there are multiple pathways to improve their performance. This Chapter conducts a complete small-perturbation characterization of DSSCs with the photochromic dye NPI. The inherent properties of the photochromic dye modify the functioning of the solar cell by the optical excitation that also acts as a probe. These properties pose unique challenges to interpreting the results using conventional models. This Chapter provides guidelines for adequate characterization protocols of photochromic solar cells and essential insights into interfacial electronic processes.

This Chapter is based on Publication 3 of this thesis: Antonio J. Riquelme *et al.* ACS Appl. Energy Mater. 2021, 4, 9, 8941 - 8952.

4.1 Introduction

As it was described in *Chapter* 1, DSSCs are an emerging PV technology that has initiated its industrial development[1]. These cells reach high PCEs of up to 14% on a laboratory scale[2–4], excellent performance upon scaling to small modules[5–7] and a remarkable stability[8–10]. The low cost of the raw materials[11] compared to other technologies and the simplicity and small environmental impact of their manufacturing make this technology suitable for large-scale production. All these features, together with the possibility to fabricate semi-transparent and colorful[6] solar cells, make them appealing for mass-market applications such as BIPV[12]. During the development of this thesis, a breakthrough concept on photochromic DSSCs was reported[13]. This kind of dye simultaneously self-adapts its level of transparency and PV performance with sunlight intensity; a PCE of more than 4% was achieved with the activated photochromic solar cells.

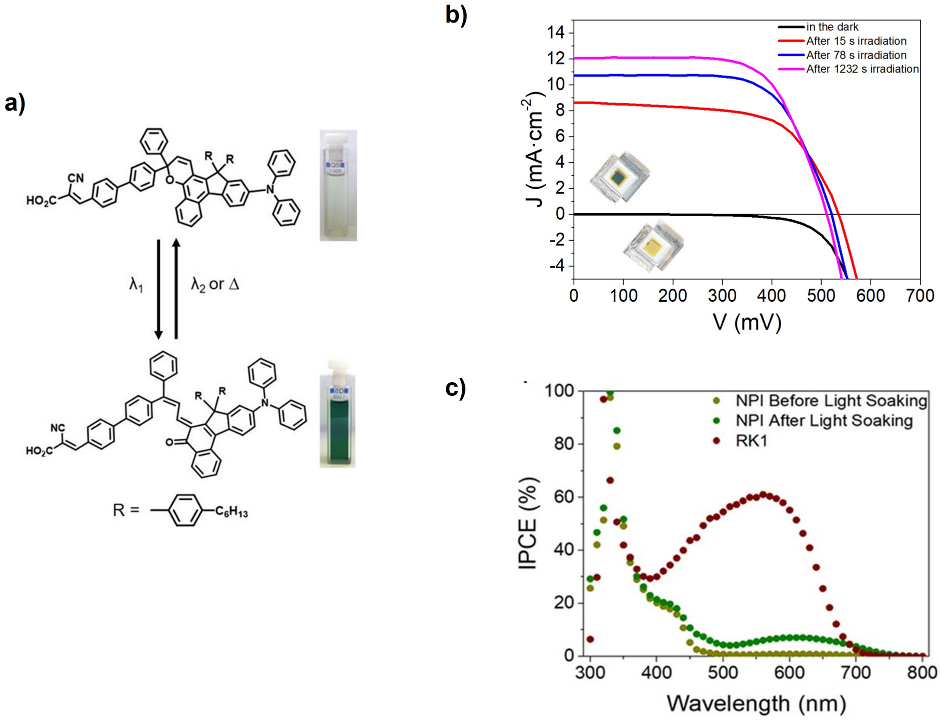

Figure 4.1: (a) The interconversion process of the NPI photochromic dye (with a 2,2-diphenyl-2H-indeno[2,1f]naphtho[1,2-b] pyran core) where the uncolored, closed-form isomer is activated by UV light absorption generating the opened, colored isomers and the reverse process is achieved thermally. (b) *JV* curve of DSSCs based on photochromic NPI with the yellow cell under dark conditions and the green cell at several times after irradiation and at the photostationary state (1232 s). (c) IPCE of a non-photochromic RK1 DSSC and photochromic NPI before and after reaching the photostationary state.

To the date of this thesis, the best photochromic dye, NPI, switches from light yellow to a dark green hue under irradiation, related to a change from the closed to an open configuration, respectively[13], as shown in Figure 4.1. In order to enhance the device's transparency, a 13 μm mesoporous TiO_2 layer was used as the working electrode, while a platinum-coated FTO served as the counter electrode. To avoid any regeneration limitation of the device, a non-viscous, iodine-based electrolyte explicitly optimized for the NPI dye was used. The light soaking effect is observed not only in the J_{SC} but also in the IPCE, which changes significantly in the 500-700 nm region, in contrast to a non-photochromic dye such as RK1. This color change happens quickly, related to the fast activation kinetics upon irradiation within the absorption range of the closed-form isomer of the dye. However, the opposite process is much slower, as it takes several hours before the photochromic dye reaches the fully deactivated state[13]. Along with the stunning photocurrent rise at the photostationary state, the activation of the dye induces a decrease of the V_{OC}. A priori, this behavior could be explained by either a band shift of the metal oxide semiconductor or by a recombination kinetics acceleration. Therefore, it is essential to clarify whether this behavior is intrinsic to the new dye material or related to the activation process. To tackle the challenge of developing new photochromic materials with higher efficiencies and faster self-adjustable optical properties, a better understanding of the interfacial processes and the recombination and transport properties of the devices is needed. To this matter, as has been discussed in *Chapter* 3, small-signal perturbation optoelectronic techniques are instrumental in providing information about the recombination and transport processes taking place within the device.

The particularities of photochromic dyes may change the system during the measurement itself because the illumination used to define a specific quasi-Fermi level in the TiO_2 film or even the modulated light intensity used in IMPS could also activate the dye molecules. This, in turn, may change the charge stored and the kinetics of the transport and recombination processes as a function of voltage and light intensity. Therefore, a clear and simple procedure to measure and analyze this novel type of photochromic device's response is needed. This *Chapter* focuses on the peculiarities of the small-signal perturbation analysis of a photochromic DSSC compared to a conventional device. It is shown how the activation of the photochromic dye accelerates recombination without shifting the band edges of the oxide. To unravel how the photochromic properties of the dye influence the PV processes of DSSCs. Furthermore, it deeps on the origin of the decrease in photovoltage observed in DSSCs prepared with the NPI photochromic dye when the cell is optically activated.

4.2 Fabrication and characterization of devices

4.2.1 Fabrication of DSSCs

Transparent photoanodes, commercially available from Solaronix, Switzerland (Ti-Nanoxide HT/SP) with a 13 μm mesoporous TiO_2 layer and an active area of 0.36 cm^2, were cleaned using ethanol and treated with a 4.1 mmol L^{-1} $TiCl_4$ aqueous suspension at 70ºC for 20 minutes followed by sintering at 500ºC for 20 minutes. The previously perforated counter electrodes were coated with a thin layer of platisol (Solaronix, Switzerland) and annealed under air at 500ºC for 20 minutes. The photoanode sensitization mixture (0.5 mM[dye] : 5 mM [CDCA]) coadsorbant dissolved in a 1:1 mixture of $CHCl_3$: *t*BuOH for NPI-based cells and 1:1 mixture of $CHCl_3$:EtOH for RK1-based cells. Both electrodes were sealed together using 60 μm Surlyn and then filled with the appropriate electrolyte solution, Solaronix HI-30 for RK1 and our optimized home-made one for NPI[13]. The pre-drilled holes were sealed with a thin glass cover with Surlyn underneath.

4.2.2 Characterization of the devices

The solar cells were characterized under one sun, using an AM1.5G simulator previously calibrated with a reference photodiode (KG-3, Schott). A mask was used prior to delimiting an illuminated active area of 0.25 cm^2. The *JV* curve in the dark and under illumination of the devices was registered by applying an external voltage bias to the devices, and the resulting photocurrent was recorded with a Keithley model 2400 digital source meter (Keithley, USA). The EIS and IMPS studies were conducted using the experimental setup described in *Chapter* 3. A 0.25 cm^2 plastic mask was used to limit the area of the cell receiving illumination during the IMPS measurements. EIS measurements under illumination were performed by applying a potential equal to the observed V_{OC} under constant illumination by white, blue (480 nm), and red (650 nm) Thorlabs LEDs over a wide range of DC light intensities. A 10 mV perturbation in the 10^{-1}-10^5 Hz range was applied. A flow chart of the EIS measurements of the NPI cells to ensure that all the different experiments were performed on both the activated and deactivated forms of the dye is presented in Figure 4.2.

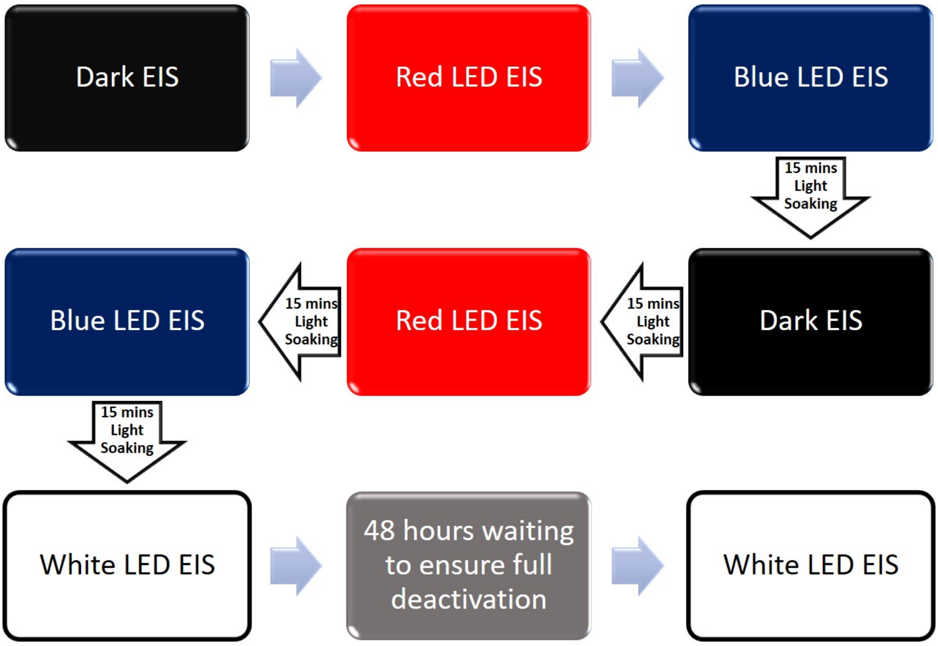

Figure 4.2: Flow chart of the order in which the EIS measurements were done. Dark EIS after light soaking was performed following the flow chart of Figure A.1 in *Appendix* A to ensure the same level of activation of the dye for all the measurements.

The EIS measurements under dark conditions were conducted, ensuring that no external source of light interfered with the experiment and by applying an external voltage from 0.1 V to the V_{OC} obtained under one sun illumination.

The frequency range of the IMPS measurement was restricted to 10^{-1}-10^{4} Hz due to limitations of the set-up (LED and LED driver). These measurements were performed under blue and red illumination and SC conditions using ILH-GD01-SC201 ILS LEDs. The order in which the IMPS measurements were done is described in Figure 4.3

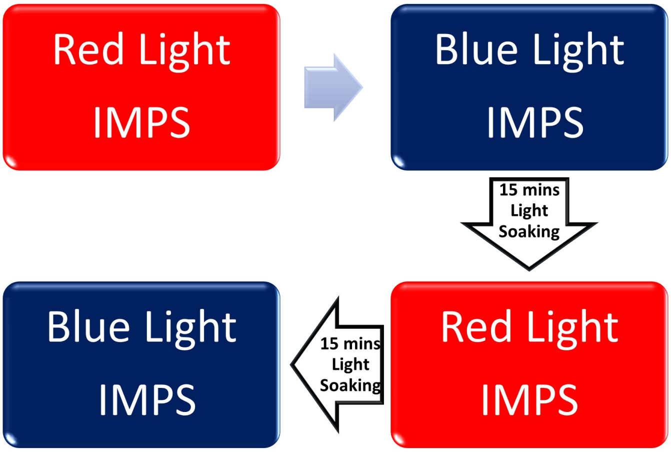

Figure 4.3: Flow chart of the order in which the IMPS measurements were performed.

In this *Chapter* the behavior of the solar cells for the deactivated and activated photochromic NPI dye is separated. The change was induced by exposing the cell to the solar simulator (ABET-Sun2000) for 15 minutes under one sun illumination with an AM1.5G filter, ensuring that the illuminated area of the solar cell had turned to a dark green color. The light intensity was recorded using a reference monocrystalline silicon solar cell with temperature output (ORIEL, 91150).

An additional experiment was conducted to study the evolution of the recombination kinetics upon deactivation of the NPI dye to understand better the relation between the activated and deactivated states of the dye and the recombination process. For that purpose, after 15 minutes of 1 sun illumination, EIS under dark conditions at a fixed 0.35 V external voltage was conducted after different time intervals to study the discoloration process. For more clarity, a flow chart of how these measurements were done is indicated in Figure 4.4

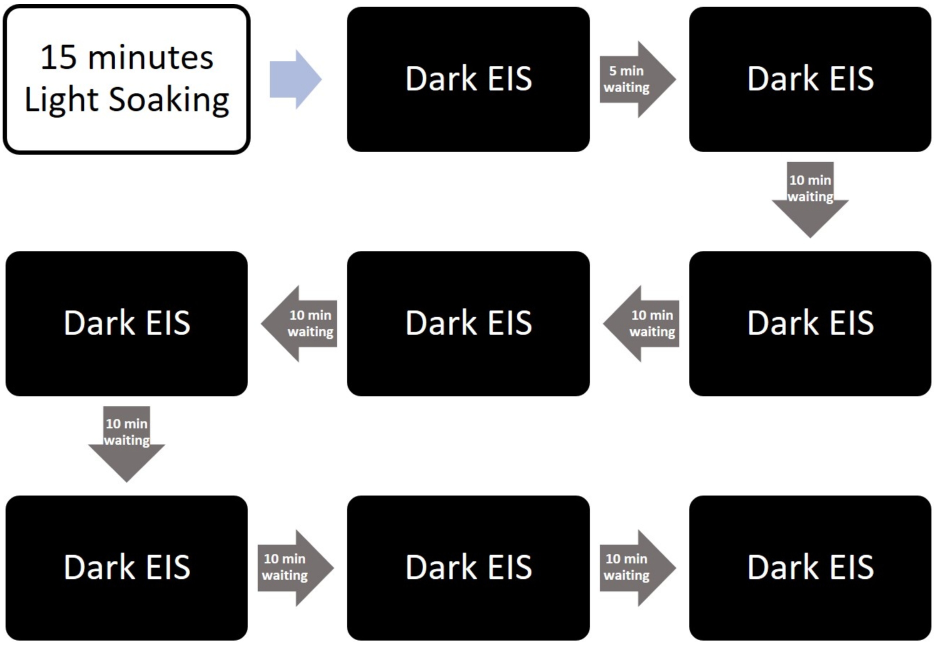

Figure 4.4: Flow chart of the deactivation kinetics study.

In order to include statistical values, two cells of each type of dye were completely characterized by EIS and IMPS.

4.3 Results and discussion

4.3.1 Recombination properties of the photochromic DSSC

The study reporting this novel photochromic dye[13] highlighted, with help of theoretical and experimental data, that the acceleration of the recombination process is the main reason behind this observation. In order to better understand all the processes that may lead to this behavior, a full small-signal perturbation study has been conducted on the photochromic DSSC, both for the activated and the deactivated state. For the sake of comparison, the same study was conducted on the well known, fully organic, non-photochromic and commercially available RK1 dye[8], whose *JV* curve is given in Figure A.2 of *Appendix* A.

As can be observed in panels a and b in Figure 4.5, the EIS results show the typical three arcs for the RK1 DSSCs, with the equivalent peaks in the Bode plot[14] described in *Chapter* 3. These three signals appear at 10 - 50 kHz, 5 - 500 Hz, and 0.1 - 1 Hz. The first, high frequency semicircle is related to the platinum counter electrode[15], as shown in Figure A.4 of *Appendix* A. The HF feature disappears by changing the counter electrode material from platinum to PEDOT. The feature at low frequencies, on the other hand, is associated with electrolyte diffusion[16,17]. These two signals are of little interest for the focus of this *Chapter* therefore, the discussion is limited to the main arc of the spectra in the 5-500 Hz range, linked to the recombination processes in the DSSC[14] as described in *Chapter* 3. In well-performing DSSCs, the recombination process corresponds to electron transfer from TiO_2 to tri-iodide in the electrolyte solution. Hence, the recombination resistance is a charge transfer resistance that can also be measured in the dark upon applying a voltage similar to the V_{OC} under illumination, following the superposition principle approximation. A decrease in the recombination resistance for the cell under illumination can be observed compared to the charge transfer resistance in the dark at the same voltage.

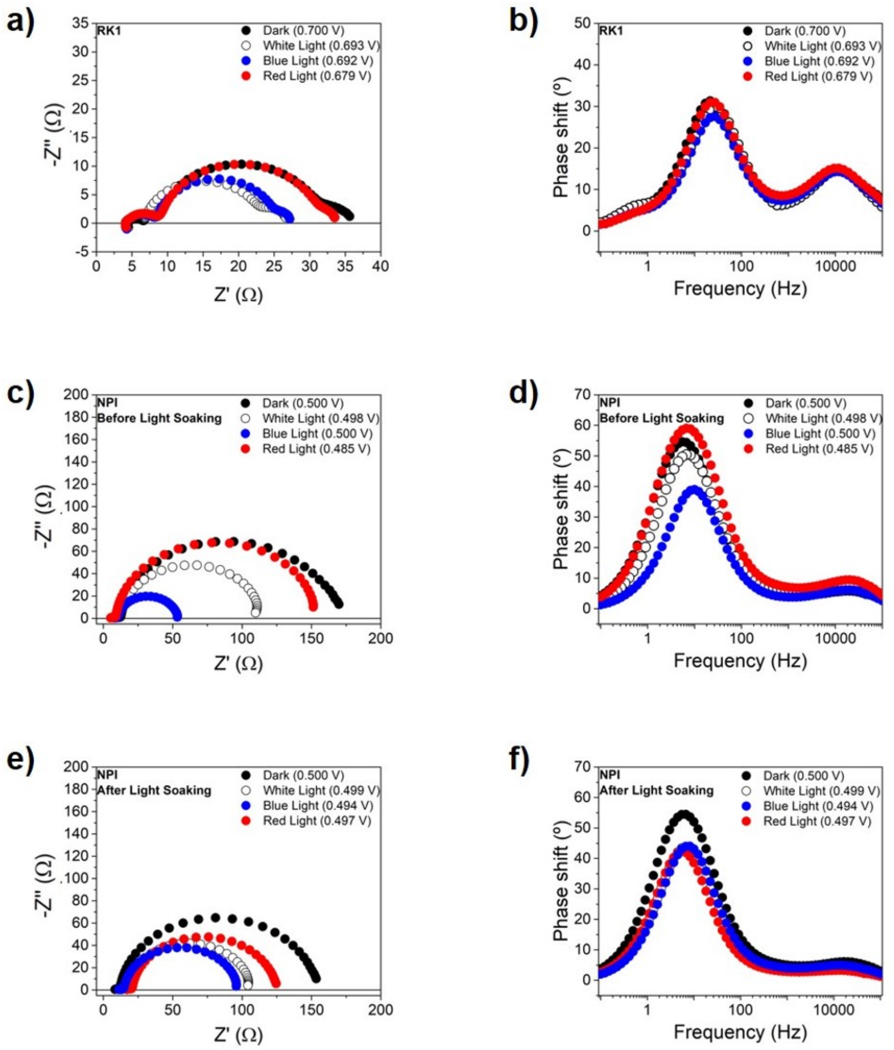

Figure 4.5: EIS results under monochromatic LED illumination for an RK1 solar cell (a and b) and an NPI solar cell, both before (c and d) and after (e and f) a light soaking treatment. The measurements were performed at an applied voltage equal to the V_{OC} that is obtained under white light one sun illumination using a solar simulator; about 0.7 V for the RK1 cell and 0.5 V for the NPI cell. The Nyquist plots are shown on the left (a, c and e) and the Bode plots on the right (b, d and f).

This observation is typical for DSSCs and is related to the local increase of the tri-iodide concentration due to the dye regeneration process, thus accelerating recombination[18,19] as explained in *Chapter* 2. In accordance to the RK1 absorbance spectrum in Figure A.6 of *Appendix* A, the absorption coefficient for the red light is almost zero, which translates to a significantly lower recombination current at V_{OC} and, thus, a lower triiodide generation rate, hence the recombination behavior is very similar to the cell under dark conditions. In the Bode plot in Figure 4.5b, no shift in the frequency of the apex of the recombination arc is observed, illustrating that the wavelength of the illumination does not affect the recombination rate.

The same experiments were carried out with NPI solar cells, and the results are presented in panels c-f in Figure 4.5. Before light soaking, the general trends are the same as for the RK1 solar cell. However, the decrease of the recombination resistance is more dramatic upon illumination, especially for the white and blue illumination, which is related to the properties of the photochromic dye. This effect is also observed when comparing the activated and deactivated states of the cell, especially for the EIS measurements under dark conditions and with red illumination. As for the blue and white light measurements, it is essential to mention that, even before light soaking, a substantial amount of dye molecules get activated during the small perturbation measurement itself (see Figure A.7 in *Appendix* A). This makes it difficult to compare the activated and non-activated states of the cells for a light excitation where the dye absorbs. This is seen in Figure 4.5d, where the impedance peak for blue light gets displaced towards higher frequencies for the dark and red illumination.

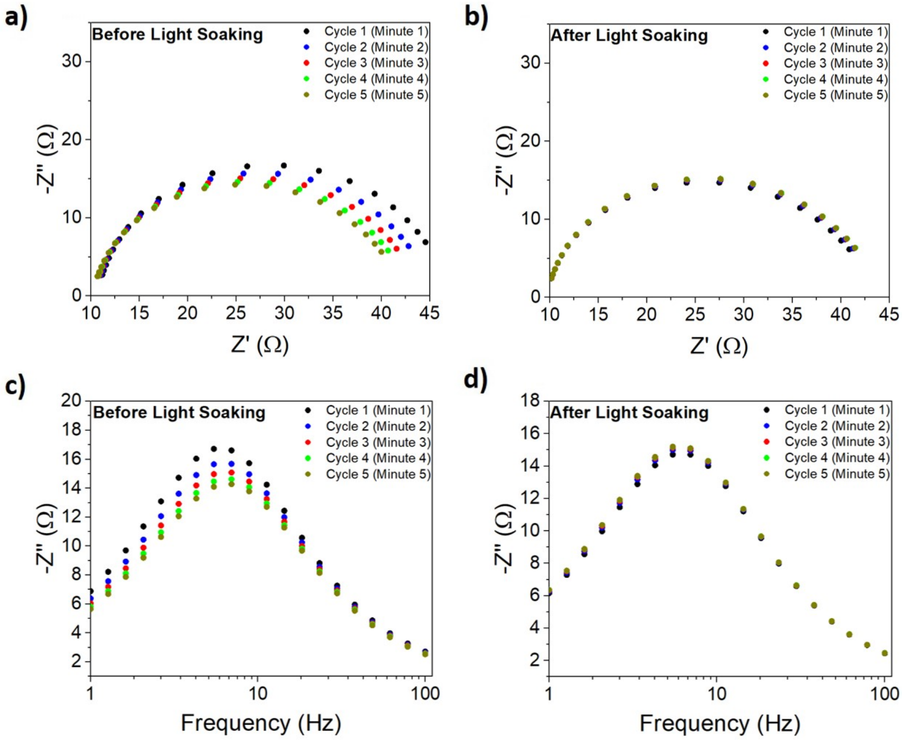

Figure 4.6: Nyquist and Cole-Cole plots of impedance measurements for the NPI cell under blue light illumination before (a and c) and after (b and d) light soaking in the 1-100 Hz frequency range.

A swift (5 minutes in total) impedance experiment under blue light illumination was run to confirm this interpretation. This measurement was restricted to the 1-100 Hz frequency range (where the recombination arc appears). The results are shown in Figure 4.6, where it can be observed that the cell quickly activates, illustrated by the acceleration of the recombination rate. This is displayed as a decrease of the semi-circle diameter, hence the recombination resistance, in the Nyquist plot and a shift of the peak towards higher frequencies (Figure 4.6c and d), corresponding to an increase in the recombination rate constant, both in the period of a few minutes.

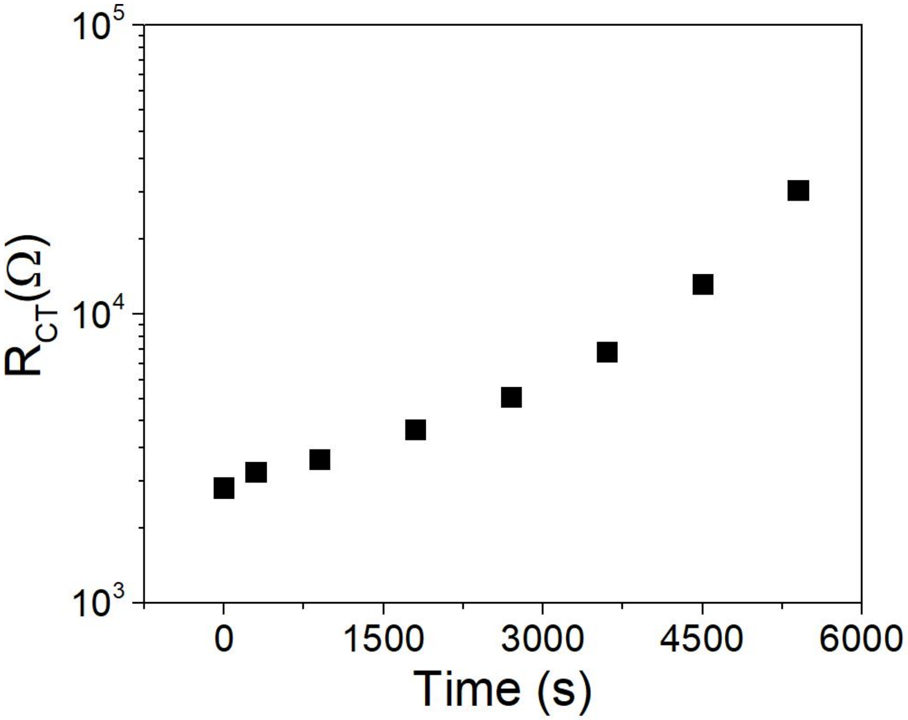

Figure 4.7: Charge transfer resistance from the EIS experiment under dark conditions at 0.35 V external voltage applied to an NPI DSSC as a function of time after 15 minutes of light soaking following the measurement procedure described in the Experimental Section.

The impact on the charge transfer resistance of the deactivation process can be observed in Figure 4.7 as a function of time after light soaking. The increase in the charge transfer resistance under dark conditions with the deactivation process of the molecule is pronounced and can be compared to Figure A.8 in *Appendix* A, where most of the deactivation of NPI in a complete cell takes place within the first 4 hours. This result also indicates that the discoloration process in a photochromic dye-based cell slows down the recombination process. In other words, the activation of the dye accelerates recombination.

From the Bode plots in Figure 4.5, in panels d and f, it can be observed that, unlike in panel b, the primary signal frequency peak shifts somewhat to higher frequencies upon dye activation, indicating that either the activation of the photochromic dye induces a faster recombination process, or produces a band shift. It is also noticeable that the LF feature observed with RK1 disappears for NPI, which can be explained by the fact that an optimized electrolyte was used for the NPI devices, as described in the Experimental Section in this *Chapter*.

The EIS results shown in Figure 4.5 can be fitted to an EC in order to analyze better the behavior of the cells under dark conditions and with illumination. It was not possible to get an accurate fit using the classical Bisquert and co-workers EC[14,20] described in *Chapter* 3. Thus, the main arc in the 5 - 500 Hz range related to the charge transfer/recombination process was fitted to a parallel -RC- element, where the resistance is considered to be the charge transfer (dark) or recombination resistance of the device (R_{CT}). At the same time, the capacitance is (C_{μ}). As a specific characteristic of DSSCs, in *Chapter* 2 it was shown how both parameters generally show an exponential voltage dependence[21], allowing for extracting α from the slope of the voltage-dependence of C_{μ} and β from the R_{CT} voltage-dependence.

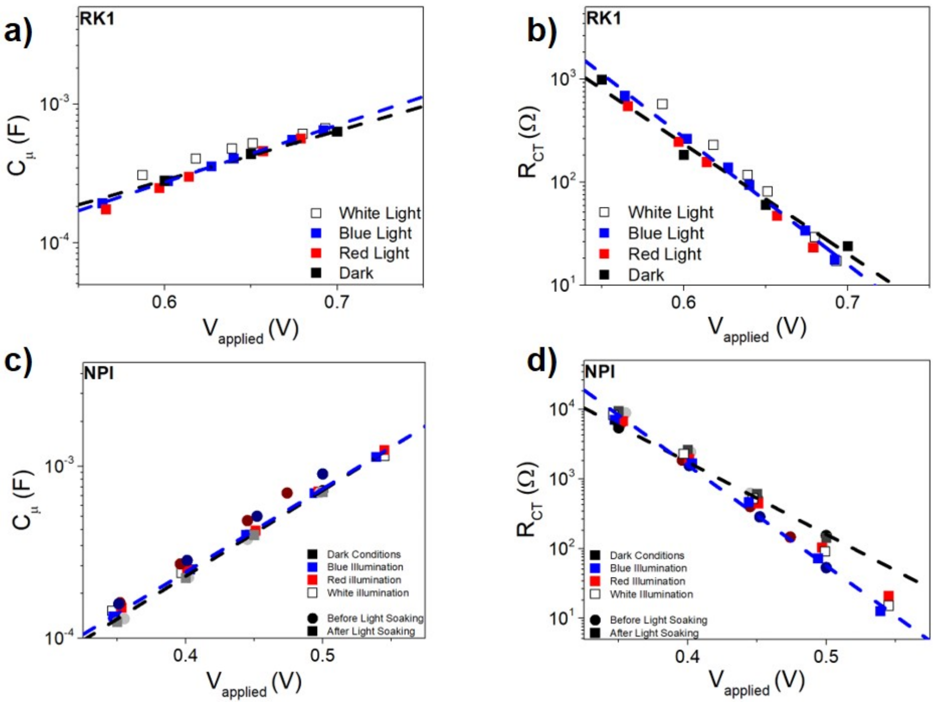

Figure 4.8: Capacitance (a and c) and resistance (b and d) vs applied voltage for RK1 (a and b) and NPI (c and d) solar cells in the dark and under LED monochromatic illumination. The results were obtained by fitting the main arcs in Figure 4.5 to a parallel -RC- circuit. Fits to equations 2.59 and 3.36 are included for the results obtained in the dark and under blue LED illumination in order to highlight the general trends observed. Note that the applied voltage under illumination corresponds to the V_{OC} obtained at the specific intensity.

Figure 4.8 shows that the resistance and capacitance of the charge transfer/recombination signal of the EIS have an exponential voltage dependence as described in *Chapter* 2. For both the RK1 and NPI solar cells, the chemical capacitance is independent of the illumination conditions, indicating that the band edges do not shift. The same result is found for the NPI-based cell in the activated and deactivated states, illustrating that the activation process induces no band shift[22,23], as suggested by DFT calculations[13]. Thus, it can be concluded that the shift towards higher frequencies of the primary signal in Figure 4.5 panels d and f is a result of an increased recombination rate. Therefore, the decrease of the V_{OC} associated with the activation of the dye is due to kinetics reasons only[23,24]. However, as shown in Figure A.5 in *Appendix* A, there is a band shift between the NPI and RK1 dyes of around 0.15 V. Looking at the values obtained for the recombination resistance, as the light intensity increases and the V_{OC} approaches the values obtained at one sun under the solar simulator and, hence, under practical operating conditions, differences between the open and closed forms of the dye become more apparent, as was already observed in the first study[13] and in Figure 4.7.

At this point, it is important to remember that, by comparing at the same applied/generated potential, it is ensured that the electron quasi-Fermi level and the electron density in the photoanode for the experiments carried out with different illumination sources are the same.[14,25,26] In this respect, the results of the chemical capacitance and the recombination resistance in Figure 4.8 are quite conclusive. Despite using different illumination conditions, the chemical capacitance is the same at the same value of the applied voltage. Furthermore, the recombination resistance is the same for the RK1 reference cell. This proves that photochromism is the only factor affecting the observed increase/decrease of the recombination resistance.

The α and β parameters included in tables A.1 and A.2 in *Appendix* A are within the range normally reported for DSSCs (0.15 - 0.35 for α and 0.5 - 0.8 for β)[22,27–29] as described in *Chapter* 2. Although there is an increase in the β values upon activation of the photochromic dye, this change is not sufficient to imply a change in the dominant recombination pathway corresponding to triiodide reduction. In addition to the α and β values obtained from the fit of the EIS to the parallel -RC- element, the time constants associated to this recombination feature, in Figures 4.9 and A.9 in *Appendix* A are also an important source of information.

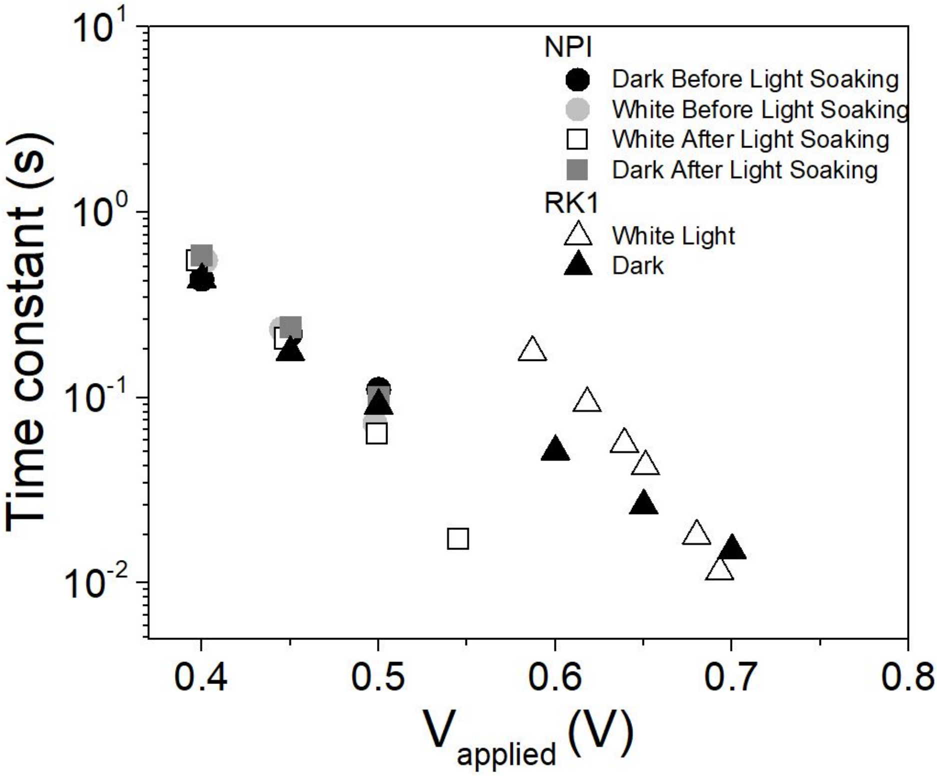

Figure 4.9: Time constants associated with the recombination feature in the Bode plots in panels (b), (d), and (f) of Figure 4.5 under dark conditions and under white light illumination for the RK1 DSSC, and the activated and deactivated NPI-based solar cell.

The time constants observed in Figure 4.9 correspond to the effective electron lifetime[30], as explained in *Chapter* 3, which decreases in a dramatic way as both the illumination intensity and the V_{OC} increase. By comparing this behavior to the trend shown by the recombination resistance in Figure 4.8, it is easy to understand that as the recombination resistance decreases and hence the recombination rate increases, the charge carriers recombine at a higher rate, therefore their lifetime decreases. Remarkably, the lifetime vs voltage plots for both RK1 and NPI devices follow the same slope for all the excitation wavelengths, as can be observed in Figure A.9 in *Appendix* A.

This is consistent with the similar α and β values observed in Tables A.1 and A.2 of the *Appendix*, and suggests that the same recombination process takes place in both devices. The only difference between the time constants obtained for the NPI and RK1 dyes is the band shift induced by the dye dipole of 0.15 V observed in Figure A.5 of the *Appendix*.

The diffusion length, which, as was explained in *Chapter* 2, can be described as the average distance that an electronic carrier can travel across the active layer before recombining, is a handy parameter of the cell since it can be directly related to the amount of charge that can be collected by the cell. As it was described in *Chapter* 3, it is possible to determine the small-perturbation diffusion length from EIS measurements. However, since it was not possible to fit the EIS to the classical Bisquert and coworkers EC[14,20] because no clear transport line was present in the spectra, equation 3.38 can not be applied to get a well-defined diffusion length.

4.3.2 Transport properties of the photochromic DSSC

For these cells EIS alone failed to provide information about the small-signal perturbation electron diffusion length. Thus, this parameter can alternatively be calculated by equation 3.32[31] where D_n is the electron diffusion coefficient. This parameter can be obtained from IMPS, and the recombination lifetime is equivalent to the electron effective lifetime, shown in Figure 4.9, provided that both parameters are measured at the same quasi-Fermi level position[32–35].

From panels a and b in Figure 4.10 in this *Chapter* and A.10 in *Appendix* A, it can be seen that there are two distinguishable signals with the conventional non-photochromic dye RK1 as previously reported for various DSSCs and other thin layer PV devices[21,36–39]. For a film thickness as large as the TiO_2 layer of these devices (13 μm), the signal observed in the 10 - 100 Hz range can be related to the electron transport in the nanostructured

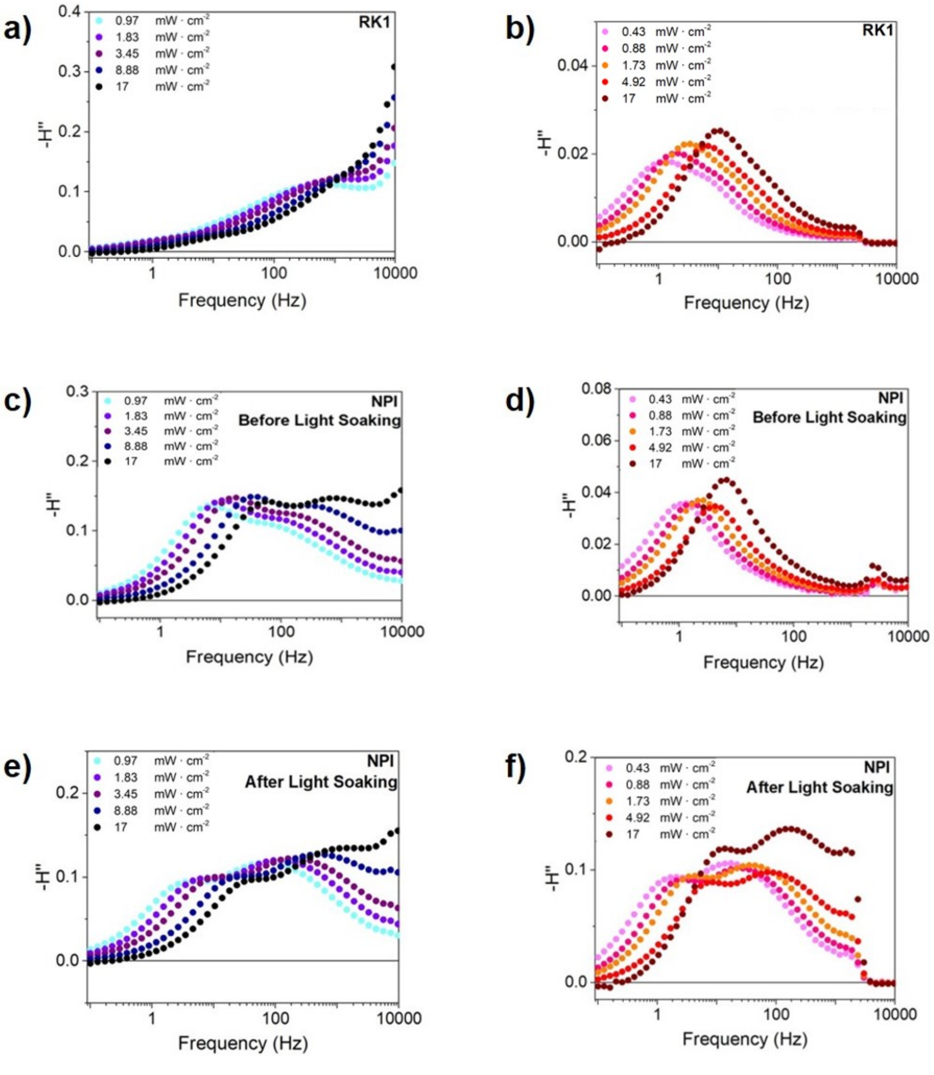

Figure 4.10: Cole-Cole plots of the IMPS measurements of an RK1 solar cell (a and b) and a photochromic NPI solar cell, both deactivated (c and d) and activated (e and f) under different light intensities with blue (a, c, and e) and red (b, d, and f) illumination.

mesoporous layer. Differences between the spectra obtained with the two excitation wavelengths are observed, such as the size of the feature appearing at high frequencies and a shift of one order of magnitude of the frequency of the signal associated with electron transport in the TiO_2 layer. However, the general shape and behavior of the two identifiable signals are consistent.

When the same IMPS experiment is carried out on deactivated and activated NPI solar cells (panels c-f of Figure 4.10), an additional signal in the 100 - 1000 Hz range appears for the activated dye, which is absent in the RK1 or NPI devices before light soaking under red illumination. However, the feature does appear in the IMPS measurement before light soaking under blue illumination. As discussed before, blue light activates the photochromic dyes making it impossible to measure the fully deactivated state. Hence, differences between the activated and the deactivated states of the dye can only be observed using red illumination. Since the additional signal only appears for the activated dye, it seems to be related to the activation process of the molecules. In addition, the 100 - 1000 Hz range where it appears corresponds to the milliseconds time regime, which would be consistent with a fast change of coloration associated with the activation process when embedded in a solar cell. This result indicates that the only way to truly assess the activation and deactivation processes via optoelectronic small perturbation techniques is by exciting at a wavelength that does not induce photochromism.

The behavior of the time constants represented in Figure 4.11 shows an exponential dependence on the light intensity that has been ascribed to the transport mechanism of multiple-trapping[22,36,40], which confirms its origin to be the transport in the mesoporous TiO_2 layer. As expected, the time constants do not change significantly when the dye is fully activated (blue illumination in both cases and red illumination after light soaking). However, electron transport when the dye is not activated (red illumination before light soaking) appears to be somehow faster. The reason is that since

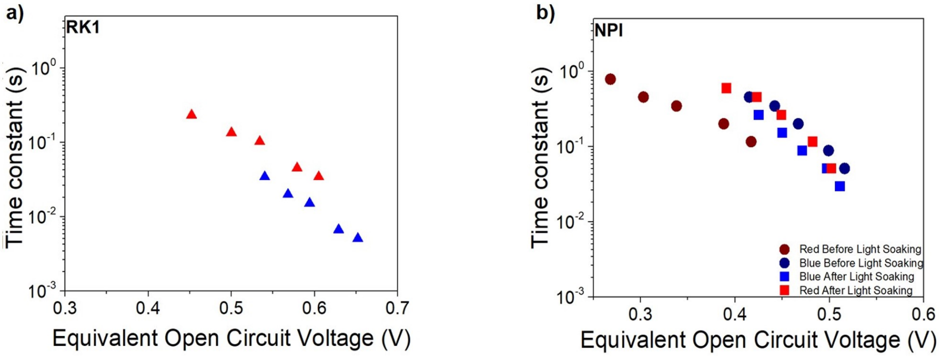

Figure 4.11: Time constants associated with the main feature of IMPS under red and blue light for an (a) RK1 and (b) NPI device, both before (circles) and after (squares) light soaking, obtained from the results shown in Figure 4.10

the non-activated dye absorbs much less in the red (Figure A.7 in *Appendix* A), the light illumination intensity required to obtain the same value of the equivalent V_{OC} is larger. Consequently, the quasi-Fermi level in TiO_2 photoanode is higher up in energies, and transport becomes faster, according to the multiple trapping model. Knowing that, the small-perturbation electron diffusion coefficient can be obtained by means of Eq. 3.29 of *Chapter* 3.

4.3.3 Small-perturbation diffusion length and quantum efficiency of the photochromic DSSC

Since these values are being used together with the data obtained from EIS at V_{OC}, we need to ensure that both parameters are obtained at the same trap occupancy (i.e., at the same position of the Fermi level relative to the conduction band). To do that, a correction, which, as mentioned in *Chapter* 3, for DSSCs is known[41] to be about 0.3 V, is applied (See Figure A.11 in *Appendix* A). However, this correction is likely overestimated for the case of the deactivated NPI dye, especially for the red LED IMPS measurements before light soaking. Due to the low absorbance of the closed dye at this wavelength, the Fermi level is very close to the position under dark conditions. For the sake of simplicity, given that no significant differences in the qualitative behavior under small perturbation techniques have been identified in this study, the same voltage correction has been applied to the NPI dye, with the precaution of only interpreting the higher light intensities values.

By extending the time constants trend line from the EIS measurements to short-circuit conditions (Figure A.12 of *Appendix* A) and doing the same with the diffusion coefficients calculated by applying Equation 3.29 to the time constants from IMPS (Figure A.13 of *Appendix* A), diffusion coefficients of $3{\cdot}10^{-11}$ m^2/s for the RK1, and $4{\cdot}10^{-12} - 8{\cdot}10^{-11}$ m^2/s for the NPI solar cell are obtained. These values are combined using Equation 3.32 to obtain the diffusion lengths (Figure A.14 of *Appendix* A) which are found to be 200 - 500 μm for RK1 and 50 - 110 μm for NPI. These large values (in comparison with the film thickness of 13 μm) suggest that charge collection in the TiO_2 photoanode approaches 100% in both cases.

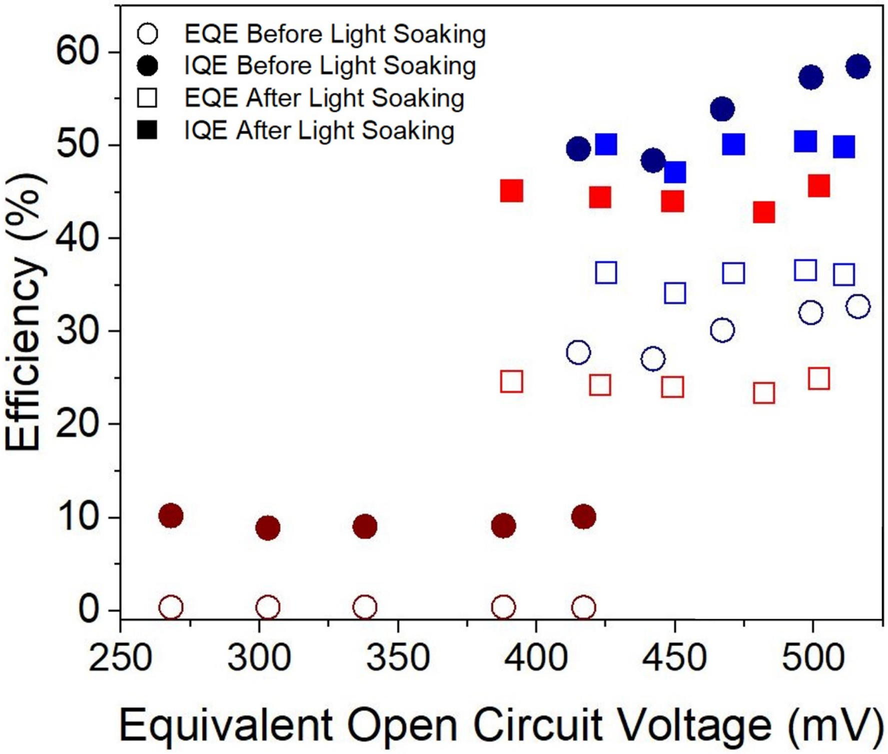

Figure 4.12: EQE (hollow symbols) and IQE (solid symbols) obtained from IMPS measurements under SC conditions for an NPI solar cell in the activated (squares) and deactivated (circles) states under red and blue monochromatic illumination.

In Figure 4.12, it is noticeable that there are no evident differences between the internal and external quantum efficiencies under blue illumination for the activated and deactivated dye. As already mentioned, the blue light activates the dye right after starting the measurement, making it impossible to characterize the deactivated state with blue light. The IQE values obtained under red light illumination on the activated cell are similar to those obtained with blue illumination, consistent with the diffusion length results. The IQE values of the activated NPI device are similar to those of the RK1 cell, as can be observed in Figure A.15 of *Appendix* A, although recombination is faster for the NPI solar cells as compared to the RK1 cells. This could result from regeneration or injection issues in RK1 cells due to limitations of the electrolyte used. The electrolyte used for the NPI cell was a homemade electrolyte optimized for this dye, so these limitations are avoided. On the other hand, the red illumination on the deactivated cell produced poorer IQE values in apparent contrast with the large diffusion length estimated for the deactivated NPI-based cell under red illumination. However, it is important to stress that the diffusion length only accounts for the charge collection efficiency. Therefore limitations in the regeneration or poor charge generation due to negligible absorbance can produce low IQE values while the charge collection efficiency inferred from the diffusion length is high.

4.4 Conclusion

This *Chapter* presents a clear and simple procedure to measure and analyze photochromic DSSCs by optoelectronic small-signal perturbation techniques, distinguishing between the activated and deactivated state of the dye molecule. For this purpose, EIS and IMPS have been used to estimate the effect of the photochromism of these cells on recombination and electronic transport. It is shown that the general behavior of the photochromic NPI dye in an EIS study is fundamentally similar to any other dye previously studied. EIS has been used to determine changes in the recombination kinetics upon activation of the photochromic dye, finding that activation of the molecule leads to a faster recombination process, which induces a lower charge extraction efficiency. This result, combined with the similar electronic diffusion coefficient for RK1 and activated NPI solar cells obtained from IMPS, illustrates a decrease in the electronic diffusion length in NPI compared to the reference RK1 dye. However, this effect is not evident in the IQE results because injection and regeneration issues related to the non-optimized electrolyte limit the RK1 cell performance. This issue was solved for the NPI cells using a homemade electrolyte designed explicitly for the NPI dye. Finally, an additional signal characterizing the activated NPI dye with IMPS has been found. Given that this signal is neither present in the deactivated state of the photochromic NPI cells nor the non-photochromic RK1 cells, these observations lead to the conclusion that this signal is related to the activation process of the dye, thus making IMPS an essential tool for assessing the activation kinetics of new photochromic dyes developed in the future. This *Chapter* shows that even when the complete deactivation of the photochromic devices is ensured before the measurement, if this is conducted using short-wavelength illumination, the cell is partially activated instantly when starting the measurement, making it impossible to study the deactivated cell. Therefore, if a study on the deactivated dye is aimed at, the use of long-wavelength excitation, which will not activate the photochromic dye, is required.

Bibliography

[1] A. Hagfeldt, G. Boschloo, L. Sun, L. Kloo, and H. Pettersson, “Dye-sensitized solar cells,” *Chemical Reviews*, vol. 110, no. 11, pp. 6595–6663, 2010.

[2] S.-Q. Fan, C. Kim, B. Fang, K.-X. Liao, G.-J. Yang, C.-J. Li, J.-J. Kim, and J. Ko, “Improved efficiency of over 10% in dye-sensitized solar cells with a ruthenium complex and an organic dye heterogeneously positioning on a single tio$_2$ electrode,” *The Journal of Physical Chemistry C*, vol. 115, no. 15, pp. 7747–7754, 2011.

[3] W. D. Zeng, Y. M. Cao, Y. Bai, Y. H. Wang, Y. S. Shi, M. Zhang, F. F. Wang, C. Y. Pan, and P. Wang, “Efficient dye-sensitized solar cells with an organic photosensitizer featuring orderly conjugated ethylenedioxythiophene and dithienosilole blocks,” *Chemistry of Materials*, vol. 22, no. 5, pp. 1915–1925, 2010.

[4] J.-M. Ji, H. Zhou, Y. K. Eom, C. H. Kim, and H. K. Kim, “14.2% efficiency dye-sensitized solar cells by co-sensitizing novel thieno[3,2-b]indole-based organic dyes with a promising porphyrin sensitizer,” *Advanced Energy Materials*, vol. 10, no. 15, p. 2000124, 2020. _eprint: https://onlinelibrary.wiley.com/doi/pdf/10.1002/aenm.202000124.

[5] R. Escalante, D. Pourjafari, D. Reyes-Coronado, and G. Oskam, “Dye-sensitized solar cell scale-up: Influence of substrate resistance,” *Journal of Renewable and Sustainable Energy*, vol. 8, no. 2, p. 023704, 2016.

[6] D. Joly, L. Pellejà, S. Narbey, F. Oswald, T. Meyer, Y. Kervella, P. Maldivi, J. N. Clifford, E. Palomares, and R. Demadrille, “Metal-free organic sensitizers with narrow absorption in the visible for solar cells exceeding 10% efficiency,” *Energy & Environmental Science*, vol. 8, no. 7, pp. 2010–2018, 2015.

[7] M. Godfroy, J. Liotier, V. M. Mwalukuku, D. Joly, Q. Huaulmé, L. Cabau, C. Aumaitre, Y. Kervella, S. Narbey, F. Oswald, E. Palomares, C. A. G. Flores, G. Oskam, and R. Demadrille, “Benzothiadiazole-based photosensitizers for efficient and stable dye-sensitized solar cells and 8.7% efficiency semi-transparent mini-modules,” *Sustainable Energy & Fuels*, vol. 5, no. 1, pp. 144–153, 2021. Publisher: Royal Society of Chemistry.

[8] D. Joly, L. Pellejà, S. Narbey, F. Oswald, J. Chiron, J. N. Clifford, E. Palomares, and R. Demadrille, “A robust organic dye for dye sensitized solar cells based on iodine/iodide electrolytes combining high efficiency and outstanding stability,” *Scientific Reports*, vol. 4, p. 4033, 2014.

[9] F. Sauvage, “A review on current status of stability and knowledge on liquid electrolyte-based dye-sensitized solar cells,” 2014-11-27. ISSN: 2356-6612 Pages: e939525 Publisher: Hindawi Volume: 2014.

[10] R. Harikisun and H. Desilvestro, “Long-term stability of dye solar cells,” *Solar Energy*, vol. 85, no. 6, pp. 1179–1188, 2011.

[11] A. Fakharuddin, R. Jose, T. M. Brown, F. Fabregat-Santiago, and J. Bisquert, “A perspective on the production of dye-sensitized solar modules,” *Energy & Environmental Science*, vol. 7, no. 12, pp. 3952–3981, 2014. Publisher: The Royal Society of Chemistry.

[12] S. Yoon, S. Tak, J. Kim, Y. Jun, K. Kang, and J. Park, “Application of transparent dye-sensitized solar cells to building integrated photovoltaic systems,” *Building and Environment*, vol. 46, pp. 1899–1904, 2011.

[13] Q. Huaulmé, V. M. Mwalukuku, D. Joly, J. Liotier, Y. Kervella, P. Maldivi, S. Narbey, F. Oswald, A. J. Riquelme, J. A. Anta, and R. Demadrille, “Photochromic dye-sensitized solar cells with light-driven adjustable optical transmission and power conversion efficiency,” *Nature Energy*, pp. 1–10, 2020.

[14] F. Fabregat-Santiago, G. Garcia-Belmonte, I. Mora-Seró, and J. Bisquert, “Characterization of nanostructured hybrid and organic solar cells by impedance spectroscopy,” *Physical Chemistry Chemical Physics*, vol. 13, no. 20, pp. 9083–9118, 2011.

[15] J. Idígoras, E. Guillén, F. J. Ramos, J. A. Anta, M. K. Nazeeruddin, and S. Ahmad, “Highly efficient flexible cathodes for dye sensitized solar cells to complement pt@TCO coatings,” *Journal of Materials Chemistry A*, vol. 2, no. 9, pp. 3175–3181, 2014.

[16] Y. Xie, P. Joshi, S. B. Darling, Q. Chen, T. Zhang, D. Galipeau, and Q. Qiao, “Electrolyte effects on electron transport and recombination at ZnO nanorods for dye-sensitized solar cells,” *J. Phys. Chem. C*, vol. 114, no. 41, pp. 17880–17888, 2010.

[17] T. Hoshikawa, T. Ikebe, R. Kikuchi, and K. Eguchi, “Effects of electrolyte in dye-sensitized solar cells and evaluation by impedance spectroscopy,” *Electrochimica Acta*, vol. 51, no. 25, pp. 5286–5294, 2006.

[18] Q. Wang, S. Ito, M. Gratzel, F. Fabregat-Santiago, I. Mora-Sero, J. Bisquert, T. Bessho, and H. Imai, “Characteristics of high efficiency dye-sensitized solar cells,” *Journal of Physical Chemistry B*, vol. 110, no. 50, pp. 25210–25221, 2006.

[19] Q. Wang, J.-E. Moser, and M. Grätzel, “Electrochemical impedance spectroscopic analysis of dye-sensitized solar cells,” *The Journal of Physical Chemistry B*, vol. 109, no. 31, pp. 14945–14953, 2005.

[20] J. Bisquert, “Theory of the impedance of electron diffusion and recombination in a thin layer,” *The Journal of Physical Chemistry B*, vol. 106, no. 2, pp. 325–333, 2002.

[21] J. A. Anta, J. Idígoras, E. Guillén, J. Villanueva-Cab, H. J. Mandujano-Ramírez, G. Oskam, L. Pellejà, and E. Palomares, “A continuity equation for the simulation of the current–voltage curve and the time-dependent properties of dye-sensitized solar cells,” *Physical Chemistry Chemical Physics*, vol. 14, no. 29, pp. 10285–10299, 2012.

[22] E. Guillén, L. M. Peter, and J. A. Anta, “Electron transport and recombination in ZnO-based dye-sensitized solar cells,” *J. Phys. Chem. C*, vol. 115, no. 45, pp. 22622–22632, 2011.

[23] S. R. Raga, E. M. Barea, and F. Fabregat-Santiago, “Analysis of the origin of open circuit voltage in dye solar cells,” *The Journal of Physical Chemistry Letters*, vol. 3, no. 12, pp. 1629–1634, 2012.

[24] J. Idígoras, L. Pellejà, E. Palomares, and J. A. Anta, “The redox pair chemical environment influence on the recombination loss in dye-sensitized solar cells,” *The Journal of Physical Chemistry C*, vol. 118, no. 8, pp. 3878–3889, 2014.

[25] L. M. Peter, “Characterization and modeling of dye-sensitized solar cells,” *Journal of Physical Chemistry C*, vol. 111, no. 18, pp. 6601–6612, 2007.

[26] D. Pourjafari, D. Reyes-Coronado, A. Vega-Poot, R. Escalante, D. Kirkconnell-Reyes, R. García-Rodríguez, J. A. Anta, and G. Oskam, “Brookite-based dye-sensitized solar cells: Influence of morphology and surface chemistry on cell performance,” *The Journal of Physical Chemistry C*, vol. 122, no. 26, pp. 14277–14288, 2018-07.

[27] J. Bisquert, A. Zaban, and P. Salvador, “Analysis of the mechanisms of electron recombination in nanoporous tio_2 dye-sensitized solar cells. nonequilibrium steady-state statistics and interfacial electron transfer via surface states,” *Journal of Physical Chemistry B*, vol. 106, no. 34, pp. 8774–8782, 2002.

[28] J. Bisquert and I. Mora-Seró, “Simulation of steady-state characteristics of dye-sensitized solar cells and the interpretation of the diffusion length,” *The Journal of Physical Chemistry Letters*, vol. 1, no. 1, pp. 450–456, 2010.

[29] J. Bisquert, “Chemical capacitance of nanostructured semiconductors: its origin and significance for nanocomposite solar cells,” *Physical Chemistry Chemical Physics*, vol. 5, no. 24, pp. 5360–5364, 2003.

[30] J. Bisquert, F. Fabregat-Santiago, I. Mora-Seró, G. Garcia-Belmonte, and S. Giménez, “Electron lifetime in dye-sensitized solar cells: Theory and interpretation of measurements,” *The Journal of Physical Chemistry C*, vol. 113, no. 40, pp. 17278–17290, 2009.

[31] J. Bisquert and V. S. Vikhrenko, “Interpretation of the time constants measured by kinetic techniques in nanostructured semiconductor electrodes and dye-sensitized solar cells,” *Journal of Physical Chemistry B*, vol. 108, no. 7, pp. 2313–2322, 2004.

[32] A. C. Fisher, L. M. Peter, E. A. Ponomarev, A. B. Walker, and K. G. U. Wijayantha, “Intensity dependence of the back reaction and transport of electrons in dye-sensitized nanocrystalline tio_2 solar cells,” *Journal of Physical Chemistry B*, vol. 104, no. 5, pp. 949–958, 2000.

[33] A. B. Walker, L. M. Peter, K. Lobato, and P. J. Cameron, “Analysis of photovoltage decay transients in dye-sensitized solar cells,” *Journal of Physical Chemistry B*, vol. 110, no. 50, pp. 25504–25507, 2006.

[34] J. Villanueva-Cab, H. Wang, G. Oskam, and L. M. Peter, “Electron diffusion and back reaction in dye-sensitized solar cells: The effect of nonlinear recombination kinetics,” *The Journal of Physical Chemistry Letters*, vol. 1, no. 4, pp. 748–751, 2010.

[35] J. R. Jennings, F. Li, and Q. Wang, “Reliable determination of electron diffusion length and charge separation efficiency in dye-sensitized solar cells,” *The Journal of Physical Chemistry C*, vol. 114, no. 34, pp. 14665–14674, 2010.

[36] A. Riquelme, F. E. Gálvez, L. Contreras-Bernal, H. Míguez, and J. A. Anta, “Internal quantum efficiency and time signals from intensity-modulated photocurrent spectra of perovskite solar cells,” *Journal of Applied Physics*, vol. 128, no. 13, p. 133103, 2020.

[37] L. Bertoluzzi and J. Bisquert, “Investigating the consistency of models for water splitting systems by light and voltage modulated techniques,” *The Journal of Physical Chemistry Letters*, vol. 8, no. 1, pp. 172–180, 2017.

[38] F. Brivio, A. B. Walker, and A. Walsh, “Structural and electronic properties of hybrid perovskites for high-efficiency thin-film photovoltaics from first-principles,” *APL Materials*, vol. 1, no. 4, p. 042111, 2013.

[39] J. Villanueva-Cab, J. A. Anta, and G. Oskam, “The effect of recombination under short-circuit conditions on the determination of charge transport properties in nanostructured photoelectrodes,” *Physical Chemistry Chemical Physics*, vol. 18, no. 4, pp. 2303–2308, 2016.

[40] L. Dloczik, O. Ileperuma, I. Lauermann, L. M. Peter, E. A. Ponomarev, G. Redmond, N. J. Shaw, and I. Uhlendorf, “Dynamic response of dye-sensitized nanocrystalline solar cells: Characterization by intensity-modulated photocurrent spectroscopy,” *The Journal of Physical Chemistry B*, vol. 101, no. 49, pp. 10281–10289, 1997.

[41] L. Bertoluzzi and S. Ma, “On the methods of calculation of the charge collection efficiency of dye sensitized solar cells,” *Physical Chemistry Chemical Physics*, vol. 15, no. 12, pp. 4283–4285, 2013.

Chapter 5

Internal quantum efficiency and time signals from intensity-modulated photocurrent spectra of perovskite solar cells

Abstract

This Chapter proposes a simplified procedure to analyze IMPS data in MHPs based on the analysis of the IQE and the time signals featured in the frequency spectra. This procedure attends to the change of each signal when optical excitation wavelength, photon flux, or temperature are varied for an archetypical $MAPbI_3$ *PSC. It includes fundamental analysis using DD modeling and a comparison with relatively more uncomplicated DSSCs with viscous and non-viscous electrolytes to gain understanding on the origin of the three signals appearing in MHP cells and the measurement of the internal quantum efficiency.*

This Chapter is based on Publication 2 of this Thesis: Antonio J. Riquelme *et al.* Journal of Applied Physics. 2020, 128, 133103.

5.1 Introduction

As it was described in *Chapter* 1, the advent of MHPs[1,2] has revolutionized the third generation PVs. In *Chapter* 2 the mixed electronic and ionic properties[3] of this semiconductor were explained. The outstanding PCE achieved by this type of materials is the result of the combination of good light harvesting properties and relatively slow recombination, which pushes the OCP of MHPs close to their radiative limit[4–7] presented in *Chapter* 2. As described in *Chapter* 3, IMPS is an optoelectronic characterization technique in which the photocurrent response of a photoelectrochemical system is measured as a function of a small optical perturbation in light intensity[8,9], allowing for the determination of the wavelength and frequency-dependent EQE and IQE. As it was mentioned in *Chapter* 3, both quantum efficiencies are connected through the optical properties of the device following Eq.3.9. This IQE is often identified with the solar cell's charge collection efficiency (CCE), defined as the ratio between the extracted carriers at the contacts and the photogenerated free carriers in the active layer. In fact, both magnitudes can be considered equivalent if exciton dissociation following photon absorption is quantitative. The relatively low exciton binding energies reported for MHPs indicate that this is the case at room temperature[6,10]. Thus, for the sake of simplicity, in this *Chapter* the term IQE is used to refer to both. In *Chapter* 3 two ways to determine the IQE widely used for DSSCs and related devices[11] were provided through Eqs. 3.27 and 3.28. In this context, Bertoluzzi and Ma[12] discussed that these expressions are only strictly valid for the straightforward case of linear recombination kinetics or in the limit of very long diffusion lengths. Bearing this in mind, only a DD numerical model that explicitly considers the kinetics of transport (via diffusion coefficients) and recombination (via rate constants) would provide a direct link with IQE[13,14]. For this reason, the single-layer DD model described in *Chapter* 3 has been applied to this study. As an additional complication, the measurement of true carrier lifetimes from electrical methods is subject to uncertainties as the capacitive discharge time decay tends to dominate the signal when the active layer is very thin, which is actually the case in a very strong absorbing material like a MHP[15]. This is a particularly worrying problem in small perturbation measurements of PSCs[16,17]. To this matter, small-perturbation techniques pose the advantage that being perturbation small, the response is linear (as can be deduced from Lissajous plots explained in *Chapter* 3), and a single characteristic time can be defined. This way, as explained in *Chapter* 3, through Eq.3.26, it is possible to relate the IMPS response to the differential quantum efficiency at a given wavelength and modulation frequency. Finally, the frequency dependence of these spectra allows for studying the kinetics of different processes taking place within the solar device, as explained in *Chapter* 3. This usefulness relies on matching excitation frequency with characteristic time constants of the system. The time constants provide kinetic information from the spectrum. In any case, a fully equipped kinetic model, including transport, recombination, and charge transfer terms, is needed to extract that information.

5.2 Fabrication and characterization of devices

In this *Chapter*, the IMPS characterization technique introduced in *Chapter* 3 with the experimental setup described in that *Chapter* was used at SC to analyze a set of PSCs and DSSCs using monochromatic illumination (465 nm (blue) and 630 nm (red)). The optical absorption properties of the PV devices to convert the EQE values into IQE were extracted via UV-Vis characterization of the films, as explained in *Chapter* 3. As numerical method, the single-layer DD detailed in the same *Chapter* was applied to rationalize the data obtained from the IMPS measurements. A web-based version of this single-layer DD model can be found in `https://solarsoft.upo.es`. The electron and hole lifetimes (τ_n and τ_p) were set to 90 ns to reproduce the V_{OC}. This value compares very well to the reported experimental data[18], as derived from photoluminescent decay transients at light intensities of the order of those considered in this *Chapter*. On the other hand, the diffusion coefficients for both electrons and holes were set to 1–5 $\text{cm}^2 \cdot \text{s}^{-1}$ [18,19]. The optical absorption coefficients introduced in the model were extracted from Figure B.1. In the calculation, a density of states of $4 \cdot 10^{18}$ cm^{-3}, a E_g of 1.55 eV and a relative permittivity of 24.1 were considered[20–22]. The PSCs prepared for this study followed the scheme described in *Chapter* 2 with the FTO/TiO_2(c)/TiO_2(mp)/$MAPbI_3$/spiro-OMeTAD/Au architecture[23–25]. To compare and highlight the analogies and differences between the two types of solar cells, DSSC devices with ACN-based electrolyte (non-viscous) and ionic liquid electrolyte (viscous) were also prepared and characterized. Further detail on the preparation process of both types of devices can be found in *Appendix* B.

5.3 Results and discussion

5.3.1 IMPS spectra of PSCs and DSSCs

Two complications arise from the analysis of Eq. 3.26 in PSCs:

1. The capacitive-discharging response of the system, which can overshadow the detection of kinetic constants relevant to solar cell functioning.
2. The ionic motion and cell degradation that affects the response at low frequencies and makes the interpretation of the results difficult.

In addition, a technical problem is also present in many published results. The extraction of differential IQE relies on a careful determination of excess illumination intensity and the absorption coefficient for each wavelength.

Many experimental setups estimate the light intensity from the electrical current running through the LED used to illuminate the cell, and the optical perturbation is applied via a small change in the current powering the LED. A typical mistake is to assume that this light intensity output-current relationship in the LED is linear when it is not. This issue requires a careful calibration of LED for each wavelength and the same amount of light perturbation required in the experiment, as described in *Chapter* 3. The optical absorption spectrum of $MAPbI_3$ and the N719 DSSC, included in this *Chapter* can be found in Figure B.1 in *Appendix* B. From these spectra, the absorption coefficient at a given wavelength for the perovskite can be extracted, resulting in $6.5 \cdot 10^4$ cm^{-1} at 465 nm (blue light) and $2.1 \cdot 10^4$ cm^{-1} at 630 nm (red light), respectively. According to the Lambert-Beer law, the optical penetration of blue light is approximately three times shorter than red light. This actually corresponds to 200 nm and 500 nm, respectively[26]. Once the absorption coefficient and calibration are available, it is possible to produce IQE data as a function of frequency for a given DC illumination and temperature. It is important to point out that in this *Chapter* the analysis is restricted to monochromatic light and relatively low light intensities (up to $\sim$ 14 $mW \cdot cm^{-2}$ for blue and $\sim$ 6.6 $mW \cdot cm^{-2}$ for red illumination). However, these light intensities, equivalent to 2.64 and 2.58 $mA \cdot cm^{-2}$ in photon current per area units, still produce V_{OC} close to the one sun AM1.5 equivalent value of $V_{OC} \sim 1$ V as can be observed in Figure B.2. This means that the measurement conditions approach the electrochemical bias acting in the solar cell under operation conditions. At the same time, working with lower light intensities improves the linearity and stability of the measurement at low frequencies, as can be deduced from Figure B.3 in *Appendix* B, which is crucial for the reliability of the data, as explained in *Chapter* 3. Alternatively, a method to improve the stability of the measurement at low frequencies has also been recently published[27].

As it was described in *Chapter* 3, IMPS is usually represented using complex numbers in Nyquist, Bode, and Cole-Cole plots. Slow transport produces a negative contribution to differential quantum efficiency with an arc in the first quadrant of the Nyquist plot or a positive peak in the Cole-Cole plot. The frequency position of the peak makes it possible to obtain the carrier diffusion coefficient and the diffusion length in the active layer using a simple diffusion model, similarly to how was described for DSSCs[28,29] in *Chapters* 3 and 4. A negative contribution to the IQE can also be originated by capacitive processes as discussed by Ravishankar *et al.*[30] for PSCs or by ion-mediated processes as discussed below. In Figure 5.1, IMPS spectra of $MAPbI_3$ PSCs of $\sim$15% PCE at one sun are reported at varying illumination stationary baseline intensities and with blue and red light. These cells can be considered state-of-the-art for $MAPbI_3$ cells with TiO_2 contacts fabricated outside glovebox[24]. The maximum light intensities studied in this *Chapter* for both wavelengths correspond to a one sun AM1.5 equivalent $V_{OC} \sim 1$ V.

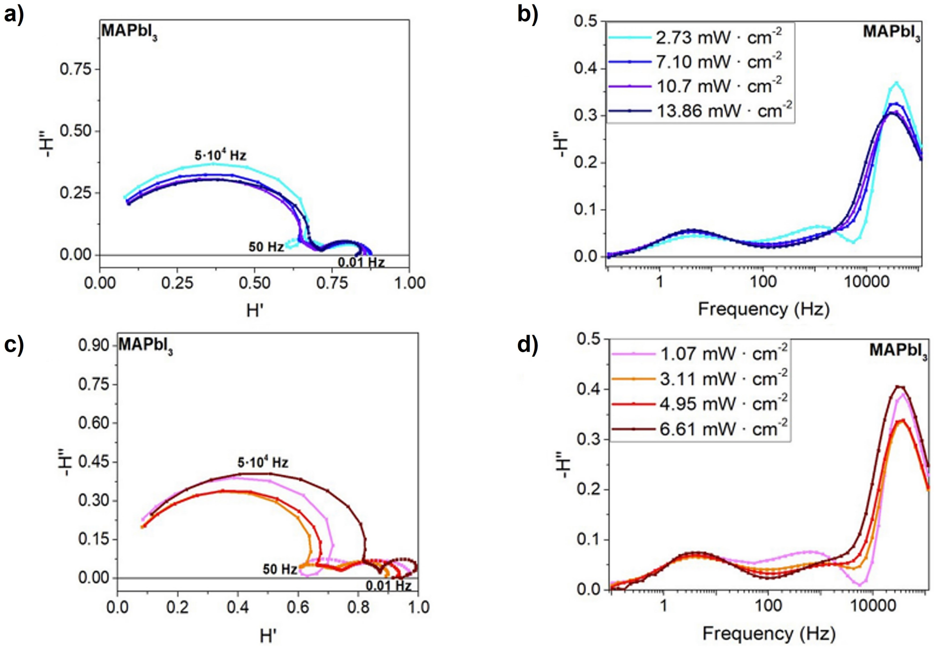

Figure 5.1: Nyquist ((a) and (c)) and Cole-Cole ((b) and (d)) plots of the IMPS response (frequency-dependent differential IQE) of MAPbI$_3$ solar cells with blue ((a) and (b)) and red ((c) and (d)) illumination. The light intensity perturbation is 10% of the baseline (DC) illumination. Maximum light intensities for each wavelength correspond to one sun AM1.5 $V_{OC} \sim 1$ V.

For the sake of comparison, in Figure 5.2 IMPS spectra of reference DSSC devices with both ACN-based and ionic liquid-based electrolyte (100% Pyr) are presented.

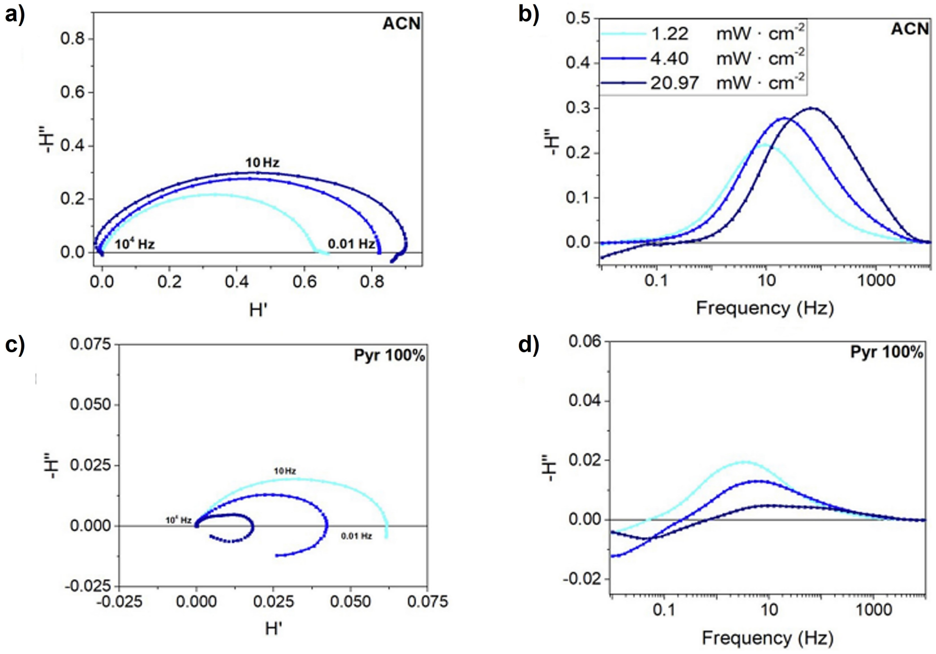

Figure 5.2: Nyquist ((a) and (c)) and Cole-Cole ((b) and (d)) plots of the IMPS response (frequency dependent differential IQE) of reference DSSC devices with an ACN-based ((a) and (b)) and ionic liquid based ((c) and (d)) electrolytes. Blue light illumination is used in both types of devices and the light intensity perturbation is 10% of the baseline (DC) illumination. Maximum light intensities for each wavelength correspond to one sun AM1.5 $V_{OC} \sim 1$ V.

There are substantial differences between the two types of devices. The spectra of $MAPbI_3$ cells are mainly characterized by three signals embodied as positive peaks in the Cole-Cole plot and arcs in the first quadrant of the Nyquist plot. An additional signal is connected to observing a loop at intermediate frequencies. In contrast, the ACN-based DSSC shows only one positive signal at mid frequencies, whereas the ionic liquid-based DSSC has an additional negative signal at low frequencies in the second quadrant of the Nyquist plot. The change in the spectra with light intensity is also quite distinct in the two devices. To interpret the signals in the $MAPbI_3$ cells, the single-layer DD model described in *Chapter* 3, inspired by that commonly used in DSSCs[28,29], is needed. A way toward developing this model is to look at the behavior of the signals for experimental control parameters, that is, excitation wavelength, photon flux, and temperature. Comparing both types of solar cells, which are deeply interlinked, as shown in *Chapter* 1, can also be extremely helpful.

5.3.2 Quantum efficiency in PSCs and DSSCs

As mentioned in *Chapter* 2, the LF limit of the IMPS transfer function modulus should recover the stationary value of the IQE. By looking at the LF limit of the Nyquist plots in Figure5.1a and c, it shows that this value is very close to a 100% collection efficiency, at all light intensities and for both blue and red light, in analogy with ACN-based electrolyte DSSCs (which are also known to have good IQE[31]), as observed in Figure 5.2.

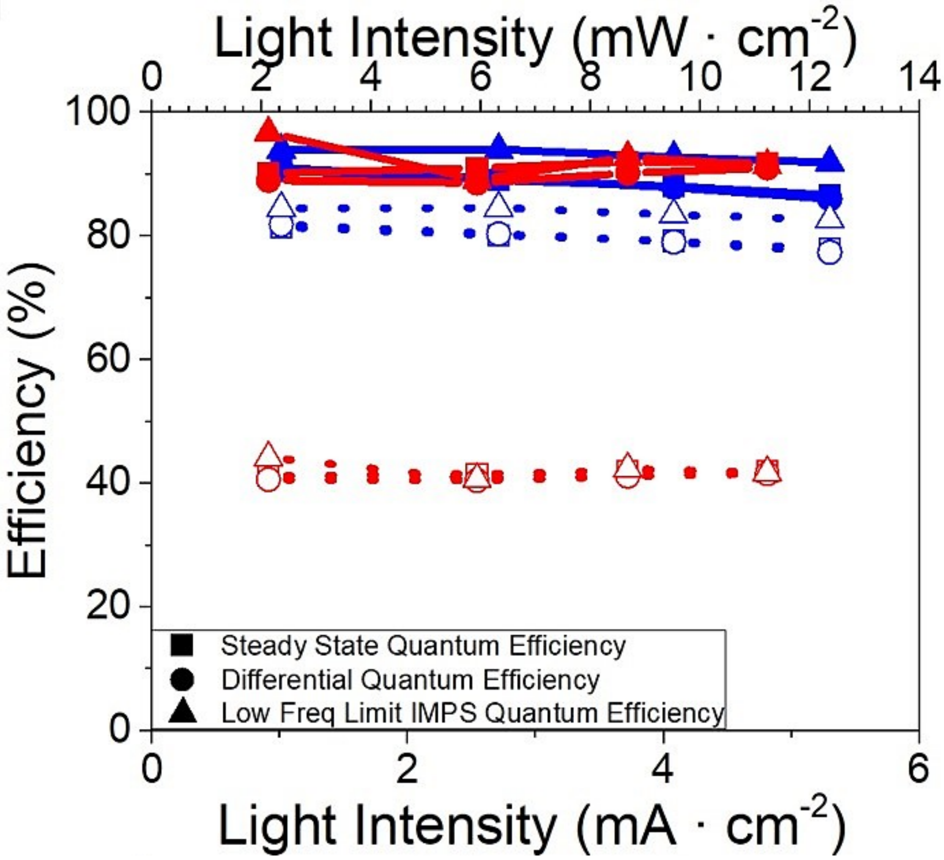

Figure 5.3: Stationary and differential EQE and IQE values with blue and red light for $MAPbI_3$ solar cells as a function of DC light intensity. Note that the DC light intensity is expressed both in units of electrical current: $q\Phi_0$ (bottom axis) and irradiance units (top axis). Lines are added to guide the eye (solid for IQE, dashed for EQE).

In Figure 5.3, the EQEs and IQEs are plotted as a function of light intensity for $MAPbI_3$ cells. In this figure, three alternative ways to estimate the IQE are presented:

1. A pure stationary value measured at constant illumination, as expressed in Eq. 3.9.

2. The ratio of the excess current to excess illumination, as a stationary version of Eq. 3.26.

3. The LF limit of the IMPS spectrum.

Figure 5.3 shows that the main loss factor in the EQE, especially at long wavelengths, is low absorption. Thus, 80% and 40% efficiencies with blue and red light are obtained. In contrast, the IQE is close to 100% in both cases, confirming that the conversion of absorbed photons into collected electrons at SC is nearly quantitative at all light intensities for $MAPbI_3$ cells. In accordance with the absorption coefficient extracted from Figure B.1 in *Appendix* B, blue light excitation generates more electron-hole pairs in the vicinity of the front contact, in comparison with the use of red light. All these results confirm that the effective diffusion length of carriers is very long[26] as it is typical of standard DSSCs[31].

Figure B.4 in *Appendix* B shows the *JV* curves and the predictions of the DD model for EQE and IQE for $MAPbI_3$ cells. The modeling predicts an IQE close to 100% for both blue and red light (the distinct values obtained for EQE are due to different absorption). Hence, experiment and modeling demonstrate unequivocally that collection is nearly quantitative regardless of the optical generation profile, illumination intensity, and perturbation size. In *Appendix* B, Figure B.5 extends this analysis to other lifetimes and electronic carrier diffusion coefficients. Lifetimes between 20 and 500 ns and diffusion coefficients above 1 $cm^2 \cdot s^{-1}$ lead to IQE values very close to 100%. These combinations correspond to diffusion lengths ranging between 1500 and 7000 nm, which is much longer than the active layer thickness (400 nm), as can be observed in Figure B.6 in *Appendix* B. Reducing the diffusion coefficient by two orders of magnitude can lower the IQE as low as 30%–40% but only if the lifetime is substantially reduced. Otherwise, the collection of charges remains nearly quantitative. Knowing that the lifetime is adjusted to reproduce the experimental V_{OC} and apparent ideality factor, this result demonstrates that, as long as recombination remains slow and its mechanism is unaltered, transport is not a critical factor in achieving a good IQE in PSCs.

5.3.3 Interpretation of IMPS time constants

To discuss the origin of the three signals observed in the PSC IMPS spectra in Figure 5.1 it is helpful to look at their variation as a function of light intensity and temperature as well the comparative behavior between the PSC and DSSC reference devices. All these results are collected in Figure 5.4.

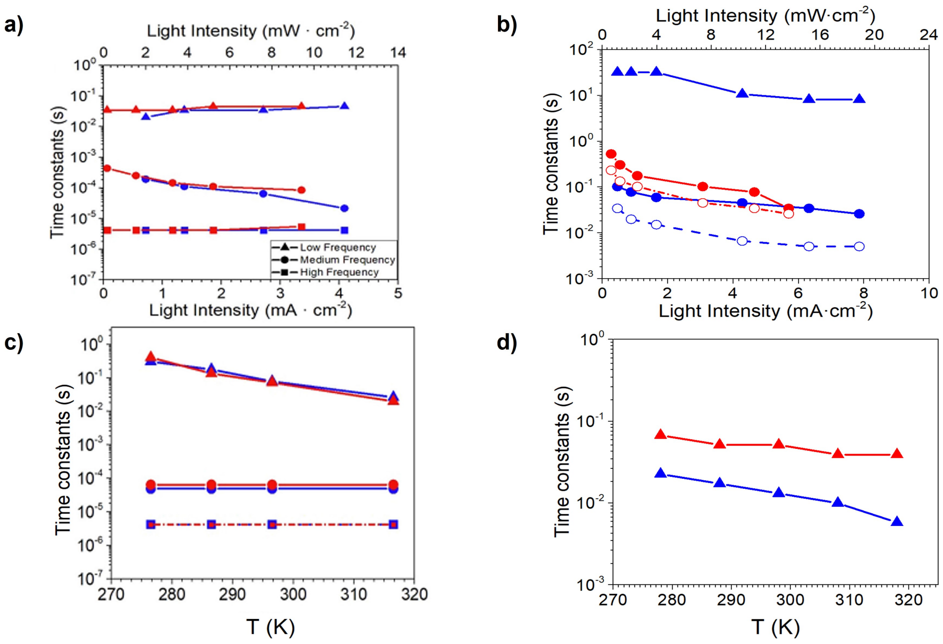

Figure 5.4: IMPS time constant (reciprocal of frequency peaks in Figures 5.1 and 5.2) for PSCs ((a) and (c)) and DSSC ((b) and (d)) as a function of DC light intensity ((a) and (b)) and temperature ((c) and (d)), with blue/red illumination. The illumination intensities in the temperature experiments were 2.64 and 2.58 mA·cm^{-2}, respectively. DSSC results included the device with (100% Pyr) ionic liquid electrolyte (solid lines) and ACN (dashed lines).

The measurements indicate that only the mid-frequency signal in the PSC shows some degree of dependence on light intensity or wavelength, a behavior typical to the two time signals detected in the DSSCs (one signal in the case of ACN based electrolyte DSSC). Regarding temperature, only the LF signal appears to change when the system is heated in the PSC, pointing to the presence of an activated kinetic process in the material, which accelerates as the temperature increases. Interestingly enough, the same thermal activation is observed in the DSSC with ionic liquid electrolyte, with similar activation energy (*vide infra*). It is interesting to see whether some of the signals would correspond to an IQE delay produced by the displacement of electrons and holes upon optical excitation. Figure 5.5 shows the result of a numerical "experiment," which consists in applying a small optical perturbation (10% of the stationary baseline illumination) and monitoring the resulting photocurrent transient. This analysis has previously been applied to DSSC devices[13,32]. It is easy to find that being the perturbation sufficiently small, the transient can be fitted to a single exponential (one time constant)

$$\frac{J(t)}{J_{max}} = 1 - b_0 \exp\left(-\frac{t-t_0}{t_{tr}}\right) \tag{5.1}$$

where b_0 is a numerical parameter, t_0 is the time in which perturbation is applied and t_{tr} is the "transport" time constant.

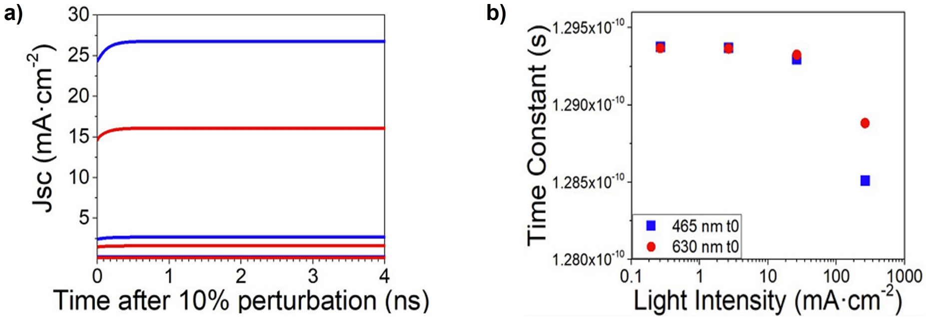

Figure 5.5: Photocurrent transients produced by a small perturbation (10% over the DC base light intensity) as predicted by the DD model (a). Light intensities used from top to bottom correspond to 26.4, 2.64 and 0.264 mW·cm^{-2} for blue light and 25.8, 2.58 and 0.258 mW·cm^{-2} for red light. Transport time constants extracted from the fit of the transients to Eq. 5.1 (b).

The transport time constants reported in Figure 5.5 show that transport gets accelerated as stationary illumination is increased and that the charge collection is also faster the more homogeneous is the optical generation profile (red), but only at relatively high light intensities. Nevertheless, most importantly, the numerical result predicts that for the same electron/hole diffusion coefficients and lifetimes that give the correct IQE and *JV* characteristics, the transport time constants show up at frequencies of the order of 10^{10} Hz, which is well beyond the frequency range accessible in the experiments, as mentioned in *Chapter* 3. Hence, the electron transport is too rapid in PSCs to be caught in a frequency modulated IQE experiment. This conclusion has also been reported by Ravishankar *et al*[33]. A straightforward analysis shows that the HF signal corresponds to the capacitive discharge of the geometrical capacitor formed by the perovskite active layer and the contacts[15,33]

$$\omega_{HF} = \frac{1}{R_S C_{geo}} \tag{5.2}$$

with R_S being the series resistance and C_{geo} the geometrical capacitance described in *Chapter* 3. The dielectric constant of $MAPbI_3$ is $\varepsilon_r = 24.1$, and the measured series resistance of the devices studied in this *Chapter* is $R_S \sim$ 10-25 Ω. For an area of 0.32 cm^2 and a thickness of $d \sim 400$ nm, Eq. 5.2 yields

$$f = \frac{\omega}{2\pi} \sim 3 \cdot 10^6 \tag{5.3}$$

However, as it was explained in *Chapters* 2 and 3, the C_{geo} calculated by Eq. 2.67 corresponds to a capacitor ideally flat, when the fact is that a certain roughness factor should be considered (of the order of 4 or 100 for a flat[16] and a mesoporous[34] device, respectively). As a matter of fact, geometrical capacitances (voltage-independent) of $\sim 10^{-7}$F have been measured in the devices studied herein[24]. Using this value, Eq. 5.2 produces $f = 5 \cdot 10^5$Hz, which is of the order of the position of the HF peak detected in the IMPS spectra. This feature, alongside the observation that the HF time constant does not vary with illumination, wavelength, or temperature, suggests that the HF signal arises from the delayed discharge of the geometrical capacitor formed by the perovskite layers and the contacts. This interpretation has also been put forward by Pockett *et al.*[16].

Attending now to the mid-frequency time constant, it is the only one that shows a clear dependence on the excitation wavelength and the light intensity (Figure 5.4) in both PSC and DSSCs. Furthermore, blue light excitation has a significantly different response with a shorter time constant. Knowing that blue photons penetrate 200 nm only, which is the approximate thickness of the mesoporous TiO_2 front layer, as can be observed in Figure B.6 of *Appendix* B. Thus, it can be inferred that this IMPS signal can be originated by electron transport in this mesoporous layer. This interpretation is supported by the fact that the light intensity dependence is very similar in both the PSC and DSSCs[29,35]. This behavior has already been explained in the literature by the multiple-trapping (MT) model[36,37]. This interpretation is confirmed by a study where the IMPS time constant is analyzed for different types of DSSCs sharing the same TiO_2 mesoporous layer[34]. The results show how the PSC and the ACN-based electrolyte DSSC share the same voltage and light intensity dependence, especially under blue light, where excitation in the mesoporous layer is more significant. In Table B.2 of *Appendix* B the slopes of the voltage and light intensity plots for both types of devices are collected, confirming the similarity of their trends. In addition, Figure B.7 in *Appendix* B presents numerical simulation of the mid-frequency time signal in the ACN based electrolyte DSSC using a linearized version of a diffusion-recombination model for electrons in the mesoporous TiO_2 layer[13,29,38]. The simulations show how the diffusion coefficient increases and its corresponding time constant decreases as the sample's exciting light intensity intensifies. Hence, the diffusion length remains approximately constant in agreement with the predictions of the multiple-trapping model.

In contrast to the other time constants, the LF time constant is the only one that shows a temperature dependence. This can be observed in Figures 5.4 and 5.6.

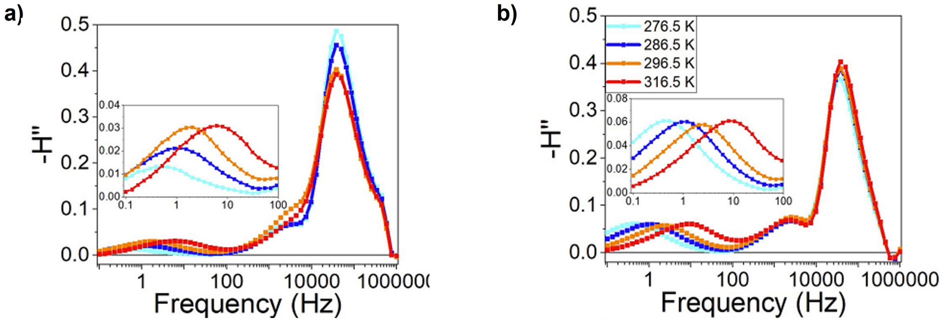

Figure 5.6: Temperature dependence of the frequency plots of the IMPS response (frequency dependent differential IQE) of a PSC with blue (a) and red (b) illumination. The light intensity perturbation is 10% of the baseline (DC) illumination.

In addition, an Arrhenius plot of the low frequency time constant vs temperature reveals activation behaviour with an activation energy of 46

(0.477) and 54 (0.56) kJ·mol^{-1} (eV) for blue and red light, respectively, as can be observed in Figure B.8 of *Appendix* B. Although the optical generation profile appears to have an effect, knowing that experiments with red light were carried out after those with blue light, a certain memory effect produced by the ions cannot be discarded. However, the devices demonstrate to be very stable after running the small-perturbation experiment, as revealed by the measurement of *JV* curves before and after the IMPS analysis in Figure B.9 in *Appendix* B. The important bit is that these activation energies are in the order of those inferred from ion-mediated phenomena[39,40]. Similar activation energy is observed in the ionic-liquid-based electrolyte DSSC reference devices. It is very important to stress that, in contrast to electronic high and mid-frequency signals, the LF time constant cannot be naively used to obtain ionic diffusion coefficients[39,41]. First, ions cannot be collected at the contacts, so they do not contribute directly to the IQE. It is more likely that the LF signal arises from a slow, ion-mediated capacitive process that indirectly affects electron collection[33]. As it was described in *Chapter* 2 and will be shown with more detail in *Chapter* 6, at low frequencies, the ions have enough time to migrate and charge/discharge the Debye layers (also called double layers or space charge layers) formed at the interfaces between the perovskite and the selective contacts. This change of the Debye layer alters the collection efficiency of the device and hence the IQE. Therefore, a shift in the LF signal toward higher/lower frequencies can be produced by an increase/decrease in the ionic diffusion coefficient. The same effect has also been described by Bernhardsgrütter and Schmid using DD modeling[14]. Suppression of ion migration has also been observed in the LF signal of impedance spectra[39,42].

Based on these considerations, it could be possible to estimate the frequency range in which the ion-induced signal would appear[43]. Taking an ion vacancy density (N_0)[3,44,45] of $1.6 \cdot 10^{25}$ m^{-3} and an ionic vacancy diffusion coefficient (D_{ion})[3,46] of $10^{-16}\mathrm{m}^{-2}\mathrm{s}^{-1}$, the following values of ionic conductivity and the corresponding resistance and ionic Debye layer capacitance[47] can be worked out

$$\sigma = \frac{q^2 N_0 D_{ion}}{k_B T} \approx 10^{-8}(\Omega m)^{-1} \longrightarrow R_{ion} = \left(\frac{\sigma A}{d}\right)^{-1} = 3 \cdot 10^6\ \Omega \quad (5.4)$$

$$C_{ion} = \frac{A \varepsilon_r \varepsilon_0}{a} = 8 \cdot 10^{-6}\ F \longrightarrow \omega_{HF} = \frac{1}{R_{ion} \cdot C_{ion}} \sim 24\ Hz \quad (5.5)$$

being a ($\approx$ 1 nm) the approximate size of an ion (and also of the order of the Debye layer predicted by modeling in *Chapter* 6). The estimated value of 24 Hz ($f = \omega/2\pi \approx 4$ Hz) lies in the region where the temperature-dependent signal shows up in the IMPS spectra at room temperature for PSCs. Together with extracted “activation” energies, this finding points to the Debye layers' ion-mediated capacitive discharge process as the most likely origin of the LF signal. It is worth mentioning that the “activation” energies obtained from the IMPS temperature experiment are significantly larger than ion migration energy barriers obtained from DFT studies, although closer to ionic formation energy[40]. This suggests that the formation of ionic defects can also contribute to the signal. Since light absorption can contribute to this, this would explain the different activation energies obtained with blue and red light. On the other hand, ion densities some orders of magnitude lower to $10^{19}\mathrm{cm}^{-3}$ have been reported[48,49], but also faster diffusion coefficients[50]. Note that it is the $N_0 \cdot D_{ion}$ product that determines the position of the LF peak, which keeps, in any case, within the frequency range in which the LF signal is detected.

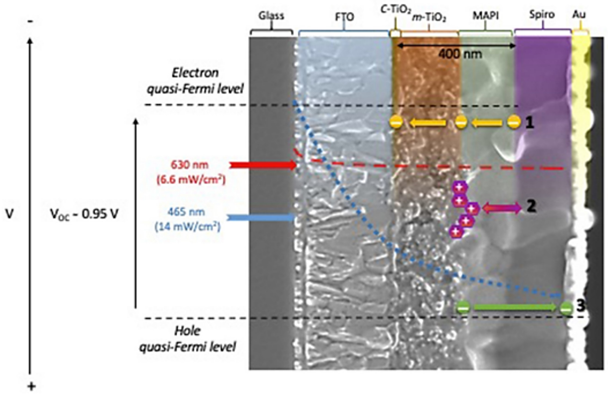

1. Electron transport in m-TiO$_2$: slow, 10^3 - 10^4 Hz (mid frequency signal in the IMPS spectrum. Wavelength dependent).

2. Ion charging/discharging at interfaces: very slow, 1 Hz (low frequency signal in the IMPS. Temperature dependet).

2-3. Electron-hole transport in perovskite: fast, 10^{10} Hz (not observed in the IMPS spectrum)

Figure 5.7: Cross-sectional image of the PSC studied in this *Chapter* together with a schematics of the energy levels and dynamical processes giving rise to the signals detected in the IMPS experiments. The red and blue dashed lines represent the optical generation profile under red and blue light illumination.

Finally, in Figure 5.7, a graphical interpretation of the origin of the three time constants is shown. This figure also illustrates how the electronic and ion-mediated processes can affect the frequency-dependent IQE of the devices.

5.4 Conclusion

In this *Chapter* a comprehensive study of the IQE and the IMPS spectra of MAPbI$_3$ PSC has been done. This was based on analyzing the three time signals appearing at low, mid, and high frequencies. The experimental data have been analyzed as a function of light intensity, frequency, optical generation profile (excitation wavelength), and temperature. This *Chapter* includes three alternative ways of measuring the IQE (stationary, differential, and LF limit of IMPS response), which leads to the same results, close to 100%. This result is kept at all light intensities studied herein, at two wavelengths and temperatures at 270-320 K intervals. This unequivocally shows that the effective diffusion length of electrons and holes is well above the thickness of the active layer for a state-of-the-art $MAPbI_3$ PSC. Second, the three time constants in the IMPS spectrum are identified. Previous literature results of the HF signal not being an electron transport but the electronic discharge of the geometrical capacitor formed by the perovskite and the contacts are confirmed . In addition, the mid-frequency and the LF signals are attributed to electron transport in the TiO_2 mesoporous layer and the ion-mediated capacitive discharge, respectively.

Bibliography

[1] H. J. Snaith, “Perovskites: The emergence of a new era for low-cost, high-efficiency solar cells,” *The Journal of Physical Chemistry Letters*, vol. 4, no. 21, pp. 3623–3630, 2013-11.

[2] N.-G. Park, “Organometal perovskite light absorbers toward a 20% efficiency low-cost solid-state mesoscopic solar cell,” *The Journal of Physical Chemistry Letters*, vol. 4, no. 15, pp. 2423–2429, 2013-08.

[3] C. Eames, J. M. Frost, P. R. F. Barnes, B. C. O’Regan, A. Walsh, and M. S. Islam, “Ionic transport in hybrid lead iodide perovskite solar cells,” *Nature Communications*, vol. 6, p. 7497, 2015-06.

[4] G. Xing, N. Mathews, S. Sun, S. S. Lim, Y. M. Lam, M. Grätzel, S. Mhaisalkar, and T. C. Sum, “Long-range balanced electron- and hole-transport lengths in organic-inorganic CH3nh3pbi3,” *Science*, vol. 342, no. 6156, pp. 344–347, 2013.

[5] S. D. Stranks, G. E. Eperon, G. Grancini, C. Menelaou, M. J. P. Alcocer, T. Leijtens, L. M. Herz, A. Petrozza, and H. J. Snaith, “Electron-hole diffusion lengths exceeding 1 micrometer in an organometal trihalide perovskite absorber,” *Science*, vol. 342, no. 6156, pp. 341–344, 2013.

[6] J. S. Manser, J. A. Christians, and P. V. Kamat, “Intriguing optoelectronic properties of metal halide perovskites,” *Chemical Reviews*, vol. 116, no. 21, pp. 12956–13008, 2016-06.

[7] W. Tress, “Perovskite solar cells on the way to their radiative efficiency limit – insights into a success story of high open-circuit voltage and low recombination,” *Advanced Energy Materials*, vol. 7, no. 14, p. 1602358, 2017-07.

[8] E. A. Ponomarev and L. M. Peter, “A generalized theory of intensity modulated photocurrent spectroscopy (IMPS),” *Journal of Electroanalytical Chemistry*, vol. 396, no. 1, pp. 219–226, 1995.

[9] D. Vanmaekelbergh and P. E. de Jongh, “Electron transport in disordered semiconductors studied by a small harmonic modulation of the steady state,” *Physical Review B*, vol. 61, no. 7, p. 4699, 2000.

[10] K. Galkowski, A. Mitioglu, A. Miyata, P. Plochocka, O. Portugall, G. E. Eperon, J. T.-W. Wang, T. Stergiopoulos, S. D. Stranks, H. J. Snaith, and R. J. Nicholas, “Determination of the exciton binding energy and effective masses for methylammonium and formamidinium lead tri-halide perovskite semiconductors,” *Energy & Environmental Science*, vol. 9, no. 3, pp. 962–970, 2016.

[11] G. Schlichthorl, N. G. Park, and A. J. Frank, “Evaluation of the charge-collection efficiency of dye-sensitized nanocrystalline TiO2 solar cells,” *Journal of Physical Chemistry B*, vol. 103, no. 5, pp. 782–791, 1999.

[12] L. Bertoluzzi and S. Ma, “On the methods of calculation of the charge collection efficiency of dye sensitized solar cells,” *Physical Chemistry Chemical Physics*, vol. 15, no. 12, pp. 4283–4285, 2013.

[13] J. A. Anta, J. Idígoras, E. Guillén, J. Villanueva-Cab, H. J. Mandujano-Ramírez, G. Oskam, L. Pellejà, and E. Palomares, “A continuity equation for the simulation of the current–voltage curve and the time-dependent properties of dye-sensitized solar cells,” *Physical Chemistry Chemical Physics*, vol. 14, no. 29, pp. 10285–10299, 2012.

[14] D. Bernhardsgrütter and M. M. Schmid, “Modeling of intensity-modulated photocurrent/photovoltage spectroscopy: Effect of mobile ions on the dynamic response of perovskite solar cells,” *The Journal of Physical Chemistry C*, vol. 123, no. 50, pp. 30077–30087, 2019-12.

[15] D. Kiermasch, A. Baumann, M. Fischer, V. Dyakonov, and K. Tvingstedt, “Revisiting lifetimes from transient electrical characterization of thin film solar cells; a capacitive concern evaluated for silicon, organic and perovskite devices,” *Energy & Environmental Science*, vol. 11, no. 3, pp. 629–640, 2018-03.

[16] A. Pockett, G. E. Eperon, T. Peltola, H. J. Snaith, A. Walker, L. M. Peter, and P. J. Cameron, “Characterization of planar lead halide perovskite solar cells by impedance spectroscopy, open-circuit photovoltage decay, and intensity-modulated photovoltage/photocurrent spectroscopy,” *The Journal of Physical Chemistry C*, vol. 119, no. 7, pp. 3456–3465, 2015-02.

[17] A. Guerrero, G. Garcia-Belmonte, I. Mora-Sero, J. Bisquert, Y. S. Kang, T. J. Jacobsson, J.-P. Correa-Baena, and A. Hagfeldt, “Properties of contact and bulk impedances in hybrid lead halide perovskite solar cells including inductive loop elements,” *The Journal of Physical Chemistry C*, vol. 120, no. 15, pp. 8023–8032, 2016-04.

[18] C. Wehrenfennig, G. E. Eperon, M. B. Johnston, H. J. Snaith, and L. M. Herz, “High charge carrier mobilities and lifetimes in organolead trihalide perovskites,” *Advanced Materials*, vol. 26, no. 10, pp. 1584–1589, 2014-03.

[19] C. C. Stoumpos, C. D. Malliakas, and M. G. Kanatzidis, “Semiconducting Tin and Lead Iodide Perovskites with Organic Cations: Phase Transitions, High Mobilities, and Near-Infrared Photoluminescent Properties,” *Inorganic Chemistry*, vol. 52, pp. 9019–9038, Aug. 2013. Publisher: American Chemical Society.

[20] Y. Zhou and A. Gray-Weale, “A numerical model for charge transport and energy conversion of perovskite solar cells,” *Physical Chemistry Chemical Physics*, vol. 18, no. 6, pp. 4476–4486, 2016-02.

[21] J. M. Frost, K. T. Butler, and A. Walsh, “Molecular ferroelectric contributions to anomalous hysteresis in hybrid perovskite solar cells,” *APL Materials*, vol. 2, no. 8, p. 081506, 2014-08.

[22] F. Brivio, A. B. Walker, and A. Walsh, “Structural and electronic properties of hybrid perovskites for high-efficiency thin-film photovoltaics from first-principles,” *APL Materials*, vol. 1, no. 4, p. 042111, 2013.

[23] L. Contreras-Bernal, C. Aranda, M. Valles-Pelarda, T. T. Ngo, S. Ramos-Terrón, J. J. Gallardo, J. Navas, A. Guerrero, I. Mora-Seró, J. Idígoras, and J. A. Anta, “Homeopathic perovskite solar cells: Effect of humidity during fabrication on the performance and stability of the device,” *The Journal of Physical Chemistry C*, 2018-02.

[24] L. Contreras-Bernal, S. Ramos-Terrón, A. Riquelme, P. P. Boix, J. Idígoras, I. Mora-Seró, and J. A. Anta, “Impedance analysis of perovskite solar cells: a case study,” *Journal of Materials Chemistry A*, vol. 7, no. 19, pp. 12191–12200, 2019-05.

[25] L. Contreras-Bernal, A. Riquelme, J. J. Gallardo, J. Navas, J. Idigoras, and J. A. Anta, “Dealing with climate parameters in the fabrication of perovskite solar cells under ambient conditions,” *ACS Sustainable Chemistry & Engineering*, 2020-04.

[26] L. Contreras-Bernal, M. Salado, A. Todinova, L. Calio, S. Ahmad, J. Idígoras, and J. A. Anta, “Origin and whereabouts of recombination in perovskite solar cells,” *The Journal of Physical Chemistry C*, vol. 121, no. 18, pp. 9705–9713, 2017.

[27] S. Ravishankar, M. Garcia-Batlle, J. Bisquert, G. Garcia-Belmonte, J. Odrobina, and C.-A. Schiller, “Removing instability-caused low-frequency features in small perturbation spectra of perovskite solar cells,” *The Journal of Physical Chemistry C*, vol. 124, no. 29, pp. 15793–15799, 2020-07.

[28] J. Halme, “Linking optical and electrical small amplitude perturbation techniques for dynamic performance characterization of dye solar cells,” *Physical Chemistry Chemical Physics*, vol. 13, no. 27, p. 12435, 2011.

[29] L. Dloczik, O. Ileperuma, I. Lauermann, L. M. Peter, E. A. Ponomarev, G. Redmond, N. J. Shaw, and I. Uhlendorf, “Dynamic response of dye-sensitized nanocrystalline solar cells: Characterization by intensity-modulated photocurrent spectroscopy,” *The Journal of Physical Chemistry B*, vol. 101, no. 49, pp. 10281–10289, 1997.

[30] S. Ravishankar, A. Riquelme, S. K. Sarkar, M. Garcia-Batlle, G. Garcia-Belmonte, and J. Bisquert, “Intensity-modulated photocurrent spectroscopy and its application to perovskite solar cells,” *The Journal of Physical Chemistry C*, vol. 123, no. 41, pp. 24995–25014, 2019.

[31] M. Grätzel, “Conversion of sunlight to electric power by nanocrystalline dye-sensitized solar cells,” *Journal of Photochemistry and Photobiology A: Chemistry*, vol. 164, no. 1, pp. 3–14, 2004-06.

[32] J. Villanueva-Cab, J. A. Anta, and G. Oskam, “The effect of recombination under short-circuit conditions on the determination of charge transport properties in nanostructured photoelectrodes,” *Physical Chemistry Chemical Physics*, vol. 18, no. 4, pp. 2303–2308, 2016.

[33] S. Ravishankar, C. Aranda, S. Sanchez, J. Bisquert, M. Saliba, and G. Garcia-Belmonte, “Perovskite solar cell modeling using light- and voltage-modulated techniques,” *The Journal of Physical Chemistry C*, vol. 123, no. 11, pp. 6444–6449, 2019-03.

[34] A. Todinova, J. Idígoras, M. Salado, S. Kazim, and J. A. Anta, “Universal features of electron dynamics in solar cells with tio_2 contact: From dye solar cells to perovskite solar cells,” *The Journal of Physical Chemistry Letters*, vol. 6, no. 19, pp. 3923–3930, 2015.

[35] E. Guillén, L. M. Peter, and J. A. Anta, “Electron transport and recombination in ZnO-based dye-sensitized solar cells,” *J. Phys. Chem. C*, vol. 115, no. 45, pp. 22622–22632, 2011.

[36] J. A. Anta and V. Morales-Florez, “Combined effect of energetic and spatial disorder on the trap-limited electron diffusion coefficient of metal-oxide nanostructures,” *Journal of Physical Chemistry C*, vol. 112, no. 27, pp. 10287–10293, 2008.

[37] J. Bisquert, “Chemical diffusion coefficient of electrons in nanostructured semiconductor electrodes and dye-sensitized solar cells,” *Journal of Physical Chemistry B*, vol. 108, no. 7, pp. 2323–2332, 2004.

[38] J. Halme, K. Miettunen, and P. Lund, “Effect of nonuniform generation and inefficient collection of electrons on the dynamic photocurrent and photovoltage response of nanostructured photoelectrodes,” *The Journal of Physical Chemistry C*, vol. 112, no. 51, pp. 20491–20504, 2008-12.

[39] L. Contreras, J. Idígoras, A. Todinova, M. Salado, S. Kazim, S. Ahmad, and J. A. Anta, “Specific cation interactions as the cause of slow dynamics and hysteresis in dye and perovskite solar cells: a small-perturbation study,” *Physical Chemistry Chemical Physics*, vol. 18, no. 45, pp. 31033–31042, 2016-11.

[40] D. Meggiolaro, E. Mosconi, and F. De Angelis, “Formation of surface defects dominates ion migration in lead-halide perovskites,” *ACS Energy Letters*, vol. 4, no. 3, pp. 779–785, 2019-03.

[41] J.-P. Correa-Baena, M. Anaya, G. Lozano, W. Tress, K. Domanski, M. Saliba, T. Matsui, T. J. Jacobsson, M. E. Calvo, A. Abate, M. Grätzel, H. Míguez, and A. Hagfeldt, “Unbroken perovskite: Interplay of morphology, electro-optical properties, and ionic movement,” *Advanced Materials*, vol. 28, pp. 5031–5037, 2016-04.

[42] A. Mahapatra, N. Parikh, H. Kumari, M. K. Pandey, M. Kumar, D. Prochowicz, A. Kalam, M. M. Tavakoli, and P. Yadav, “Reducing ion migration in methylammonium lead tri-bromide single crystal via lead sulfate passivation,” *Journal of Applied Physics*, vol. 127, no. 18, p. 185501, 2020-05.

[43] D. Moia, I. Gelmetti, P. Calado, W. Fisher, M. Stringer, O. Game, Y. Hu, P. Docampo, D. Lidzey, E. Palomares, J. Nelson, and P. R. F. Barnes, “Ionic-to-electronic current amplification in hybrid perovskite solar cells: ionically gated transistor-interface circuit model explains hysteresis and impedance of mixed conducting devices,” *Energy & Environmental Science*, vol. 12, no. 4, pp. 1296–1308, 2019.

[44] A. Walsh, D. O. Scanlon, S. Chen, X. G. Gong, and S.-H. Wei, “Self-regulation mechanism for charged point defects in hybrid halide perovskites,” *Angewandte Chemie (International Ed. in English)*, vol. 54, no. 6, pp. 1791–1794, 2015-02.

[45] D. A. Jacobs, H. Shen, F. Pfeffer, J. Peng, T. P. White, F. J. Beck, and K. R. Catchpole, “The two faces of capacitance: New interpretations for electrical impedance measurements of perovskite solar cells and their relation to hysteresis,” *Journal of Applied Physics*, vol. 124, no. 22, p. 225702, 2018-12.

[46] A. Riquelme, L. J. Bennett, N. E. Courtier, M. J. Wolf, L. Contreras-Bernal, A. Walker, G. Richardson, and J. A. Anta, “Deducing the key physical properties of a perovskite solar cell from its impedance response: insights from drift-diffusion modelling,” *arXiv:2003.07386 [physics]*, 2020-03.

[47] G. Richardson, S. E. J. O’Kane, R. G. Niemann, T. A. Peltola, J. M. Foster, P. J. Cameron, and A. B. Walker, “Can slow-moving ions explain hysteresis in the current–voltage curves of perovskite solar cells?,” *Energy & Environmental Science*, vol. 9, pp. 1476–1485, 2016-02.

[48] L. Bertoluzzi, C. C. Boyd, N. Rolston, J. Xu, R. Prasanna, B. C. O’Regan, and M. D. McGehee, “Mobile ion concentration measurement and open-access band diagram simulation platform for halide perovskite solar cells,” *Joule*, vol. 4, no. 1, pp. 109–127, 2019.

[49] S. A. L. Weber, I. M. Hermes, S.-H. Turren-Cruz, C. Gort, V. W. Bergmann, L. Gilson, A. Hagfeldt, M. Graetzel, W. Tress, and R. Berger, “How the formation of interfacial charge causes hysteresis in perovskite solar cells,” *Energy & Environmental Science*, vol. 11, pp. 2404–2413, 2018.

[50] M. H. Futscher, J. M. Lee, L. McGovern, L. A. Muscarella, T. Wang, M. I. Haider, A. Fakharuddin, L. Schmidt-Mende, and B. Ehrler, “Quantification of ion migration in CH3nh3pbi3 perovskite solar cells by transient capacitance measurements,” *Materials Horizons*, vol. 6, no. 7, pp. 1497–1503, 2019-08.

Chapter 6

Identification of recombination losses and charge collection efficiency in a perovskite solar cell by comparing impedance response to a drift-diffusion model

Abstract

Interpreting the EIS of PSCs is significantly more challenging than for most other PV materials. This is for a variety of reasons, of which the most significant are the mixed ionic-electronic conduction properties of MHPs and the difficulty in fabricating stable and reproducible devices. The impedance response has commonly been analyzed in terms of sophisticated equivalent circuits that can be hard to relate to the underlying physics. This Chapter combines experiment and DD modeling of the cell's ion and charge carrier transport and recombination. This comparison shows that the HF response contains all the critical information relating to the steady-state performance of a PSC.

This Chapter is based on Publication 1 of this Thesis: Antonio J. Riquelme *et al.* Nanoscale. 2020, 12, 17385-17398.

6.1 Introduction

As it was described in *Chapter* 1, one of the most notable characteristics of MHPs is that they have a mixed ionic-electronic conduction character, stemming from the high mobility of ionic vacancies in the perovskite structure[1,2]. This material property appears to be related to their exceptional optoelectronic properties, in particular, to their excellent photovoltaic charge separation behaviour[3–5], but is also associated with their chemical instability[6]. Further improvements in efficiency and stability necessitate a better understanding of the molecular mechanisms determining PV conversion and degradation. Combined theoretical modeling and accurate optoelectronic characterization techniques are powerful tools in this context. As explained in *Chapter* 3, EIS has proven to be an indispensable tool for gaining insight into the physical behavior of solar cells and other photoelectrochemical devices and has been widely used to characterize organic solar cells and DSSCs[7]. The equivalent circuit, devised by Bisquert *et al.*[7–9] and described in *Chapter* 3 allows for extracting useful information about the electron dynamics of the device, such as diffusion coefficients, chemical capacitances, electron recombination lifetimes and diffusion lengths. However, the same degree of success has not been achieved for PSCs. This failure may be primarily attributed to two causes:

1. The problem is inherently more complex, involving the motion of both electronic (electrons and holes) and ionic charge carriers. The motions of these elements are associated with very different time scales, and they interact differently with the internal interfaces within the cell.
2. The chemical instability of many of the perovskite materials employed in these cells may lead to a lack of reproducibility of experimental data. In particular, the chemical instability of the perovskite can give rise to exotic features in the impedance spectra of a PSC that are not

> systematically observed in all configurations and, more frustratingly, may not be observed in all specimens of the same configuration.

The aforementioned complications associated with PSC physics means that, to date, no well-defined (in terms of underlying physical processes) simple model is to be found in the literature, although some linear equivalent circuits[10–13] have been proposed (see *Chapter* 3). Some more sophisticated models include additional elements and inductors in an attempt to reproduce exotic features such as loops and negative capacitances[14–17]. However, adding more elements to a given equivalent circuit does not necessarily aid in the interpretation of the measured response of the system, particularly if each equivalent circuit element does not have a well-defined physical meaning. Furthermore, the more elements added to a circuit, the more likely it is that an alternative equivalent circuit can be found that provides an identical response. This increases the ambiguity in the physical interpretation of circuit elements, and consequently, the utility of the equivalent circuit description is lost[18].

As explained in *Chapter* 3, DD models of solar cells provide an alternative (and more fundamental) way of understanding the system and its impedance response. The parameters included in DD models, such as diffusion coefficients, lifetimes, dielectric constants, doping densities, work functions, etc., have precise physical meanings. For this reason, a link between the microkinetic processes taking place in the solar cell and its macroscopic characteristics can more readily be established. DD models have successfully been used to simulate *JV* curves of a variety of PSCs and helped researchers to understand the origin of the hysteresis observed in many cases in terms of dynamic ionic redistribution throughout the voltage scan[19–25]. Recent developments include models that explicitly account for the influence of the selective contact materials on a cell's behaviour[22] and predictions of the response of the solar cell to small-signal perturbations in applied voltage and light intensity[26–28]. The latter area is the focus of this *Chapter*. In this context, Jacobs *et al.*[26] analyzed the apparent capacitance of PSCs and its relation to the hysteresis. They used DD modeling to demonstrate that ion-mediated recombination is behind the low frequency "giant" capacitance and the inductive loops observed in the EIS data. Moia *et al.*[27] also used DD modeling to understand the LF response in terms of the electronic coupling between ion and electronic motion at the interfaces. Meanwhile, Neukom *et al.*[29] were able to reproduce, within a single DD framework and with a single parameter set, a wide variety of experimental data for a specific PSC configuration (inverted architecture), including small-signal perturbation frequency-modulated experiments such as EIS at SC. Crucially, none of these works focused on the HF impedance response and how it can be used as a tool to deduce the physics associated with the all-important steady-state performance of the cell.

In this *Chapter* DD numerical simulations are used together with experimental EIS to elucidate how the fundamental properties that dictate the efficiency of a device can be extracted from the impedance response. It is shown that the three-layer ionic-electronic DD model described in *Chapter* 3 (*IonMonger*) can reproduce the main characteristics found in the impedance spectra (also described in the same *Chapter*) and provides a wide-ranging description of the EIS features that determine the PCE of PSC, noting that the main purpose of EIS measurements is to detect and quantify loss mechanisms in a particular device. This can only be achieved using a well-defined electrical model or if particular spectra features can be identified with particular loss mechanisms. In this *Chapter* SEC described in *Chapter* 3 is used to fit the numerical EIS data and to extract the resistances and capacitances associated with the high and LF signals. It is established which parts of the spectrum are required to quantify recombination and charge collection and the effects of the ionic subsystem on the spectrum is also discussed. Finally, it is shown how the essential properties of the PSC steady-state performance along with the *JV* curve are captured by the HF impedance response. In contrast, the LF impedance response is only associated with ion motion in the perovskite layer. However, the ionic distribution affects both the HF response and the apparent ideality factor. In this context, the insights from DD simulation of the impedance response are used to critically analyze the traditional interpretation of the V_{OC} and recombination resistances in terms of ideality factors. It is demonstrated that this should be reformulated for PSCs to consider the impact of the steady-state ionic distributions on recombination and collection. From this, it is also concluded that a comparison between the electrical properties of different devices should be made using HF impedance measurements performed in the steady-state voltage regime in which the cell is expected to operate.

6.2 Numerical and experimental methods

6.2.1 Numerical method

JV curves and impedance spectra are numerically simulated using the three-layer DD mode described in *Chapter* 3, used to reproduce a planar PSC with TiO_2 acting as ETL, $MAPbI_3$ as perovskite absorbing material and Spiro-OMeTAD as HTL. Within the perovskite layer, the recombination losses are assumed to occur *via* a combination of the bimolecular and SRH recombination mechanisms, considering for the standard set of parameters the recombination between the perovskite layer and the selective contacts to be negligible, for the sake of simplicity. The key model parameters are listed in Table C.1 of *Appendix* C with the source and justification of each value. To fit the DD simulation to the *JV* curve and impedance spectra of this particular experimental device, the changes in the parameter values are included in Table C.2 of the same *Appendix*. For simplicity, the parameters in both tables are chosen to ensure that bulk recombination is electron-limited and the perovskite is effectively p-type. Whether perovskites are n-type or p-type is a long debate and depends strongly on the substrate, the particular perovskite formulation and the preparation conditions[30,31] as was explained in *Chapter* 2. For the particular case studied in this *Chapter*, the disparity between the electron and hole quasi-lifetimes ($\tau_n = 100\tau_p$) and the disparity between the energy band offset at each interface (E_C - E_{FE} = 0.2 eV while E_{FH} - E_V = 0.18 eV), means that the electron density in the perovskite layer is relatively small and long-lived, compared to the hole density. Consequently, the recombination rate is limited by the electron density.

As can be noticed in Table C.1 of *Appendix* C, the "effective" doping density for the ETL and HTL is considered. This is for two reasons. Firstly, this DD model makes use of two simplifying assumptions[22]. The assumptions are:

1. The doping density in each transport layer equals the effective density of states in the relevant energy band.
2. The minority carrier density is negligible.

The result of the first assumption is that the conduction band energy in the ETL and the valence band energy in the HTL is equal to the Fermi level in each transport layer, respectively. In other words, it is assumed that the transport layers are sufficiently highly doped that they behave like "quasi-metals". However, it must be noted that this first assumption is incompatible with Boltzmann statistics. In this model, the Boltzmann approximation derives the perovskite/transport layer interface conditions, even though this approximation is not valid when the Fermi level approaches the conduction/valence band edge. Therefore, the value used here is only an "effective" doping density. The second reason is that this DD model is designed for a planar PSC in which charge transport is approximately one-dimensional, which means it does not take into account the mesoporous nature of the TiO_2 ETL. The chosen value is an estimate for the DoS of TiO_2 nanoparticles, which is assumed to be a good approximation for the DoS in the nanostructured TiO_2 electrodes used in this *Chapter*.

Simulated *JV* curves and impedance spectra are obtained using the same measurement protocol used in the experiment, described in the next section. To be consistent with the experiments, all *JV* curves were generated with a scan rate of 100 $mV \cdot s^{-1}$ after 20 seconds of pre-conditioning at 1.2 V. Impedance data were extracted for a 20 mV perturbation in the 0.01 - 10^6 Hz range. The illumination considered in both the *JV* curve generation and the EIS simulation was monochromatic blue light (465 nm) fixed at varying intensities in the 5 - 1000 $W \cdot m^{-2}$ range.

In both the simulation and the experiment (*vide infra*), two situations were considered for the EIS:

1. For a range of illumination intensities, the voltage was perturbed around the V_{OC} consistent with the applied illumination intensity, and the parameters are extracted, analyzed, and plotted as a function of the V_{OC}.
2. For fixed illumination intensity, the voltage was perturbed around a range of applied DC voltages, and the parameters were extracted, analyzed, and plotted as a function of the DC voltage. We refer to this "experiment" with the acronym NOC (Non Open Circuit conditions).

6.2.2 Experimental details

Numerical simulations are compared to experimental results taken from the literature[10–14,32,33] and to devices, with a regular configuration consisting on a compact TiO_2 layer, a mesoporous layer of the same material, $MAPbI_3$ perovskite as absorbing material and Spiro-OMeTAD. The fabrication process was the same as described in *Appendix* B for the PSCs studied in *Chapter* 5.

Experimental current-voltage characteristics of the devices were obtained, as described in *Chapter* 3, using a solar simulator (ABET-Sun2000) under 1000 W$\cdot$m^{-2} illumination with an AM1.5G filter. The light intensity was recorded using a reference monocrystalline silicon solar cell with temperature output (ORIEL, 91150). A metal mask was used to define an active area of 0.16 cm^2. The *JV* characteristics were then determined by applying an external potential bias to the cell and measuring the photocurrent using an Autolab/PGSTAT302N potentiostat with a scan rate of 100 mV $\cdot$ s^{-1} and a sweep delay of 20 s. A blue LED provided the illumination for the EIS measurements over a wide range of DC light intensities (10 - 500 W$\cdot$m^{-2}). As mentioned in the previous section, two types of EIS experiments were analyzed: at OC and NOC conditions[13]. In the latter case, the parameters are corrected for voltage drop arising from the induced DC and the corresponding series resistance. In both OC and NOC conditions, a 20 mV (peak) perturbation in the 10^{-2} - 10^6 Hz range was applied. A response analyzer module (PGSTAT302N/FRA2, Autolab) was utilized to analyze the frequency response of the devices.

6.3 Results and discussion

6.3.1 *JV* characteristics and impedance spectra shapes

Figure C.1 of *Appendix* C provides the experimental photovoltaic performance under simulated AM1.5G 1000 W$\cdot$m^{-2} illumination and optical absorption data of the device used to validate the model discussed in this *Chapter* and described in *Chapter* 3. The experimental *JV* curve yields a $V_{OC} > 1$ V and 15% average PCE. This performance is close to state-of-the-art values for TiO$_2$/MAPbI$_3$/Spiro-OMeTAD devices fabricated at ambient conditions[13,34]. Experimental and simulation results for this PSC under blue illumination, both steady-state and impedance, as obtained using the DD model are presented in Figure 6.1 and Figure C.2 of *Appendix* C.

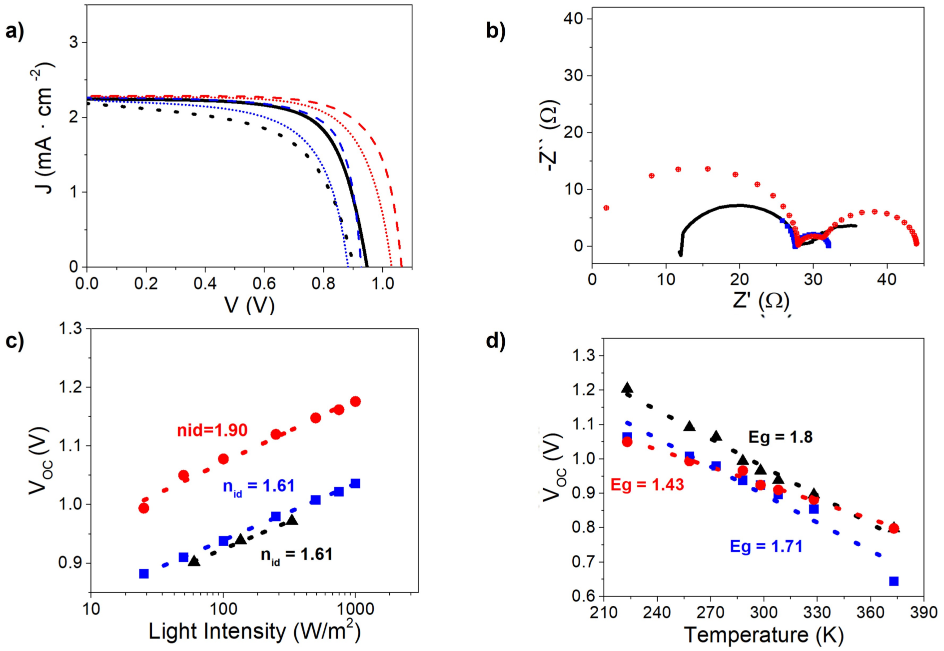

Figure 6.1: Experimental and simulated results under blue light illumination: (a) steady-state *JV* curves in forward (solid lines) and reverse (dashed lines) scans (b), impedance spectra at OC, (c) V_{OC} vs light-intensity including apparent ideality factors (d) V_{OC} vs temperature. Color code: black is experimental data, blue is DD simulation with parameters from Table C.2 in *Appendix* C. Red is DD simulation without surface recombination. In (c) dashed lines are linear fits to Eq. 2.25 extracting the apparent ideality factor. In (d) dashed lines are linear fits to Eq. 6.1 to extract E_g.

Numerical results confirm that the three-layer ionic-electronic DD model is capable of reproducing the *JV* characteristics, the hysteresis and the V_{OC} - ln (I) plot with an n_{AP} that is close to 2, as observed in many experimental reports for cells with a regular configuration[12,13,33,35,36]. Incorporation of surface recombination into the model enables better fitting to the *JV* curve of the particular device fabricated for this *Chapter* but reduces the value of the apparent ideality factor. Later in this *Chapter* it is shown how changing the ionic density while keeping the recombination mechanism unaltered results in a significant change to the apparent ideality factor. This is closely related to what was explained in *Chapter* 2 about ectypal and electronic ideality factors in PSCs. These concepts are also applied in *Chapters* 7 and 8. On the other hand, the modifications included in Table C.2 in *Appendix* C along with the introduction of surface recombination, allows for a perfect fit of the HF arc of the impedance spectrum. However, in the following, for the sake of simplicity in this *Chapter* the modeled spectra correspond to the standard set of parameters without surface recombination (Table C.1 of *Appendix* C).

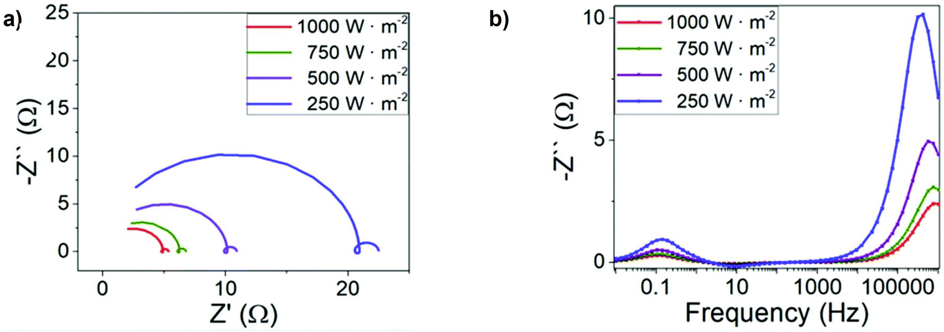

Figure 6.2: Simulated impedance spectra at OC conditions and variable illumination intensity for the parameters indicated in Table C.1 of *Appendix* C. (a) Nyquist plot and (b) Cole-Cole plot.

In Figure 6.2 the simulated impedance spectra for a standard cell configuration are presented. In Figure C.3 in *Appendix* C additional impedance spectra at lower light intensities for the same parameter set are presented. As usual for PSCs (see *Chapter* 3) two signals in the impedance spectra are obtained in the form of arcs in the Nyquist plot and peaks in the Cole-Cole plot. The HF peaks appear at frequencies around 10^5-10^6 Hz, whereas the LF peaks occur below 1 Hz. The shape of the spectra, the way it changes shape with modification of the illumination intensity, and the positions in the frequency domain of the maximum response are all consistent with what is typically seen in experimental impedance measurements of PSCs, in both regular and inverted configurations[10–14,18,32,33]. To confirm the generality of the model's predictions additional DD simulations for the inverted cell configuration studied by Neukom *et al.*[29] were carried out in Figure C.4 of *Appendix* C. With the same parameter set used by these authors, this DD model produces the same two signals with analogous behavior of the high and low frequency components.

6.3.2 High frequency and apparent ideality factor

Knowing that there are two well-defined frequency signals, the simplest (empirical) description is based on a Voight model with two RC elements in series (-(RC)-(RC)-), as described in *Chapter* 3. Alternatively, a "nested" arrangement can be used, which provides the same results[18]. Numerical values associated with the high and LF components of the resistance and the capacitance need to be extracted by fitting them to an EC. Note that this EC does not have any particular physical meaning. It is only an instrumental procedure to extract resistance and capacitance values from the two time signals observed in the simulated and the experimental spectra.

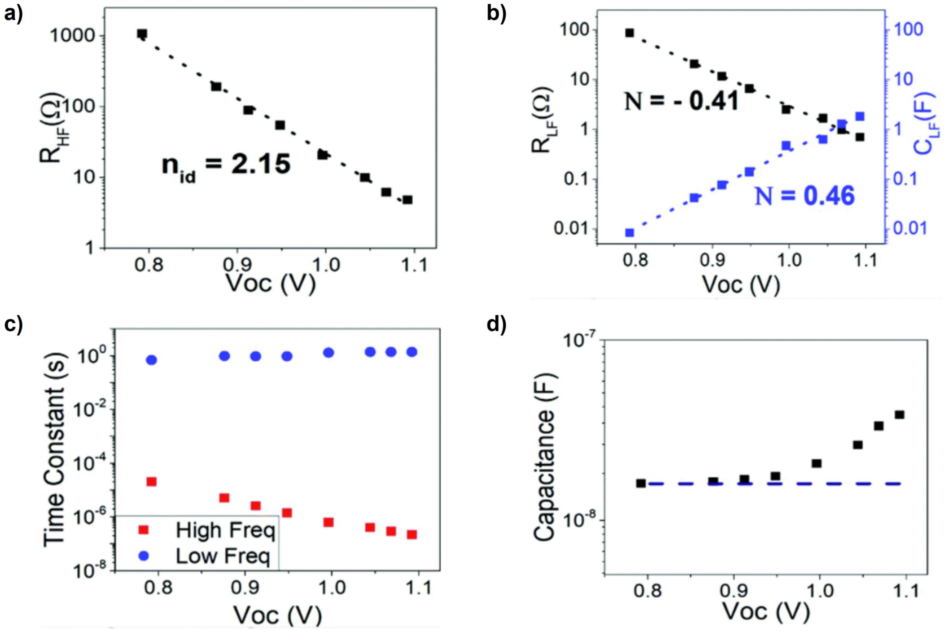

Figure 6.3: EC parameters from DD simulation of the impedance response for the parameters indicated in Table C.1 of *Appendix* C. (a) High-frequency resistance, with the dashed line a linear fit to Eq. 2.25 extracting the apparent ideality factor. (b) LF resistance and capacitance. Dashed lines are fits to Eqs. 6.2 and 6.3. (c) High and low frequency time constants as obtained from the frequency peaks in Cole-Cole plot. (d) High-frequency capacitance and theoretical value of the capacitance (dashed line) as predicted from Eq. 2.67.

Results from the simulations performed at V_{OC} and with no R_S are shown in Figure 6.3. In line with widely reported experimental trends[11–14,32,33], both high and low frequency resistances exhibit an exponential dependence on the V_{OC}, (which is function of the incident light intensity). However, in contrast to some reports[11,33], the slopes of $\ln(R_{HF})$ and $\ln(R_{LF})$, although similar, are not equal. In fact, as explained later in this *Chapter*, only the slope of $\ln(R_{HF})$ (the logarithm of the high frequency resistance) when plotted against V_{OC}/k_BT should be interpreted as the apparent ideality factor of the solar cell. Hence, in this *Chapter* it is claimed that $\ln(R_{LF})$ cannot be used to extract this ideality factor as inferred from previous works[11,33]. As described in *Chapter* 2, the most common method of determining the ideality factor of a PV devices is from a plot of the V_{OC} against the logarithm of the light intensity, using the relation Eq.2.20 (although as it has been explained in *Chapter* 2 this cannot be considered a pure ideality factor in PSCs). Notably, in the simulations conducted for this *Chapter*, these two ways of computing the "ideality factor" yield the same result. The same is confirmed by the experiments as, for example, reported on for TiO_2(c)/TiO_2(mp)/$MAPbI_3$/Spiro-OMeTAD devices[12,13]. Using basic semiconductor theory[12,37] it can be easily shown that imposing OC conditions to Eq.2.25 in *Chapter* 2 the V_{OC} can be expressed as

$$V_{OC} = \frac{E_g}{q} - \frac{n_{AP} k_B T}{q} \ln\left(\frac{J_0}{qdG}\right) \tag{6.1}$$

This relation also predicts a linear dependence of V_{OC} vs absolute temperature (as shown in Figure 6.1), with V_{OC} being E_g when $T \longrightarrow 0$ K. This is another common experimental result[12,35,38] and is also approximately reproduced by the DD numerical simulation (Figure 6.1d and C.2 of *Appendix* C). Therefore, this simple model shows that n_{AP} can be estimated from the logarithm of the recombination resistance measured a V_{OC} under different light intensities, as in previous works[12,13]. However, as explained in Chapter 2, it is important to clarify that these analyses involving the ideality factor are based on the assumption that the ionic distribution has reached "steady-state" conditions in which the ionic charge exists in equilibrium with the DC voltage. Hence, it is expected that the n_{AP} is dependent, not only on the recombination mechanisms, but also on the ion vacancy concentration[39], as explained for the concept of ectypal factor in *Chapter* 2. In Figure C.5 of *Appendix* C, this dependence of n_{AP} on the ionic properties of the device is illustrated, finding different values for different anion vacancy concentrations, despite the recombination mechanism being unchanged. This result show that the traditional diode equation theory and the concept of n_{ID} both need to be modified for PSCs, as described in *Chapter* 2 and reported by the works of Courtier[39] and Bennett *et al.*[40]. In fact, the location of the dominant form of recombination and the size of the potential barrier to recombination resulting from charge accumulation at the interfaces is expected to affect n_{AP}. For the chosen rates of surface recombination, the location of the dominant loss mechanism in the cell shifts from the bulk to the perovskite/HTL interface, and hence the potential barrier to electron-limited recombination is increased. This is observed in the n_{AP} obtained with and without surface recombination in Figure 6.1c. The ionic profiles in the two simulations are indistinguishable, suggesting that the reduction of n_{AP} is the result of the increased barrier to electron-limited recombination. The fact that the three-layer ionic-electronic DD model reproduces the experimental observations is a notable result and implies that the electronic system can be decoupled from the ionic system at high frequency. This allows recombination parameters to be extracted directly from the HF IS data, as for most other types of solar cells. However, evidence that both electronic and ionic signals are still connected is shown in Figure 6.4 and explained later in this *Chapter*.

6.3.3 High frequency capacitance

In contrast to low and high frequency resistances, the low and high frequency capacitances exhibit markedly different behaviors. The HF capacitance (Figure 6.3d) is voltage-independent until V_{OC} exceeds around 1 V. In fact, the simulated value in the "flat" zone coincides very well with the C_g of the device, given by Eq. 2.67. Flat capacitances are observed in the experiments, even for PSCs with mesoporous TiO_2 contacts. In the experimental case, a roughness factor of around 100 has to be introduced into Eq. 2.67 to match the value yielded by the EIS analysis[41], as mentioned in *Chapters* 3 and 5. The increase of the capacitance at high voltages is due to the accumulation of charges in the bulk of the perovskite, as discussed by Kiermasch *et al*[42].

6.3.4 Low frequency resistance, capacitance and time constant

The theoretical results from the DD model (Figure 6.3b) also show the low frequency capacitance to be an exponentially increasing function of V_{OC} which is in agreement with experimental findings[13,33]. Notably the slope of the $\ln(C_{LF})$ vs V_{OC} curve is almost exactly the reciprocal of the slope of the $\ln(R_{LF})$ vs V_{OC} curve

$$R_{LF} \sim \exp\left(-N\frac{qV}{k_BT}\right) \tag{6.2}$$

$$C_{LF} \sim \exp\left(N\frac{qV}{k_BT}\right) \tag{6.3}$$

with $N \sim 0.41$ - 0.46. Consequently, it is possible to define a low frequency time constant

$$\omega_{LF} = \frac{1}{R_{LF} \cdot C_{LF}} \tag{6.4}$$

which remains constant as the illumination, and hence V_{OC}, is adjusted. This feature, which is systematically observed in the experiments[13,33] is exactly reproduced by the three-layer ionic-electronic DD model (Figure 6.3b and c). Again, this demonstrates that the slow ionic motion of a single positive species coupled with the electronic motion of electrons and holes is the only microscopic assumption required to reproduce the LF behavior. The ionic resistance and capacitance have been described by Moia *et al.*[43]. Alternatively, Ebadi *et al.*[44] claimed that it is the modification of the injection barriers at the interfaces that causes the LF features. However, the coupling observed between the LF resistance and capacitance has remained unexplained. On the other hand, an "ionically modulated recombination" has also been proposed[11,24,26]. However, it has also been demonstrated in this *Chapter* (and will also be discussed in detail in *Chapter* 8) that only the HF resistance yields the correct value of n_{AP}, suggesting that the recombination mechanisms can only be deduced from the HF signal. This is in agreement with the work by Bennett *et al.*[40]. This is because the slow-moving ion vacancies are unaffected by the HF signal and so remain in the steady-state configuration that they adopt when the cell is used to generate current. This mechanism is discussed in detail later in this *Chapter*.

6.3.5 Impact of ionic distributions on the low frequency and high frequency signals

To shed more light on the nature of the LF signal, Figure 6.4 includes the results of simulating the impedance spectra at OC for various sets of the ionic parameters but keeping everything else fixed. The results demonstrate that modification of the ionic diffusion coefficient (while keeping the density of vacancies fixed) shifts the frequency at which the LF peak is observed, whereas the HF peak remains unaltered. Modifying the density of vacancies (while keeping the diffusion coefficient fixed) does not shift the LF peak in the studied range of values but appreciably reduces the intensity of the HF signal and increases that of the LF signal.

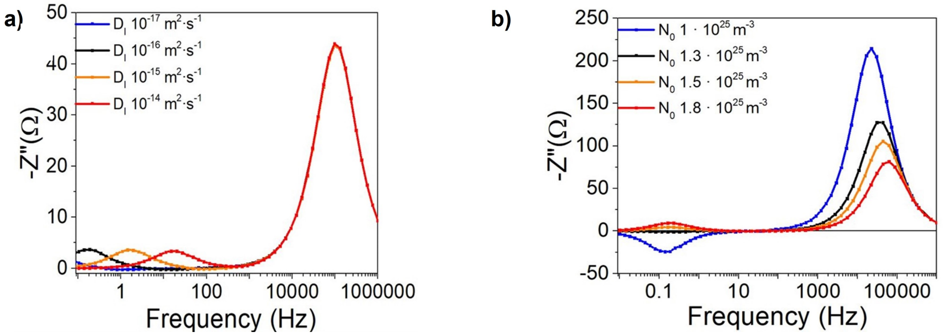

Figure 6.4: Cole-Cole plots at OC for varying values of the ionic vacancy diffusion coefficient (a) and the density of vacancies (b). The rest of the parameters are from Table C.1 of *Appendix* C.

Vacancy concentrations above $1.3{\cdot}10^{25}$ m^{-3} produce two peaks at high and low frequencies. Below this threshold, however, a negative LF peak is observed. Indeed, this is the negative signal responsible for the apparent inductive loops that can appear in the Nyquist plots of the EIS. The inductive loop is also observed in the inverted configuration studied by Neukom *et al.*[29](Figure C.4 in *Appendix* C). Concentrations of around $2{\cdot}10^{25}$ m^{-3} for charge-neutral iodine vacancies have been predicted for $\mathrm{MAPbI_3}$ by Walsh *et al*[12]. Defect formation energies calculated by Yang *et al.*[45] also yield values around 10^{26} m^{-3}. In contrast, Bertoluzzi *et al.*[46] obtained $4 \cdot 10^{23}$ m^{-3} for $\mathrm{MAPbI_3}$ using an analytical DD model. The wide range of possible ion vacancy densities can be used to explain why, for some materials such as $\mathrm{CsPbBr_3}$ which have different defect formation energetics to $\mathrm{MAPbI_3}$, the LF signal may not appear[13]. This also clarifies why certain specimens show negative signals and others do not, since the ionic defect density depends strongly on temperature[47] and the experimental preparation of the device. The trend of decreasing LF peak (and increasing HF peak) with decreasing the ion vacancy density can be explained by considering what fraction of the total potential drop occurs across the perovskite layer (as opposed to the electron and hole transport layers). It must be borne in mind that the impedance signal is the response of the collection of electronic carriers to an electric potential perturbation, which depends not only on the applied voltage but also on the distribution of ions in the device. For relatively high ion vacancy concentration in the perovskite, the potential drop occurs mainly across the transport layers, which act to screen most of the electric field from the perovskite layer (as explained by Courtier *et al.*[24]). In contrast, for low ion vacancy concentrations, most of the potential drop occurs in the perovskite layer, giving rise to large internal electric fields (within the perovskite layer) that vary significantly with changes in the applied voltage. When the predominant loss mechanism is recombination within the perovskite material, these electric fields determine the collection efficiency by either driving carriers towards, or away from, the appropriate contacts. In Figure C.6 and C.7 of *Appendix* C the electric potential and ionic vacancies density profiles at steady-state are plotted at different DC voltages for the standard parameter set of Table C.1 in *Appendix* C. As previously demonstrated[21,24], and described in *Chapter* 2, ionic charge accumulates in narrow layers, called Debye layers (or space-charge layers), adjacent to the perovskite interfaces until, at steady-state, the electric field in the bulk of the perovskite layer is completely screened. All of the potential difference across a PSC occurs across the Debye layers at steady-state. Additionally, due to the high density of mobile ionic charges, the electric potential across the perovskite layer of PSC is determined almost solely by the distribution of ions (and not the relatively small density of electronic charges)[21,24]. The resulting electric potential distribution controls the distribution of electronic charge carriers across the PSC and the potential barriers that aid or hinder their extraction from the device. In Figure 6.5 the variation of the ionic distribution and the electric potential during the impedance experiment is shown. At high frequencies, the voltage perturbation occurs mainly in the perovskite layer, whereas at low frequencies, the electric potential in the perovskite remains unaltered. This is easily understood, bearing in mind that ions do not have time to move at high frequencies and therefore remain fixed in their steady-state distribution at that applied DC voltage. Consequently, the potential drops across all four Debye layers also remain fixed. The periodic perturbations in the applied voltage induced by the EIS protocol lead to a corresponding change in voltage drop across the central bulk region of the perovskite layer; this manifests itself as a uniform time-periodic electric field that permeates this bulk region. In summary, the HF voltage perturbation leads to an alternating positive/negative electric field (negative/positive slope in Figure 6.5 (a) and (c)) across the bulk of the perovskite layer that causes enhanced/reduced extraction of the electronic carriers. This fluctuating recombination current is hence in-phase with the voltage perturbations. The out-of-phase component of the impedance response comes from capacitive contributions either at the interfaces (geometrical capacitance)[14,32]), or in the bulk (chemical capacitance)[42], high voltage region in Figure 6.3d. Consequently, $Z' < 0$. This is the origin of the high frequency peak in Figures 6.2, 6.4 and C.4 in *Appendix* C.

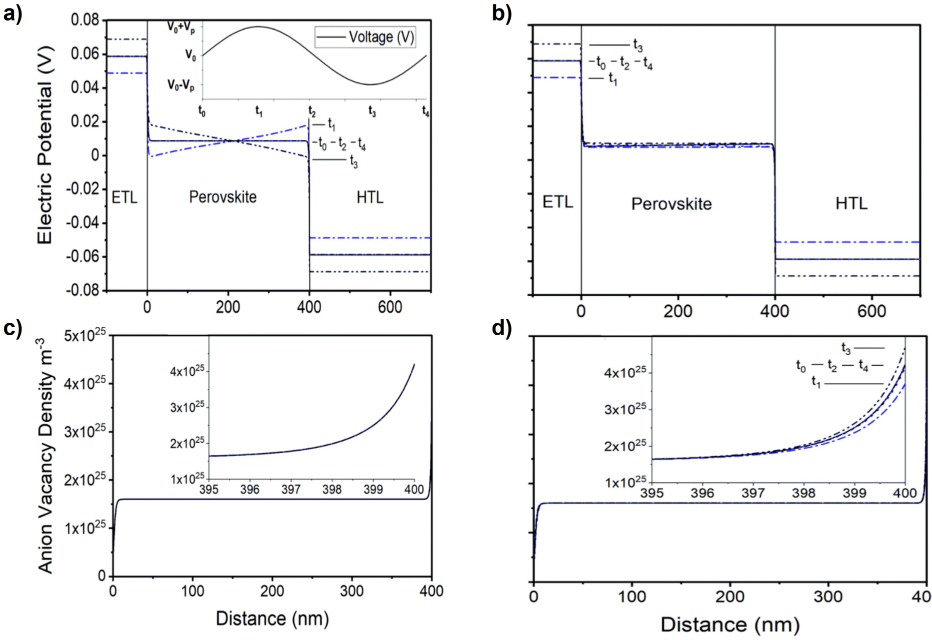

Figure 6.5: Evolution of the electric potential ((a) and (b)) and anion vacancy density ((c) and (d)) over a frequency period in the impedance experiment under illumination (1000 W·m^{-2}) at V = 1.1 V with the standard parameter set of Table C.1 of *Appendix* C. Results at both high (10^4 Hz (a) and (c)) and low (10^{-2} Hz, (b) and (d)) frequencies are shown. Increasing time is indicated by a gradient from a solid blue line to a dotted black line. (a) inset indicates the time points plotted over a period, and (c) and (d) insets show the right Debye layer within the perovskite at the perovskite/HTL interface.

In contrast, at low frequencies, the ions do have sufficient time to migrate in and out of the Debye layers at the interfaces over the period of the voltage perturbation. The potential drops occurring across these Debye layers can thus adjust quickly enough over a single period to offset some of the perturbation in the applied voltage across the cell. Indeed, at sufficiently low frequencies, the Debye layers have sufficient time to fully adjust to the perturbation in the applied voltage, so the electric field in the bulk of the perovskite is zero. Reorganization of ions in the Debye layers at LF voltage perturbations causes increases/decreases in the electric field across the bulk of the perovskite, which correspond to decreases/increases in the sizes of the potential drops across the Debye layers (*i.e.* positive bulk fields correspond to under-filled Debye layers which are charging, while negative bulk fields correspond to overfilled Debye layers which are discharging). Therefore, the LF voltage perturbations have opposing effects on recombination. This can be seen, for example, in Figure 6.4b, where it is shown that the LF signal can be either positive (for ion vacancy densities higher than $1.3 \cdot 10^{25}\ \text{m}^{-3}$) or negative (for lower ion vacancy densities). The reason is that, at low frequencies, bulk recombination in combination with large internal electric fields can cause a negative response (often referred to as an “inductive” response). In contrast, the effects of the interfaces cause a positive response (often referred to as a “capacitive” response). This is why, in Figure 6.4b, the smallest vacancy density (with the largest internal electric fields) produces both the highest HF peak and the negative LF peak[24]. Hence, it is demonstrated here that it is possible to see negative impedance from a PSC limited by bulk recombination when the density of mobile ionic charge in its perovskite layer is sufficiently low. In contrast to the interpretation by Moia *et al.*[27], the LF resistance is not directly an ionic transport resistance but a recombination resistance modulated by ion transport from the bulk to/from the Debye layers. Importantly, as both LF resistance and capacitance contributions arise from the charging/discharging of the same interfacial ionic distribution, the voltage dependence is the same. This explains the opposite slopes for the LF components of recombination and capacitance in Figure 6.3b. It also explains the shift of the peak towards higher frequencies when the ions have a higher diffusion coefficient (which allows faster charging/discharging of the Debye layers).

6.3.6 High frequency signal and charge collection efficiency at steady-state

In the discussion above, it has been stated that only the HF signal provides information about the recombination and the "ideality factor." To confirm this, additional impedance simulations with fixed illumination and a variable external DC voltage (NOC conditions) were done to recreate the extraction of charge and the generation of a photocurrent along the *JV* curve. The resistances and capacitances obtained the fit using SEC (described in *Chapter* 2, see Figure 3.13) as a function of the external DC voltage are shown in Figure 6.6.

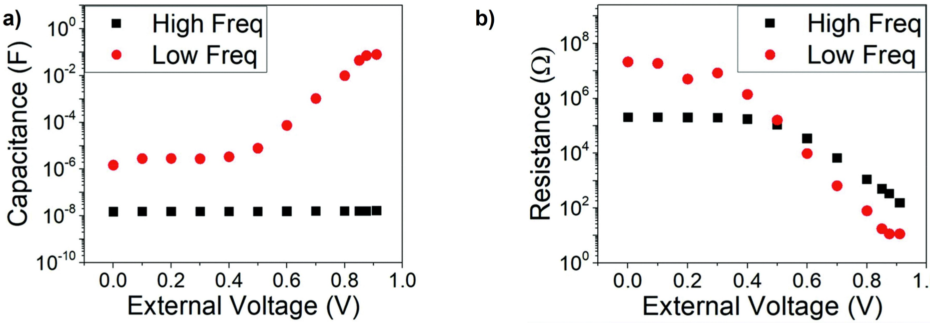

Figure 6.6: (a) Capacitance and (b) resistance values extracted from SEC and the simulated impedance spectra with parameters from Table C.1 a NOC: constant 100 W·m^{-2} illumination and variable external DC voltage.

The most visible difference concerning OC conditions is that the low and HF resistances and the LF capacitance only vary exponentially with applied voltage in the vicinity of the maximum power point and close to OC. At conditions close to SC, these magnitudes reach a plateau and remain effectively constant down to $V = 0$. In contrast, the HF capacitance retains its geometrical character at all voltages. This behavior is entirely consistent with what is observed in EIS experiments of PSCs[13,33,48] further confirming that the model utilized with the set of parameters in Table C.1 of *Appendix* C is enough to reproduce the overall impedance response of the cell. The following expression has been proposed to estimate the charge collection efficiency (CCE) from impedance data[13,33]

$$CCE \approx 1 - \frac{R_{rec(OC)}}{R_{rec(NOC)}} \tag{6.5}$$

Figure 6.7 presents the CCE predicted by this equation when the equivalence $R_{rec} = R_{HF}$ is assumed. This assumption is based on the recombination character of the HF signal, as indicated by the discussions above.

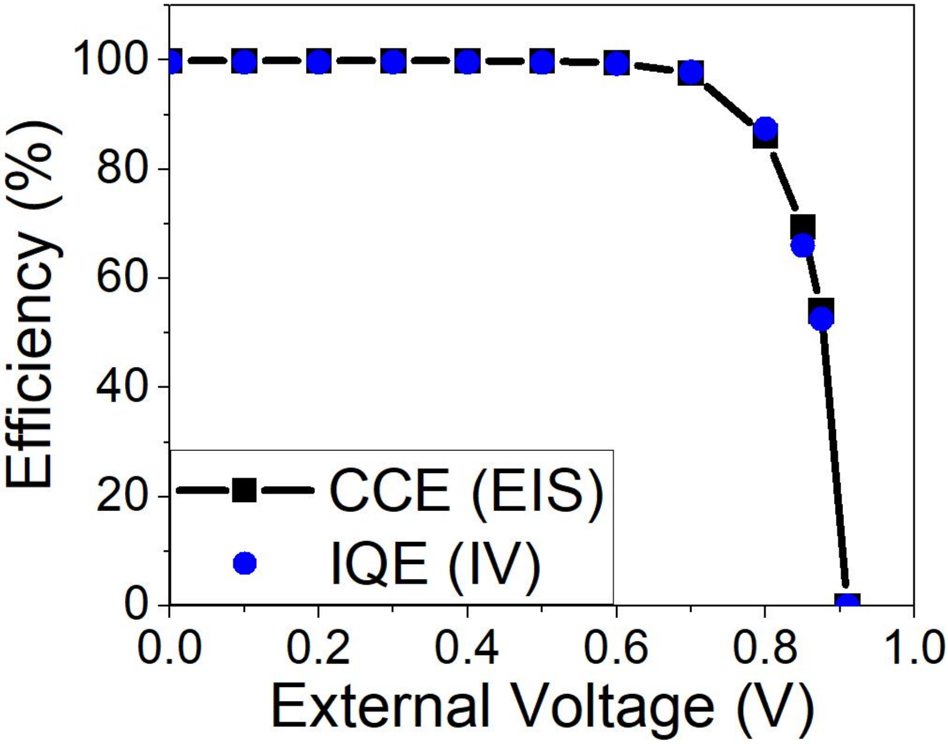

Figure 6.7: Simulated CCE as predicted from Eq. 6.5 and the impedance parameters of Figure 6.6b when the identity $R_{rec} = R_{HF}$ is assumed (black line). The stationary IQE derived from the simulated JV curve is included in the graph (blue circles). Simulation parameters are those in Table C.1 of *Appendix* C.

As expected, CCE is zero at the OCV (see Figure 6.1a) and reaches a maximum at SC. In fact, a value of 100% is predicted at SC conditions, in line with measured values for state-of-the-art devices[13,33,36,49]. The result of Eq. 6.5 can be compared with a direct "measurement" of the IQE, defined in *Chapter* 3 and also mentioned in *Chapter* 5. Knowing that in the DD simulation, each absorbed photon produces one and only one electron-hole pair, these two efficiencies should be identical. Figure 6.7 demonstrates that this is indeed the case. Furthermore, the agreement between the two ways of calculating the CCE/IQE confirms that the HF resistance is a true recombination resistance, in line with the coincidence between its voltage slope and the "ideality factor."

A similar analysis of the CCE for $MAPbI_3$ based PSCs has been done in an experimental work[13]. In that case, the agreement between the result of Eq. 6.5 (with $R_{rec} = R_{HF}$) and the IQE derived from the experimental photocurrent was only approximate. Although the coincidence between the two magnitudes is improved for devices of better efficiency, there is always a difference between the two, indicating that in real devices, the connection between both magnitudes is only approximate, $R_{rec} \approx R_{HF}$.

6.4 Conclusion

In this *Chapter* a DD model, which explicitly accounts for the motion of electrons, holes, and positive ion vacancies, was used to interpret EIS data of PSCs with an ETL/Perovskite/HTL architecture. The main focus of this *Chapter* is proposing a recipe for the interpretation of impedance response data in terms of the physics of its steady-state operation. From a practical point of view understanding the steady-state operation of the cell is key to its development as a useful photovoltaic device. In addition, it has been demonstrated how the efficiency-determining parameters of the solar cell can be obtained from experimental data. It has been shown that recombination in the bulk of the perovskite material combined with slow ionic motion is sufficient to reproduce the most common features of the impedance response for a wide variety of PSC devices, including flat HF capacitance, LF negative capacitance features, and inductive loops. It has been found that the electrical properties that determine device efficiency under operational conditions (*i.e.* at steady-state) can be deduced solely from the HF impedance response. This is the case for the recombination resistance, the so-called "ideality factor," and the CCE of the device. However, it has also been shown that, for a fair comparison to be made between different devices, the electrical properties should be deduced from HF impedance measurements performed at the values of the applied DC voltage for which the cells are expected to operate (*i.e.* close to the maximum power point in the *JV* curve). In contrast, the LF impedance response is primarily determined by the interfacial Debye layers' charging and discharging in response to ion vacancy motion within the perovskite. The LF impedance response can thus be used to infer ionic mobility and the capacitances of the Debye layers. In summary, by conducting a side-by-side comparison between theory and experiment, this *Chapter* provides a sound basis with which to extract information about recombination and CCE from actual impedance measurements in PSCs, regardless of the ionic character of the perovskite material. These results also imply that the traditional diode equation theory and the interpretation of the "ideality factor" both need to be reformulated in the context of PSCs, as discussed in *Chapter* 2.

Bibliography

[1] C. Eames, J. M. Frost, P. R. F. Barnes, B. C. O'Regan, A. Walsh, and M. S. Islam, "Ionic transport in hybrid lead iodide perovskite solar cells," *Nature Communications*, vol. 6, p. 7497, 2015-06.

[2] A. Walsh, D. O. Scanlon, S. Chen, X. G. Gong, and S.-H. Wei, "Self-regulation mechanism for charged point defects in hybrid halide perovskites," *Angewandte Chemie (International Ed. in English)*, vol. 54, no. 6, pp. 1791–1794, 2015-02.

[3] G. Xing, N. Mathews, S. Sun, S. S. Lim, Y. M. Lam, M. Grätzel, S. Mhaisalkar, and T. C. Sum, "Long-range balanced electron- and hole-transport lengths in organic-inorganic CH3nh3pbi3," *Science*, vol. 342, no. 6156, pp. 344–347, 2013.

[4] S. D. Stranks, G. E. Eperon, G. Grancini, C. Menelaou, M. J. P. Alcocer, T. Leijtens, L. M. Herz, A. Petrozza, and H. J. Snaith, "Electron-hole diffusion lengths exceeding 1 micrometer in an organometal trihalide perovskite absorber," *Science*, vol. 342, no. 6156, pp. 341–344, 2013.

[5] F. Deschler, M. Price, S. Pathak, L. E. Klintberg, D.-D. Jarausch, R. Higler, S. Hüttner, T. Leijtens, S. D. Stranks, H. J. Snaith, M. Atatüre, R. T. Phillips, and R. H. Friend, "High photoluminescence efficiency and optically pumped lasing in solution-processed mixed halide perovskite semiconductors," *The Journal of Physical Chemistry Letters*, vol. 5, no. 8, pp. 1421–1426, 2014-04.

[6] N. Rolston, A. D. Printz, J. M. Tracy, H. C. Weerasinghe, D. Vak, L. J. Haur, A. Priyadarshi, N. Mathews, D. J. Slotcavage, M. D. McGehee, R. E. Kalan, K. Zielinski, R. L. Grimm, H. Tsai, W. Nie, A. D. Mohite, S. Gholipour, M. Saliba, M. Grätzel, and R. H. Dauskardt, "Effect of cation composition on the mechanical stability of perovskite solar cells," *Advanced Energy Materials*, vol. 8, no. 9, p. 1702116, 2018.

[7] F. Fabregat-Santiago, G. Garcia-Belmonte, I. Mora-Seró, and J. Bisquert, "Characterization of nanostructured hybrid and organic solar cells by impedance spectroscopy," *Physical Chemistry Chemical Physics*, vol. 13, no. 20, pp. 9083–9118, 2011.

[8] J. Bisquert, "Theory of the impedance of electron diffusion and recombination in a thin layer," *The Journal of Physical Chemistry B*, vol. 106, no. 2, pp. 325–333, 2002.

[9] F. Fabregat-Santiago, J. Bisquert, G. Garcia-Belmonte, G. Boschloo, and A. Hagfeldt, "Influence of electrolyte in transport and recombination in dye-sensitized solar cells studied by impedance spectroscopy," *Solar Energy Materials and Solar Cells*, vol. 87, no. 1, pp. 117–131, 2005.

[10] A. R. Pascoe, N. W. Duffy, A. D. Scully, F. Huang, and Y.-B. Cheng, "Insights into planar CH3nh3pbi3 perovskite solar cells using impedance spectroscopy," *The Journal of Physical Chemistry C*, vol. 119, no. 9, pp. 4444–4453, 2015-03.

[11] A. Pockett, G. E. Eperon, N. Sakai, H. J. Snaith, L. M. Peter, and P. J. Cameron, "Microseconds, milliseconds and seconds: deconvoluting the dynamic behaviour of planar perovskite solar cells," *Physical Chemistry Chemical Physics*, vol. 19, no. 8, pp. 5959–5970, 2017-02.

[12] L. Contreras-Bernal, M. Salado, A. Todinova, L. Calio, S. Ahmad, J. Idígoras, and J. A. Anta, "Origin and whereabouts of recombination in perovskite solar cells," *The Journal of Physical Chemistry C*, vol. 121, no. 18, pp. 9705–9713, 2017.

[13] L. Contreras-Bernal, S. Ramos-Terrón, A. Riquelme, P. P. Boix, J. Idígoras, I. Mora-Seró, and J. A. Anta, "Impedance analysis of perovskite solar cells: a case study," *Journal of Materials Chemistry A*, vol. 7, no. 19, pp. 12191–12200, 2019-05.

[14] A. Guerrero, G. Garcia-Belmonte, I. Mora-Sero, J. Bisquert, Y. S. Kang, T. J. Jacobsson, J.-P. Correa-Baena, and A. Hagfeldt, "Properties of contact and bulk impedances in hybrid lead halide perovskite solar cells including inductive loop elements," *The Journal of Physical Chemistry C*, vol. 120, no. 15, pp. 8023–8032, 2016-04.

[15] F. Fabregat-Santiago, M. Kulbak, A. Zohar, M. Vallés-Pelarda, G. Hodes, D. Cahen, and I. Mora-Seró, "Deleterious effect of negative capacitance on the performance of halide perovskite solar cells," *ACS Energy Letters*, vol. 2, no. 9, pp. 2007–2013, 2017-09.

[16] O. Almora, K. T. Cho, S. Aghazada, I. Zimmermann, G. J. Matt, C. J. Brabec, M. K. Nazeeruddin, and G. Garcia-Belmonte, "Discerning recombination mechanisms and ideality factors through impedance analysis of high-efficiency perovskite solar cells," *Nano Energy*, vol. 48, pp. 63–72, 2018.

[17] S. Ravishankar, C. Aranda, S. Sanchez, J. Bisquert, M. Saliba, and G. Garcia-Belmonte, "Perovskite solar cell modeling using light- and voltage-modulated techniques," *The Journal of Physical Chemistry C*, vol. 123, no. 11, pp. 6444–6449, 2019-03.

[18] A. Todinova, L. Contreras-Bernal, M. Salado, S. Ahmad, N. Morillo, J. Idígoras, and J. A. Anta, "Towards a Universal Approach for the Analysis of Impedance Spectra of Perovskite Solar Cells: Equivalent Circuits and Empirical Analysis," *ChemElectroChem*, vol. 4, no. 11, pp. 2891–2901, 2017.

[19] S. van Reenen, M. Kemerink, and H. J. Snaith, "Modeling anomalous hysteresis in perovskite solar cells," *The Journal of Physical Chemistry Letters*, vol. 6, no. 19, pp. 3808–3814, 2015.

[20] Y. Zhou and A. Gray-Weale, “A numerical model for charge transport and energy conversion of perovskite solar cells,” *Physical Chemistry Chemical Physics*, vol. 18, no. 6, pp. 4476–4486, 2016-02.

[21] G. Richardson, S. E. J. O’Kane, R. G. Niemann, T. A. Peltola, J. M. Foster, P. J. Cameron, and A. B. Walker, “Can slow-moving ions explain hysteresis in the current–voltage curves of perovskite solar cells?,” *Energy & Environmental Science*, vol. 9, pp. 1476–1485, 2016-02.

[22] N. E. Courtier, G. Richardson, and J. M. Foster, “A fast and robust numerical scheme for solving models of charge carrier transport and ion vacancy motion in perovskite solar cells,” *Applied Mathematical Modelling*, vol. 63, pp. 329–348, 2018-07.

[23] P. Lopez-Varo, J. A. Jiménez-Tejada, M. García-Rosell, J. A. Anta, S. Ravishankar, A. Bou, and J. Bisquert, “Effects of ion distributions on charge collection in perovskite solar cells,” *ACS Energy Letters*, vol. 2, no. 6, pp. 1450–1453, 2017-06.

[24] N. E. Courtier, J. M. Cave, J. M. Foster, A. B. Walker, and G. Richardson, “How transport layer properties affect perovskite solar cell performance: insights from a coupled charge transport/ion migration model,” *Energy & Environmental Science*, vol. 12, pp. 396–409, 2018-12.

[25] N. Tessler and Y. Vaynzof, “Insights from device modeling of perovskite solar cells,” *ACS Energy Letters*, 2020-03.

[26] D. A. Jacobs, H. Shen, F. Pfeffer, J. Peng, T. P. White, F. J. Beck, and K. R. Catchpole, “The two faces of capacitance: New interpretations for electrical impedance measurements of perovskite solar cells and their relation to hysteresis,” *Journal of Applied Physics*, vol. 124, no. 22, p. 225702, 2018-12.

[27] D. Moia, I. Gelmetti, P. Calado, W. Fisher, M. Stringer, O. Game, Y. Hu, P. Docampo, D. Lidzey, E. Palomares, J. Nelson, and P. R. F. Barnes, “Ionic-to-electronic current amplification in hybrid perovskite solar cells: ionically gated transistor-interface circuit model explains hysteresis and impedance of mixed conducting devices,” *Energy & Environmental Science*, vol. 12, no. 4, pp. 1296–1308, 2019.

[28] M. Neukom, S. Züfle, S. Jenatsch, and B. Ruhstaller, “Opto-electronic characterization of third-generation solar cells,” *Science and Technology of Advanced Materials*, vol. 19, no. 1, pp. 291–316, 2018-12.

[29] M. T. Neukom, A. Schiller, S. Züfle, E. Knapp, J. Ávila, D. Pérez-del Rey, C. Dreessen, K. P. Zanoni, M. Sessolo, H. J. Bolink, and B. Ruhstaller, “Consistent device simulation model describing perovskite solar cells in steady-state, transient, and frequency domain,” *ACS Applied Materials & Interfaces*, vol. 11, no. 26, pp. 23320–23328, 2019-07.

[30] A. Guerrero, E. J. Juarez-Perez, J. Bisquert, I. Mora-Sero, and G. Garcia-Belmonte, “Electrical field profile and doping in planar lead halide perovskite solar cells,” *Applied Physics Letters*, vol. 105, no. 13, p. 133902, 2014-09.

[31] L. A. Frolova, N. N. Dremova, and P. A. Troshin, “The chemical origin of the p-type and n-type doping effects in the hybrid methylammonium–lead iodide (MAPbI3) perovskite solar cells,” *Chemical Communications*, vol. 51, no. 80, pp. 14917–14920, 2015-09.

[32] A. Pockett, G. E. Eperon, T. Peltola, H. J. Snaith, A. Walker, L. M. Peter, and P. J. Cameron, “Characterization of planar lead halide perovskite solar cells by impedance spectroscopy, open-circuit photovoltage decay, and intensity-modulated photovoltage/photocurrent spectroscopy,” *The Journal of Physical Chemistry C*, vol. 119, no. 7, pp. 3456–3465, 2015-02.

[33] I. Zarazúa, S. Sidhik, T. Lopéz-Luke, D. Esparza, E. De la Rosa, J. Reyes-Gomez, I. Mora-Seró, and G. Garcia-Belmonte, “Operating mechanisms of mesoscopic perovskite solar cells through impedance spectroscopy and j–v modeling,” *The Journal of Physical Chemistry Letters*, pp. 6073–6079, 2017-11.

[34] C. Aranda, C. Cristobal, L. Shooshtari, C. Li, S. Huettner, and A. Guerrero, “Formation criteria of high efficiency perovskite solar cells under ambient conditions,” *Sustainable Energy Fuels*, vol. 1, no. 3, pp. 540–547, 2017.

[35] W. L. Leong, Z.-E. Ooi, D. Sabba, C. Yi, S. M. Zakeeruddin, M. Graetzel, J. M. Gordon, E. A. Katz, and N. Mathews, “Identifying fundamental limitations in halide perovskite solar cells,” *Advanced Materials*, vol. 28, no. 12, pp. 2439–2445, 2016.

[36] W. Tress, M. Yavari, K. Domanski, P. Yadav, B. Niesen, J. P. C. Baena, A. Hagfeldt, and M. Graetzel, “Interpretation and evolution of open-circuit voltage, recombination, ideality factor and subgap defect states during reversible light-soaking and irreversible degradation of perovskite solar cells,” *Energy & Environmental Science*, vol. 11, pp. 151–165, 2018.

[37] J. Nelson, *The Physics of Solar Cells*. Imperial College Press, 1 ed., 2003-09.

[38] K. Valadez-Villalobos, J. Idígoras, L. P. Delgado, D. Meneses-Rodríguez, J. A. Anta, and G. Oskam, “Correlation between the effectiveness of the electron-selective contact and photovoltaic performance of perovskite solar cells,” *The Journal of Physical Chemistry Letters*, vol. 10, no. 4, pp. 877–882, 2019-02.

[39] N. Courtier, “Interpreting Ideality Factors for Planar Perovskite Solar Cells: Ectypal Diode Theory for Steady-State Operation,” *Physical Review Applied*, vol. 14, p. 024031, Aug. 2020.

[40] L. J. Bennett, A. J. Riquelme, N. E. Courtier, J. A. Anta, and G. Richardson, “A new ideality factor for perovskite solar cells and an analytical theory for their impedance spectroscopy response,” *arXiv:2105.11226 [cond-mat, physics:physics]*, May 2021. arXiv: 2105.11226.

[41] A. Todinova, J. Idígoras, M. Salado, S. Kazim, and J. A. Anta, “Universal features of electron dynamics in solar cells with tio$_2$ contact: From dye solar cells to perovskite solar cells,” *The Journal of Physical Chemistry Letters*, vol. 6, no. 19, pp. 3923–3930, 2015.

[42] D. Kiermasch, A. Baumann, M. Fischer, V. Dyakonov, and K. Tvingstedt, “Revisiting lifetimes from transient electrical characterization of thin film solar cells; a capacitive concern evaluated for silicon, organic and perovskite devices,” *Energy & Environmental Science*, vol. 11, no. 3, pp. 629–640, 2018-03.

[43] I. Zarazua, J. Bisquert, and G. Garcia-Belmonte, “Light-induced space-charge accumulation zone as photovoltaic mechanism in perovskite solar cells,” *The Journal of Physical Chemistry Letters*, pp. 525–528, 2016.

[44] F. Ebadi, N. Taghavinia, R. Mohammadpour, A. Hagfeldt, and W. Tress, “Origin of apparent light-enhanced and negative capacitance in perovskite solar cells,” *Nature Communications*, vol. 10, no. 1, p. 1574, 2019-04.

[45] D. Yang, W. Ming, H. Shi, L. Zhang, and M.-H. Du, “Fast diffusion of native defects and impurities in perovskite solar cell material CH3nh3pbi3,” *Chemistry of Materials*, vol. 28, no. 12, pp. 4349–4357, 2016-06.

[46] L. Bertoluzzi, C. C. Boyd, N. Rolston, J. Xu, R. Prasanna, B. C. O’Regan, and M. D. McGehee, “Mobile ion concentration measurement and open-access band diagram simulation platform for halide perovskite solar cells,” *Joule*, vol. 4, no. 1, pp. 109–127, 2019.

[47] D. Meggiolaro, E. Mosconi, and F. De Angelis, “Formation of surface defects dominates ion migration in lead-halide perovskites,” *ACS Energy Letters*, vol. 4, no. 3, pp. 779–785, 2019-03.

[48] I. Zarazua, G. Han, P. P. Boix, S. Mhaisalkar, F. Fabregat-Santiago, I. Mora-Seró, J. Bisquert, and G. Garcia-Belmonte, “Surface recombination and collection efficiency in perovskite solar cells from impedance analysis,” *The Journal of Physical Chemistry Letters*, vol. 7, no. 24, pp. 5105–5113, 2016-12.

[49] E. Edri, S. Kirmayer, S. Mukhopadhyay, K. Gartsman, G. Hodes, and D. Cahen, “Elucidating the charge carrier separation and working mechanism of CH3nh3pbi3-xClx perovskite solar cells,” *Nature Communications*, vol. 5, 2014-03.

Chapter 7

Illumination intensity dependence of the recombination mechanism in mixed perovskite solar cells

Abstract

Recombination mechanisms in solar cells are frequently assessed by determining ideality factors. In this Chapter an abrupt change of the value is reported for n_{AP} *in high-efficiency* $FA_{0.71}MA_{0.29}PbI_{2.9}Br_{0.1}$ *based mesoscopic PSCs as a function of light intensity. This change is manifested as a transition from a regime characterized by* $n_{AP} \sim 1.8\text{-}2.5$ *at low light intensities (*< 10 *mW·cm*$^{-2}$*) to one characterized by* $n_{AP} \sim 1$*. By using DD simulation, it is observed that the apparent ideality factor is, in fact, affected by the ion vacancy concentration, so it is not the optimal parameter to assess the dominant recombination mechanism. This implies that a procedure based on* n_{EL} *is better suited to determine the recombination route that dictates the photovoltage.*

This Chapter is based on Publication 4 of this Thesis: Alejandra Castro-Chong *et al.* ChemPlusChem. 2021, 86, 9, 1347 - 1356.

7.1 Introduction

As it has been described in *Chapter* 2, the build-up and collection of charges in solar cells are limited by charge carrier recombination, which determines the V_{OC}. As shown in Figure 2.6 and explained in detail in that *Chapter*, different recombination mechanisms can coexist in a solar cell. Hence, identifying the carrier recombination mechanisms is fundamental for effectively designing PV devices.

The exact sources of nonradiative recombination in perovskite materials are still a matter of discussion. While the formation of defects is known to be highly probable in this type of material[1], the carrier lifetime is still impressively long with τ of several hundreds of ns and even longer[2,3]. Nevertheless, PSCs performing close to the radiative limit have not been reported. Thus, considerable scope remains for reducing nonradiative recombination in these devices. In general, in this type of solar cell, it has been claimed that the recombination processes that determine the V_{OC} are mainly governed by the defect physics of the perovskite layer bulk[4–7]. However, the importance of recombination at interfaces has been highlighted by several authors that showed those surface treatments significantly improve performance, presumably by suppressing recombination[8,9]. As it has been shown in *Chapters* 1 and 2, the defect physics of the absorber plays a critical role in determining the nonradiative recombination behavior. Perovskite materials exhibit unique defect properties, which are very much attributed to their well-established ion migration under illumination and electrical bias[10,11]. The ionic environment in PSCs can moderate the rate of charge injection and electron-hole recombination in several ways, such as electronic-ionic coupling, surface dipole introduction, and screening of the built-in electric field at the interfaces[12–15]. The interpretation of ionic-electronic coupling affecting the collection probability of photogenerated charges has gained strength. According to Pockett *et al.*[12], a new ionic distribution, upon light or electrical excitation, might be favorable in reducing the recombination rate through a reduction in trap capture cross-section and/or ionic modulation of the band offsets in the device. Jacobs *et al.*, as mentioned in *Chapter* 6, rationalized the manifestations of ion migration ("giant" photoinduced capacitance, inductive loop and "negative" capacitance), as a phase delayed recombination current contributing to the measured impedance at low frequencies[15]. This was confirmed in *Chapter* 6, where DD numerical simulations showed that ionic redistribution at the transport layers interfaces gives rise to the low-frequency signal of the impedance spectrum and can produce negative capacitance features and loops. Although all these signals can be reproduced with trap-limited bulk-recombination only, the DD simulations also show that surface recombination contributes significantly to the electrical losses in PSCs and that this contribution is needed to fit both *JV* curves and the impedance spectra.

To elucidate the dominant recombination mechanism in a particular device, as has been explained before, the diode ideality factor is a key parameter, which is regularly adopted to analyze recombination losses occurring during solar cell operation[16]. Charge carrier kinetic properties at the interfaces and the generation of surface defects are among the features that have been identified by using ideality factors in PSCs[5,6]. In classical theory, the diode ideality factor may be extracted from the analysis of the V_{OC} as a function of illumination intensity. However, as it can be inferred from the ionic dependence of this classical ideality factor observed in *Chapter* 6 (see Figure C.5 of *Appendix* C), the measured values of the ideality factor depend not only on the type of recombination but also on the effect of ionic accumulation on the electric potential. For this reason, in PSCs it is necessary to distinguish between the apparent/classic ideality factor (n_{AP}), n_{EC} and n_{EL}. Both concepts are explained with detail in *Chapter* 2. When the classical theory is applied to PSCs, values of n_{AP} varying from 1.4 to 2 have been associated with the SRH recombination mechanism in the bulk[4,17,18] with the lower values (<2) corresponding to solar cells based on mixed-cation lead mixed-halide perovskite materials[6]. As the value of n_{AP} is approximately equal to the reciprocal of the proportion of the potential difference that forms a barrier to recombination (see *Chapter* 2), non-integer and voltage-dependent values are expected. Both bimolecular and surface recombination produces a value of 1. However, for bulk SRH, a value of around 2 is predicted only for a cell with an approximately symmetric potential distribution across the cell, while values above or below 2 may signify bulk SRH in an asymmetric cell. Surface recombination between the perovskite and the transport layer interfaces can also return a range of values, depending on the potential distribution across the cell. All these results evidence how important is to bear in mind that the ionic distribution (which determines the potential) impacts the measured value of n_{AP}. In this *Chapter*, the charge recombination mechanisms in $FA_{0.71}MA_{0.29}PbI_{2.9}Br_{0.1}$ based mesoscopic PSCs are investigated by means of the n_{AP} values extracted from the analysis of V_{OC} as a function of illumination intensity, and from EIS measurements at OC. Two different values of the n_{AP} were identified, depending on the illumination intensity. For low light intensity (< 10 mW $\cdot$cm^{-2}), values of n_{AP} = 2.4 - 1.8 are observed, pointing to recombination losses dominated by bulk SRH-type recombination in the perovskite layer. In contrast, for higher light intensities, n_{AP} = 1.1, which shows that a change in the governing recombination mechanism and/or in the ionic characteristics of the perovskite takes place when the concentration of photogenerated carriers exceeds a certain threshold. With the help of DD simulations and novel theoretical insights[19,20], the origin of this change of regime is discussed.

7.2 Fabrication and characterization of devices

7.2.1 Device fabrication

Mesoscopic TiO_2-based PSCs were prepared using the mixed perovskite $FA_{0.71}MA_{0.29}PbI_{2.9}Br_{0.1}$. Glass substrates patterned with ITO were cleaned in an ultrasonic bath sequentially immersed in detergent, deionized water, acetone, and isopropanol. Subsequently, a 20-nm thick compact TiO_2 layer was deposited through e-beam evaporation (Angstrom Engineering) of Ti at a rate of $1Å\cdot s^{-1}$ using a partial O_2 pressure of $1.7\cdot 10^{-4}$ torr. Consecutively, a 120-nm mesoporous TiO_2 layer was prepared by spin-coating an anatase dispersion in ethanol at 1.2 wt%: 60 μL were spin-coated at 4500 rpm for 30 s; the number of repetitions was adjusted to achieve the desired thickness. The films were annealed at 450ºC for 30 min. The mixed perovskite absorbing material was prepared through the intramolecular exchange method as reported by Seok *et al.*[21], using the two-step spin-coating sequential process[22,23]. Using this methodology, two solutions are prepared: solution A consists of 1.25 M PbI_2 in a mixture of DMF/DMSO: (90/10, v/v) and solution B consists of $CH(NH_2)_2I$, CH_3NH_3I (MAI) and CH_3NH_3Br (MABr) (71:19:10 molar ratio) in isopropanol. The solution chemistry and spin coating conditions were selected for proper infiltration of a 120-nm-thick mesoporous TiO_2 layer, according to Castro-Chong *et al.*[24] Spiro-OMeTAD was used as HTL and Au as electrode[24].

7.2.2 Characterization and numerical simulation

The PV characteristics of the devices were measured under ambient atmosphere using an Autolab PGSTAT302N and a xenon arc lamp, Oriel 66924, equipped with AM1.5G and water filters; calibration was performed with a Newport calibrated reference Si solar cell with an incorporated KG-5 optical filter. The devices were measured from forward to reverse bias and from reverse to forward bias, at a scan rate of 0.05 V·s^{-1}, using a shadow mask to define the active pixel area of 0.08 cm^2. EIS was performed on the mesoscopic PSCs with PCE $\sim$17%. The impedance response of the three devices, with 12 individual pixels each, was investigated at V_{OC} using a Gamry electrochemical workstation. The V_{OC} was set by controlling the light intensity of a Xe-arc lamp with an AM1.5G optical filter and a 10 cm water filter. Impedance measurements were performed at eight different illumination intensities: 0.4, 1, 3, 5, 10, 20, 40 and 100 mW·cm^{-2}. The spectra were recorded from 10^{6}Hz to 10^{-2}Hz, using an amplitude of 10 mV. To minimize the effect of degradation of the devices in the analyzed results, the spectra were recorded starting from the lower illumination intensity working up to the highest; the V_{OC} and *JV* curves were monitored throughout the recorded spectra (see Figure D.1 in *Appendix* D), ensuring the reliability of the data, similarly, as it has been done in the rest of the Thesis and as suggested by Pitarch-Tena *et al*[25].

EIS spectra was numerically simulated using the three layers *IonMonger* code[26,27] described in detail in *Chapter* 3 and also used in *Chapter* 6.

7.3 Results and discussion

7.3.1 V_{OC} illumination intensity

Representative *JV* curves at different illumination intensities are shown in Figure 7.1a. The recorded PV parameters of the devices illuminated at 1 sun are: J_{SC} = 23.5±1.8 mA·cm^{-2}, V_{OC} = 1.1±0.2 V, *FF* = 67±2% and PCE = 17.3±2.1%. The V_{OC} generated at 1 sun is close to 1.1 V, which is around or even above the values reported for similar perovskite compositions[22,28]. The V_{OC} generated at the different illumination intensities are included in Figure 7.1b.

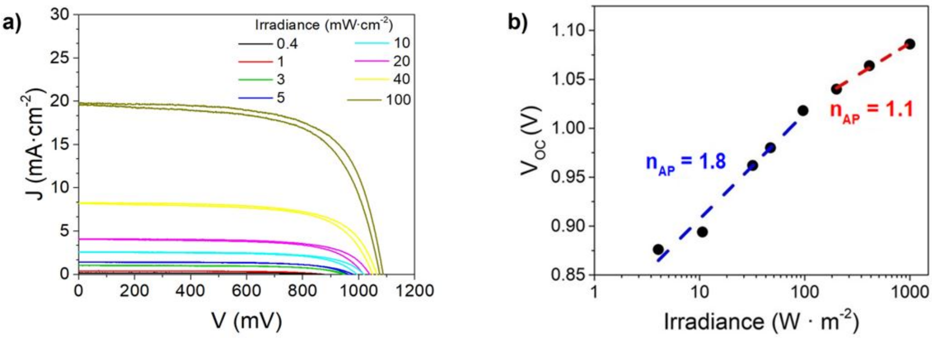

Figure 7.1: (a) Representative *JV* curves of mesoscopic PSCs used for the EIS analysis under different irradiance values; the scan rate is set to 0.05 V·s^{-1}. (b) V_{OC} vs light intensity, lines show a logarithmic fit and the numbers indicate the n_{AP} obtained from the slope according to Eq. 6.1 of *Chapter* 6 as derived from the application of OC conditions to Eq. 2.25 in *Chapter* 2.

Two different slopes of the V_{OC} vs light intensity response were observed, depending on the illumination intensity regime. Following Eq. 6.1 in *Chapter* 6, the value of the n_{AP} was found to be 1.8 for low light intensity (<10 mW·cm^{-2}), while for high light intensity (≥10 mW·cm^{-2}) n_{AP}=1.1. This crossover indicates a change in the recombination mechanism, but it is not possible to entirely rule out that this is indicative of some other physical effect. A similar behaviour has been described by Caprioglio *et al.*[29,30]. It is worth mentioning that here the V_{OC} values were only measured after the devices had reached a steady state (50 to 200 s of initial delay). Furthermore, the devices were discharged before each new measurement by short-circuiting in the dark. The time required to reach a nearly null dark current was at least 60 s. This protocol aims at avoiding uncertainty related to preconditioning and V_{OC} evolution due to slow ionic redistribution.

7.3.2 Impedance spectroscopy

Representative Nyquist plots measured at OC at different irradiance values are shown in Figure 7.2. The impedance response presents the classical two semi-circles shape[15] commonly shown in this Thesis (see *Chapters* 3 and 6). As it can be confirmed from Figure D.1 of *Appendix* D, the cells did not suffer from degradation during the EIS analysis. Bode plots corresponding to the Nyquist of Figure 7.2 can be observed in Figure D.2 in *Appendix* D.

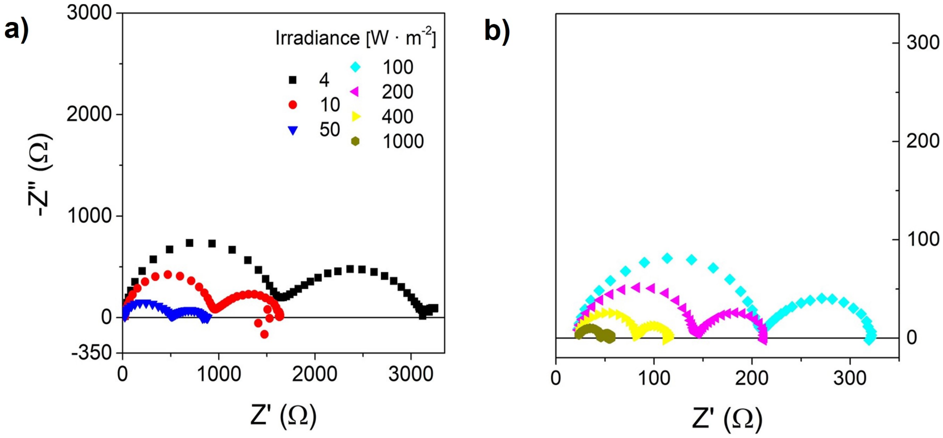

Figure 7.2: Nyquist plots measured at OC at different irradiance values. (a) shows the spectra in the region where n_{AP} ~2 and (b) shows the spectra where n_{AP} ~1.

The impedance spectra were fit using SEC[13,31] described in *Chapter* 3 (see Figure 3.13) and already used in *Chapter* 6. As described in *Chapter* 3, the capacitive elements were modelled as a CPE (see *Chapter* 3). The HF arc produced P values ranging from 0.9 to 1 while P is between 0.75 and 0.85 for the LF arc.

In Figure 7.3, the resistive (R_{HF} and R_{LF}) and capacitive (C_{HF} and C_{LF}) elements of the fit of the EIS spectra in Figure 7.2 to the equivalent circuit depicted in Figure 3.13 in *Chapter* 3 are displayed as a function of the V_{OC} generated at the different irradiance values. In general, both R_{HF} and R_{LF}

decrease exponentially as the V_{OC} increases, as expected from recombination resistance[4,32,33] and observed in *Chapter* 6. Contreras-Bernal *et al.* reported that only the n_{AP} extracted from the slope of the logarithm of the R_{HF} strictly coincides with the n_{AP} derived from the slope of the V_{OC} vs illumination[7]. In addition, in *Chapter* 6 it was described how the low frequency signal was related to charging/discharging of ionic accumulation layers at interfaces, which would produce a R_{LF} and C_{LF} with opposite slopes. Here, n_{AP} was calculated using Eq.2.25 in *Chapter* 6.

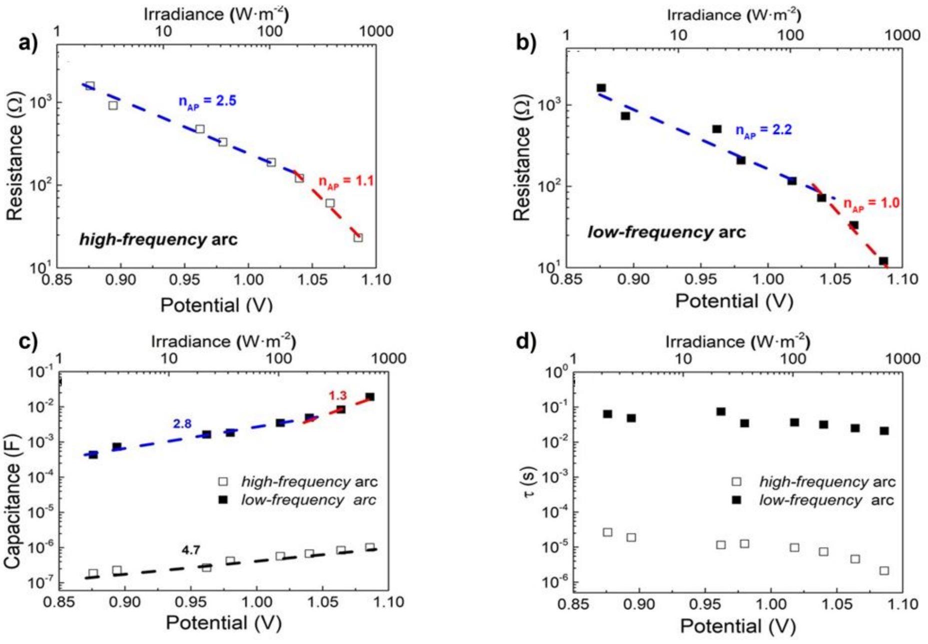

Figure 7.3: Electrical elements obtained from the EIS analysis. (a) and (b) Resistive elements at the high and low frequency domains (R_{HF} and R_{LF}). (c) Capacitive elements (C_{HF} and C_{LF}) and (d) time constant (τ). The lines correspond to the logarithmic fit and the numbers indicate the n_{AP} values extracted from the reciprocals of the slopes (Eq. 6.1 and Eq. 6.2 in *Chapter* 6).

In Figure 7.3 It is observed that, for the first time, both, R_{HF} and R_{LF}

yield two different slopes depending on the V_{OC}, consistent with the behaviour observed in the dependence of the V_{OC} with illumination intensity. Following the reasoning of the link between R_{HF} and the recombination mechanism extracted from what was described in *Chapter* 6 and Contreras-Bernal *et al.*[7], n_{AP} was extracted from the high frequency component. Specifically, $n_{AP} = 2.5$ for irradiance <10 mW·cm^{-2} and $n_{AP} \sim 1$ for irradiance ≥ 10 mW·cm^{-2} (Figure 7.3a, b). This behaviour was observed in three devices measured independently (see Figure D.3 in *Appendix* D). In both regimes, n_{AP} is approximately coincident with that obtained, in the conventional manner, from the V_{OC} vs light intensity plot, confirming the internal consistency of these devices with Eq. 6.1 and 2.25 and the reliability of the n_{AP} derived from the two types of experiment (steady state and small perturbation).

In this line of reasoning, it could be expected that using $R_{rec} = R_{LF} + R_{HF}$ in Eq. 2.25 would be a more sensible choice to extract the apparent ideality factor as this corresponds to the DC limit of the current-voltage response of the solar cell. However, using low frequency features of the spectra is more sensitive to non-reversible ionic migration and/or degradation of the device during the measurement. As shown theoretically by Bennett *et al.*[20] (and described in *Chapter* 3), the slope of the R_{HF} dependence on V_{OC} can be related to n_{AP}, and explains the common experimental observation[4,7,18] that Eqs. 6.1 and 2.25 of *Chapter* 6 yield the same results when $R_{rec} = R_{HF}$.

The change of n_{AP} with the illumination intensity is evidence that recombination takes place via a different mechanism, which depends on the concentration of charge carriers in the active layer. The low-irradiance n_{AP} values are the typical values reported for similar PSCs. This observation has been attributed to SRH (trap-mediated) recombination in the bulk[4–6,18]. However, at high irradiances, the n_{AP} values indicate a change in the dominant recombination mechanism or, possibly, that some other physical change occurs within the cell.

As it has been described in *Chapters* 3 and 6, the origins of C_{HF} and C_{LF} have been ascribed to different charge polarisation processes[13,34–36]. C_{HF} is generally ascribed to the bulk dielectric response of the perovskite layer[31,33,37] and is defined as the geometric capacitance (see Eq. 2.67 in *Chapter* 2). According to this, C_g should be voltage independent. However, in Figure 7.3 it can be observed how C_{HF} rises exponentially with electric potential, although the slope is much smaller than that of R_{HF}. This dependence with V_{OC} could be due to a chemical effect of charge accumulation in the mesoporous TiO_2 layer and/or in the perovskite[38,39]. Another option would be a change in the permittivity of the perovskite material with illumination[6,40]. However, the fact that this phenomena was also observed in *Chapter* 6 (and later in this *Chapter*) suggests that accumulation of charges in the bulk of the active layer could be the only mechanism needed to rationalize this experimental feature. On the other hand, C_{LF} exhibits the exponential increase with V_{OC} observed in *Chapter* 6, which is an ubiquitous observation in PSCs[4,6,7,32,35,41], which can be described by Eq. 6.3. As it has been mentioned in *Chapter* 6, this exponential dependence of C_{LF} has been ascribed to charge accumulation at the interfaces[40–42]. However, it has been shown that charge accumulation alone, either ionic or electronic, is not sufficient to justify the very high values (of the order of 0.1-1 $F{\cdot}cm^{-2}$) of the capacitance observed in the EIS of PSCs at low frequencies[15]. Thus, C_{LF} must contain two contributions: charge accumulation and phase-delayed recombination current due to the ion displacement[15]. In this *Chapter* it is observed that C_{LF} displays two different slopes; exactly as the R_{LF} with the same values but opposite signs, following the numerical DD simulations in *Chapter* 6. As this crossover takes place at the same values of voltage as the R_{HF}, which stems from recombination, the low-frequency response can be related to ionic-electronic coupling affecting the recombination current and thus the measured capacitance through a phase delayed response. This analysis is in line with the interpretation of Jacobs *et al.*[15] and Pockett *et* *al*[12].

The time constant (τ) in Figure 7.3d was calculated from Eq. 6.4 of *Chapter* 6. As R_{LF} and C_{LF} have reciprocal slopes at both illumination regimes, the time constant is found to be nearly independent of light intensity. This is what is normally observed in experiments[4,7,12,32,42,43] and predicted by DD simulations in *Chapter* 6. In contrast, in the high-frequency regime the resistive and capacitive elements are uncoupled as they stem from different mechanisms. Consequently, the corresponding time constant displays a slight exponential dependence on illumination intensity, as expected for PSCs (see *Chapters* 3 and 6). In general, the steady-state and impedance results indicate the existence of two regimes occurring at different light intensities: At irradiances lower than 10 mW·cm^{-2} n_{AP} is 1.8-2.5. Above this irradiance threshold, n_{AP} is close to unity. Values of n_{AP} close to 2 have commonly been observed in PSCs with TiO_2/perovskite/Spiro architecture[4–7]. According to classical theory, an ideality factor of 2 is usually considered an indication of trap-mediated SRH recombination in the bulk of the active layer[5], as it has been explained in *Chapter* 2. On the other hand, an ideality factor close to 1 can stem from two alternative recombination mechanisms: band-to-band radiative recombination or surface recombination at the perovskite/transport layer interfaces (low selectivity of the contacts)[5]. From the values of V_{OC} at 1-sun illumination obtained for the devices studied in this *Chapter*, far from the radiative limit (see *Chapter* 2) that for mixed perovskites is around $\sim$1.3 V[44], it can be inferred that surface recombination is the more likely explanation of the ideality factor measured at high irradiances. However, the reasons for surface recombination becoming more important at high irradiances is unclear. It is worth mentioning that Caprioglio *et al.*[30] also reported this abrupt change of the V_{OC} vs light intensity slope and used this observation to distinguish "internal" and "external" ideality factors. This indicates that a deeper understanding of the meaning of n_{AP}, along with n_{EC}[19] and n_{EL}[20] described in *Chapter* 2, and the underlying mechanisms that govern recombination in PSCs, is much needed.

7.3.3 Drift-diffusion simulations

As stated previously, the ideality factor obtained from both the steady-state measurement of Figure 7.1b and the small-perturbation result of Figure 7.3a (obtained via Eqs. 6.1 and 2.25, respectively) is n_{AP}. This value is not only determined by charge recombination mechanisms within the cell but is also directly affected by the ionic distribution within the active layer. The effect of the ion vacancies in the perovskite layer is not considered by the classical diode theory used to infer the recombination mechanism from the n_{AP}. Indeed, in *Chapter* 6 numerical DD simulations show that n_{AP} (obtained from steady-state and impedance measurements) changes in response to changes in the internal vacancy distribution. In this connection, an extension of the traditional diode equation to take into account the ionic properties of PSC (n_{EC}[19] described in *Chapter* 2) is applied. This concept shows an ionic influence on n_{AP}, which should be considered when inferring the correct recombination mechanism. This recombination mechanism can be deduced applying the n_{EL} proposed by Bennett *et al.*[20] also described in *Chapter* 2. To cast light on the origin of the slope change, in the steady-state measurements and impedances with light intensity, numerical DD simulations were done. The relative weights of bulk and surface recombination were varied, as well as the concentration of ionic vacancies in order to see their impact on the spectra and the apparent ideality factor.

Figure D.4 in *Appendix* D includes DD simulations results when the bulk SRH mechanism is the only recombination route (apart from the always present bimolecular recombination). The DD model predicts an n_{AP} of $\sim$2 in this situation. However, the shape of the spectra is quite different from the experimental spectra recorded at low light intensities, with two arcs of comparable size (see Figure 7.2). In Figure 7.4 the effect of introducing surface recombination in addition to bulk recombination can be observed. The two arcs become of comparable size at all light intensities and n_{AP} drops below 2, while still maintaining the consistency between steady-state and impedance values (see Figure D.5 in *Appendix* D).

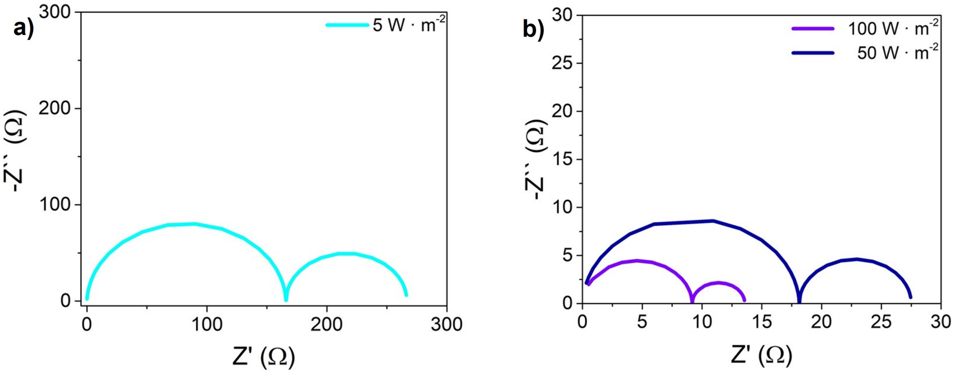

Figure 7.4: Simulated impedance spectra at V_{OC} at different light intensities for a mechanism where both bulk SRH recombination (electron lifetime of $9{\cdot}10^{-7}$) and surface recombination take place (recombination velocities at the TiO_2 and Spiro-OMeTAD interfaces, 20 and 10 $m{\cdot}s^{-1}$, respectively). The rest of the simulation parameters are similar to the standard set used in *Chapter* 6.

In this case, the DD simulated spectra have more resemblance to the measured spectra and are similar to those previously reported in the literature for mixed perovskites[6,24]. As pointed out in *Chapter* 6, the model, which assumes a planar device with a constant dielectric constant, predicts a slight exponential dependence of C_{HF} at high voltages, as can also be observed in Figure D.6, in agreement with the experiment. This indicates that the accumulation of charges at high voltages in the bulk of the active layer can cause an increase in C_{HF}. Hence, the model appears to provide a reasonably good description of the impedance response, indicating that both bulk SRH and surface recombination are required to best reflect experimental observations, as also explained in *Chapter* 6. Hence, the change in n_{AP} can be explained as a transition towards a situation where recombination across the TiO_2 and Spiro-OMeTAD interfaces becomes progressively more important as the cell is illuminated with a higher irradiance. Indeed, the modelling predicts a higher accumulation of electronic carriers and ions at the TiO_2 and Spiro-OMeTAD interfaces at high illumination intensities (see Figures D.7 and D.8 in *Appendix* D). In particular, more holes at the TiO_2 interface and more electrons at the Spiro-OMeTAD one. This effect can promote enhanced surface recombination across the respective interfaces. Still, the simulated n_{AP} predicted for mixed bulk/surface recombination is well above the value of $\sim$1 observed in the experiment at high light intensity (see Figure D.4 of *Appendix* D).

As it has been repeated several times in this Thesis, n_{AP} as obtained from Eqs. 6.1 and 2.25 is actually affected by the ionic distribution. In Figure 7.5 n_{AP} predicted by the DD model for two concentrations of ion vacancies in the active perovskite layer is plotted. The reference ion vacancy density was similar to the used in *Chapter* 6, and an additional set of simulations was done for an ion vacancy 10 times less.

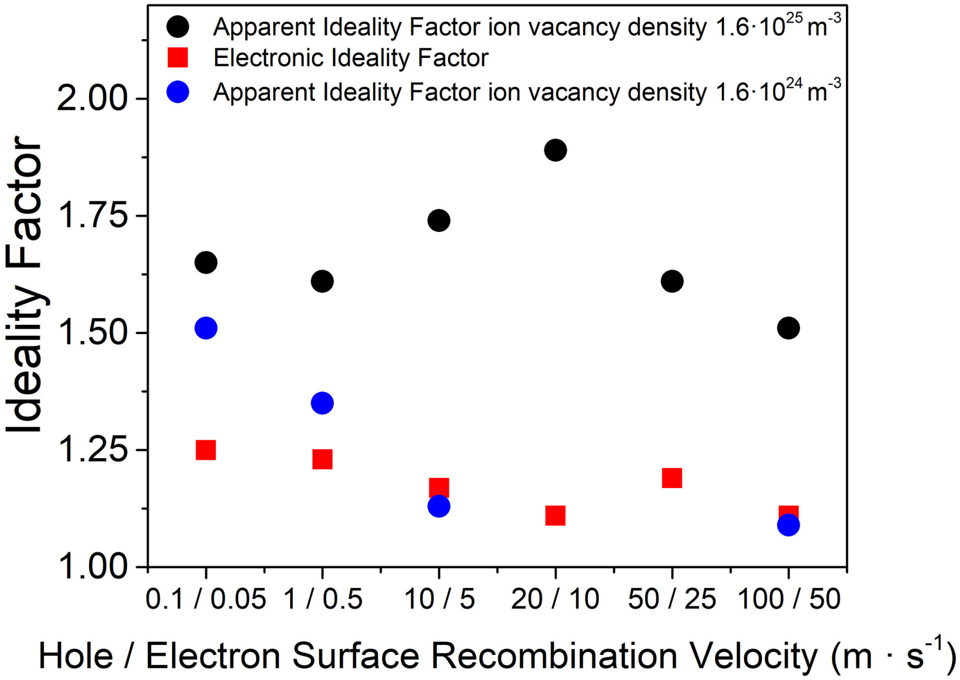

Figure 7.5: n_{AP} and n_{EL} as predicted by the numerical DD model as a function of the surface recombination velocities (holes at the ETL interface and electrons at the HTL interface) and two values of the ion vacancy density. Note that n_{EC} is the same (within the numerical error) for both values of the ion vacancy density.

Two important conclusions can be extracted from Figure 7.5:

1. The value of n_{AP} decreases as the surface recombination velocities increase.
2. The value of n_{AP} is lower, for lower concentrations of ionic vacancies.

The simulation results points to a mixed mechanism to explain the experimental behaviour: an increase of surface recombination[29] and a diminution of ionic vacancies as the illumination intensity increases. Additional, in Figure 7.5 the n_{EL}[20] determined using Eq. 2.79 (see *Chapter* 2) is included.

It is a real possibility that the number of ionic vacancies can vary with illumination in organic lead halide perovskites. Mosconi *et al.* described a mechanism of vacancy-ion annihilation in the $CH_3NH_3PbI_3$ perovskite[45]. Several authors have also reported "defect curing" effects upon illumination[46], also for mixed perovskites[47]. There are also studies in the literature where a beneficial effect of light soaking is reported, via a reduction of structural defects and/or ionic migration[48,49]. However, it is important to note that there are also reports where increases of photoconductivity upon illumination for isolated perovskite films are observed[50], attributed to the formation of ionic defects upon illumination also has a theoretical interpretation[51]. Despite these divergent works, Motti *et al.*[52] showed theoretically that processes of "defect curing" and "defect formation" can coexist and compete. This means that a plethora of behaviors can be found depending on the perovskite's nature and preparation routes. In this case, given the DD simulation results, a reduction of the number of mobile ions at high irradiance can offer the best plausible explanation for the simultaneous reduction of n_{AP} observed in both the steady-state V_{OC} measurements and the impedance. The concurrent enhancement of surface recombination can also contribute to this regime change when the illumination intensity is high enough.

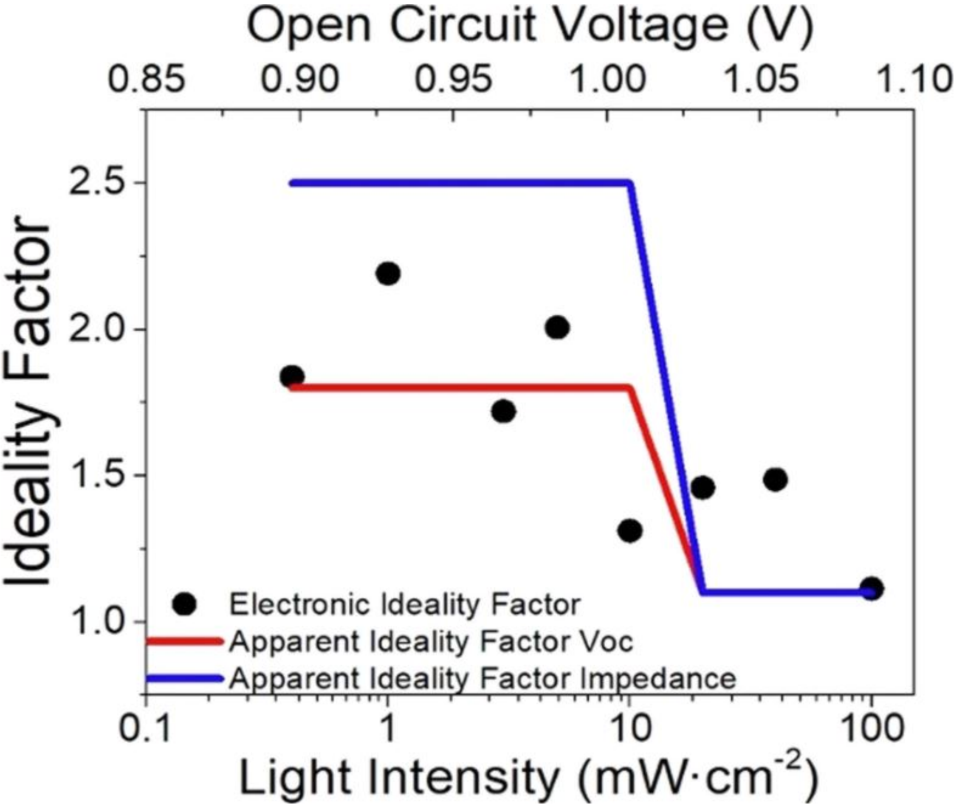

Figure 7.6: n_{AP} and n_{EL} as derived from Eqs. 6.1, 2.25 and 2.79 from the experimental results of Figure 7.2

In Figures 7.5 and 7.6 n_{EL} obtained via Eq. 2.79 (see *Chapter* 2) from the DD simulations and experiments is compared with n_{AP} obtained from Eqs. 6.1 and 2.25. As expected, n_{EL} is found to be the same for different concentrations of ionic vacancies (only n_{AP} is changed by modifying the concentration of vacancies). This result is confirmed in the simulations of Figure 7.5. On the other hand, n_{EL} becomes smaller as the contribution of surface recombination is increased, reflecting the change in the recombination mechanism. This behavior is also observed in the experimental data of Figure 7.6, where this parameter moves from values larger than 2 ± 0.25 at a low light intensity to values close to unity at high illumination intensity.

The n_{AP} reaches higher values but also shows a tendency to lower its value as the light intensity is increased. As mentioned before, this parameter depends on the ionic density, which appears to decrease when the cell is subjected to higher irradiance. As shown by the simulation, in Figure 7.6, only when the ion density is sufficiently low does n_{AP} attain a value as low as 1. In summary, the transition observed in the experiments appears to be a combination of a change of recombination mechanism (with a growing contribution coming from surface recombination) and a reduction of the density of ionic defects in the perovskite material as the light intensity is increased.

7.4 Conclusion

This *Chapter* describes a change of behavior of the recombination-related parameters in mesoscopic mixed perovskite ($FA_{0.71}MA_{0.29}PbI_{2.9}Br_{0.1}$) solar cells with changes in illumination intensity. This feature appears to be a crossover from a regime characterized by a n_{AP} of 1.8-2.5 at low irradiances to another characterized by an ideality factor approaching unity at high irradiances. This regime change is observed in steady-state measurements of the OCP and small-perturbation impedance measurements at OC, both as a function of the light intensity. The transition takes place in both experiments at potentials of 1.03 V, corresponding to an AM1.5G irradiance of 10 $mW{\cdot}cm^{-2}$. With the help of DD simulations, this peculiar behavior can be attributed to a combination of two effects. The first corresponds to a transition from a regime in which surface recombination across the transport layer interfaces is less critical than bulk SRH recombination in the perovskite to another one where surface recombination is dominant. The second effect corresponds to a reduction of ionic vacancies in the perovskite active layer with increases in illumination intensity, leading to a reduction of the values of n_{AP}. DD simulations show that n_{AP} derived from steady-state measurements of the OCP vs light intensity or, equivalently, from R_{HF} extracted from the impedance spectra is affected by the concentration of mobile ionic vacancies present in the perovskite material. The description based on n_{EL} turns out to be a better tool with which to determine the dominant recombination mechanism in a particular solar cell device.

Bibliography

[1] C. Eames, J. M. Frost, P. R. F. Barnes, B. C. O'Regan, A. Walsh, and M. S. Islam, "Ionic transport in hybrid lead iodide perovskite solar cells," *Nature Communications*, vol. 6, p. 7497, 2015-06.

[2] S. D. Stranks, G. E. Eperon, G. Grancini, C. Menelaou, M. J. P. Alcocer, T. Leijtens, L. M. Herz, A. Petrozza, and H. J. Snaith, "Electron-hole diffusion lengths exceeding 1 micrometer in an organometal trihalide perovskite absorber," *Science*, vol. 342, no. 6156, pp. 341–344, 2013.

[3] D. Kiermasch, P. Rieder, K. Tvingstedt, A. Baumann, and V. Dyakonov, "Improved charge carrier lifetime in planar perovskite solar cells by bromine doping," *Scientific Reports*, vol. 6, p. 39333, Dec. 2016.

[4] L. Contreras-Bernal, M. Salado, A. Todinova, L. Calio, S. Ahmad, J. Idígoras, and J. A. Anta, "Origin and whereabouts of recombination in perovskite solar cells," *The Journal of Physical Chemistry C*, vol. 121, no. 18, pp. 9705–9713, 2017.

[5] W. Tress, M. Yavari, K. Domanski, P. Yadav, B. Niesen, J. P. C. Baena, A. Hagfeldt, and M. Graetzel, "Interpretation and evolution of open-circuit voltage, recombination, ideality factor and subgap defect states during reversible light-soaking and irreversible degradation of perovskite solar cells," *Energy & Environmental Science*, vol. 11, pp. 151–165, 2018.

[6] O. Almora, K. T. Cho, S. Aghazada, I. Zimmermann, G. J. Matt, C. J. Brabec, M. K. Nazeeruddin, and G. Garcia-Belmonte, "Discerning recombination mechanisms and ideality factors through impedance analysis of high-efficiency perovskite solar cells," *Nano Energy*, vol. 48, pp. 63–72, 2018.

[7] L. Contreras-Bernal, S. Ramos-Terrón, A. Riquelme, P. P. Boix, J. Idígoras, I. Mora-Seró, and J. A. Anta, "Impedance analysis of perovskite solar cells: a case study," *Journal of Materials Chemistry A*, vol. 7, no. 19, pp. 12191–12200, 2019-05.

[8] M. Stolterfoht, C. M. Wolff, J. A. Márquez, S. Zhang, C. J. Hages, D. Rothhardt, S. Albrecht, P. L. Burn, P. Meredith, T. Unold, and D. Neher, "Visualization and suppression of interfacial recombination for high-efficiency large-area pin perovskite solar cells," *Nature Energy*, vol. 3, no. 10, p. 847, 2018-10.

[9] M. Stolterfoht, P. Caprioglio, C. M. Wolff, J. A. Márquez, J. Nordmann, S. Zhang, D. Rothhardt, U. Hörmann, Y. Amir, A. Redinger, L. Kegelmann, F. Zu, S. Albrecht, N. Koch, T. Kirchartz, M. Saliba, T. Unold, and D. Neher, "The impact of energy alignment and interfacial recombination on the internal and external open-circuit voltage of perovskite solar cells," *Energy & Environmental Science*, vol. 12, no. 9, pp. 2778–2788, 2019-09.

[10] W.-J. Yin, T. Shi, and Y. Yan, "Unusual defect physics in CH3nh3pbi3 perovskite solar cell absorber," *Applied Physics Letters*, vol. 104, no. 6, p. 063903, 2014.

[11] J. M. Azpiroz, E. Mosconi, J. Bisquert, and F. D. Angelis, "Defect migration in methylammonium lead iodide and its role in perovskite solar cell operation," *Energy & Environmental Science*, vol. 8, no. 7, pp. 2118–2127, 2015.

[12] A. Pockett, G. E. Eperon, N. Sakai, H. J. Snaith, L. M. Peter, and P. J. Cameron, "Microseconds, milliseconds and seconds: deconvoluting the dynamic behaviour of planar perovskite solar cells," *Physical Chemistry Chemical Physics*, vol. 19, no. 8, pp. 5959–5970, 2017-02.

[13] A. Guerrero, G. Garcia-Belmonte, I. Mora-Sero, J. Bisquert, Y. S. Kang, T. J. Jacobsson, J.-P. Correa-Baena, and A. Hagfeldt, "Properties of contact and bulk impedances in hybrid lead halide perovskite solar cells including inductive loop elements," *The Journal of Physical Chemistry C*, vol. 120, no. 15, pp. 8023–8032, 2016-04.

[14] R. A. Belisle, W. H. Nguyen, A. R. Bowring, P. Calado, X. Li, S. J. C. Irvine, M. D. McGehee, P. R. F. Barnes, and B. C. O'Regan, "Interpretation of inverted photocurrent transients in organic lead halide perovskite solar cells: proof of the field screening by mobile ions and determination of the space charge layer widths," *Energy & Environmental Science*, vol. 10, pp. 192–204, Jan. 2017.

[15] D. A. Jacobs, H. Shen, F. Pfeffer, J. Peng, T. P. White, F. J. Beck, and K. R. Catchpole, "The two faces of capacitance: New interpretations for electrical impedance measurements of perovskite solar cells and their relation to hysteresis," *Journal of Applied Physics*, vol. 124, no. 22, p. 225702, 2018-12.

[16] J. Nelson, *The Physics of Solar Cells.* Imperial College Press, 1 ed., 2003-09.

[17] A. Gagliardi and A. Abate, "Mesoporous Electron-Selective Contacts Enhance the Tolerance to Interfacial Ion Accumulation in Perovskite Solar Cells," *ACS Energy Letters*, vol. 3, pp. 163–169, Jan. 2018.

[18] I. Zarazua, G. Han, P. P. Boix, S. Mhaisalkar, F. Fabregat-Santiago, I. Mora-Seró, J. Bisquert, and G. Garcia-Belmonte, "Surface recombination and collection efficiency in perovskite solar cells from impedance analysis," *The Journal of Physical Chemistry Letters*, vol. 7, no. 24, pp. 5105–5113, 2016-12.

[19] N. Courtier, “Interpreting Ideality Factors for Planar Perovskite Solar Cells: Ectypal Diode Theory for Steady-State Operation,” *Physical Review Applied*, vol. 14, p. 024031, Aug. 2020.

[20] L. J. Bennett, A. J. Riquelme, N. E. Courtier, J. A. Anta, and G. Richardson, “A new ideality factor for perovskite solar cells and an analytical theory for their impedance spectroscopy response,” *arXiv:2105.11226 [cond-mat, physics:physics]*, May 2021. arXiv: 2105.11226.

[21] W. S. Yang, J. H. Noh, N. J. Jeon, Y. C. Kim, S. Ryu, J. Seo, and S. I. Seok, “High-performance photovoltaic perovskite layers fabricated through intramolecular exchange,” *Science*, vol. 348, no. 6240, pp. 1234–1237, 2015-06.

[22] L. Qiu, L. K. Ono, Y. Jiang, M. R. Leyden, S. R. Raga, S. Wang, and Y. Qi, “Engineering interface structure to improve efficiency and stability of organometal halide perovskite solar cells,” *The Journal of Physical Chemistry B*, 2017-05.

[23] M. L. Davies, M. Carnie, P. J. Holliman, A. Connell, P. Douglas, T. Watson, C. Charbonneau, J. Troughton, and D. Worsley, “Compositions, colours and efficiencies of organic–inorganic lead iodide/bromide perovskites for solar cells,” *Energy Materials*, vol. 9, pp. 482–485, Dec. 2014.

[24] A. Castro-Chong, W. Qiu, J. Bastos, N. Tchamba Yimga, R. García-Rodríguez, J. Idígoras, J. A. Anta, T. Aernouts, and G. Oskam, “Impact of the implementation of a mesoscopic TiO2 film from a low-temperature method on the performance and degradation of hybrid perovskite solar cells,” *Solar Energy*, vol. 201, pp. 836–845, 2020-05.

[25] D. Pitarch-Tena, T. T. Ngo, M. Vallés-Pelarda, T. Pauporté, and I. Mora-Seró, “Impedance spectroscopy measurements in perovskite solar cells: Device stability and noise reduction,” *ACS Energy Letters*, vol. 3, no. 4, pp. 1044–1048, 2018.

[26] N. E. Courtier, G. Richardson, and J. M. Foster, “A fast and robust numerical scheme for solving models of charge carrier transport and ion vacancy motion in perovskite solar cells,” *Applied Mathematical Modelling*, vol. 63, pp. 329–348, 2018-07.

[27] N. E. Courtier, J. M. Cave, A. B. Walker, G. Richardson, and J. M. Foster, “IonMonger: a free and fast planar perovskite solar cell simulator with coupled ion vacancy and charge carrier dynamics,” *Journal of Computational Electronics*, vol. 12, pp. 396–409, 2019-09.

[28] T. J. Jacobsson, J.-P. Correa-Baena, M. Pazoki, M. Saliba, K. Schenk, M. Grätzel, and A. Hagfeldt, “Exploration of the compositional space for mixed lead halogen perovskites for high efficiency solar cells,” *Energy & Environmental Science*, vol. 9, pp. 1706–1724, May 2016.

[29] P. Caprioglio, C. M. Wolff, O. J. Sandberg, A. Armin, B. Rech, S. Albrecht, D. Neher, and M. Stolterfoht, “On the origin of the ideality factor in perovskite solar cells,” *Advanced Energy Materials*, vol. 10, no. 27, p. 2000502, 2020.

[30] P. Caprioglio, M. Stolterfoht, C. M. Wolff, T. Unold, B. Rech, S. Albrecht, and D. Neher, “On the Relation between the Open-Circuit Voltage and Quasi-Fermi Level Splitting in Efficient Perovskite Solar Cells,” *Advanced Energy Materials*, vol. 9, no. 33, p. 1901631, 2019.

[31] A. Todinova, L. Contreras-Bernal, M. Salado, S. Ahmad, N. Morillo, J. Idígoras, and J. A. Anta, “Towards a Universal Approach for the Analysis of Impedance Spectra of Perovskite Solar Cells: Equivalent Circuits and Empirical Analysis,” *ChemElectroChem*, vol. 4, no. 11, pp. 2891–2901, 2017.

[32] I. Zarazúa, S. Sidhik, T. Lopéz-Luke, D. Esparza, E. De la Rosa, J. Reyes-Gomez, I. Mora-Seró, and G. Garcia-Belmonte, “Operating mechanisms of mesoscopic perovskite solar cells through impedance spectroscopy and j–v modeling,” *The Journal of Physical Chemistry Letters*, pp. 6073–6079, 2017-11.

[33] A. Pockett, G. E. Eperon, T. Peltola, H. J. Snaith, A. Walker, L. M. Peter, and P. J. Cameron, “Characterization of planar lead halide perovskite solar cells by impedance spectroscopy, open-circuit photovoltage decay, and intensity-modulated photovoltage/photocurrent spectroscopy,” *The Journal of Physical Chemistry C*, vol. 119, no. 7, pp. 3456–3465, 2015-02.

[34] E. J. Juarez-Perez, R. S. Sanchez, L. Badia, G. Garcia-Belmonte, Y. S. Kang, I. Mora-Sero, and J. Bisquert, “Photoinduced giant dielectric constant in lead halide perovskite solar cells,” *The Journal of Physical Chemistry Letters*, pp. 2390–2394, 2014-06.

[35] O. Almora, I. Zarazua, E. Mas-Marza, I. Mora-Sero, J. Bisquert, and G. Garcia-Belmonte, “Capacitive dark currents, hysteresis, and electrode polarization in lead halide perovskite solar cells,” *The Journal of Physical Chemistry Letters*, vol. 6, no. 9, pp. 1645–1652, 2015-05.

[36] L. Contreras, J. Idígoras, A. Todinova, M. Salado, S. Kazim, S. Ahmad, and J. A. Anta, “Specific cation interactions as the cause of slow dynamics and hysteresis in dye and perovskite solar cells: a small-perturbation study,” *Physical Chemistry Chemical Physics*, vol. 18, no. 45, pp. 31033–31042, 2016-11.

[37] J.-P. Correa-Baena, S.-H. Turren-Cruz, W. Tress, A. Hagfeldt, C. Aranda, L. Shooshtari, J. Bisquert, and A. Guerrero, “Changes from bulk to surface recombination mechanisms between pristine and cycled perovskite solar cells,” *ACS Energy Letters*, vol. 2, no. 3, pp. 681–688, 2017.

[38] S. Wheeler, D. Bryant, J. Troughton, T. Kirchartz, T. Watson, J. Nelson, and J. R. Durrant, “Transient Optoelectronic Analysis of the Impact of Material Energetics and Recombination Kinetics on the Open-Circuit Voltage of Hybrid Perovskite Solar Cells,” *The Journal of Physical Chemistry C*, vol. 121, pp. 13496–13506, June 2017.

[39] J. Jiménez-López, B. M. D. Puscher, D. M. Guldi, and E. Palomares, “Improved Carrier Collection and Hot Electron Extraction Across Perovskite, C60, and TiO2 Interfaces,” *Journal of the American Chemical Society*, vol. 142, pp. 1236–1246, Jan. 2020.

[40] M. J. Hong, L. Zhu, C. Chen, L. Tang, Y.-H. Lin, W. Li, R. Johnson, S. Chattopadhyay, H. J. Snaith, C. Fang, and J. G. Labram, “Time-Resolved Changes in Dielectric Constant of Metal Halide Perovskites under Illumination,” *Journal of the American Chemical Society*, vol. 142, pp. 19799–19803, Nov. 2020. Publisher: American Chemical Society.

[41] I. Zarazua, J. Bisquert, and G. Garcia-Belmonte, “Light-induced space-charge accumulation zone as photovoltaic mechanism in perovskite solar cells,” *The Journal of Physical Chemistry Letters*, pp. 525–528, 2016.

[42] O. Almora, C. Aranda, and G. Garcia-Belmonte, “Do Capacitance Measurements Reveal Light-Induced Bulk Dielectric Changes in Photovoltaic Perovskites?,” *The Journal of Physical Chemistry C*, vol. 122, pp. 13450–13454, June 2018.

[43] S.-M. Yoo, S. J. Yoon, J. A. Anta, H. J. Lee, P. P. Boix, and I. Mora-Seró, “An equivalent circuit for perovskite solar cell bridging sensitized to thin film architectures,” *Joule*, 2019-08.

[44] W. Tress, “Perovskite solar cells on the way to their radiative efficiency limit – insights into a success story of high open-circuit voltage and low recombination,” *Advanced Energy Materials*, vol. 7, no. 14, p. 1602358, 2017-07.

[45] E. Mosconi, D. Meggiolaro, H. J. Snaith, S. D. Stranks, and F. D. Angelis, “Light-induced annihilation of Frenkel defects in organo-lead halide perovskites,” *Energy & Environmental Science*, vol. 9, pp. 3180–3187, Oct. 2016.

[46] D. W. deQuilettes, W. Zhang, V. M. Burlakov, D. J. Graham, T. Leijtens, A. Osherov, V. Bulović, H. J. Snaith, D. S. Ginger, and S. D. Stranks, “Photo-induced halide redistribution in organic–inorganic perovskite films,” *Nature Communications*, vol. 7, p. 11683, May 2016.

[47] F. Zheng, X. Wen, T. Bu, S. Chen, J. Yang, W. Chen, F. Huang, Y. Cheng, and B. Jia, “Slow Response of Carrier Dynamics in Perovskite Interface upon Illumination,” *ACS Applied Materials & Interfaces*, vol. 10, pp. 31452–31461, Sept. 2018.

[48] H.-S. Kim and A. Hagfeldt, “Photoinduced Lattice Symmetry Enhancement in Mixed Hybrid Perovskites and Its Beneficial Effect on the Recombination Behavior,” *Advanced Optical Materials*, vol. 7, no. 9, p. 1801512, 2019.

[49] A. Pockett, D. Raptis, S. M. P. Meroni, J. Baker, T. Watson, and M. Carnie, “Origin of exceptionally slow light soaking effect in mesoporous carbon perovskite solar cells with AVA additive,” *The Journal of Physical Chemistry C*, vol. 123, no. 18, pp. 11414–11421, 2019-05.

[50] G. Y. Kim, A. Senocrate, T.-Y. Yang, G. Gregori, M. Grätzel, and J. Maier, “Large tunable photoeffect on ion conduction in halide perovskites and implications for photodecomposition,” *Nature Materials*, vol. 17, pp. 445–449, May 2018.

[51] D. Barboni and R. A. D. Souza, “The thermodynamics and kinetics of iodine vacancies in the hybrid perovskite methylammonium lead iodide,” *Energy & Environmental Science*, 2018-08.

[52] S. G. Motti, D. Meggiolaro, A. J. Barker, E. Mosconi, C. A. R. Perini, J. M. Ball, M. Gandini, M. Kim, F. De Angelis, and A. Petrozza, “Controlling competing photochemical reactions stabilizes perovskite solar cells,” *Nature Photonics*, vol. 13, pp. 532–539, Aug. 2019.

Chapter 8

Understanding equivalent circuits in perovskite solar cells. Insights from drift-diffusion simulation

Abstract

In general, equivalent circuits are used to evaluate the EIS results of PSCs. Frequently these are justified via empirical constructions, and the actual physical meaning of the elements remains disputed. In this Chapter, planar PSCs are simulated using IonMonger DD model to generate impedance spectra, avoiding intrinsic experimental difficulties. The ionic and electronic properties of the device can be changed individually in the simulations, so their effects can be directly observed. This Chapter evaluates the resulting EIS spectra by comparing two commonly used equivalent circuits with series and parallel connections, respectively, which can be used to analyze the EIS of a PSC. This Chapter provides an analysis of the physical interpretation of the elements of each circuit and how to correlate the elements of one circuit with the elements of the other to have a direct picture of the physical processes occurring in the device.

This Chapter is based on Publication 5 of this Thesis: Antonio J. Riquelme *et al.* Submitted to Physical Chemistry Chemical Physics.

8.1 Introduction

The dual nature of perovskites has attracted much attention from the scientific community, and EIS arises as one of the main tools to understand the fundamental/microscopic mechanisms occurring within the device. Potentially, it can give access to diffusion coefficients, chemical capacitances or electronic recombination properties via parameters such as diffusion lengths or lifetimes[1–7]. This technique is frequency-dependent (see *Chapter* 3), which allows to separate different kinetic processes, but their inherent chemical instability[8] of the system caused by the MHP dual nature and its lack of reproducibility complicate the measurement and interpretation of the results[9–11]. Most impedance studies rely on equivalent circuits to fit the experimental results and give the data a meaningful physical interpretation, as described in *Chapter* 3[7,12–16]. However, some aspects of these equivalent circuits can be problematic while identifying the actual physical process behind each circuit element and choosing between different equivalent circuits that produce similar fitting results. Also, the presence of unknown additional processes in the studied material, which are not accounted for in the equivalent circuits, may interfere with the results. In addition, the measurement itself can affect the system under study, altering the results. For this reason, using DD modeling[17–19], where the situation is fully controlled with a set of fixed parameters, is an ideal scenario for testing different equivalent circuits avoiding the mentioned uncertainty of the experiments, looking for the physical interpretation of equivalent circuit elements.

As it has been said before (see *Chapters* 3, 6 and 7) most standard Nyquist plots of halide PSCs present two arcs at HF and LF regions. The two equivalent circuits described in *Chapter* 3 (see Figures 3.13 and 3.14) can fit this sort of spectra using the minimum number of elements and both have been used in the PSC literature.

The equivalent circuit in Figure 3.13 of *Chapter* 3 (SEC) links each main signal in the impedance, separated by different frequency regions, to a single -RC- element in a sequence connected in series. R_{HF} and C_{HF} represent the combination of resistance and capacitance that produce the signal of high frequencies. On the other hand, R_{LF} and C_{LF} correspond to the arc at low frequencies. As mentioned in *Chapter* 6, to account for extra features that are sometimes found in impedance spectra of PSCs, there are extensions of this model reported in the literature trying to reproduce exotic phenomena like loops or signals in the negative quadrant[20–23]. However, increasing the complexity of the equivalent circuit does not help to gain insight into the source of these phenomena unless these additional elements have a well-defined physical meaning.

Moreover, the circuit shown in Figure 3.14[15] of *Chapter* 3, (PEC), also can originate two arcs in the Nyquist plot. It is derived by the popular equivalent circuit devised to analyse DSSCs[6,24,25] (see Figure 3.11 in *Chapter* 3) and their solid state version in particular. PEC has also been proposed by Pascoe et al[4] and Moia et al[26] following a different approach. Different works in the literature using this model have been reviewed in detail[21]. A detailed description of this model can be found in *Chapter* 3, along with the derivation of R_{HF}, R_{LF} and R_{DC} from its parameters (see Eqs. 3.39, 3.40 and 3.41).

Both circuits can be adequately used to fit the EIS spectra, but the physical interpretation of each element depending on the circuit employed differs. This *Chapter* focuses on the physical meaning of elements in both models and the correlations in order to obtain ones from the others for a complete picture of PSC physical interpretation. For example, PEC aims to adequately separate the DC resistive components of the solar cell (via Eq.3.41) from the indirect effect of the dielectric relaxation-like element contained in the R_{dr}/C_{dr} branch. However, the exact physical/molecular meaning of R_{dr} and C_{dr} parameters remain unclear. On the other hand, the quest for understanding the behavior of PSC at DC conditions has been tackled in different manners, for instance, by assessing which resistance allows for the determination of CCE at different points of the *JV* curve, as shown in *Chapter* 6 (see Eq. 6.5).

To obtain insight into the dominant recombination mechanism acting in the absorbing layer of the PSC, one of the most used tool is n_{AP}[2,22,27,28], which can be extracted using Eqs. 6.1 and 2.25 of *Chapter* 6. In addition to this, two novel "ideality factors" concepts have been proposed by Courtier[29] and Bennett *et al.*[30]: n_{EC} that depends on the ionic properties of the device like n_{AP}, and n_{EL} that accounts only for the electronic recombination mechanism, removing the interference from the ionic distribution. Both concepts of ideality factors are described in detail in *Chapter* 3 and are also used in *Chapter* 7.

DD modeling, extensively used in this thesis, provides complete control over the device and measurement parameters included as inputs into the model. This kind of tool has been widely applied to PSCs trying to address different topics, such as inductive loops and oversized LF capacitances[31], or the source of the LF response[26]. Modeling may also shed light on open questions such as the causes of the different inverted device response[32], the role of ions as efficiency-limiting species in PSCs[33] or the equivalence under ideal conditions between the CCE obtained from the recombination resistance[34] in Eq. 6.5 with the IQE of the device.

One of the advantages of DD modeling is that one can specify beforehand the dominant recombination mechanism (in contrast to experiments). Therefore, applying Eq.2.79 and 2.70 it would be possible to distinguish between the real electronic recombination resistance[22,35] and any other aspect affecting the charge collection and recombination of carriers, like modulations in the electric potential produced by ion migration. Besides, DD simulations permit individual changes of each system element, avoiding interferences between them, as in real devices. Therefore, analyzing the impact of different parameters on different circuit elements can help unravel the physical processes behind them and the physical interpretation of the EC element. In this *Chapter*, DD simulations are used to compare two widely used equivalent circuits to attempt to understand the physical meaning of their elements and their role in determining the device's properties at a steady state.

8.2 Numerical methods

8.2.1 Drift-Diffusion Modeling

Simulated impedance spectra were generated using the three layer *IonMonger*[17,18] DD model described in *Chapter* 3. The key common parameters used in the simulations were the same included in Table C.1 in *Appendix* C (see *Chapter* 6). These parameters remain constant unless stated otherwise, for instance when they are modified to assess the impact of a certain parameter on the studied circuit elements. Two recombination scenarios were considered:

- Scenario 1: Only SRH recombination in the bulk
- Scenario 2: Only SRH recombination at the bulk interfaces with the ETL and the HTL.

The same carrier pseudolifetimes as in *Chapter* 6, (see Table C.1 in *Appendix* C). For surface recombination, the velocities included in Table E.2 in *Appendix* E were considered. These velocities produce a similar J_{SC} to that obtained with the bulk recombination of Scenario 1.

For each case study included in this *Chapter*, *JV* curves were simulated under five different light intensities (1000 W·m^{-2}, 500 W·m^{-2}, 100 W·m^{-2}, 50 W·m^{-2} and 5 W·m^{-2}) of monochromatic light of 465 nm, recording the

J_{SC} and V_{OC}. The *JV* curves were produced at a 0.01 mV·s^{-1}, simulating steady-state conditions. The obtained V_{OC} is the DC voltage applied for each impedance simulation under OC conditions (see *Chapter* 3). An additional set of impedance simulations were done to determine the CCE using Eq. 6.5. For this set, instead of considering V_{OC} as DC voltage, an applied bias V, taking values between 0 and V_{OC}, was imposed, at a fixed illumination of 1000 W·m^{-2} (NOC conditions). The resulting *JV* curves under 1000 W·m^{-2} of monochromatic light of 465 nm for each recombination scenario and the values of V_0 at which impedance simulations were conducted for the NOC study can be seen in Figure 8.1 together with the DD simulated EIS spectra using the same parameters that for the *JV* curves simulation, with DC voltage being the V_{OC} of the respective *JV* curves.

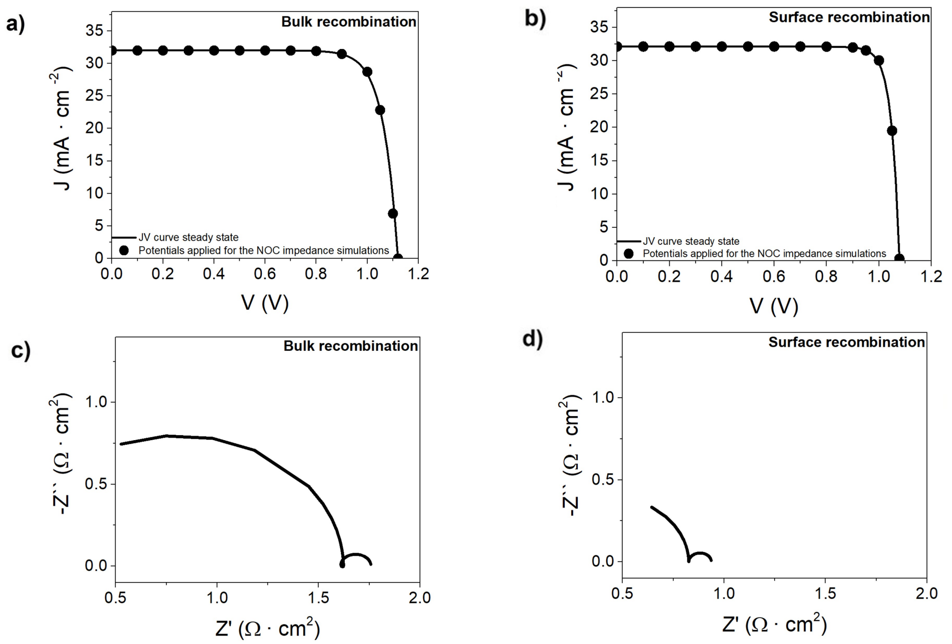

Figure 8.1: Simulated *JV* curves under 1000 W·m^{-2} of 465 nm monochromatic illumination using the standard set of parameters of *Chapter* 6 and (a) bulk recombination of Table E.1 and (b) surface recombination of Table E.2 of *Appendix* E. Circles represent applied potentials at which additional impedance spectra were simulated to determine the CCE outside OC conditions. DD simulated impedance spectra at V_{OC} under 1000 W·m^{-2} of 465 nm monochromatic illumination using the standard set of parameters of *Chapter* 6 and (c) bulk recombination and (d) surface recombination. Note that as the simulated illumination is at a wavelength where PSCs' absorption is maximized, so in panels (a) and (b) J_{SC} values are larger than what would be expected from a *JV* curve using a solar simulator.

The resistances obtained from the fits were used to calculate CCE from Eq.6.5 and compared to the steady-state internal quantum efficiency (IQE) at the same voltages each impedance was run. The IQE was obtained converting the photocurrent at each voltage of the *JV* curve into quantum efficiency via Eq. 3.9 (see *Chapters* 3 and 5).

8.2.2 Impedance Characterization

After obtaining the simulated impedance spectra, the results are fitted using the equivalent circuits described in Figure 3.13 (SEC) and 3.14 (PEC) with the *Scribner ZView* 2 software. In addition, for the circuit in Figure 3.14, R_{HF} and R_{LF} where calculated applying Eq. 3.39 and 3.40 (see *Chapter* 3).

The capacitor elements are represented in the equivalent circuits as CPE (like in *Chapters* 6 and 7) including capacitive and resistive elements, as was described in *Chapter* 3.

8.3 Results and discussion

8.3.1 Impedance spectra from drift-diffusion simulations

Using the three layers *IonMonger* DD model with the standard parameters set of *Chapter* 6 and the two recombination scenarios (SRH in the bulk or in the surface) in Tables E.1 and E.2 in *Appendix* E, two typical spectra are obtained, as depicted in Figure 8.1 (c) and (d). It is found that for both conditions the spectra respond to the typical 2-semicircle pattern commonly observed for PSCs[2], as described in *Chapter* 3 and observed in *Chapters* 6 and 7. For the bulk recombination (see Figure 8.1c) a small loop appears between the two semicircles, as previously observed experimentally in some cases[20,21,36,37] and observed in *Chapter* 6. As for the surface recombination case (see Figure 8.1d) it is observed that the HF arc is shifted to higher frequencies, making it barely observable in the selected frequency range. However, as can be observed in Figure E.1 in *Appendix* E, the first arc moves toward lower frequencies as the light intensity decreases, showing a full semicircle below 100 W·m^{-2}.

8.3.2 Analysis of resistances and capacitances resulting from the fits

Both sets of spectra were fitted applying the equivalent circuits described in *Chapter* 3 for PSCs (see Figures 3.13 and 3.14). In Figure 8.1c, a small inductive loop is observed between the two main arcs. SEC does not account for this feature, while the PEC model can fit loops without any additional elements, a small loop between the two main semicircles, as can be seen in Figure E.2 of *Appendix* E. Thus, the SEC fit of these spectra was done with and without an inductor between the two RC elements to confirm that this feature does not interfere with the final results. As for PEC, the DD simulated device is a perfectly planar device so the simplified general model can be used[15].

From the fit using both equivalent circuits and applying Eq. 3.39 and 3.40 (see *Chapter* 3) for PEC results, several resistances and capacitances can be obtained. Results are presented in Figures 8.2 and 8.3.

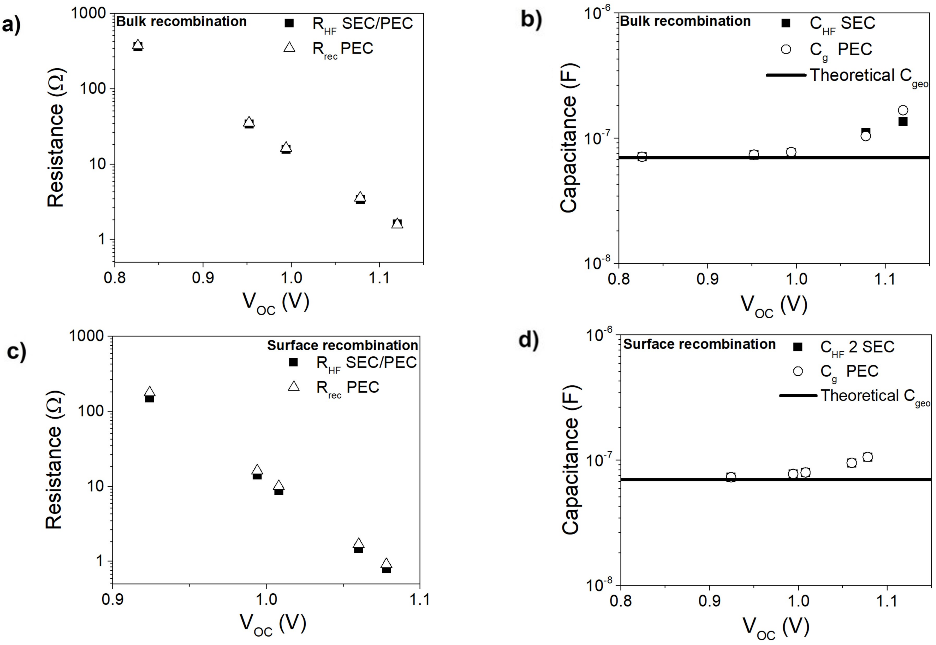

Figure 8.2: Resistances and capacitances extracted from the fit using SEC and PEC to the DD impedance simulated spectra with bulk recombination (a, b) and pure surface recombination (c, d). R_{HF} and R_{rec} (a, c) and C_{HF} and C_g (b, d).

By definition, the R_{HF} calculated in Eq. 3.39 from the parameters of PEC is equivalent to the R_{HF} extracted from SEC. As both resistances showed, as expected, equivalent values, only differing due to numerical error in the fitting process, in Figure 8.2 and throughout this *Chapter*, they are considered equivalent.

The same happens for the capacitances included in the b and d panels of Figure 8.2, where similar results for C_{HF} in SEC and C_g in PEC are obtained. It can be observed how at low voltages, they present a flat behavior, while as the light intensity and the generated V_{OC} increases, the capacitances start an exponential rise, as has been discussed in literature[38]. It has also been shown in *Chapters* 6 and 7. As for the flat region of the capacitances, it can be confirmed that, as expected and observed in *Chapter* 6, it coincides with the geometrical capacitance of the device[23,39] given by Eq. 2.67

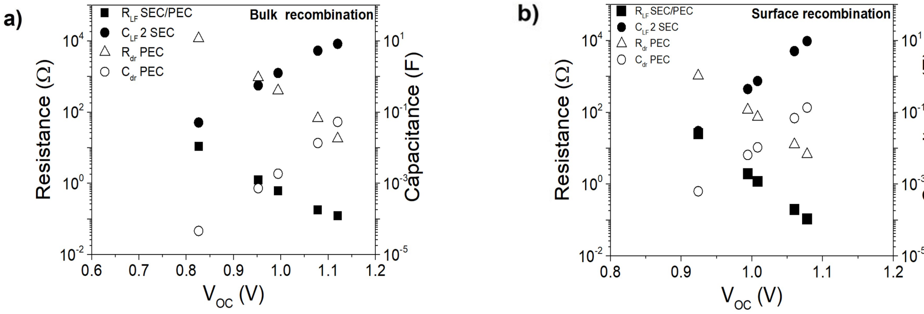

Figure 8.3: LF and dielectric relaxation-like capacitances and resistances extracted from the fit using SEC and PEC to the DD impedance simulated spectra with bulk recombination (a) and surface recombination (b).

As happened for R_{HF}, by definition the R_{LF} calculated via Eq. 3.40 from the circuit parameters of PEC is equivalent to the R_{LF} extracted from SEC. Thus, in Figure 8.3 and along the rest of this *Chapter*, they are considered equivalent as R_{LF}. This equivalence between models has already been discussed in the literature[14,16].

Finally, regarding the LF and *dr* resistances and capacitances in Figure 8.3, R_{LF} from both circuits, and the *dr* resistance from the PEC show an exponential voltage dependence with a slope which is reciprocal of the slope of the LF and *dr* capacitances[2,34]. The *dr* elements from PEC do not coincide with the elements of LF RC from SEC, but the trend lines of their voltage-dependence are very similar. Therefore, although the *dr* branch of PEC is not equivalent to the LF RC element in SEC, it can be said that they share a common origin.

8.3.3 Electronic ideality factor

As has been previously mentioned (see *Chapters* 3, 6 and 7), the resistance that quantifies the recombination loss is of major interest in most characterization studies applied to PSCs. To gain insight into this issue, R_{HF} and the values for R_{rec} obtained from PEC were inserted into Eq. 2.25 to obtain n_{AP}. The result was compared to the value obtained from the dependence of V_{OC} on light intensity in Eq.6.1. The values of n_{EL} and n_{EC} were also calculated using Eqs. 2.79 and 2.70. Note that the set of parameters was chosen so that the recombination lifetime and the electronic diffusion coefficient give a diffusion length much larger than the thickness of the perovskite layer so that there is no transport limitation. This means that the $R_{rec}+R_t/3$ resistance from PEC can be simplified as R_{rec}. Results are presented in Figure 8.4.

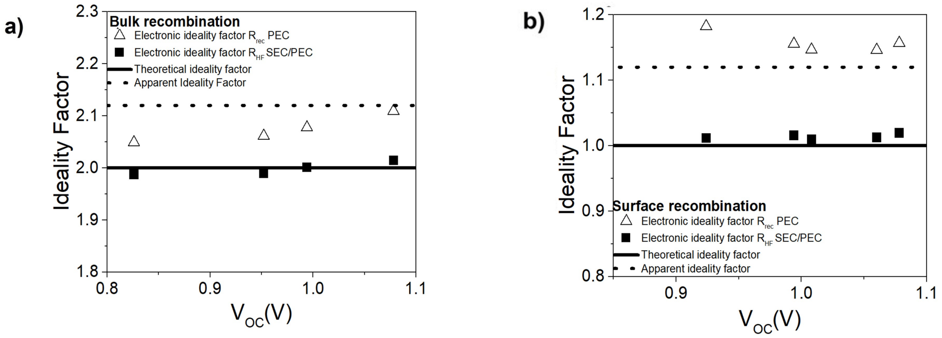

Figure 8.4: Theoretical ideality factor for each pure recombination mechanism and n_{AP} (solid and dashed lines) and n_{EL} calculated with Eq.2.79 R_{HF} (squares) and $R_{rec}+R_t/3$ (triangles) from the fit of impedance spectra with bulk recombination (a) and pure surface recombination (b).

First of all, the recombination process can be unambiguously fixed as for the DD simulations. Thus, it can be confirmed that an n_{EL} of exactly 2 and 1 are found for bulk recombination and surface recombination, respectively.

The value of n_{AP} calculated from both Eq. 2.25 with R_{HF} and $R_{rec}+R_t/3$ and from Eq. 6.1 is very similar. However, the values are slightly higher than the expected values for the pure recombination processes (2 and 1 for bulk and surface recombination, respectively). This fact confirms the observation described by Courtier[29] and Bennett and coworkers[30] that this so-called ideality factor not only contains information about the electronic recombination mechanism but also has an ionic contribution (see *Chapter* 3). With regards to n_{EL} calculated from Eq.2.79, it is observed that when the R_{HF} from both equivalent circuits is introduced, the value matches with the expected value for both pure recombination scenarios. On the other hand, n_{EL} calculated when the included resistance is taken to be R_{rec} is closer to n_{AP} than to the expected ideality factor value for a pure recombination mechanism. This is not a surprise, looking at Eq.3.40, R_{rec} results from adding R_{HF} and R_{LF}. This value is similar to the resistance included in Eq.2.70 to determine n_{EC}. As explained in *Chapter* 3, this ectypal factor includes the same ionic contribution like n_{AP}. These results indicate that the main electronic recombination process can be extracted from the R_{HF} while the R_{rec} from PEC provides n_{AP}, that is the ideality factor also extracted from the *JV* curve and from the relation V_{OC} vs light intensity. In previous works, as mentioned in *Chapter* 6, an "ionically modulated recombination process" has also been proposed[31,40,41], so while R_{HF} allows to get insight into the main electronic recombination process, R_{rec} includes information about the ionic influence on recombination.

8.3.4 Charge collection efficiency

As mentioned in *Chapters* 5 and 6, the CCE via Eq.6.5 can be compared to the IQE obtained from the *JV* curve applying Eq.3.9. Assuming that there exist no external sources of charge loss such as poor injection or parasitic resistances, CCE and IQE have to be equivalent. This requirement is naturally fulfilled in the DD simulations.

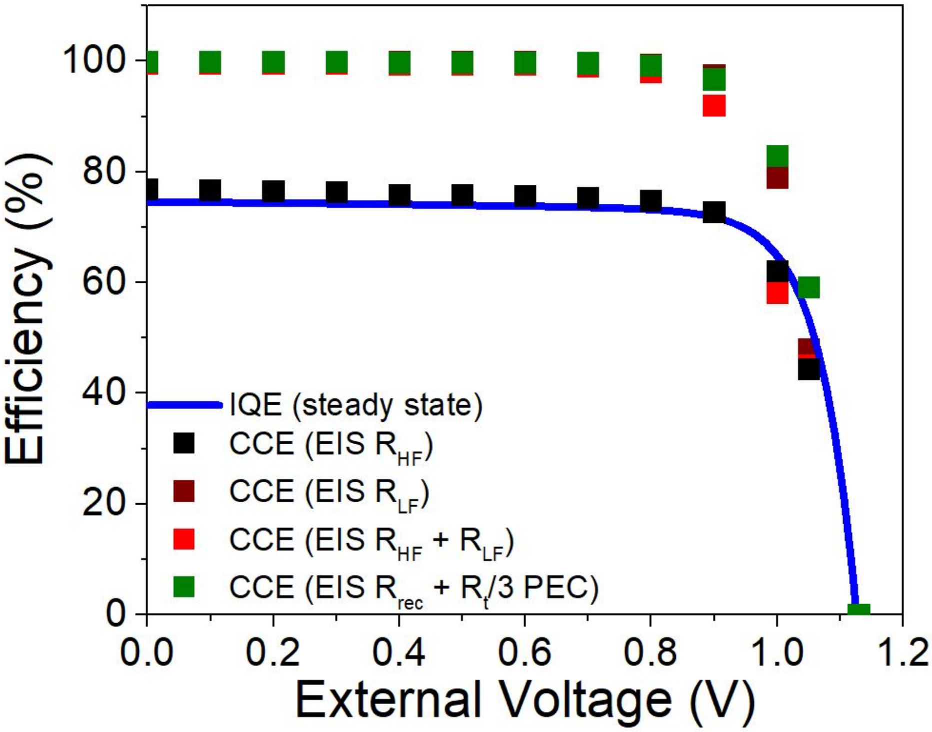

Figure 8.5: CCE obtained by applying Eq.6.5 for several choices of the resistance (as extracted fromm SEC and PEC). The calculations were done for an artificially "bad" cell by introducing a transport limitation. The illumination was fixed and the V varied between 0 and V_{OC}. It includes a comparison to the IQE calculated using Eq.3.9 with the JV curve obtained at a 0.01 mV·s^{-1} scan rate using standard parameters of *Chapter* 6. Note that as this set of parameters produce negative values for R_{dr} leading to unrealistic CCE calculations, these were not included in this Figure. Results for the standard set of data (without transport limitation) can be found in Figure E.3 of *Appendix* E.

Little information can be extracted from Figure E.3 in *Appendix* E as all combinations lead to similar results as is expected when the absence of charge collection limitations leads to a 100% quantum efficiency at short-circuit. However, when an artificial charge transport limitation is introduced in the bulk recombination system by setting the value of the electronic (electrons and holes) diffusion coefficient one order of magnitude lower than the value of the standard set of parameters used in *Chapter* 6, it is found that only by using R_{HF} in Eq.6.5 a coincidence between CCE and IQE for both equivalent circuits is obtained, as can be observed in Figure 8.5. This suggests that R_{HF} acts as a true recombination resistance, as it is enough to reproduce the collection efficiency, at least for the stationary situation.

For further insight into the behavior of the different resistances according to the CCE determination, a mixed recombination scenario was considered, using the changes that were introduced in *Chapter* 6 to the standard parameter set to reproduce a real device (see Table C.2 in *Appendix* C). Figure 8.6 presents a comparison between the results obtained from Eq.6.5 for the different choices of the recombination resistance in both equivalent circuits.

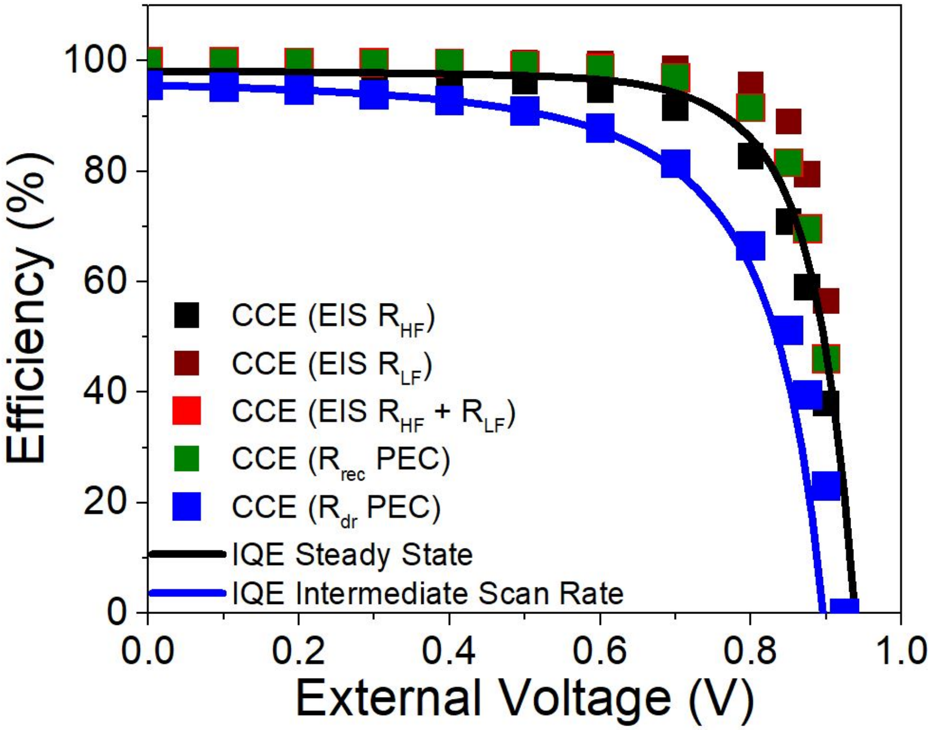

Figure 8.6: CCE obtained from applying Eq.6.5 for several choices of the resistance (as extracted from SEC and PEC). The parameters used in DD simulation were similar to the used in *Chapter* 6 to reproduce the experimental spectra of a PSC. CCE values are compared to the IQE calculated using Eq.3.9 for a *JV* curve at a scan rate of 0.01 mV·s^{-1}, to simulate the *JV* curve at both steady-state (black line), and a scan rate of 500 mV·s^{-1} (blue line).

As can be observed in Figure 8.6, although the *dr* branch of PEC is not supposed to intervene in the charge collection of the device, the IQE extracted from a *JV* using a scan rate of 500 mV·s^{-1}, is only reproduced by the CCE calculated using R_{dr}. In this case, the scan rate results from dividing the whole range of voltages applied during the *JV* scan by the time constant resulting from the LF feature in the impedance spectra obtained with this set of parameters. In addition, to reproduce the IQE extracted from the *JV* curve at a steady-state, the use of both R_{rec} and R_{HF} approximate the calculation of CCE to the steady-state IQE. However, as can be observed in Figure E.5 in *Appendix* E, the CCE extracted from R_{HF} is slightly lower than IQE while the CCE from R_{rec} is slightly higher than the IQE. Furthermore, CCE from R_{HF} seems to reproduce better the IQE at potentials close to 0 V, while R_{rec} produces a better match between CCE and IQE close to V_{OC}. As for the behavior of the *JV* outside the steady-state, the only way of catching the changes happening at different scan rates is by considering R_{dr}.

8.3.5 Impact of drift-diffusion parameters on circuit elements

Finally, as mentioned before, a key advantage of using a DD model instead of actual devices is that complete control of the parameters is possible in numerical simulations. For instance, each parameter can be modified individually, avoiding the interactions and domino effects happening in experiments by changing one element of the device.

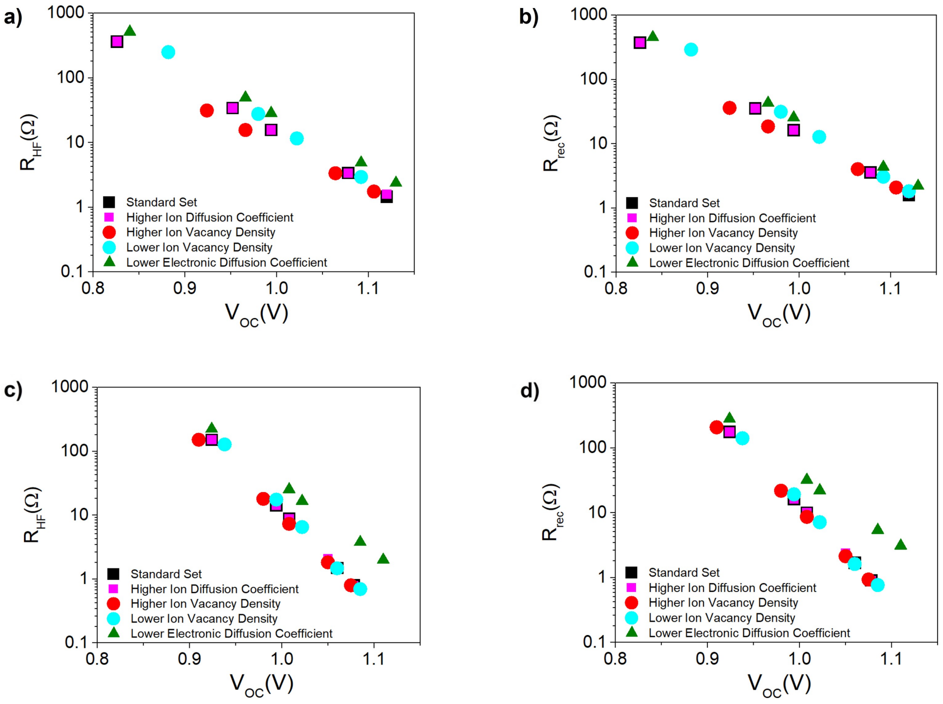

Figure 8.7: R_{rec}+$R_t/3$ and R_{HF} extracted by applying PEC and SEC to the spectra resulting from the DD simulations using the standard parameter set of *Chapter* 6. The following changes were introduced: Increase the ion diffusion coefficient by one order of magnitude (magenta squares), increase and reduce by a factor of 2 the ion vacancy density (red and cyan circles) and reduce the electronic diffusion coefficient by one order of magnitude (green triangles) with bulk recombination (a, b) and surface recombination (c, d).

In this line of thought, the effect of altering the ionic properties of the system and the electronic transport is analyzed in Figure 8.7. As shown in Figure 8.2, R_{HF} obtained from SEC and PEC are similar so that they can be used indiscriminately. For the bulk recombination scenario, the ion vacancy density slightly affects both R_{rec} and R_{HF}, not only quantitatively but also in the slope of the voltage-dependence and, consequently, n_{AP}. However, for the surface recombination dominated simulated device, both resistances are not affected by any changes in the ionic elements of the parameters. Therefore, the impact of the Debye layer thickness (see Figure 2.7 in *Chapter* 3) on the recombination processes inside the device seems to be more relevant when the dominating recombination process takes place in the bulk of the perovskite, while surface recombination is not affected by this feature. In general, all these results confirm the dominant electronic nature of the HF component of the resistance.

On the other hand, the transport limitation introduced by decreasing one order of magnitude of the electronic diffusion coefficient affects the surface recombination simulated device much more than the bulk recombination scenario. This can indicate that the transport component in the $R_{rec}+R_t/3$ resistance is much more relevant when the dominating recombination process takes place at the interface than when it only happens in the bulk. The effect of the transport limitation is also perceptible in R_{HF}, which indicates that the HF arc contains information on electronic transport processes too. This result suggests that different information can be extracted from the same circuit element depending on the physical characteristics of a particular device, such as the dominant recombination process.

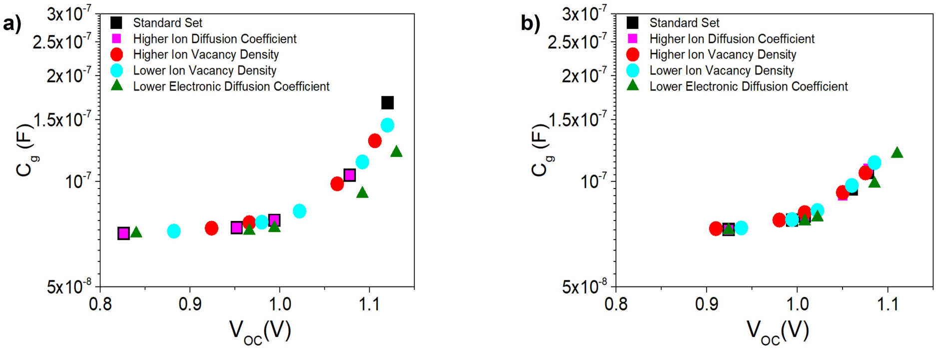

Figure 8.8: C_g extracted by applying PEC and SEC to the spectra resulting from the DD simulations using the standard set of parameters of *Chapter* 6. The following changes were introduced: Increase the ion diffusion coefficient by one order of magnitude (magenta squares), increase and reduce by a factor of two the ion vacancy density (red and cyan circles) and reduce the electronic diffusion coefficient by one order of magnitude (green triangles) with bulk recombination (a) and only surface recombination (b).

As displayed in Figure 8.8, the increase of C_{HF} for high values of the voltage is standard for all parameter sets. However, while the ionic parameters do not affect this feature for any of the recombination scenarios considered (as expected for the HF signal of the impedance), decreasing the electronic diffusion coefficient makes the increase of the capacitance less pronounced. In addition, the impact on the HF capacitance is more noticeable when recombination takes place in the bulk of perovskite than when the device is ruled by surface recombination. This can indicate that the exponential increase observed in C_g loses its geometric character and is more likely to be related to electronic charge accumulation in bulk, as discussed by Kiermasch *et al.*[38] rather than to the formation of the Debye layers or charge accumulation at the interfaces.

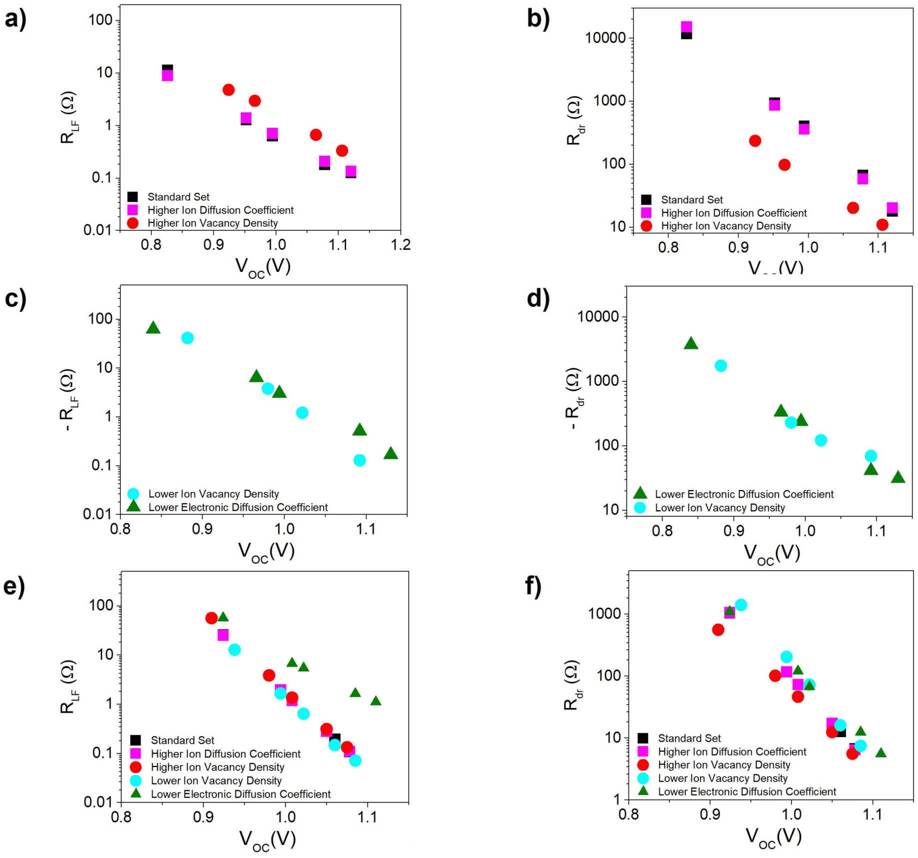

Figure 8.9: R_{LF} and R_{dr} extracted by applying PEC and SEC to the spectra resulting from the DD simulations using the standard set of parameters of *Chapter* 6. The following changes were introduced: Increase the ion diffusion coefficient by one order of magnitude (magenta squares), increase and reduce by a factor of two the ion vacancy density (red and cyan circles) and reduce the electronic diffusion coefficient by one order of magnitude (green triangles) with bulk recombination (up) and only surface recombination (bottom). For some parameter changes (decreasing the ion vacancy density and the electronic diffusion coefficient), the resistances change to negative sign. Therefore, bulk limited scenarios are split between positive ((a) and (b)) and negative ((c) and (d)) resistance values. For surface recombination, no change in the sign was observed, so all the values are included in panels (e) for R_{LF} and (f) for R_{dr}.

Focusing on the low frequency of the spectra, in Figure 8.9 LF resistances in both equivalent circuits are plotted for different choices of the ionic parameters and the "speed" of the electronic motion. It can be observed that for a bulk recombination simulated device, a decrease in the ion vacancy density generates a switch of the sign of the real and imaginary values of the LF feature, as has been already reported[19]. Furthermore, R_{LF} and R_{dr} respond in the same way, giving negative values. On the other hand, the ionic diffusion coefficient has no impact on the size of the LF feature but increasing the ion vacancy density increases the size of this feature, as also observed in *Chapter* 6. However, when recombination takes place at the interfaces, ionic parameters have a much smaller impact on both R_{dr} and R_{LF}, indicating that changes in the formation of the Debye layers and the consequent ion-modulated recombination process are most relevant when recombination happens in the bulk of the perovskite and can be somehow neglected if recombination takes place at the interfaces.

As regards the impact of a decrease in the electronic diffusion coefficient, this significantly affects both recombination scenarios, changing the sign of R_{dr} and R_{LF} for bulk recombination. In contrast, with surface recombination, R_{dr} is only slightly affected while R_{LF} shows not only a meaningful increase but also a change in its slope of the voltage-dependence. These results indicate that the source of the LF feature of the impedance spectra is affected by a coupling of the formation of the Debye layers and the charge collection processes, which affect both the high and LF responses, as can be deduced from the derivation of PEC[15].

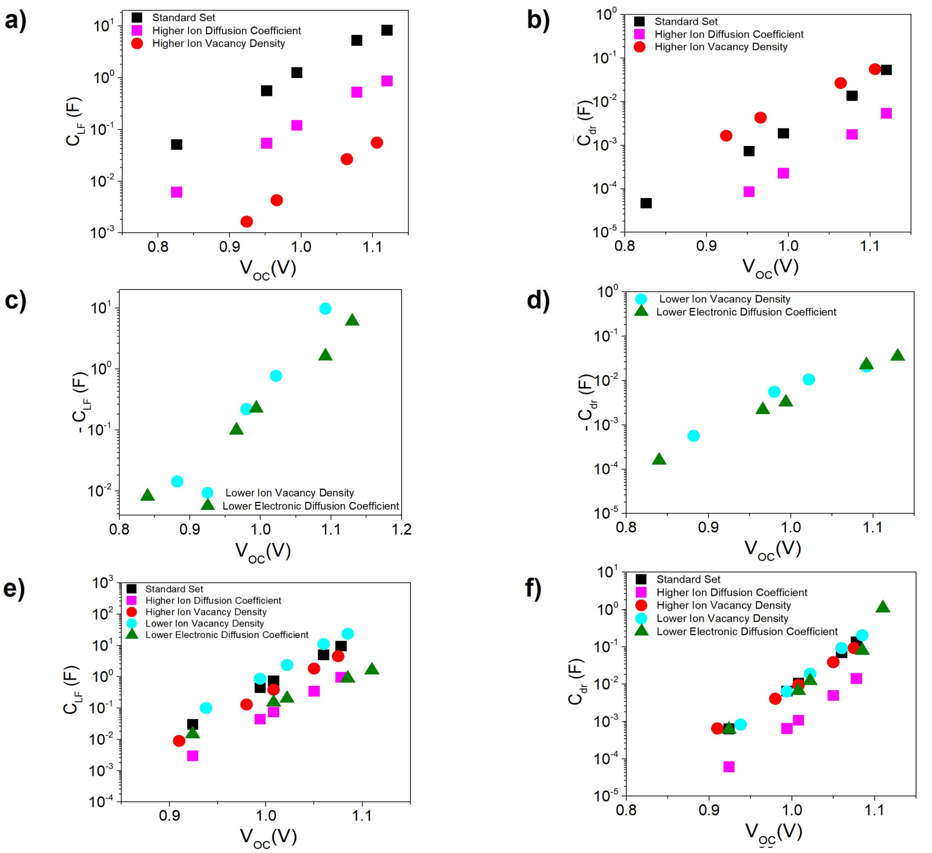

Figure 8.10: C_{dr} and C_{LF} extracted by applying PEC and SEC to the spectra resulting from the DD simulations using the standard set of parameters in *Chapter* 6. The following changes were introduced: Increase the ion diffusion coefficient by one order of magnitude (magenta squares), increase and reduce by a factor of two the ion vacancy density (red and cyan circles) and reduce the electronic diffusion coefficient by one order of magnitude (green triangles). For some parameter changes (decreasing the ion vacancy density and the electronic diffusion coefficient), the capacitances change to a negative sign as happens with the resistances in Figure 8.9. Therefore, bulk limited scenarios are split between positive ((a) and (b)) and negative ((c) and (d)) capacitance values. For surface recombination, no change in the sign was observed, so all the values are included in panels (e) for C_{dr} and (f) for C_{LF}.

In Figure 8.10 it can be observed how the ion vacancy density and the electronic diffusion coefficient affect the C_{LF} and C_{dr} in a similar way as the corresponding resistances. The ionic diffusion coefficient, on the other hand, which does not affect R_{LF} nor R_{dr}, does affect C_{LF} and C_{dr} for both recombination scenarios. The effect of the ionic parameters on both C_{dr} and C_{LF} as well as the electronic diffusion coefficient confirms that the origin of the LF feature in both equivalent circuits is the coupling of ionic accumulation and migration with the electronic transport/recombination properties. In addition, the fact that for the surface recombination case, C_{dr} is only affected by the ion diffusion coefficient while C_{LF} is affected by both ionic and electronic parameters suggests that the *dr* elements are affected mainly by the ionic properties of the device while C_{LF} also includes charge transport processes.

8.3.6 Summary of information extracted from the circuit elements

Finally, in Table 8.1 a summary of the impact of different parameters on the elements of both equivalent circuits are included. Furthermore, the key information obtained from them, as discussed earlier in this *Chapter*, is also mentioned.

Table 8.1: DD simulation parameters impact on different elements of the equivalent circuits.

SEC

Element	**Information extracted**
R_{HF}	It is equivalent to (R_{HF}) calculated from PEC. It is highly affected by the recombination mechanism and slightly affected by the ion vacancy density. It allows for the calculation of n_{EL} using Eq. 2.79 and the determination of CCE at steady-state through Eq. 6.5.
R_{LF}	It is equivalent to (R_{LF}) calculated from the PEC. It is strongly affected by the primary recombination process, the ion vacancy density, and electronic transport limitations while not dependent on the ionic diffusion coefficient. When the main recombination mechanism is surface recombination, it is only affected by the electronic diffusion coefficient. Combining bulk recombination with low ion vacancy densities or slow electronic diffusion coefficient can produce negative values.
C_{HF}	It presents similar values to the C_g extracted from the PEC. For low V_{OC} values, it coincides with the geometrical capacitance calculated by Eq. 2.67.
C_{LF}	This parameter shows negative values when bulk recombination is combined with lower ion vacancy density or electronic diffusion coefficient. It is affected by all the parameters studied (ionic and electronic). The influence of these parameters in combination with bulk recombination is much more intense than under the influence of surface recombination. With surface recombination, the transport limitation changes the slope.

PEC

Element	**Information extracted**
R_{rec}+$R_t/3$	It shows a behaviour similar to R_{HF} although it presents values a little larger and a slightly higher dependence on the electronic diffusion coefficient. Using this resistance with Eq. 2.79 gives values similar to n_{AP}.
R_{dr}	Like R_{LF}, its behavior strongly depends on the primary recombination mechanism, and the ion diffusion coefficient does not influence it. For bulk recombination, low ion vacancy density and electronic diffusion coefficient produce negative R_{dr} values, while for surface recombination, the influence of ionic parameters is minimal. Moreover, the impact of transport limitations is smaller for this element than for R_{LF}. It allows for the calculation of CCE through Eq. 6.5 at a given scan rate corresponding to the time constant of the LF signal of impedance.
C_g	Its behavior is similar to the described for C_{HF} of SEC.
C_{dr}	Like C_{LF}, it is affected by all the parameters included in this study under the presence of bulk recombination, producing negative values for low ion vacancy densities and electronic diffusion coefficients. However, unless for C_{LF}, under surface recombination, the only parameter affecting this element is the ion diffusion coefficient.
R_{HF}	Its behavior is similar to the described for R_{HF} of SEC.
R_{LF}	Its behavior is similar to the described for R_{LF} of SEC.

From the information gathered in table 8.1 the parallelisms are noticeable between the elements of both equivalent circuits. Some practical information can be extracted from the properties of the different elements analyzed in this *Chapter*. For instance, to avoid the interference of ionic driven mechanisms in the device's performance and obtain n_{EL} or the CCE at a steady-state, it is necessary to focus on the high frequencies of the impedance. On the other hand, to better understand the scan rate dependence of the CCE, it is required to consider the R_{dr}. This is because R_{dr} contains the ion-mediated dynamics of the device, which controls the collection efficiency away from the steady-state. The ionic parameters mainly influence the *LF* and the *dr* RC elements of SEC and PEC. Although the effect of the ion vacancy density and the ionic diffusion coefficient is usually entangled, R_{LF} and R_{dr} are not affected by the ionic diffusion coefficient.

8.4 Conclusion

This *Chapter* illustrates how DD modeling using the three layers *IonMonger* model can be very useful for simulating complete impedance spectra and analyzing the information extracted from different equivalent circuits used in the literature while avoiding most experimental uncertainties. Two equivalent circuits are compared in this *Chapter*: the widely extended empirical SEC and PEC used by Yoo et al., developed from the traditional equivalent circuit applied to DSSCs.

In general, the elements of both equivalent circuits give similar information, as shown in previous works discussing different configurations of the circuit elements used to reproduce the EIS of PSCs. The equivalence between the R_{HF} and R_{LF} extracted from SEC and the size of the arcs calculated from the elements of PEC are confirmation of this equivalence. In addition, there is a coincidence between the C_{HF} of SEC and C_g of PEC, while R_{LF} and C_{LF} from SEC qualitatively show a similar pattern to *dr* branch elements of PEC. This similarity is expected, as both equivalent circuits successfully reproduce a complex physicochemical system as PSCs.

From the calculation of n_{EL} and the CCE at a steady state, it can be concluded that the resistance caused by electronic recombination mechanisms is reflected in the high frequencies of the spectra. On the other hand, R_{rec}+$R_t/3$ extracted from PEC is confirmed to show a slightly stronger dependence on the electronic transport properties of the device than R_{HF} as expected from the $R_t/3$ presence on this circuit element. This also affects the calculation of CCE using this resistance and explains why it is impossible to match the CCE calculated with this resistance with the IQE extracted from the steady-state *JV* curve for electronic transport limited simulation. In addition, unless R_{HF} fails to reproduce the expected n_{EL} for the two pure recombination mechanisms studied in this perspective, it approximates n_{AP}. This confirms the interference of ionic-driven mechanisms in this circuit element.

The LF region of the spectra is governed by the LF RC element in SEC and the *dr* branch in PEC. As shown in this *Chapter*, these elements contain information related to ionic motion and, under the influence of bulk recombination, the electronic transport properties of the device. The qualitative properties of both elements are similar, attending to their dependence on the different parameters of the DD studied in this perspective, and there is a broad equivalence between R_{LF} and R_{dr} and between C_{LF} and C_{dr}, respectively. However, although no information can be extracted from using R_{LF} to calculate the CCE of the device, R_{dr} allows for reproducing the CCE of the cell outside the steady-state. Specifically, the CCE obtained from this resistance coincides with the IQE extracted from a simulated *JV* curve at a scan-rate reciprocal to the time constant of the LF arc of the impedance spectra. Finally, analyzing the impact on these circuit elements of different parameters of the DD simulation, it is observed that although the source of the LF signal is the combination of electron transport properties and ion motion, it is possible to isolate the effect produced by each of these DD parameters by comparing its impact on the resistance and capacitance of these circuit elements. Thus, if, for instance, the analysis of two devices produces different values for C_{LF} or C_{dr} but coincides for R_{LF} or R_{dr}, it can be inferred that there are changes in the ionic diffusion coefficient, given that both devices have the same primary recombination mechanism. Furthermore, if it is confirmed through n_{EL} that surface recombination is dominant, changes in the slope of R_{LF} or C_{LF} can suggest the presence of electronic transport limitations.

In summary, DD simulations have been applied to gain insight into the physical meaning of the different elements of two widely used equivalent circuits by analyzing the dependence of each element on different alterations artificially introduced in a completely controlled environment, as is numerical DD simulation, where each aspect of the device can be decided beforehand. By doing this, it is determined that only the R_{HF} contains information on the electronic recombination process of the device solely, allowing for the determination of n_{EL} and the steady-state CCE, avoiding the influence of ionic driven processes. It is also shown how to distinguish between the impact of the ionic diffusion coefficient and the density of ion vacancies by comparing the resistance and capacitance included in the LF element of SEC and the *dr* branch of PEC.

Bibliography

[1] A. Dualeh, T. Moehl, N. Tétreault, J. Teuscher, P. Gao, M. K. Nazeeruddin, and M. Grätzel, "Impedance spectroscopic analysis of lead iodide perovskite-sensitized solid-state solar cells," *ACS Nano*, vol. 8, no. 1, pp. 362–373, 2014.

[2] L. Contreras-Bernal, S. Ramos-Terrón, A. Riquelme, P. P. Boix, J. Idígoras, I. Mora-Seró, and J. A. Anta, "Impedance analysis of perovskite solar cells: a case study," *Journal of Materials Chemistry A*, vol. 7, no. 19, pp. 12191–12200, 2019.

[3] C. Aranda, J. Bisquert, and A. Guerrero, "Impedance spectroscopy of perovskite/contact interface: Beneficial chemical reactivity effect," *The Journal of Chemical Physics*, vol. 151, no. 12, p. 124201, 2019.

[4] A. R. Pascoe, N. W. Duffy, A. D. Scully, F. Huang, and Y.-B. Cheng, "Insights into planar CH3nh3pbi3 perovskite solar cells using impedance spectroscopy," *The Journal of Physical Chemistry C*, vol. 119, no. 9, pp. 4444–4453, 2015.

[5] "Impedance spectroscopy: Theory, experiment, and applications," 2005.

[6] F. Fabregat-Santiago, G. Garcia-Belmonte, I. Mora-Seró, and J. Bisquert, "Characterization of nanostructured hybrid and organic solar cells by impedance spectroscopy," *Physical Chemistry Chemical Physics*, vol. 13, no. 20, pp. 9083–9118, 2011.

[7] A. Guerrero, J. Bisquert, and G. Garcia-Belmonte, "Impedance Spectroscopy of Metal Halide Perovskite Solar Cells from the Perspective of Equivalent Circuits," *Chemical Reviews*, vol. 121, no. 23, pp. 14430–14484, 2021. Publisher: American Chemical Society.

[8] N. Rolston, A. D. Printz, J. M. Tracy, H. C. Weerasinghe, D. Vak, L. J. Haur, A. Priyadarshi, N. Mathews, D. J. Slotcavage, M. D. McGehee, R. E. Kalan, K. Zielinski, R. L. Grimm, H. Tsai, W. Nie, A. D. Mohite, S. Gholipour, M. Saliba, M. Grätzel, and R. H. Dauskardt, "Effect of cation composition on the mechanical stability of perovskite solar cells," *Advanced Energy Materials*, vol. 8, no. 9, p. 1702116, 2018.

[9] D. Pitarch-Tena, T. T. Ngo, M. Vallés-Pelarda, T. Pauporté, and I. Mora-Seró, "Impedance spectroscopy measurements in perovskite solar cells: Device stability and noise reduction," *ACS Energy Letters*, vol. 3, no. 4, pp. 1044–1048, 2018.

[10] A. Bou, A. Pockett, D. Raptis, T. Watson, M. J. Carnie, and J. Bisquert, "Beyond impedance spectroscopy of perovskite solar cells: Insights from the spectral correlation of the electrooptical frequency techniques," *The Journal of Physical Chemistry Letters*, pp. 8654–8659, 2020.

[11] A. Guerrero, J. You, C. Aranda, Y. S. Kang, G. Garcia-Belmonte, H. Zhou, J. Bisquert, and Y. Yang, "Interfacial degradation of planar lead halide perovskite solar cells," *ACS Nano*, 2015.

[12] J. Bisquert, I. Mora-Sero, and F. Fabregat-Santiago, "Diffusion–recombination impedance model for solar cells with disorder and nonlinear recombination," *ChemElectroChem*, pp. 289–296, 2013.

[13] A. Todinova, J. Idígoras, M. Salado, S. Kazim, and J. A. Anta, "Universal features of electron dynamics in solar cells with TiO contact: From dye solar cells to perovskite solar cells," *The Journal of Physical Chemistry Letters*, vol. 6, no. 19, pp. 3923–3930, 2015.

[14] A. Todinova, L. Contreras-Bernal, M. Salado, S. Ahmad, N. Morillo, J. Idígoras, and J. A. Anta, "Towards a Universal Approach for the Analysis of Impedance Spectra of Perovskite Solar Cells: Equivalent Circuits and Empirical Analysis," *ChemElectroChem*, vol. 4, no. 11, pp. 2891–2901, 2017.

[15] S.-M. Yoo, S. J. Yoon, J. A. Anta, H. J. Lee, P. P. Boix, and I. Mora-Seró, "An equivalent circuit for perovskite solar cell bridging sensitized to thin film architectures," *Joule*, 2019.

[16] E. v. Hauff and D. Klotz, "Impedance spectroscopy for perovskite solar cells: characterisation, analysis, and diagnosis," *Journal of Materials Chemistry C*, vol. 10, no. 2, pp. 742–761, 2022.

[17] N. E. Courtier, G. Richardson, and J. M. Foster, "A fast and robust numerical scheme for solving models of charge carrier transport and ion vacancy motion in perovskite solar cells," *Applied Mathematical Modelling*, vol. 63, pp. 329–348, 2018.

[18] N. E. Courtier, J. M. Cave, A. B. Walker, G. Richardson, and J. M. Foster, "IonMonger: a free and fast planar perovskite solar cell simulator with coupled ion vacancy and charge carrier dynamics," *Journal of Computational Electronics*, vol. 12, pp. 396–409, 2019.

[19] A. Riquelme, L. J. Bennett, N. E. Courtier, M. J. Wolf, L. Contreras-Bernal, A. B. Walker, G. Richardson, and J. A. Anta, "Identification of recombination losses and charge collection efficiency in a perovskite solar cell by comparing impedance response to a drift-diffusion model," *Nanoscale*, vol. 12, pp. 17385–17398, Aug. 2020. Publisher: The Royal Society of Chemistry.

[20] A. Guerrero, G. Garcia-Belmonte, I. Mora-Sero, J. Bisquert, Y. S. Kang, T. J. Jacobsson, J.-P. Correa-Baena, and A. Hagfeldt, "Properties of contact and bulk impedances in hybrid lead halide perovskite solar cells including inductive loop elements," *The Journal of Physical Chemistry C*, vol. 120, no. 15, pp. 8023–8032, 2016.

[21] M. Anaya, W. Zhang, B. C. Hames, Y. Li, F. Fabregat-Santiago, M. E. Calvo, H. J. Snaith, H. Míguez, and I. Mora-Seró, “Electron injection and scaffold effects in perovskite solar cells,” *Journal of Materials Chemistry C*, vol. 5, no. 3, pp. 634–644, 2017.

[22] O. Almora, K. T. Cho, S. Aghazada, I. Zimmermann, G. J. Matt, C. J. Brabec, M. K. Nazeeruddin, and G. Garcia-Belmonte, “Discerning recombination mechanisms and ideality factors through impedance analysis of high-efficiency perovskite solar cells,” *Nano Energy*, vol. 48, pp. 63–72, 2018.

[23] S. Ravishankar, C. Aranda, S. Sanchez, J. Bisquert, M. Saliba, and G. Garcia-Belmonte, “Perovskite solar cell modeling using light- and voltage-modulated techniques,” *The Journal of Physical Chemistry C*, vol. 123, no. 11, pp. 6444–6449, 2019.

[24] J. Bisquert, A. Zaban, and P. Salvador, “Analysis of the mechanisms of electron recombination in nanoporous TiO dye-sensitized solar cells. nonequilibrium steady-state statistics and interfacial electron transfer via surface states,” *Journal of Physical Chemistry B*, vol. 106, no. 34, pp. 8774–8782, 2002.

[25] F. Fabregat-Santiago, J. Bisquert, G. Garcia-Belmonte, G. Boschloo, and A. Hagfeldt, “Influence of electrolyte in transport and recombination in dye-sensitized solar cells studied by impedance spectroscopy,” *Solar Energy Materials and Solar Cells*, vol. 87, no. 1, pp. 117–131, 2005.

[26] D. Moia, I. Gelmetti, P. Calado, W. Fisher, M. Stringer, O. Game, Y. Hu, P. Docampo, D. Lidzey, E. Palomares, J. Nelson, and P. R. F. Barnes, “Ionic-to-electronic current amplification in hybrid perovskite solar cells: ionically gated transistor-interface circuit model explains hysteresis and impedance of mixed conducting devices,” *Energy & Environmental Science*, vol. 12, no. 4, pp. 1296–1308, 2019.

[27] J. Nelson, *The Physics of Solar Cells*. Imperial College Press, 1 ed., 2003.

[28] L. Contreras-Bernal, M. Salado, A. Todinova, L. Calio, S. Ahmad, J. Idígoras, and J. A. Anta, “Origin and whereabouts of recombination in perovskite solar cells,” *The Journal of Physical Chemistry C*, vol. 121, no. 18, pp. 9705–9713, 2017.

[29] N. Courtier, “Interpreting ideality factors for planar perovskite solar cells: Ectypal diode theory for steady-state operation,” *Physical Review Applied*, vol. 14, no. 2, p. 024031, 2020. Publisher: American Physical Society.

[30] L. J. Bennett, A. J. Riquelme, N. E. Courtier, J. A. Anta, and G. Richardson, “A new ideality factor for perovskite solar cells and an analytical theory for their impedance spectroscopy response,” *arXiv:2105.11226 [cond-mat, physics:physics]*, May 2021. arXiv: 2105.11226.

[31] D. A. Jacobs, H. Shen, F. Pfeffer, J. Peng, T. P. White, F. J. Beck, and K. R. Catchpole, “The two faces of capacitance: New interpretations for electrical impedance measurements of perovskite solar cells and their relation to hysteresis,” *Journal of Applied Physics*, vol. 124, no. 22, p. 225702, 2018.

[32] M. T. Neukom, A. Schiller, S. Züfle, E. Knapp, J. Ávila, D. Pérez-del Rey, C. Dreessen, K. P. Zanoni, M. Sessolo, H. J. Bolink, and B. Ruhstaller, “Consistent device simulation model describing perovskite solar cells in steady-state, transient, and frequency domain,” *ACS Applied Materials & Interfaces*, vol. 11, no. 26, pp. 23320–23328, 2019.

[33] J. Diekmann, P. Caprioglio, M. H. Futscher, V. M. Le Corre, S. Reichert, F. Jaiser, M. Arvind, L. P. Toro, E. Gutierrez-Partida, F. Peña-Camargo, C. Deibel, B. Ehrler, T. Unold, T. Kirchartz, D. Neher, and M. Stolterfoht, “Pathways toward 30% efficient single-junction perovskite solar cells and the role of mobile ions,” *Solar RRL*, vol. 5, no. 8, p. 2100219, 2021.

[34] I. Zarazúa, S. Sidhik, T. Lopéz-Luke, D. Esparza, E. De la Rosa, J. Reyes-Gomez, I. Mora-Seró, and G. Garcia-Belmonte, “Operating mechanisms of mesoscopic perovskite solar cells through impedance spectroscopy and j–v modeling,” *The Journal of Physical Chemistry Letters*, pp. 6073–6079, 2017.

[35] W. Tress, M. Yavari, K. Domanski, P. Yadav, B. Niesen, J. P. C. Baena, A. Hagfeldt, and M. Graetzel, “Interpretation and evolution of open-circuit voltage, recombination, ideality factor and subgap defect states during reversible light-soaking and irreversible degradation of perovskite solar cells,” *Energy & Environmental Science*, vol. 11, pp. 151–165, 2018.

[36] D. Klotz, “Negative capacitance or inductive loop? – a general assessment of a common low frequency impedance feature,” *Electrochemistry Communications*, vol. 98, pp. 58–62, 2019-01.

[37] E. Ghahremanirad, A. Bou, S. Olyaee, and J. Bisquert, “Inductive loop in the impedance response of perovskite solar cells explained by surface polarization model,” *The Journal of Physical Chemistry Letters*, vol. 8, no. 7, pp. 1402–1406, 2017.

[38] D. Kiermasch, A. Baumann, M. Fischer, V. Dyakonov, and K. Tvingstedt, “Revisiting lifetimes from transient electrical characterization of thin film solar cells; a capacitive concern evaluated for silicon, organic and perovskite devices,” *Energy & Environmental Science*, vol. 11, no. 3, pp. 629–640, 2018.

[39] A. Pockett, G. E. Eperon, T. Peltola, H. J. Snaith, A. Walker, L. M. Peter, and P. J. Cameron, “Characterization of planar lead halide perovskite solar cells by impedance spectroscopy, open-circuit photovoltage decay, and intensity-modulated photovoltage/photocurrent spectroscopy,” *The Journal of Physical Chemistry C*, vol. 119, no. 7, pp. 3456–3465, 2015.

[40] A. Pockett and M. J. Carnie, "Ionic influences on recombination in perovskite solar cells," *ACS Energy Letters*, vol. 2, no. 7, pp. 1683–1689, 2017.

[41] N. E. Courtier, J. M. Cave, J. M. Foster, A. B. Walker, and G. Richardson, "How transport layer properties affect perovskite solar cell performance: insights from a coupled charge transport/ion migration model," *Energy & Environmental Science*, vol. 12, pp. 396–409, 2018.

Chapter 9

Inverted hysteresis in n-i-p and p-i-n perovskite solar cells

Abstract

A combination of experimental studies and DD modeling has been used in this Chapter to investigate the appearance of inverted hysteresis, where the area under the JV curve for the reverse scan is lower than in the forward scan in PSCs. It is found that solar cells in the p-i-n configuration show inverted hysteresis at a sufficiently high scan rate, whereas n-i-p tend to have normal hysteresis. By examining the influence of the composition of charge transport layers, the perovskite film crystallinity, and the pre-conditioning treatment, the possible causes of the presence of normal and inverted hysteresis are identified. It is shown that during JV scans, the accumulation and depletion of ionic charge at the interfaces modify carrier transport within the perovskite layer and alter the injection and recombination of carriers at the interfaces. Additionally, it can be observed how the scan rate dependence of the degree of hysteresis has a universal shape, where the crossover scan rate between normal and inverted hysteresis depends on the ion diffusion coefficient and the nature of the transport layers.

This Chapter is based on Publication 6 of this Thesis: Rodrigo García-Rodríguez *et al.* Submitted to SolarRRL.

9.1 Introduction

As it was described in *Chapter* 2, hybrid MHP present mixed ionic-electronic properties[1] and exceptional optoelectronic properties, making them very appealing for a variety of applications[2–7] where robustness and stability of the material are crucial. The ionic nature of perovskites makes ion migration to play a significant role in all stability issues under operational conditions, that often are triggered by irreversible ionic displacements[8]. Mobile ion defects have been widely acknowledged to influence charge transport in PSCs through the generation of an electrostatic field profile that partially screens the field due to the applied bias and V_{bi}[9,10]. One of the most studied manifestations of ion migration PSCs is *JV* hysteresis, described in *Chapter* 2 (see Figure 2.8). Experimentally, it has been reported that hysteresis in *JV* curves varies with scan rate, scan direction, temperature, the crystallinity of the material, and nature of the contacts[11,12]. It is well established that the accumulation at the perovskite/selective contact interfaces causes hysteresis by modifying the internal electric field that drives charge carriers to the selective contacts[13–19], as shown in Figure 2.7 of *Chapter* 2. In addition, a second effect related to changes in charge carrier injection or extraction at the transport layer interfaces has also been linked to the occurrence of hysteresis[9,20,21]. As it was described in *Chapter* 2, the hysteresis is best quantified by the DoH[15,19], defined by Eq. 2.69. Positive values of DoH can be related to regular or normal hysteresis, while negative values correspond to inverted hysteresis.

Richardson[13] and Courtier *et al.*[15] used *IonMonger* DD model, extensively used in this Thesis (see description in *Chapter* 3 and its use in *Chapters* 6 7 and 8) to show that normal hysteresis can be explained by the slow accumulation of the mobile ions at the transport layer interfaces when the external voltage changes. This behavior causes a favorable internal electric field for charge collection in the reverse scan and an unfavorable internal electric field in the forward scan, hence DoH > 0. Cave *et al.*[19] showed that the scan rate at which the DoH reaches a maximum gives a measure of the time taken by the mobile ions responsible for moving through the perovskite layer, determined by D_{ion}. In contrast, inverted hysteresis has been much less studied. Although it has also been associated with the accumulation of charge at the interfaces and the formation of energy barriers[21–24], its origin is not well understood yet[10]. Experimentally, inverted hysteresis effects have been related to compositional changes in the perovskite[21,24] or to chemical treatments of the interfaces[25].

As explained in *Chapter* 2, PSCs can be built following n-i-p or p-i-n architectures, being the n-i-p configuration the most used in this Thesis. This *Chapter* includes systematic experimental and modelling studies of *JV* hysteresis in both n-i-p and p-i-n PSCs (see Figure 9.1). The experimental results show that inverted hysteresis, like normal hysteresis, is sensitive to several parameters:

1. The crystallinity of the perovskite layer (affecting ion and charge carrier transport through the perovskite layer).
2. The pre-bias potential (affecting ion accumulation and depletion near the perovskite/transport layer interfaces).
3. The nature of the transport layers (affecting charge extraction, injection and recombination at these interfaces).

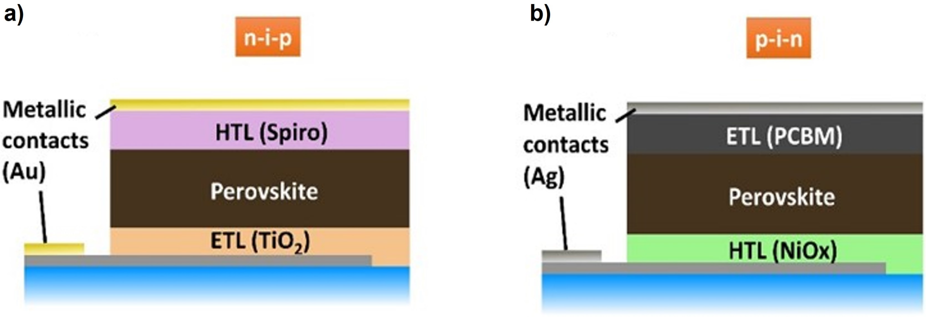

Figure 9.1: Schematic diagram of (a) n-i-p and (b) p-i-n PSC architectures studied in this *Chapter*.

It is shown in this *Chapter* that inverted hysteresis can be seen in both p-i-n and n-i-p cell configurations if a sufficiently large range of scan rates is explored. A simplified description of a PSC, based on the electron-hole-ion *IonMonger* DD model, widely used in this Thesis, backs up these results, reproducing the crossover from normal to inverted hysteresis well. Analysis of the DD simulation also helps identify how perovskite and charge transport layer properties affect the shape of the *JV* curves.

9.2 Fabrication and characterization of devices

9.2.1 Devices fabrication

All the devices included in this study use $MAPbI_3$ as the perovskite active layer. The cell used as a reference has a planar p-i-n structure, where the HTL is spin-coated mesoporous and planar NiO_x and the ETL is a PCBM ([6,6]-phenyl-C_6-butyric acid methyl ester) layer with bathocuproine and a silver contact. This configuration was selected due to its reported low hysteretic behaviour[20,26]. For comparison, mesoporous n-i-p cells with TiO_2 and spiro-OMeTAD as selective contacts were also studied. The n-i-p cells were prepared following a similar procedure to the described in

Chapter 5. Details of the fabrication of the p-i-n devices[27] with two different crystallinities (see Figure F.1) can be found in *Appendix* F. Devices were prepared in two different laboratories and with two different methodologies to ensure the universality of the results.

9.2.2 Characterization and modeling of the results

Following the procedure of previous works[20,27], two types of illumination were used. Cells were measured at one sun under a solar simulator AM1.5G and at 42.5 mW·cm^{-2} using a 465 nm blue LED. Unless otherwise stated, all *JV* measurements were carried out as follows: under the solar simulator, a pre-bias of 1.2 V was applied for 5 seconds to maximize the attainable photocurrent, followed by a potential linear scan from 1.2 V to 0 V and from 0 V to 1.2 V with a step size of 10 mV. At 1 sun, *JV* measurements were recorded at 100 mV·s^{-1}. Under blue LED illumination, a pre-bias of 1.2 V was applied for 20 seconds, followed by a potential linear scan similar to the one conducted under one sun illumination. The scan rate varied between 1 mV·s^{-1} and 1000 mV·s^{-1}. The range of scan rates used was tailored depending on the stability of the individual device being measured and the reliability of the results obtained at the fastest scan rates, evaluated by the shape of the *JV* scans. Longer pre-bias times were not investigated to prevent cell degradation. The characterization under one sun was done by measuring *JV* curves with a Keithley 2601A potentiostat. The illumination was provided by a single source, Class AAA solar simulator (T S Space Systems LTS, Bucks, United Kingdom). The illumination intensity was calibrated with a certified WPVS monocrystalline silicon reference cell with a KG3 filter (Fraunhofer, ISE). A mask of (0.25 cm^2) was employed to avoid contributions from scattered light from the glass. The influence of preconditioning was evaluated with two illumination sources. In addition to the one sun set up described above, a blue LED (470 nm, Thorlabs M470L3) was used at a light intensity of 42.5 mW·cm^{-2} with a ModuLab

XM PhotoEchem system (Solartron Analytical). Under one sun illumination, five pre-bias potentials (1200, 600, 0, -100, and again 1200 mV) were applied for 20 seconds before each measurement. With the blue LED illumination system, nine different pre-bias potentials were applied for 20 seconds before each measurement (1200, 900, 600, 300, 0, 300, 600, 900 and 1200 mV). The temperature was controlled with a Peltier element and a Precision Peltier Temperature Controller TEC-1091 (Meerstetter Engineering, Rubingen, Switzerland) to discard the influence of the possible heating of the sample under illumination.

To study the scan rate dependence of the hysteresis, the samples were characterized in the same set-up as for blue LED illumination described above. The cell was illuminated with a blue LED at OC for 15 minutes to ensure a stable V_{OC}. A pre-bias of 1.2 V was applied for 20 seconds before each scan. The cell was measured from OC to SC and immediately from SC to OC. After each scan, the cell was illuminated at V_{OC} for 2 minutes. The scan rates were selected following the procedure of a previous work[27], and the samples were measured from fast to slow scan rates with a step size of 10 mV between each point and no delay time between each point. The only delay time employed was 5 seconds under illumination before each sweep.

To determine the chemical composition and the effect of the solvent annealing on the crystallinity of the perovskite layer, X-ray diffraction measurements were employed with an STOE Transmission diffractometer system (STADI), employing Cu-Kα radiation, scanning from 10º to 60º (2θ), with a 0.01 step size and an integration time of 20 seconds per point.

The DD simulated *JV* curves were obtained using *IonMonger* model (see *Chapter* 3 for further details). For n-i-p devices the DD simulations were done using the standard set of parameters in *Chapter* 6 (see Table C.1 in *Appendix* C) and p-i-n devices were simulated using the set of parameters included in Table F.1.

9.3 Results and discussion

9.3.1 Experimental results

The p-i-n and n-i-p architectures devices studied in this *Chapter* produced the PV parameters collected in Table 9.1 under one sun illumination.

Table 9.1: PV parameters and experimental details of the devices studied in this *Chapter*. Efficiencies reported for p-i-n devices correspond to forward scan and for n-i-p in the reverse scan.

Device	J_{SC} **(mA·cm^{-2})**	**V$_{OC}$ (V)**	**Efficiency (%)**	**DoH (%)**
p-i-n mesoporous/planar spin coated NiO$_x$	18.1 ± 0.8	0.97 ± 0.01	12 – 14	-10/-60
p-i-n planar spin coated NiO$_x$	22.3 ± 1.8	1.02 ± 0.08	14 – 16	0/-25
n-i-p in glove box	19.8 ± 1.3	1.01 ± 0.04	12 – 15	-25/+25
n-i-p at ambient conditions	22.8 ± 1.5	1.04 ± 0.05	14 – 17	0/+13

Efficiencies obtained under one sun illumination for the p-i-n lie around 12-14% for the devices incluying mesoporous NiO$_x$ layer and 14-16% for the planar devices (see Figure F.2), in line with average values reported in the literature for p-i-n MAPbI$_3$-based solar cells with undoped NiO$_x$ layer as the HTL and PCBM as the ETL[28–30]. Although higher efficiencies have been reported for inverted PSCs with similar components to the ones studied in this *Chapter*[29–34] they usually require doping of the selective layers or to modify the perovskite layer to improve the efficiency. This *Chapter* aims at studying the hysteretic behavior of inverted perovskite devices without modification of the selective layers.

The scan rate variation of the DoH (see Eq. 2.69 in *Chapter* 2) was measured under blue illumination. Figure 9.2a shows results for cells with p-i-n configuration using only spin-coated planar NiO_x as HTL. Additionally, in Figure F.3 in *Appendix* F, the scan rate dependent DoH is compared for both n-i-p and p-i-n architectures and different types of NiO_x layers. In all cases, it is observed that the DoH changes sign for p-i-n cells at scan rates exceeding 5 $mV{\cdot}s^{-1}$. In contrast, in the most common configuration of a mesoporous n-i-p cell, the DoH is positive, being only negative at scan rates greater than 1000 $mV{\cdot}s^{-1}$. Extreme care was taken with high scan rate measurements to ensure that it was still possible to obtain sensible measurements under these conditions[25]. To confirm this, one device was measured from slow to fast scan rates, reproducing the same behavior, as can be observed in Figure 9.2a.

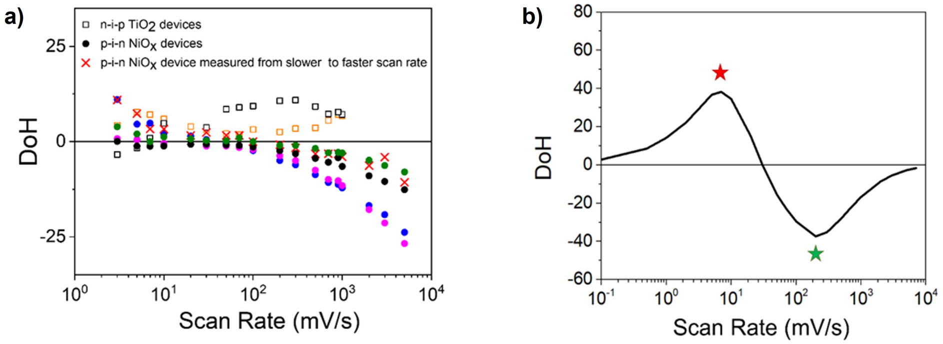

Figure 9.2: Measured (a) and simulated (b) DoH (%) vs scan rate ($mV{\cdot}s^{-1}$) under blue LED illumination (465 nm) and a preconditioning bias of 1.2 V for 20 s. In (a), circles correspond to p-i-n PSCs and squares to n-i-p PSCs. The hysteresis procedure starts with scanning at the highest scan rate, with successive scans towards slow scan rates, except in one test device (represented by crosses), where the opposite procedure was used for consistency. Simulated results (b) show the modelled DoH vs scan rate for the p-i-n PSC resulting from DD simulations using parameters of Table F.1 in *Appendix* F. The red star shows DoH_{max} the maximum regular hysteresis at a scan rate of 5 $mV{\cdot}s^{-1}$, and the green star DoH_{min} the maximum inverted hysteresis at a scan rate of 400 $mV{\cdot}s^{-1}$.

The results in Figure 9.2 and F.3 of *Appendix* F show that the nature of the contacts (e.g. TiO_2 and spiro-OMeTAD or NiO_x and PCBM) influence the hysteresis more than whether the layer is nanostructured or not. In addition, it can be observed that the more efficient devices have, in general, less hysteresis than less efficient ones (see Table 9.1). In Figure F.4, it can be observed that the inverted hysteresis effect goes beyond the P_{MP} and also affects the V_{OC}[23]. It should also be noted that the perovskite film may crystallize differently on a TiO_2 film compared to on a NiO_x film, as well as in different environments (glove box vs ambient conditions) or depending on the post-treatment, as will be discussed later in this *Chapter*, which could account for the different responses measured. To evaluate the influence of the crystallinity on inverted hysteresis, solvent annealing (see experimental details in *Appendix* F and Figure F.1) was used. The main PV parameters for solvent annealed samples can be observed in Figure F.5 of *Appendix* F. The normalised and non-normalised X-ray diffraction (XRD) spectra for a standard perovskite film and a solvent annealed film are reported in Figures F.6 and F.7 in *Appendix* F, respectively. These data show the characteristic tetragonal peak at 14.2° (110)[27], but the solvent annealed samples do not have the characteristic (004) peak at 28.11° and do have a sharper peak at 28.36° (220). There is a clear difference in the intensity of the diffraction peaks in a non-normalized diffraction plot. This observation is a strong indication of higher crystallinity of the sample with solvent annealing and has been reported for other samples treated in this way[35,36]. The impact of crystallinity on the hysteresis can be observed in Figure F.8 in *Appendix* F where *JV* curves of 3 devices with and without solvent annealing treatment are compared and in the DoH shown in Figure 9.3. Most of the solvent annealed cells showed inverted hysteresis, although a few showed standard hysteresis at 100 $mV{\cdot}s^{-1}$. However, in general, it can be observed that the DoH is considerably lower for solvent annealed PSCs than for regular devices at 100 $mV{\cdot}s^{-1}$ shifting to DoH_{min} towards faster scan rates. Interestingly, the hysteresis is much higher under illumination from a blue LED than sunlight.

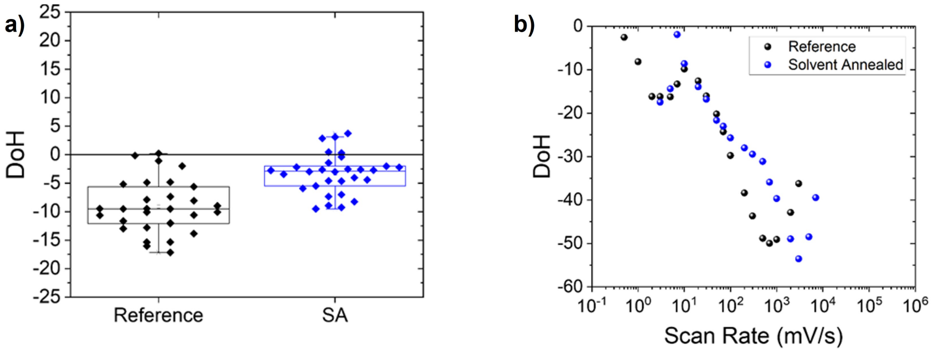

Figure 9.3: (a) DoH for 22 p-i-n PSCs with solvent annealing (SA, blue diamonds) and without solvent annealing (reference, black diamonds) at one sun, 25ºC, and 100 mV·s^{-1} scan rate. (b) Comparison of DoH vs scan rate between two PSCs with (blue) and without (black) solvent annealing under blue LED illumination (465 nm). The hysteresis procedure starts with scanning at the highest scan rate, with successive scans towards slower scan rates.

The influence of pre-conditioning on the occurrence of inverted hysteresis in the solvent-annealed cells was also investigated. Results of cells with solvent annealing under different pre-bias can be found in Figure F.9 in *Appendix* F (*JV* curves) and in Figure 9.4 (DoH). It is found that the hysteresis depends on the pre-bias potential, and comparing DoH values from pre-bias of 1200 mV (black and green diamonds in Figure 9.4a) suggests that these changes are somewhat reversible (although it is clear that some devices were indeed changing due to stress produced by the pre-conditioning and the solar illumination). Better reproducibility is obtained when the characterization is performed under blue illumination (Figure 9.4b), where the reversibility effect is more clearly seen. In any case, although the DoH is strongly dependent on the pre-conditioning potential, inverted hysteresis is detected in all cases.

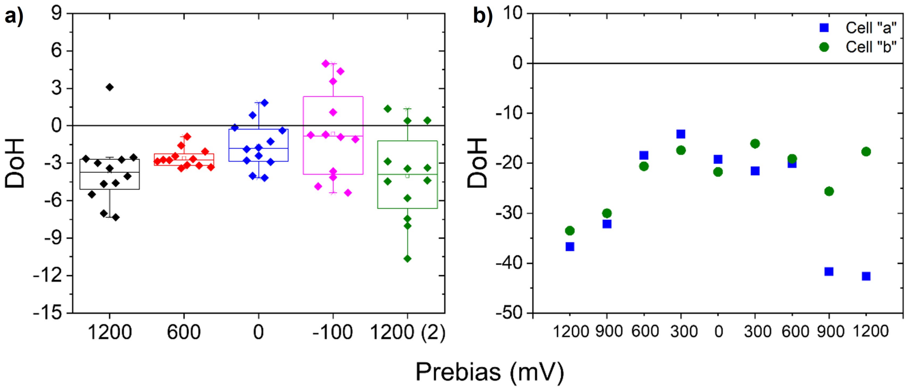

Figure 9.4: (a) DoH for 12 p-i-n PSCs with solvent annealing at 1 sun, 100 mV·s^{-1} scan rate and preconditioning biases of 1200, 600, 0, -100, 1200 mV applied for 20 s. (b) DoH for two p-i-n PSCs (blue squares and green circles) vs pre-bias potential (mV) at 25ºC under blue LED illumination and 100 mV·s^{-1} scan rate. Devices included in panel b correspond to the *JV* curves in Figure F.9 in *Appendix* F.

All these experimental observations can be summarized as follows:

1. Regardless of the configuration and the deposition method of NiO_x or laboratory where the cells were made, hysteresis was present in all devices, and the value of DoH depends on the scan rate as previously reported[27].
2. Both p-i-n and n-i-p PSCs can show inverted hysteresis for sufficiently high scan rates.
3. As has previously been reported for normal hysteresis, inverted hysteresis is also sensitive to the nature of the contacts, the crystallinity of the perovskite layer, and the pre-bias applied to the PSC before the *JV* measurement.

9.3.2 Modelling and discussion

In order to get some rationale of the hysteretic behaviour reported in the section above, DD simulations using the *IonMonger* code (see *Chapters* 3, 6, 7 and 8) were run. Simulated *JV* curves at different scan rates for the case studied in Figure 9.2b are collected in Figure F.10 in *Appendix* F. For simplicity, the DD simulated study included in this *Chapter* is restricted to a situation where recombination is assumed to take place only in the bulk of the perovskite layer. However, extending the DD simulations to other scenarios (pure surface recombination and mixed surface/bulk recombination) led to the same predictions for the hysteresis-scan rate dependence, as shown in Figure F.11 in *Appendix* F. The key features of the model, which give rise to hysteresis, are that ions move much more slowly than the electron and holes and that they have a concentration that is high enough to screen the external potential effectively ($V_{bi} + V$) at sufficiently long times, but only partially at shorter times. The consequence of the formation of Debye layers (see *Chapter* 2) in the vicinity of the ETL and HTL produces a dynamic alteration of the internal electrical potential depending on the scan rate, scan direction, and the preconditioning history of the device (see Figure 9.5).

Figure 9.2b shows the prediction of the DD model for the scan rate dependence of the DoH in the p-i-n cell. Figure F.11 in *Appendix* F is the same hysteresis index plot with alternative choices for the recombination mechanism. The modeling can generally replicate the crossover from normal to inverted hysteresis observed in the experiments as the measurements go from lower to higher scan rates. Interestingly enough, this behavior is maintained even in the scenario with only bimolecular recombination. As proof of internal self-consistency, it is verified that no hysteresis is predicted at sufficiently low or high scan rates (not necessarily reachable in the experiments). This is explained by the fact that if the scan is slow enough, ions do have time to reorganize themselves in the Debye layers at all times. If the scan is fast enough, ions get "frozen" in the initial distribution at all times. In either case, the electric potential at a given bias is the same, regardless of the scan direction, and no hysteresis is observed[19]. Clearly, the actual scan rates where maximum hysteresis is found (either normal or inverted) would depend on the ionic diffusion coefficient[19] or the transport layer properties[15].

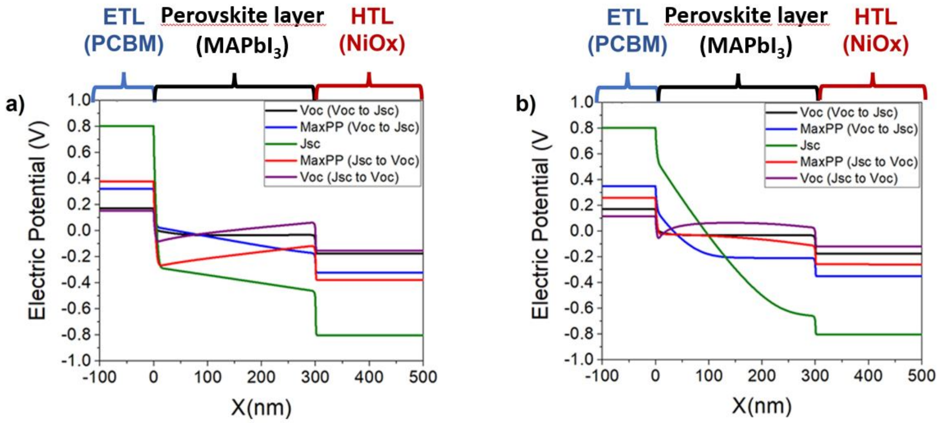

Figure 9.5: Snapshots of electric potential vs distance from ETL/perovskite interface x (nm) for the p-i-n architecture shown in Figure 9.1 in *Chapter* 9, where $x = 0$ represents the ETL/perovskite interface and $x = 300$ the perovskite/HTL interface. (a) shows the results at the scan rate for maximum regular hysteresis (red star in Figure 9.2b). (b) corresponds to the scan rate showing maximum inverted hysteresis (green star in Figure 9.2b). In all simulations a 40 s preconditioning bias of 1.2 V has been applied.

Figure 9.5a shows potential profile snapshots at DoH_{max} where normal hysteresis is seen. From the potential profile where $V = V_{MP}$ during the reverse scan, it can be seen that in the perovskite films, the potential has a negative slope driving electrons towards the ETL and holes towards the HTL, increasing J. In contrast, the potential profile at V_{MP} during the forward scan has a positive slope driving the charges in the opposite direction. These changes in slope between the reverse and the forward scan are originated from the reorganization of the ions at the interfaces (see Figure F.12 in

Appendix F), which is the reason why DoH depends on the scan rate and the ion diffusion coefficients as shown below. This mechanism explains why there is more hysteresis with monochromatic blue light in comparison with sunlight in the less efficient cells. Hysteresis arises from the interplay between recombination (which determines charge collection at the transport layers) and the acting electric field (which depends on scan rate, direction, and preconditioning). The optical penetration depth for blue light in $MAPbI_3$ is about 200 nm[37]. The perovskite film in the cells studied in this *Chapter* is $\sim$ 300 nm thick, implying that the blue light will be absorbed close to the NiO_x contact. The diffusion length using the parameters of Table F.1 in *Appendix* F is 200–300 nm for electrons and $\gg$ 300 nm for holes. A strong impact on the collection is expected if electrons are photogenerated far from the ETL. Hence, changes in the acting electric field caused by ionic reorganization would give rise to more hysteresis with blue light than with white light, where carriers are more homogeneously photogenerated. Figure 9.5b shows potential profile snapshots at DoH_{min}. In the case of inverted hysteresis, the slopes of the potential profile snapshot when reaching V_{MP} during forward and reverse scans are also different, but the change of slope is less pronounced and appears to be restricted to the vicinity of the ETL only whereas in the rest of the active layer the electric profiles tend to be flat. This observation is connected with the fact that the ionic distributions do not change much with scan direction in this case since inverted hysteresis only appears at high scan rates, and ions do not have time to adapt to voltage changes (Figure F.12 (b) and (d) in *Appendix* F). This also helps to explain the experimental result of why the V_{OC} changes more dramatically between scan directions at higher scan rates (see Figure F.9 in *Appendix* F). Hence, inverted hysteresis is always associated with a less intense alteration of the ion distribution with the scan direction due to a fast change of the applied voltage.

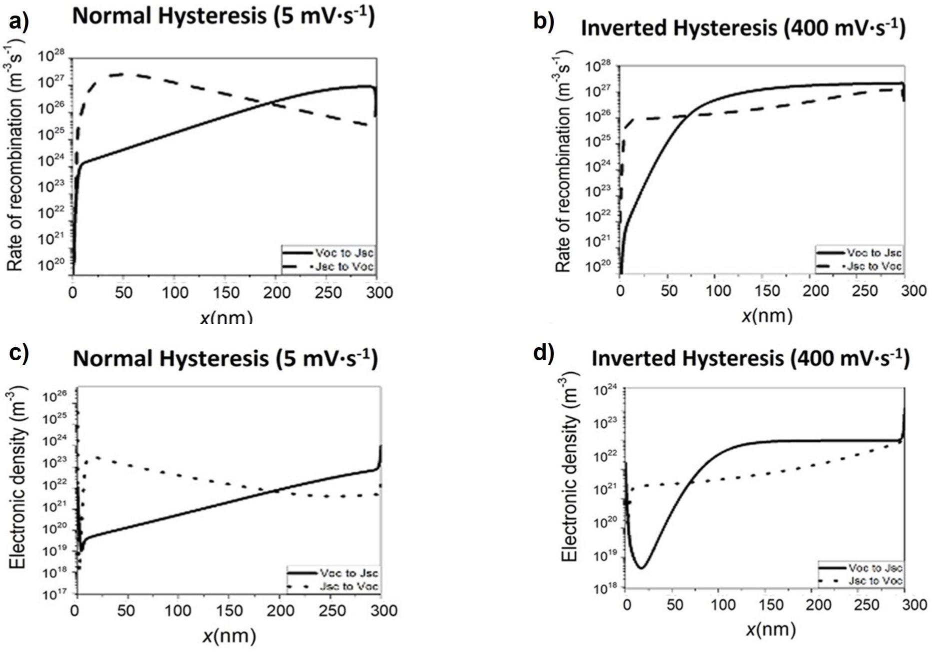

Figure 9.6: Snapshots of SRH recombination rate (a and b) and total density of electronic species (electrons and holes) (c) and (d) vs distance from the ETL/perovskite interface.

To cast more light on the origin of the different behavior observed for normal and inverted hysteresis, Figure 9.6 shows the recombination and electronic density profiles (sum of the electron and hole concentrations) at the P_{MP} at two scan directions. As the model calculates the recombination rates from the local electronic density (using the SRH model, the recombination rate is proportional to the density of electronic carriers as explained in *Chapter* 2), the recombination profiles reflect the electronic density profiles. Bearing this in mind, in the case of normal hysteresis, both the electronic density and the recombination profiles reflect the same change of slope between the forward and the reverse scan that is observed in the electrical potential (Figure 9.5a). As said above, this change of slope favors collection in the reverse scan with respect to the forward scan producing the regular hysteresis pattern. In contrast, the recombination rate and the electronic density profiles change dramatically between forward and reverse scans for inverted hysteresis but only in the vicinity of the ETL interface. This explains why changing the contacts (Figure 9.2) modifies the onset of the transition from the regular to the inverted regime. As a matter of fact, as it can be observed by comparing both panels in Figure 9.5, the electric potential values for both scan directions at the ETL when there is inverted hysteresis are swapped at the P_{MP} (where the difference between scan directions is most significant) with respect to the normal hysteresis case. This means that there is an additional energy barrier for electron injection in the reverse scan with respect to the forward scan, leading to a lower current in the reverse scan, hence producing inverted hysteresis.

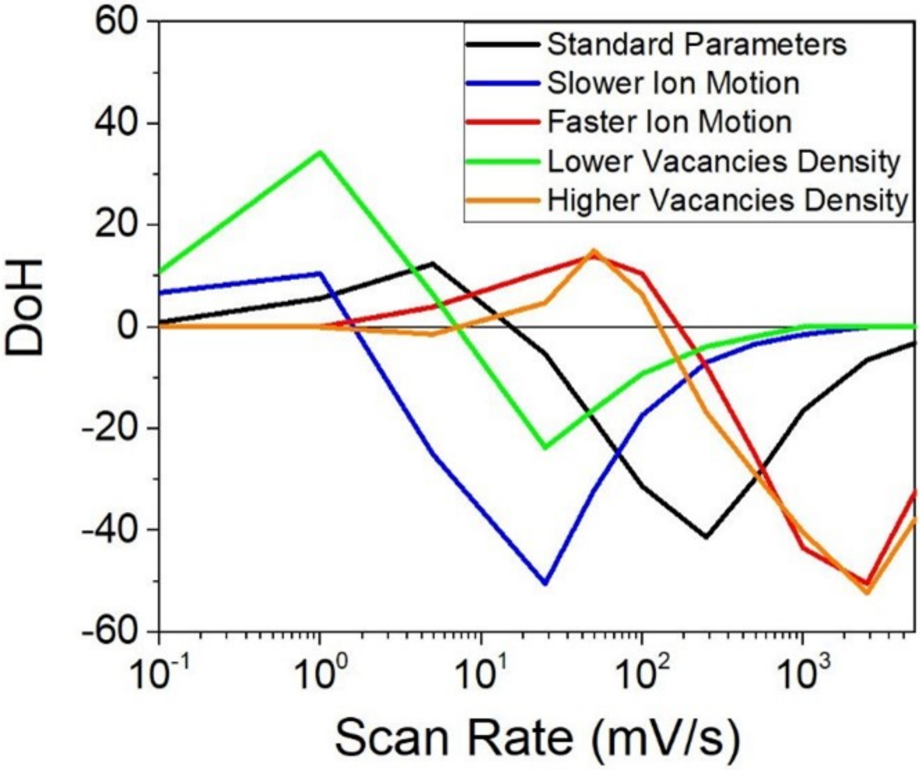

Figure 9.7: Comparison of the resulting from DD modelling DoH vs scan rate for mobile ion parameters. Standard parameters in Table F.1 of *Appendix* F (black), D_{ion} = 10^{-17} $m^2{\cdot}s^{-1}$ (blue), D_0 = 10^{-15} $m^2{\cdot}s^{-1}$ (red), N_0 = $1.6{\cdot}10^{24}$ m^{-3} (green) and N_0 = $1.6{\cdot}10^{26}$ m^{-3} (brown). These results are for the p-i-n architecture shown in Figure 9.1.

In Figure 9.7 it is shown that, according to the model, the mobile ion diffusion coefficient determines the scan rates for maximum normal and inverted hysteresis. These results show that an increase in D_{ion} or in N_0 causes the scan rates for DoH_{max} and DoH_{min} to increase. In fact, it can be said that the DoH-scan rate plot can be represented by an S-shaped universal curve, whose position in time scale depends on the drift velocity and ability of the ions to respond to external voltage changes (which in turn depend on the active layer and transport layer properties). Figure 9.7 helps to explain the experimental results of Figure 9.3, and the distinct behavior observed when cells using different deposition procedures are compared. It is unlikely that solvent annealing would increase N_0, so the modeling predictions lead to the conclusion that solvent annealing increases D_{ion}. As mentioned, solvent annealing leads to higher crystallinity[35]. Hence, the increase of the ionic mobility in the solvent annealed sample can be understood as a consequence of having fewer grain boundaries. This conclusion is consistent with ions moving faster in the grain bulk than along grain boundaries, as shown by atomistic simulations and experimental observations that show that defects are trapped at the grain boundaries[38], thus inhibiting their diffusion.

9.4 Conclusion

Measurements of the scan rate dependence of the DoH for n-i-p and p-i-n hybrid PSCs prepared using several different experimental procedures (planar and mesoporous oxides, solvent annealing) reveal a universal curve in which the hysteresis switches from normal to inverted when the scan rate is sufficiently increased. The fully coupled electron-ion DD model *IonMonger* replicates this behavior and demonstrates that the actual scan rates for which maximum normal or inverted hysteresis is observed, as well as the crossover scan rate between the two regimes, depending on the ion diffusion coefficient, the ion concentration and the nature of the electron and hole transport layers. The model also shows that inverted hysteresis is always associated with a less intense variation of the ionic distribution at the interfaces due to a fast change of the applied voltage (i.e., the scan rate). These results provide unique insight into the mechanisms of charge transport in these hybrid perovskite materials, which may prove essential for the design and development of stable PSCs.

Bibliography

[1] C. Eames, J. M. Frost, P. R. F. Barnes, B. C. O'Regan, A. Walsh, and M. S. Islam, "Ionic transport in hybrid lead iodide perovskite solar cells," *Nature Communications*, vol. 6, p. 7497, 2015.

[2] Y. Hou, E. Aydin, M. De Bastiani, C. Xiao, F. H. Isikgor, D.-J. Xue, B. Chen, H. Chen, B. Bahrami, A. H. Chowdhury, A. Johnston, S.-W. Baek, Z. Huang, M. Wei, Y. Dong, J. Troughton, R. Jalmood, A. J. Mirabelli, T. G. Allen, E. Van Kerschaver, M. I. Saidaminov, D. Baran, Q. Qiao, K. Zhu, S. De Wolf, and E. H. Sargent, "Efficient tandem solar cells with solution-processed perovskite on textured crystalline silicon," *Science (New York, N.Y.)*, vol. 367, pp. 1135–1140, Mar. 2020.

[3] H. J. Snaith, "Perovskites: The emergence of a new era for low-cost, high-efficiency solar cells," *The Journal of Physical Chemistry Letters*, vol. 4, no. 21, pp. 3623–3630, 2013.

[4] J. Ling, P. K. K. Kizhakkedath, T. M. Watson, I. Mora-Seró, L. Schmidt-Mende, T. M. Brown, and R. Jose, "A Perspective on the Commercial Viability of Perovskite Solar Cells," *Solar RRL*, vol. 5, no. 11, p. 2100401, 2021.

[5] X. Lin, A. S. R. Chesman, S. R. Raga, A. D. Scully, L. Jiang, B. Tan, J. Lu, Y.-B. Cheng, and U. Bach, "Effect of grain cluster size on back-contact perovskite solar cells," *Advanced Functional Materials*, vol. 28, no. 45, p. 1805098, 2018.

[6] X.-Y. Zhu and V. Podzorov, "Charge carriers in hybrid organic–inorganic lead halide perovskites might be protected as large polarons," *The Journal of Physical Chemistry Letters*, vol. 6, no. 23, pp. 4758–4761, 2015-12.

[7] W. Heiss and C. Brabec, "Perovskites target X-ray detection," *Nature Photonics*, vol. 10, pp. 288–289, May 2016.

[8] K. Domanski, B. Roose, T. Matsui, M. Saliba, S.-H. Turren-Cruz, J.-P. Correa-Baena, C. R. Carmona, G. Richardson, J. M. Foster, F. D. Angelis, J. M. Ball, A. Petrozza, N. Mine, M. K. Nazeeruddin, W. Tress, M. Grätzel, U. Steiner, A. Hagfeldt, and A. Abate, "Migration of cations induces reversible performance losses over day/night cycling in perovskite solar cells," *Energy & Environmental Science*, vol. 10, no. 2, pp. 604–613, 2017-02.

[9] S. A. L. Weber, I. M. Hermes, S.-H. Turren-Cruz, C. Gort, V. W. Bergmann, L. Gilson, A. Hagfeldt, M. Graetzel, W. Tress, and R. Berger, "How the formation of interfacial charge causes hysteresis in perovskite solar cells," *Energy & Environmental Science*, vol. 11, pp. 2404–2413, 2018.

[10] J. Liu, M. Hu, Z. Dai, W. Que, N. P. Padture, and Y. Zhou, "Correlations between Electrochemical Ion Migration and Anomalous Device Behaviors in Perovskite Solar Cells," *ACS Energy Letters*, vol. 6, pp. 1003–1014, Mar. 2021.

[11] S. N. Habisreutinger, N. K. Noel, and H. J. Snaith, "Hysteresis index: A figure without merit for quantifying hysteresis in perovskite solar cells," *ACS Energy Letters*, vol. 3, no. 10, pp. 2472–2476, 2018-10.

[12] L. Contreras-Bernal, C. Aranda, M. Valles-Pelarda, T. T. Ngo, S. Ramos-Terrón, J. J. Gallardo, J. Navas, A. Guerrero, I. Mora-Seró, J. Idígoras, and J. A. Anta, "Homeopathic perovskite solar cells: Effect of humidity during fabrication on the performance and stability of the device," *The Journal of Physical Chemistry C*, 2018-02.

[13] G. Richardson, S. E. J. O'Kane, R. G. Niemann, T. A. Peltola, J. M. Foster, P. J. Cameron, and A. B. Walker, "Can slow-moving ions explain hysteresis in the current–voltage curves of perovskite solar cells?," *Energy & Environmental Science*, vol. 9, pp. 1476–1485, 2016.

[14] S. Ravishankar, O. Almora, C. Echeverría-Arrondo, E. Ghahremanirad, C. Aranda, A. Guerrero, F. Fabregat-Santiago, A. Zaban, G. Garcia-Belmonte, and J. Bisquert, "Surface polarization model for the dynamic hysteresis of perovskite solar cells," *The Journal of Physical Chemistry Letters*, vol. 8, no. 5, pp. 915–921, 2017-03.

[15] N. E. Courtier, J. M. Cave, J. M. Foster, A. B. Walker, and G. Richardson, "How transport layer properties affect perovskite solar cell performance: insights from a coupled charge transport/ion migration model," *Energy & Environmental Science*, vol. 12, pp. 396–409, 2018.

[16] D. A. Jacobs, H. Shen, F. Pfeffer, J. Peng, T. P. White, F. J. Beck, and K. R. Catchpole, "The two faces of capacitance: New interpretations for electrical impedance measurements of perovskite solar cells and their relation to hysteresis," *Journal of Applied Physics*, vol. 124, no. 22, p. 225702, 2018.

[17] F. Ebadi, N. Taghavinia, R. Mohammadpour, A. Hagfeldt, and W. Tress, "Origin of apparent light-enhanced and negative capacitance in perovskite solar cells," *Nature Communications*, vol. 10, no. 1, p. 1574, 2019-04.

[18] M. T. Neukom, A. Schiller, S. Züfle, E. Knapp, J. Ávila, D. Pérez-del Rey, C. Dreessen, K. P. Zanoni, M. Sessolo, H. J. Bolink, and B. Ruhstaller, "Consistent device simulation model describing perovskite solar cells in steady-state, transient, and frequency domain," *ACS Applied Materials & Interfaces*, vol. 11, no. 26, pp. 23320–23328, 2019.

[19] J. M. Cave, N. E. Courtier, I. A. Blakborn, T. W. Jones, D. Ghosh, K. F. Anderson, L. Lin, A. A. Dijkhoff, G. J. Wilson, K. Feron, M. Saiful Islam, J. M. Foster, G. Richardson, and A. B. Walker, “Deducing transport properties of mobile vacancies from perovskite solar cell characteristics,” *Journal of Applied Physics*, vol. 128, p. 184501, Nov. 2020.

[20] M. D. Bastiani, G. Dell’Erba, M. Gandini, V. D’Innocenzo, S. Neutzner, A. R. S. Kandada, G. Grancini, M. Binda, M. Prato, J. M. Ball, M. Caironi, and A. Petrozza, “Ion migration and the role of preconditioning cycles in the stabilization of the j–v characteristics of inverted hybrid perovskite solar cells,” *Advanced Energy Materials*, vol. 6, no. 2, p. 1501453, 2016.

[21] W. Tress, J. P. Correa Baena, M. Saliba, A. Abate, and M. Graetzel, “Inverted current–voltage hysteresis in mixed perovskite solar cells: Polarization, energy barriers, and defect recombination,” *Advanced Energy Materials*, pp. n/a–n/a, 2016-07.

[22] D. A. Jacobs, Y. Wu, H. Shen, C. Barugkin, F. J. Beck, T. P. White, K. Weber, and K. R. Catchpole, “Hysteresis phenomena in perovskite solar cells: the many and varied effects of ionic accumulation,” *Physical Chemistry Chemical Physics*, vol. 19, pp. 3094–3103, Jan. 2017.

[23] G. A. Nemnes, C. Besleaga, V. Stancu, D. E. Dogaru, L. N. Leonat, L. Pintilie, K. Torfason, M. Ilkov, A. Manolescu, and I. Pintilie, “Normal and Inverted Hysteresis in Perovskite Solar Cells,” *The Journal of Physical Chemistry C*, vol. 121, pp. 11207–11214, June 2017.

[24] H. Shen, D. A. Jacobs, Y. Wu, T. Duong, J. Peng, X. Wen, X. Fu, S. K. Karuturi, T. P. White, K. Weber, and K. R. Catchpole, “Inverted hysteresis in CH3nh3pbi3 solar cells: Role of stoichiometry and band alignment,” *The Journal of Physical Chemistry Letters*, vol. 8, no. 12, pp. 2672–2680, 2017-06.

[25] A. O. Alvarez, R. Arcas, C. A. Aranda, L. Bethencourt, E. Mas-Marzá, M. Saliba, and F. Fabregat-Santiago, “Negative capacitance and inverted hysteresis: Matching features in perovskite solar cells,” *The Journal of Physical Chemistry Letters*, pp. 8417–8423, 2020-09.

[26] H.-S. Kim, I.-H. Jang, N. Ahn, M. Choi, A. Guerrero, J. Bisquert, and N.-G. Park, “Control of i–v hysteresis in CH3nh3pbi3 perovskite solar cell,” *The Journal of Physical Chemistry Letters*, vol. 6, no. 22, pp. 4633–4639, 2015-11.

[27] R. García-Rodríguez, D. Ferdani, S. Pering, P. J. Baker, and P. J. Cameron, “Influence of bromide content on iodide migration in inverted MAPb(i 1-x br x) 3 perovskite solar cells,” *Journal of Materials Chemistry A*, vol. 7, no. 39, pp. 22604–22614, 2019.

[28] Odabaşı and R. Yıldırım, “Performance analysis of perovskite solar cells in 2013–2018 using machine-learning tools,” *Nano Energy*, vol. 56, pp. 770–791, 2019.

[29] T. Wang, D. Ding, X. Wang, R. Zeng, H. Liu, and W. Shen, “High-Performance Inverted Perovskite Solar Cells with Mesoporous NiO x Hole Transport Layer by Electrochemical Deposition,” *ACS omega*, vol. 3, pp. 18434–18443, Dec. 2018.

[30] C. C. Boyd, R. C. Shallcross, T. Moot, R. Kerner, L. Bertoluzzi, A. Onno, S. Kavadiya, C. Chosy, E. J. Wolf, J. Werner, J. A. Raiford, C. de Paula, A. F. Palmstrom, Z. J. Yu, J. J. Berry, S. F. Bent, Z. C. Holman, J. M. Luther, E. L. Ratcliff, N. R. Armstrong, and M. D. McGehee, “Overcoming redox reactions at perovskite-nickel oxide interfaces to boost voltages in perovskite solar cells,” *Joule*, 2020-07.

[31] J. He, E. Bi, W. Tang, Y. Wang, Z. Zhou, X. Yang, H. Chen, and L. Han, “Ligand-Free, Highly Dispersed NiOx Nanocrystal for Efficient, Stable, Low-Temperature Processable Perovskite Solar Cells,” *Solar RRL*, vol. 2, no. 4, p. 1800004, 2018.

[32] W. Chen, Y. Zhou, L. Wang, Y. Wu, B. Tu, B. Yu, F. Liu, H.-W. Tam, G. Wang, A. B. Djurišić, L. Huang, and Z. He, “Molecule-Doped Nickel Oxide: Verified Charge Transfer and Planar Inverted Mixed Cation Perovskite Solar Cell,” *Advanced Materials*, vol. 30, no. 20, p. 1800515, 2018.

[33] X. Hu, C. Liu, Z. Zhang, X.-F. Jiang, J. Garcia, C. Sheehan, L. Shui, S. Priya, G. Zhou, S. Zhang, and K. Wang, “22% Efficiency Inverted Perovskite Photovoltaic Cell Using Cation-Doped Brookite TiO2 Top Buffer,” *Advanced Science*, vol. 7, no. 16, p. 2001285, 2020.

[34] Y. Wu, H. Pan, Y. Xu, M. Hou, Q. Huang, Y. Ding, G. Hou, Y. Zhao, and X. Zhang, “A facile light managing strategy in inverted perovskite solar cells,” *Journal of Physics: Energy*, vol. 3, p. 035004, June 2021.

[35] Z. Xiao, Q. Dong, C. Bi, Y. Shao, Y. Yuan, and J. Huang, “Solvent Annealing of Perovskite-Induced Crystal Growth for Photovoltaic-Device Efficiency Enhancement,” *Advanced Materials*, vol. 26, no. 37, pp. 6503–6509, 2014.

[36] Y. Ma, P. Mwitumwa Hangoma, W. Ik Park, J.-H. Lim, Y. Kyung Jung, J. Hyun Jeong, S. Heum Park, and K. Ho Kim, “Controlled crystal facet of MAPbI 3 perovskite for highly efficient and stable solar cell via nucleation modulation,” *Nanoscale*, vol. 11, no. 1, pp. 170–177, 2019.

[37] L. Contreras-Bernal, M. Salado, A. Todinova, L. Calio, S. Ahmad, J. Idígoras, and J. A. Anta, “Origin and whereabouts of recombination in perovskite solar cells,” *The Journal of Physical Chemistry C*, vol. 121, no. 18, pp. 9705–9713, 2017.

[38] N. Phung, A. Al-Ashouri, S. Meloni, A. Mattoni, S. Albrecht, E. L. Unger, A. Merdasa, and A. Abate, “The Role of Grain Boundaries on Ionic Defect Migration in Metal Halide Perovskites,” *Advanced Energy Materials*, vol. 10, no. 20, p. 1903735, 2020.

General conclusions

In this thesis, two of the most relevant third-generation PV technologies (PSCs and DSSCs) have been the object of fundamental studies pursuing a better understanding of the different electronic and ionic properties of these devices and their role in driving PV performance. To that matter, experimental optoelectronic characterization techniques have been applied together with numerical drift-diffusion (DD) simulations.

In *Chapters* 4 and 5, conventional DSSCs were analyzed together with a novel photochromic dye and PSCs, respectively, to gain an understanding of the properties of these two complex systems by comparing them to regular DSSCs widely studied and with well-understood behaviour. In particular, in *Chapter* 4, after confirming that, from an optoelectronic point of view, there are no significant differences between photochromic and regular DSSCs, EIS and IMPS were used to estimate the effect of the photochromism on recombination and transport properties of the device. The main conclusion of this *Chapter* is that activation of the photochromic dye accelerates the recombination process, leading to poorer charge extraction efficiency. Finally, this *Chapter* proposes a clear and straightforward procedure to account for accidental activation of the photochromic dye under illumination during the optoelectronic characterization. *Chapter* 5 combines the characterization using IMPS of $MAPbI_3$ based PSCs as a function of light intensity, excitation wavelength, and temperature with the use of a numerical DD model to determine the origin of the three time signals commonly observed in IMPS spectra of this kind of devices. As reported in the literature, the high-frequency signal is the electronic discharge of the geometrical capacitor formed by the perovskite and the contacts rather than an electron transport. The similar behaviour of the medium-frequency signal to the observed in DSSCs allows attributing this feature to electron transport in the TiO_2 while the dependence on temperature of the low-frequency signal connects it to ion-mediated capacitive discharge. This *Chapter* also includes three alternative ways of measuring the IQE, all of them leading to the same results, close to 100%. Another interesting feature in this *Chapter* is that much insight can be gained by comparing the behaviour of different types of solar cells, DSSC and PSC in this case.

In *Chapter* 6 a numerical DD model that allows for reproducing *JV* and EIS spectra of ETL/Perovskite/HTL PSCs is used to reproduce the universal features observed in experimental EIS of PSCs, showing that recombination in the bulk of the perovskite together with slow ionic motion is sufficient to reproduce these universal features commonly observed in PSCs. However, surface recombination needs to be introduced in the simulations to reproduce the spectrum of a particular experimental device. This *Chapter* describes how the electrical properties of the devices, determining their performance at steady-state, such as the charge collection efficiency (CCE) or the electronic ideality factor (n_{EL}), can only be deduced from the high-frequency impedance response, while the low-frequency region can be used as a tool to gain information about the ionic mobility and the capacitances of the Debye layers.

This DD model is also used in *Chapters* 7, 8 and 9. In *Chapters* 7 and 9 DD model calculations are combined with experimental results to shed light on two exotic features observed in PSCs: In *Chapter* 7 the presence of a crossover in the apparent ideality factor (n_{AP}) at different illumination regimes, and inverted hysteresis phenomena in *Chapter* 9. In *Chapter* 7, experimental results showing a change of behaviour of n_{AP} at different illumination regimes of a mesoscopic mixed perovskite ($FA_{0.71}MA_{0.29}PbI_{2.9}Br_{0.1}$) solar cells were analyzed combining the use of DD numerical modeling with the calculation of n_{EL}. The transition from a n_{AP} of 1.8-2.5 to a n_{AP} close to unity takes place at potentials of 1.03 V or irradiance of 10 mW·cm^{-2}. Using DD simulations, this crossover can be attributed to a combination of two effects: a transition from bulk recombination dominated regime at low irradiances to a more important role of surface recombination at higher light intensities and the reduction of ionic vacancies in the perovskite layer, lowering the value of n_{AP}. The impact of this second effect leads to the conclusion that the description based on n_{EL} is a more reliable tool for determining the dominant recombination in a particular solar cell. In *Chapter* 9, the measurements of the scan rate dependence of the *DoH* for n-i-p and p-i-n PSCs prepared with different procedures reveal a universal curve where hysteresis switches from normal to inverted at sufficiently fast scan rates. This behaviour was replicated using DD numerical calculations, showing that the scan rates where the regular and inverted hysteresis and the crossover between both regimes depend on the ionic properties and the nature of the selective contacts of the PSC.

Chapter 8 focuses on the use of *IonMonger* DD model to simulate and interpret complex impedance spectra of PSCs, avoiding most experimental uncertainties. This allows for the comparison of two widely used equivalent circuits (SEC and PEC), understanding the physical meaning of their circuit elements. This is achieved by assessing how well they can be used to determine PV parameters like CCE or n_{EL} (known prior to setting the conditions of the simulations) and by analyzing the isolated impact of different properties of the PSC, which can be modified in the DD simulation. Both circuits give similar information as both configurations reproduce the EIS of PSCs, and the elements of each circuit can be extracted from the parameters of the other. The calculation of CCE at steady-state and n_{EL} determines that only R_{HF} contains information about the electronic recombination process, avoiding the influence of ionic driven processes. As for the low-frequency region of the impedance spectra, comparing the resistance and capacitance in the LF element of SEC to the "dielectric" branch of PEC, it is possible to distinguish between the impact of the ionic diffusion coefficient and the density of ion vacancies.

In summary, this thesis has shown, from a microscopic or fundamental point of view, the relevance of understanding the electronic and ionic driven mechanisms limiting the performance of DSSCs and PSCs. This thesis shows how to connect the properties of relatively simple and well-understood systems like conventional DSSCs to understand better and analyze more complex problems like photochromism or the properties of PSCs. In addition, this thesis presents the possible synergies between experimental characterization and numerical DD modeling as tools to understand the interconnected electronic and ionic properties that make PSCs a unique challenge. As it has been shown with the calculation of the steady-state CCE or the determination of n_{EL}, the separation of these dual properties of PSCs is crucial to better understanding this technology. Profound knowledge of the electronic properties of these devices is undoubtedly precious to determine the device's performance under operation conditions, while the role of ionic driven processes is crucial to the pursuit of long-term stability of the devices. A fundamental understanding of the properties of these technologies paves the way to their optimization for different applications and their large-scale implementation.

Resumen

El desarrollo de fuentes de energía alternativas y con bajas emisiones ha ganado importancia para la sociedad a medida que la demanda energética a nivel mundial aumenta y el impacto ambiental generado por la combustión de combustibles fósiles a lo largo de los años se hace más evidente produciendo el cambio climático. Como respuesta a este problema, la comunidad científica ha enfocado sus esfuerzos en desarrollar nuevas fuentes de energía. Una de las tecnologías que ha atraído más atención es la energía fotovoltaica, que permite explotar directamente la enorme cantidad de luz solar que llega a la superficie terrestre. Mientras que las celdas basadas en el silicio han dominado el panorama fotovoltaico durante muchos años, la búsqueda de alternativas que reduzcan la dependencia de materiales escasos o de procesos de fabricación que requieren una gran cantidad de energía ha llevado al desarrollo de las fotovoltaicas de tercera generación. En este contexto, las celdas sensibilizadas por colorantes representaron un gran avance en el campo ya que pueden fabricarse con materiales abundantes y de bajo coste y con procesos de fabricación relativamente simples.

Además, su adaptabilidad y la variedad de elementos disponibles las hacen muy atractivas a mercados emergentes y nuevas aplicaciones como la fotovoltaica integrada en edificios o aplicaciones en interiores. Las celdas de perovskita han emergido rápidamente partiendo de ser un tipo particular de celda de colorante a convertirse en una nueva familia de tecnología fotovoltaica por derecho propio, alcanzando elevadas eficiencias gracias a sus excelentes propiedades optoelectrónicas. Asimismo, la alta disponibilidad en la naturaleza de los precursores que intervienen en la síntesis de este material contribuyen a que esta tecnología sea tan prometedora. Sin embargo, la falta de estabilidad en condiciones ambientales, el uso de materiales de elevado coste para fabricar los dispositivos, junto a limitaciones ténicas como la necesidad de atmósfera inerte en el proceso de fabricación han

dificultado su penetración en el mercado y su implantación a gran escala. Por esta razón, es necesario ampliar el conocimiento fundamental de las propiedades electrónicas e iónicas detrás de los aspectos positivos y negativos de estos materiales para aportar información clave para la optimización de sus elementos.

El principal objetivo de esta tesis es comprender las dinámicas iónica y electrónica y los procesos físicoquímicos que determinan el desempeño fotovoltaico en condiciones de operación y la estabilidad a largo plazo de estos materiales híbridos nanoestructurados. Para lograr este objetivo, se han utilizado técnicas optoelectrónicas de pequeña perturbación en conjunto con simulaciones numéricas drift-diffusion. Usadas en conjunto, ayudan a arrojar luz a los fenómenos electrónicos e iónicos que determinan el funcionamiento de los dispositivos y la interconexión de las propiedades electrónicas e iónicas. En este contexto, combinar estas técnicas experimentales con simulaciones numéricas ha demostrado ser una aproximación tremendamente útil para comprender el significado físico de los elementos que pueden identificarse en los espectros obtenidos experimentalmente, permitiendo la interpretación y racionalización de su papel y determinar las propiedades fotovoltaicas de los dispositivos en condiciones de operación.

Conclusiones generales

En esta tesis, dos de los materiales más relevantes de la tercera generación de tecnologías fotovoltaicas (PSCs y DSSCs) han sido objeto de estudios fundamentales para aumentar la comprensión de sus propiedades electrónicas e iónicas, y de su impacto al determinar el desempeño fotovoltaico de los dispositivos. Para ello, se han utilizado técnicas de caracterización optoelectrónicas experimentales junto a simulaciones numéricas basadas en drift-diffusion (DD).

En los *Capítulos* 4 y 5, se analizaron DSSCs convencionales, junto a celdas con colorantes fotocrómicas y PSCs, respectivamente, para entender mejor las propiedades de estos dos sistemas complejos comparándolas con DSSCs regulares, que han sido ampliamente estudiadas y cuyo comportamiento está bien entendido. Concretamente, en el *Capítulo* 4, tras confirmar que, desde el punto de vista optoelectrónico, no hay diferencias significativas entre DSSCs regulares y fotocrómicas, se usó EIS e IMPS para estimar el efecto del fotocromismo en las propiedades de recombinación y transporte del dispositivo. La principal conclusión de este *Capítulo* es que la activación del colorante fotocrómico acelera el proceso de recombinación, causando un empeoramiento de la eficiencia de recolección de cargas. Finalmente, en este *Capítulo* se propone un procedimiento claro y directo para considerar la activación accidental del colorante fotocrómico bajo la iluminación recibida durante la caracterización optoelectrónica.

En el *Capítulo* 5 se combina la caracterización usando IMPS de una PSC basada en $MAPbI_3$ en función de la intensidad de luz, la longitud de onda de excitación y la temperatura, con el uso de un modelo numérico DD para determinar el origen de las tres constantes de tiempo que se observan normalmente en los espectros IMPS de este tipo de dispositivos. Tal y como se ha reportado en la bibliografía, la señal de alta frecuencia corresponde a la descarga electrónica del capacitor geométrico formado por la perovskita y los contactos y no a un transporte electrónico. El comportamiento de la señal de media frecuencia es similar al observado en DSSCs, lo que permite atribuir este rasgo al transporte de electrones en la capa de TiO_2, mientras que la dependencia con la temperatura de la señal de baja frecuencia la conecta a una descarga capacitiva mediada por iones. Este *Capítulo* también incluye tres maneras alternativas de medir la IQE, las cuales generan resultados similares, cercanos al 100%. Otro aspecto interesante de este *Capítulo* es que se puede obtener gran cantidad de información comparando el comportamiento de tipos diferentes de celdas solares, como en este caso DSSC y PSC.

En el *Capítulo* 6, un modelo DD numérico que permite reproducir las curvas *JV* y los espectros de EIS de PSCs con configuración ETL/Perovskita/HTL se utiliza para reproducir las características universales observadas experimentalmente en mediciones EIS de PSCs, mostrando que recombinación en el bulk de la perovskita junto con migración iónica lenta es suficiente para reproducir estas propiedades universales observadas comúnmente en PSCs. Sin embargo, es necesario introducir recombinación superficial en las simulaciones para reproducir el espectro de un dispositivo experimental particular. Este *Capítulo* describe como las propiedades eléctricas de los dispositivos que determinan su comportamiento en estado estacionario, como la eficiencia de recolección de carga (CCE) o el factor de idealidad electrónico (nEL), solo pueden ser deducidos a partir de la respuesta de alta frecuencia de la impedancia, mientras que la región de baja frecuencia puede ser empleada como herramienta para obtener información del movimiento iónico y las capacitancias de las capas de Debye.

Este modelo DD también ha sido utilizado en los *Capítulos* 7, 8 y 9. En los *Capítulos* 7 y 9, los cálculos usando el modelo DD se combinan con resultados experimentales para contribuir a aclarar dos comportamientos exóticos observados en PSCs: En el *Capítulo* 7 la presencia de una transición en el factor de idealidad aparente (n_{AP}) a diferentes regímenes de iluminación, y el fenómeno de histéresis invertida en el *Capítulo* 9. En el *Capítulo* 7, se muestran resultados experimentales donde se observa un cambio en el comportamiento de n$_{AP}$ a diferentes regímenes de iluminación de celdas solares basadas en perovskita mixta ($FA_{0.71}MA_{0.29}PbI_{2.9}Br_{0.1}$). Estos resultados se analizan combinándolos con el uso de modelizaciones numéricas DD y el cálculo de n$_{EL}$. La transición desde un n$_{AP}$ de 1.8-2.5 a un n$_{AP}$ cercano a la unidad tiene lugar a potenciales cercanos a 1.03 V o irradiancias de 10 mW·cm^{-2}. Usando simulaciones DD, este cruce puede atribuirse a la combinación de dos efectos: la transición desde un régimen dominado por recombinación en el bulk a bajas irradiancias a otro con un rol más importante de recombinación en las interfases, a mayores intensidades de luz, y la reducción de vacantes iónicas en la capa de perovskita, contribuyendo a un descenso en el valor de n$_{AP}$. El impacto de este segundo efecto conduce a la conclusión de que la descripción basda en n$_{EL}$ es una herramienta más fiable para determinar el mecanismo de recombinación dominante en una celda solar particular. En el *Capítulo* 9, la medición de la dependencia del DoH para PSCs n-i-p y p-i-n preparadas con distintos procedimientos revela una curva universal donde la histéresis pasa de normal a invertida a velocidades de escaneo suficientemente rápidos. Este comportamiento ha sido replicado usando cálculos numéricos DD, mostrando que las velocidades de escaneo donde la histéresis regular e invertida y el cruce entre los dos regímenes dependen de las propiedades iónicas y la naturaleza de los contactos selectivos de la PSC.

El *Capítulo* 8 se centra en el uso del modelo DD *IonMonger* para simular e interpretar espectros de impedancia de PSCs, evitando gran parte de las incertidumbres y limitaciones experimentales. Esto permite la comparación de dos circuitos equivalentes ampliamente utilizados por la comunidad (SEC y PEC), para comprender el significado físico de sus distintos elementos. Esto se consigue evaluando su idoneidad para determinar parámetros fotovoltaicos como la CCE o el n$_{EL}$ (conocidos de antemano al determinar las condiciones de las simulaciones) y analizando el impacto aislado de diferentes propiedades de la PSC, que pueden modificarse en la simulación DD. Ambos circuitos producen información similar puesto que las dos configuraciones son capaces de reproducir la EIS de PSCs, y los elementos de cada circuito se pueden extraer utilizando los parámetros del otro. El cálculo de la CCE a estado estacionario y el n_{EL} determinan que solo R_{HF} contiene información sobre el proceso de recombinación electrónico, evitando la influencia de procesos de origen iónico. En cuanto a la región de bajas frecuencias del espectro de impedancia, comparando la resistencia y la capacitancia del elemento LF de SEC a la rama "dieléctrica" de PEC, es posible distinguir entre el impacto del coeficiente de difusión iónico y la densidad de vacantes iónicas.

En resumen, esta tesis expone, desde un punto de vista microscópico o fundamental, la relevancia de comprender los mecanismos electrónicos e iónicos que limitan el desempeño de DSSCs y PSCs. Esta tesis presenta como conectar las propiedades de sistemas relativamente simples y bien comprendidos como DSSCs convencionales para comprender mejor y analizar problemas más complejos como el fotocromismo o las propiedades de PSCs. Además, esta tesis presenta las posibles sinergias entre la caracterización experimental y los modelos numéricos DD como herramientas complementarias para comprender la interconexión entre las propiedades electrónicas e iónicas que convierten a las PSCs en un desafío único. Tal y como se ha mostrado con el cálculo de la CCE en estado estacionario o la determinación de n_{EL}, la separación de estas propiedades duales de las PSCs es crucial para comprender mejor esta tecnología. El conocimiento profundo de las propiedades electrónicas de estos dispositivos es, sin lugar a dudas, de enorme valor para comprender el desempeño de estos materiales en condiciones de operación, mientras que el rol de los procesos iónicos es crucial para mejorar la estabilidad a largo plazo de los dispositivos. La comprensión fundamental de las propiedades de estas tecnologías allana el camino para su optimización para diferentes aplicaciones y su implementación a gran escala.

Agradecimientos

En primer lugar, quisiera agradecer a mis directores Juan Antonio Anta y Gerko Oskam por su tiempo, dedicación y paciencia durante estos años. Si he podido completar con éxito este camino ha sido gracias a su guía. Gracias Juan por introducirme no solo a los conceptos básicos de los que se nutre esta tesis sino también a lo que implica dedicarse al mundo de la investigación y por darme la confianza de plantearte mis inquietudes durante todo el proceso. Y gracias Gerko por ayudarme con tu mesura y experiencia en los últimos años del doctorado y por tu nivel de precisión mostrándome la importancia del detalle. Gracias a los dos por ayudarme a crecer durante estos años como científico y como persona, sin duda, esta carrera de obstáculos no habría sido igual sin dos supervisores con vuestra experiencia, conocimiento y calidad personal.

Sin desmerecer la labor de mis directores, no puedo evitar agradecer a quienes para mí han sido dos mentores, dos hermanos mayores, gracias Jesús y Lidia por haberme ayudado pacientemente tanto a desenvolverme en el día a día en el laboratorio, por vuestra compañía y por haberme sentido arropado desde el primer momento. Gracias Lidia por estar ahí en los momentos más duros de la tesis. Gracias también a Susana, con quien comencé este camino y con quien compartí y sigo compartiendo la frustración de las perovskitas. Tu negatividad me hace parecer más optimista.

Gracias también a los compañeros de grupo que me han acompañado al final del doctorado, gracias Karen, Renán, Patricia y Juan Carlos por estar ahí cuando ha hecho falta. Gracias también a todos los compañeros que han venido de estancia y dejado un trocito de ellos en el laboratorio. Por supuesto, gracias a nuestros vecinos de laboratorio, el grupo Omegas y los compañeros de simulación. El día a día en el laboratorio no habría sido lo mismo sin vosotros. Gracias en especial a Paco, una de las mejores personas que he tenido el gusto de conocer siempre dispuesto a echar una mano en lo que haga falta, aunque tenga que sacar tiempo de donde no lo hay.

A Germà García-Belmonte y Juan Bisquert por permitirme la oportunidad de trabajar en su grupo en el INAM de la Universitat Jaume I de Castellón. A Sandheep por ayudarme a comprender mejor el funcionamiento del IMPS y a los compañeros con quienes compartí tantos buenos ratos dentro y fuera del laboratorio. Gracias Agustín (a los dos), Clara, Marisé y Ramón por acogerme y hacerme sentir parte del grupo.

Gracias a Alison Walker por invitarme a trabajar con su grupo en la Universidad de Bath. Una experiencia que sin duda marcó el desarrollo de mi doctorado. Gracias también a Petra Cameron y Giles Richardson por abrirme las puertas de sus grupos e introducirme en los mundos de las celdas invertidas de perovskita y de la simulación numérica, respectivamente. Gracias también a Matt por acompañarme codo con codo durante toda la estancia, a Laurie por enseñarme a utilizar *IonMonger*, pilar fundamental de mi tesis, y por su amistad. Gracias también a compañeros como Thijs, Lewis y Nicola por su tiempo y amabilidad durante esta estancia en el extranjero.

A Renaud Demadrille por abrirme las puertas del CEA de Grenoble y enseñarme los fundamentos de los colorantes fotocrómicos y mostrarme el lado más sintético de la ciencia. Gracias a los compañeros que me acompañaron durante esta estancia, especialmente a Valid, José María, Samuel, Cyril y Johan por hacerme sentir tan bienvenido y enseñarme los vericuetos de la fabricación de dispositivos que me he especializado en caracterizar.

Gracias a mi familia y amigos por acompañarme durante todo el camino, por soportarme cuando el estrés y la frustración podían conmigo y por ayudarme a desahogarme y enseñarme a tomarme las cosas de otro modo. Gracias Sergio, Daniel y Juan por estar ahí siempre y hacerme compañía cuando necesitaba desconectar de la Tesis. Gracias a los compañeros de

Accenture, especialmente a Mario, por aconsejarme y apoyarme cuando tomé la decisión menos fácil y me marché para comenzar esta aventura.

Por último, quisiera agradecer a los distintos grupos de investigación que han formado parte de alguna manera del desarrollo de esta tesis:

- Al grupo de Hernán Míguez en el Centro Superior de Investigaciones Científicas (CSIC) (España).
- Al grupo de Iván Mora en el Institute of Advanced Materials (INAM) (España).
- Al grupo de Pablo Boix en la Universitat de Valencia (España).
- Al grupo de Tom Aernouts en Interuniversity Microelectronics Centre (IMEC) (Bélgica).
- Al grupo de Martin Stolterfoht de la Universidad de Postdam (Alemania).
- A la empresa Fluxim AG (Suiza).
- Al grupo de Daniel Ramírez en la Universidad de Valparaíso (Chile).

List of Abbreviations

AC	Alternate current
ACN	Acetonitrile
AM 0	Air mass 0 Global
AM 1.5G	Air mass 1.5 Global
BIPV	Building integrated photovoltaics
BMII	1-butyl-3-methylimidalozliumiodide
CB	Conduction band
CCE	Charge collection efficiency
CPE	Constant phase element
DC	Direct current
DD	Drift-diffusion
DFT	Density functional theory
DoH	Degree of Hysteresis
DoS	Density of states
DSSC	Dye-sensitized solar cells
EC	Equivalent circuit
textbfEIS	Electrical impedance spectroscopy
EQE	External quantum efficiency
ETL	Electron transport layer
FF	Fill factor
HF	High-frequency
HOMO	Highest occupied molecular orbital
HTL	Hole transport layer
IMPS	Intensity-modulated photocurrent spectroscopy
IMVS	Intensity-modulated photovoltage spectroscopy
IPCE	Incident photon to current efficiency
IQE	Internal quantum efficiency
JV	Current-voltage
LED	Light-emitting diode
LF	Low-frequency

LUMO	Lowest unoccupied molecular orbital
MAPbI$_3$	$CH_3NH_3PbI_3$
MHP	Metal halide perovskite
MP	Maximum power
MT	Multiple trapping
n$_{AP}$	Apparent ideality factor
n$_{EC}$	Ectypal factor
n$_{EL}$	Electronic ideality factor
n$_{ID}$	Ideality factor
OC	Open-circuit
OCP	Open-circuit photovoltage
OPV	Organic photovoltaics
PCE	Power conversion efficiency
PEC	Parallel equivalent circuit
PSC	Perovskite solar cells
PV	Photovoltaic
QD	Quantum dots
RTIL	Room temperature ionic-liquid
SC	Short-circuit
SEC	Series equivalent circuit
SEM	Scanning electron microscopy
SRH	Shockley-Read-Hall
TBP	4-tertbutylpiridine
UV	Ultraviolet
VB	Valence band
XRD	X-ray diffraction

Physical Constants

c_0 Speed of Light $= 2.997\,924\,58 \times 10^{8}\,\mathrm{m\,s^{-1}}$

F Faraday's constant $= 96.485\,\mathrm{C\,mol^{-1}}$

h Planck's constant $= 6.626\,070\,04 \times 10^{-34}\,\mathrm{J\,s}$

k_B Boltzmann's constant $= 8.617\,333\,262\,145 \times 10^{-5}\,\mathrm{eV\,K^{-1}}$

K_s Solar constant $= 1.361\,\mathrm{W\,m^{-2}}$

q Elementary charge $= 1.602\,176\,634 \times 10^{-19}\,\mathrm{C}$

R Ideal gas constant $= 8.314\,462\,618\,153\,24\,\mathrm{J\,K^{-1}\,mol^{-1}}$

List of Symbols

a	Size of an ion
A	Area
A_{abs}	Absorbance
A_{for}	Area under the forward current-voltage curve
A_{tauc}	Proportionality constant
A_{rev}	Area under the reverse current-voltage curve
b_E	Thickness of ETL
b_H	Thickness of HTL
b_0	Transient numerical parameter
B_n	Electron capture coefficient
B_p	Hole capture coefficient
c	Concentration
C	Capacitance
C_{dr}	Dielectric relaxation-like capacitance
C_{HF}	High-frequency capacitance
c_i	Charge carriers concentration
C_{ion}	Ionic Debye layer capacitance
C_{LF}	Low-frequency capacitance
C_g	Geometric capacitance extracted from equivalent circuit
C_{geo}	Theoretical geometric capacitance
C_{pt}	Double-layer capacitance
C_0	Chemical capacitance prefactor
C_μ	Chemical capacitance
d	Thickness
D	Diffusion coefficient
d_E	Effective doping density of the ETL
D_E	Electronic diffusion coefficient in the ETL
d_H	Effective doping density of the HTL
D_H	Electronic diffusion coefficient in the HTL
D_i	Charge carriers diffusion coefficient

D_{ion}	Anion vacancy diffusion coefficient
D_n	Diffusion coefficient of electrons
D_p	Diffusion coefficient of holes
D_0	Diffusion coefficient of electrons in the dark
D_μ	Chemical electron diffusion coefficient
E	Energy
E_C	Lower energy edge of the conduction band
$\mathrm{E}_{C,E}$	Energy of the ETL conduction band
${}_n\mathrm{E}_F$	Quasi Fermi level caused by the trap distribution
E_F	Fermi level
E_{FE}	Fermi level in the ETL
E_{FH}	Fermi level in the HTL
E_F^n	Fermi level of the n-type selective material
E_F^p	Fermi level of the p-type selective material
$\mathrm{E}_{F,redox}$	Fermi level at the redox potential
E_g	Energy band gap
E_{redox}	Redox potential
E_V	Higher energy edge of the valence band
$\mathrm{E}_{V,H}$	Energy of the HTL valence band
f	Frequency
F_P	Ionic flux
F_{ph}	Photonic flux
G_n	Photogenerated carriers density
g_c	Density of states of the perovskite conduction band
$g_{c,E}$	Density of states of the ETL conduction band
g_E	Energy trap distribution
g_v	Density of states of the perovskite valence band
$g_{v,H}$	Density of states of the HTL valence band
G	Photogeneration
G_{th}	Thermal generation
I	Current response
I_0	Amplitude of the current response
I_{inc}	Incident light intensity
I_{tr}	Transmitted light intensity
J	Current density
J_{ex}	Current exchange density
J_{dark}	Dark current density
J_{DC}	Current density at the DC voltage

J_{diff}	Total diffusion current
J_{drift}	Total drift current
$J_{n,diff}$	Electron diffusion current
$J_{n,drift}$	Electron drift current
$J_{p,diff}$	Hole diffusion current
$J_{p,drift}$	Hole drift current
J_{gen}	Generation current density
J_{MP}	Maximum power point current density
J_n	Electron current density
J_p	Hole current density
J_{rec}	Recombination current density
J_{SC}	Short-circuit current density
$J_{SC(int)}$	Integrated photocurrent
J_0	Dark saturation current
J_{00}	Recombination rate prefactor
k_{dec}	Excited state decay rate constant
k_E	Ratio of carrier densities at the each side of the ETL interface
k_H	Ratio of carrier densities at the each side of the HTL interface
k_{inj}	Electron injection rate constant
k_r	Back reaction prefactor
k_{rec}	Recombination constant
k_1	Deep trap approximation constant at the ETL interface
k_2	Deep trap approximation constant at the HTL interface
k_3	Deep trap approximation constant
L_n	Diffusion length of electrons
L_p	Diffusion length of holes
m	Mass
n	Electron density
N	Power law exponent
n_0	Electron density in the conduction band
N_A	Acceptor atoms doping density
n_c	Electron density in the conduction band edge
N_c	Density of states in the conduction band edge
N_{cat}	Cation vacancy density
N_D	Donor atoms doping density
n_i	Intrinsic concentration of charge carriers
N_{ion}	Total density of mobile ions
n_{reac}	Electrons involved in the reduction reaction

n_s	Electron density at the surface
n_t	Electron density when Fermi level equals to trap level
N_t	Trap density
N_v	Density of states in the valence band edge
N_0	Anion vacancy density
p	Hole density
P	Perturbation
P_{CPE}	Numerical parameter of CPE
$P_{incident}$	Power density of the incident light
P_{MP}	Maximum power point
p_s	Hole density at the surface
p_t	Hole density when Fermi level equals to trap level
p_v	Hole density in the valence band edge
p_0	Hole density in the valence band
R	Resistance
$R_{CT_{ce}}$	Counter-electrode charge transfer resistance
Rec	Recombination rate
R_d	Bimolecular recombination rate
R_{DC}	DC resistance
R_{dr}	Dielectric relaxation-like resistance
R_{rf}	Reflectance
R_{HF}	High-frequency resistance
R_{ion}	Ionic Debye layer resistance
R_l	Surface recombination rate at the ETL interface
R_{LF}	Low-frequency resistance
R_r	Surface recombination rate at the HTL interface
R_{rec}	Recombination resistance
R_S	Series resistance
R_{SH}	Shunt resistance
R_{SRH}	Shockley-Read-Hall recombination rate
R_{surf}	Surface recombination flux
R_{th}	Thermal recombination
R_t	Transport resistance
R_{00}	Recombination resistance prefactor
$R(\omega \to 0)$	Low-frequency limit resistance
S	Signal
S_n	Surface recombination velocity for electrons
S_p	Surface recombination velocity for holes

t	Time
t_{tr}	Transport time
t_0	Perturbation time
T	Absolute temperature
T_{CPE}	Pseudocapacitance of CPE
T_{tr}	Transmittance
U_n	Recombination rate
V	Potential
V_{bi}	Built-in potential
v_{dn}	Average drift velocity for electrons
v_{dp}	Average drift velocity for holes
V_{DC}	Direct-current voltage
v_n	Thermal velocity of the electron
v_{nE}	Electron recombination velocity within the ETL interface
v_{nH}	Electron recombination velocity within the HTL interface
v_p	Thermal velocity of the hole
v_{pE}	Hole recombination velocity within the ETL interface
v_{pH}	Hole recombination velocity within the HTL interface
V_{MP}	Maximum power point voltage
V_{OC}	Open-circuit voltage
$V_{OC,rad}$	Thermodynamic limit of open-circuit voltage
V_T	Thermal voltage
V_0	Amplitude of the voltage perturbation
Y	IMPS transfer function
Y_{PV}	IMVS transfer function
Z	Impedance transfer function
Z_{tr}	Generic transfer function
α	Trap parameter
α_{abs}	Absorption coefficient
β	Recombination parameter
β_{bim}	Bimolecular recombination parameter
β_{rad}	Thermal recombination parameter
γ	Reaction order
γ_{IMPS}	IMPS lifetime numerical factor
ε	Dielectric constant
ε_E	Permittivity of the ETL
ε_H	Permittivity of the HTL

ε_{mol}	Molar absorption coefficient
ε_p	Permittivity of the perovskite material
ε_0	Permittivity of vacuum
ζ	Electric field
λ	Wavelength
μ	Chemical potential
μ_{mob}	Charged particle mobility
μ_n	Electron mobility
μ_p	Hole mobility
ν	Overpotential
ρ	Net charge density
σ	Ionic conductivity
σ_n	Electron capture cross section
σ_p	Hole capture cross section
τ_{EIS}	Impedance time constant
τ_{IMPS}	IMPS time constant
τ_{IMVS}	IMVS time constant
τ_n	Electron lifetime
τ_p	Hole lifetime
τ_{rec}	Recombination lifetime
τ_t	Electron transport lifetime
θ	Angle
ϕ	Phase shift
ϕ_{por}	Porosity
φ_{inj}	Electron injection efficiency
φ_{BB}	Infrared black body spectrum
Φ_a	Absorbed photon flux
$\Phi_{em,0}$	Emission spectrum
Φ_{sun}	Angle of elevation of the Sun
Φ_0	Incident photon flux
ω	Angular frequency
ω_{HF}	Angular frequency of high-frequency IMPS signal

Appendix A

Characterization of photochromic dye-sensitized solar cells using small-signal perturbation techniques

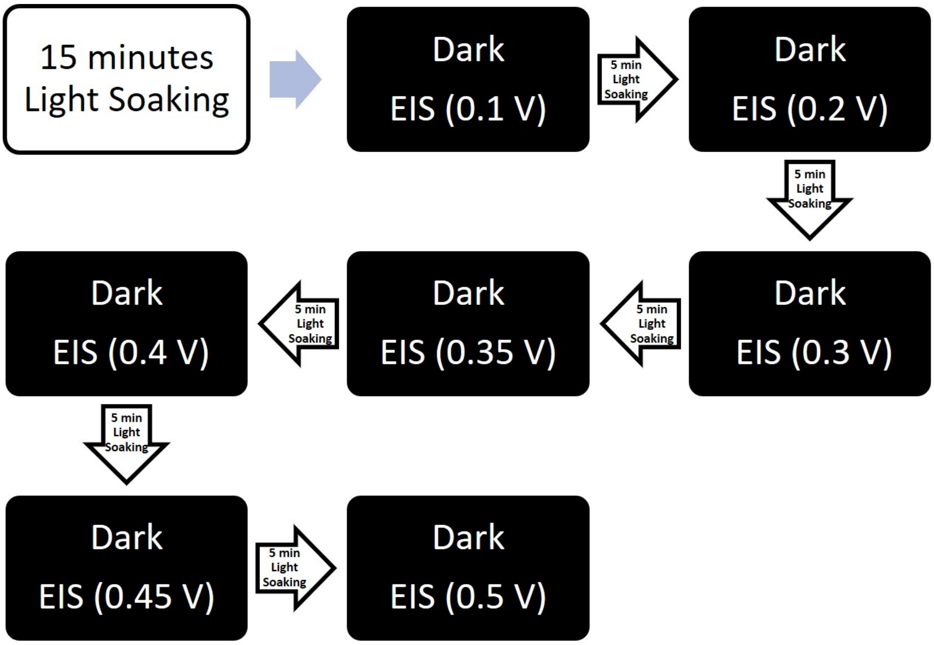

Figure A.1: Flow chart of the order of experiments for the EIS measurements in the dark after light soaking in order to ensure a similar degree of activation for all the measurements.

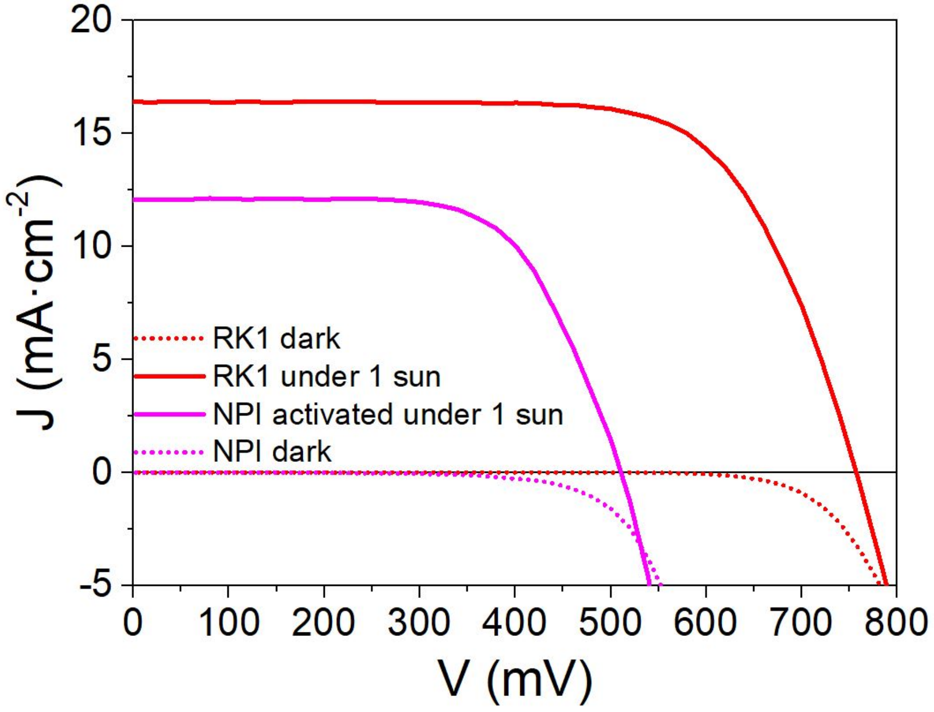

Figure A.2: *JV* curves under dark conditions and one sun illumination of the non-photochromic RK1 DSSC compared to the photochromic NPI DSSC in the photostationary state.

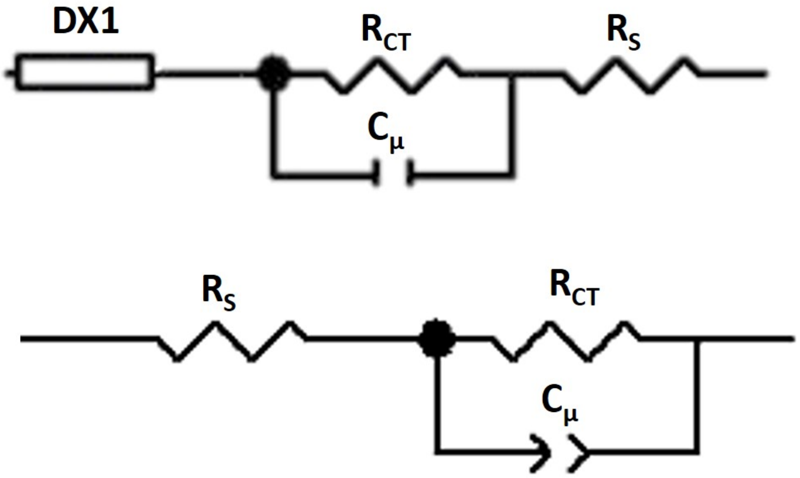

Figure A.3: Typical EC used to fit the EIS results of DSSCs (up), being DX1 is an element that takes into account the diffusion-recombination transmission line. The simplified EC used to fit the spectra obtained in this study (bottom).

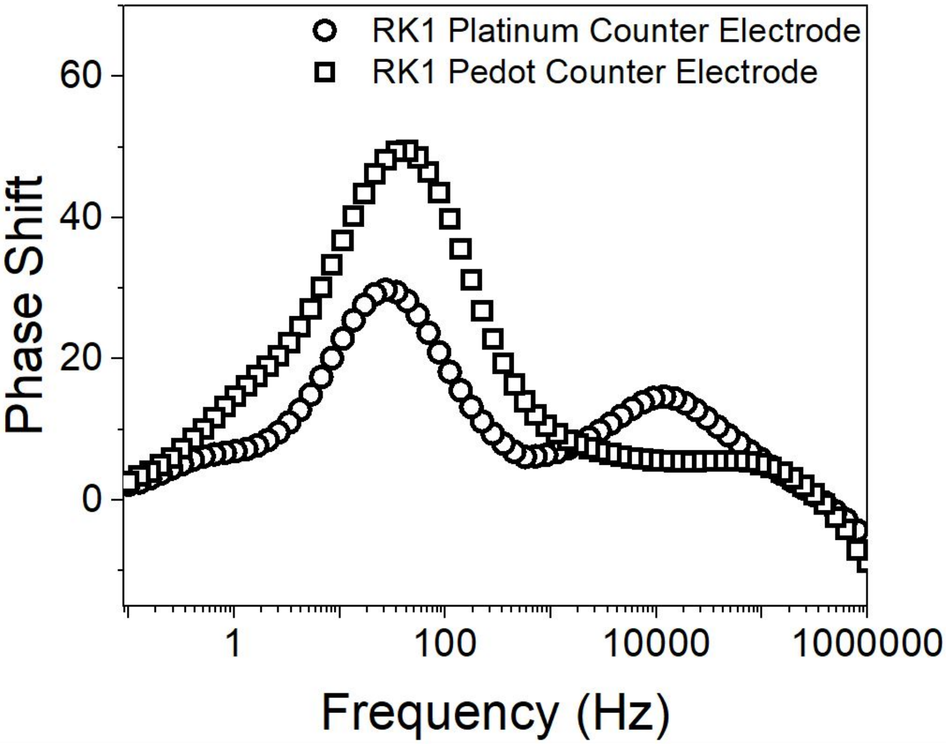

Figure A.4: Bode plots from EIS for an RK1 dye solar cell at an applied voltage of 0.7 V, which is equal to the V_{OC} under white illumination for a cell with a platinum (circles) and a PEDOT (squares) counter electrode.

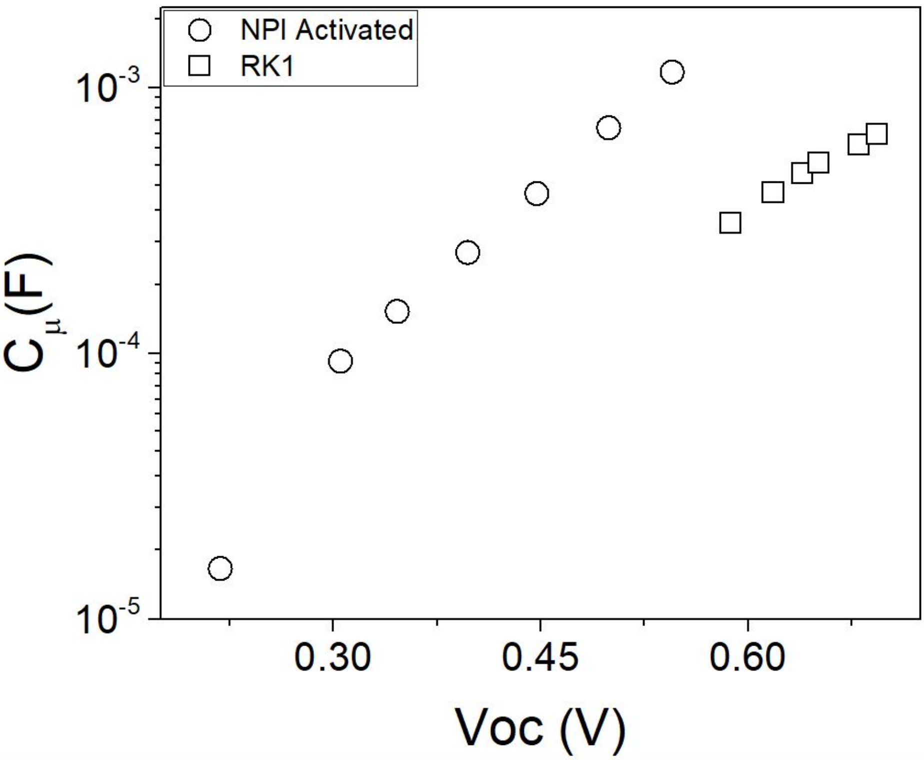

Figure A.5: C_μ vs V obtained from EIS with white light for RK1 and activated NPI devices.

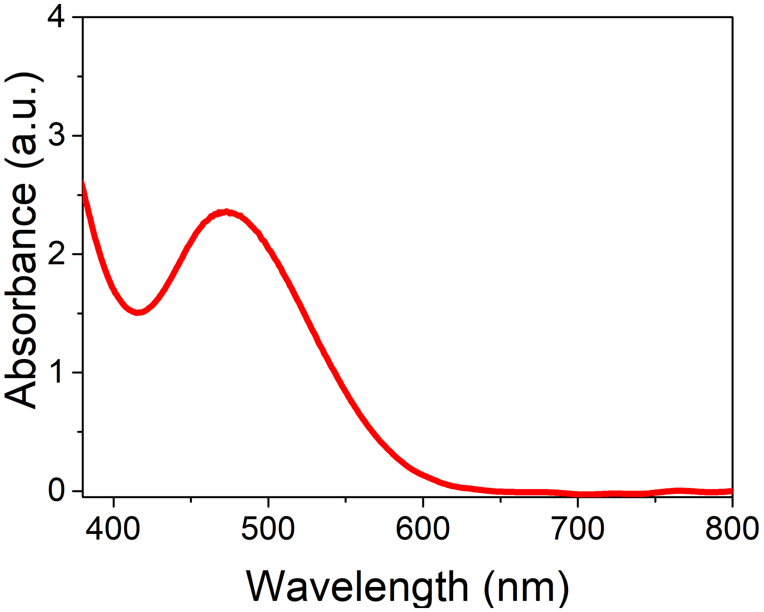

Figure A.6: Absorbance spectrum for the 380 – 800 nm wavelength range of the RK1 dye on a 2 μm TiO_2 electrode.

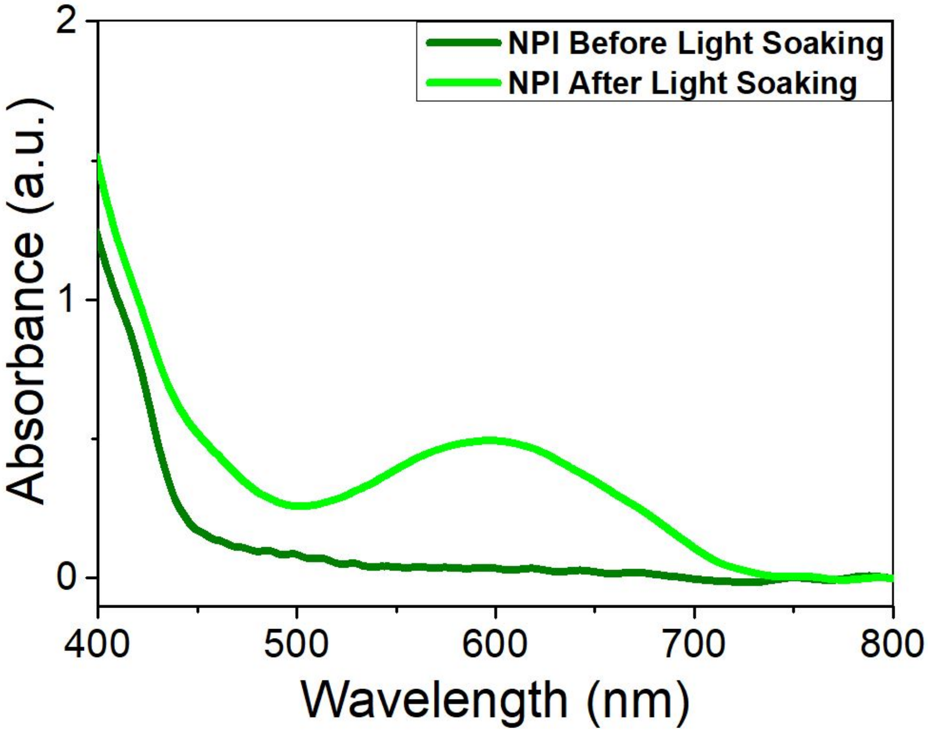

Figure A.7: Absorbance spectrum for the 400 – 800 nm wavelength range of the photochromic NPI dye before and after light soaking on a 2 μm TiO_2 electrode.

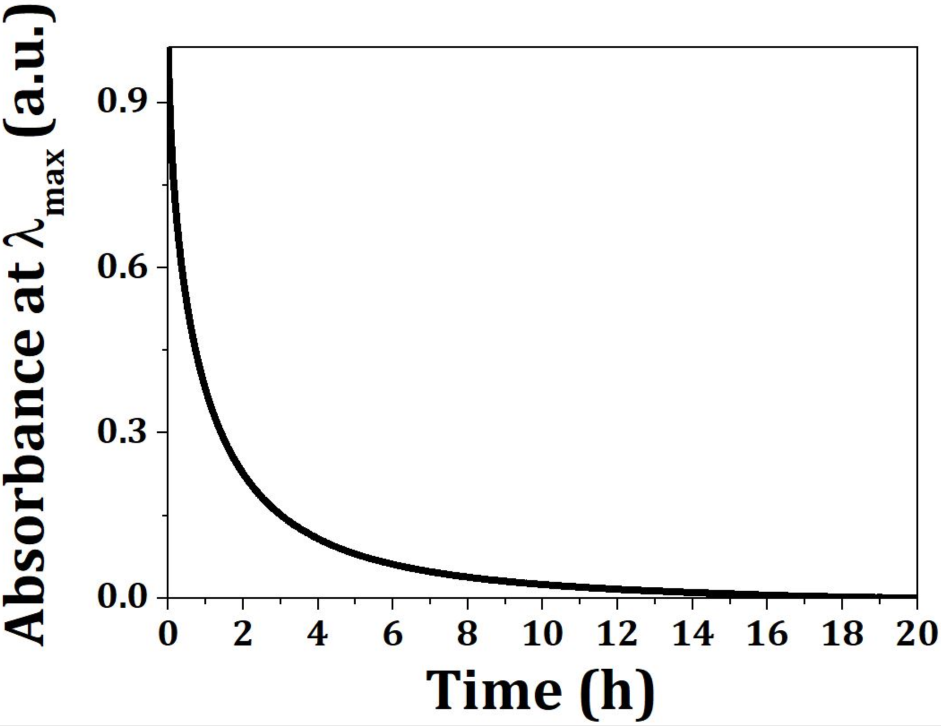

Figure A.8: Deactivation kinetics of the photochromic NPI dye measured on a complete cell with a 13 μm TiO_2 electrode.

Table A.1: α and β values obtained from fitting the EIS results of the RK1 solar cells to the parallel -RC- element.

Color Illumination	**α value**	**β value**
Dark	0.35 ± 0.03	0.63 ± 0.01
White	0.28 ± 0.01	0.87 ± 0.02
Blue	0.24 ± 0.01	0.79 ± 0.07
Red	0.26 ± 0.04	0.75 ± 0.06

Table A.2: α and β values obtained from fitting the EIS results of the NPI solar cells before and after light soaking to the parallel -RC- element.

Color Illumination	α value	β value
Dark before light soaking	0.31 ± 0.01	0.55 ± 0.09
Dark after light soaking	0.27 ± 0.04	0.50 ± 0.06
White before light soaking	0.28 ± 0.01	0.80 ± 0.10
White after light soaking	0.27 ± 0.06	0.77 ± 0.02
Blue before light soaking	0.30 ± 0.04	0.83 ± 0.09
Blue after light soaking	0.29 ± 0.04	0.85 ± 0.07
Red before light soaking	0.31 ± 0.05	0.77 ± 0.04
Red after light soaking	0.28 ± 0.04	0.75 ± 0.08

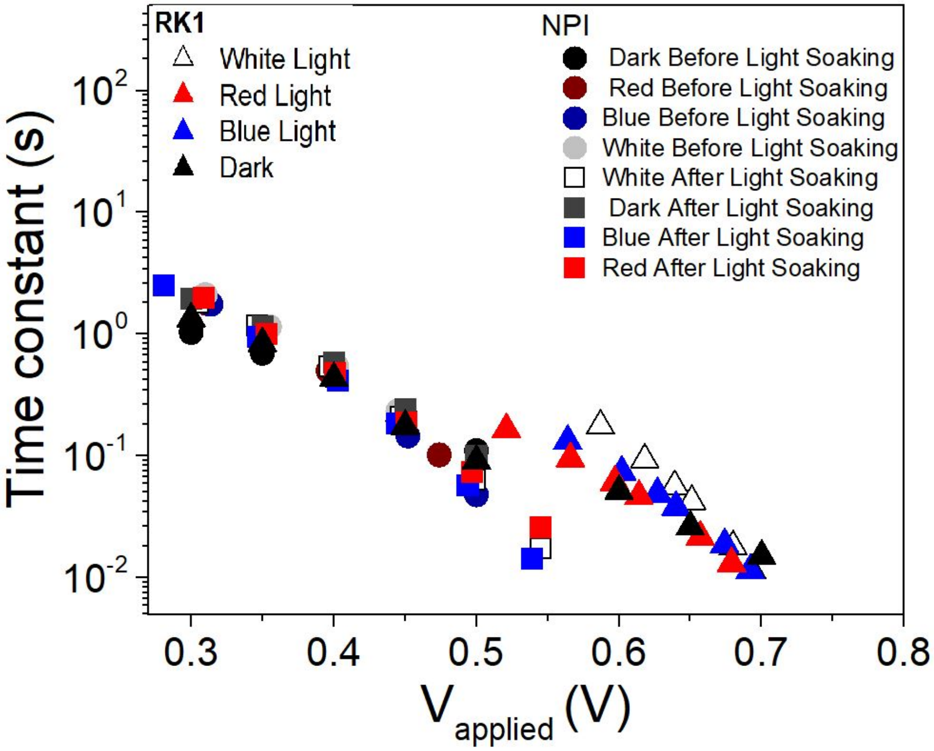

Figure A.9: Time constants associated with the recombination feature of the EIS results under different sources of illumination for an RK1 and an NPI device extracted from the frequency of the main peak of the Bode plots in Figure 4.5.

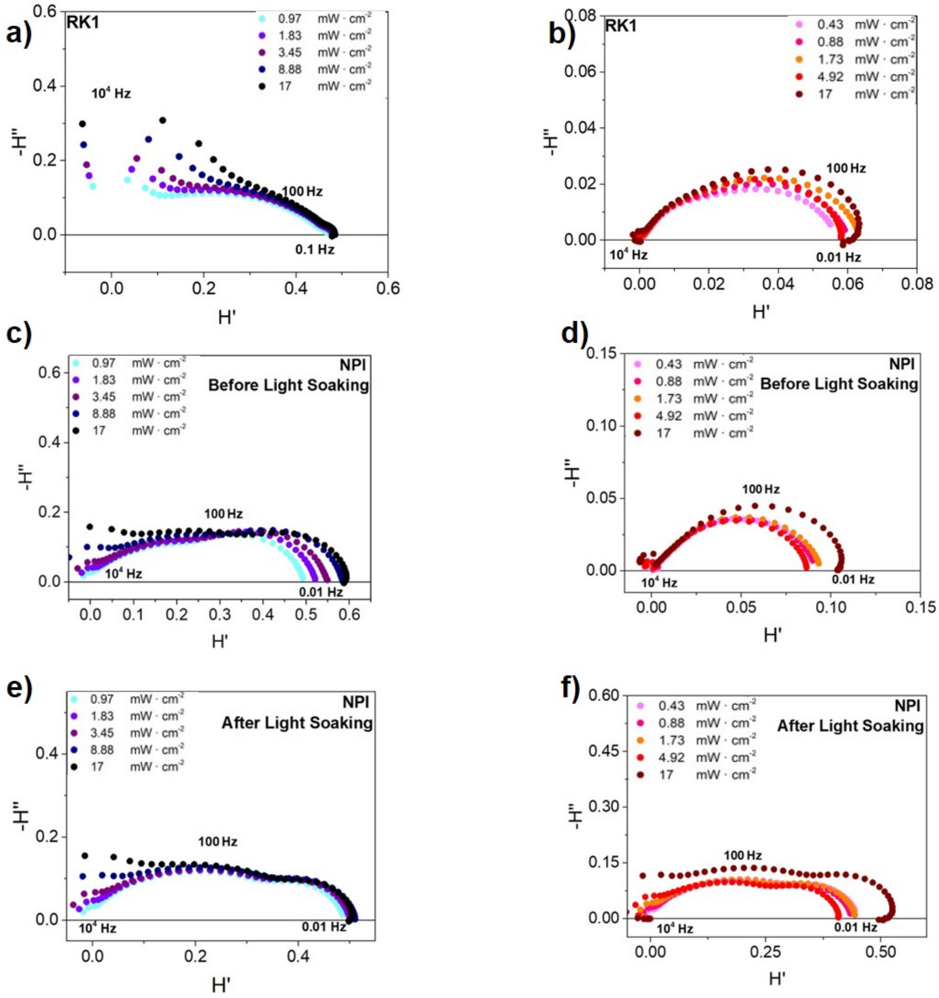

Figure A.10: Nyquist plots of IMPS measurements for an RK1 DSSC (a and b) and a deactivated (c and d) and activated (e and f) NPI DSSC cell under different light intensities with blue (left) and red (right) illumination.

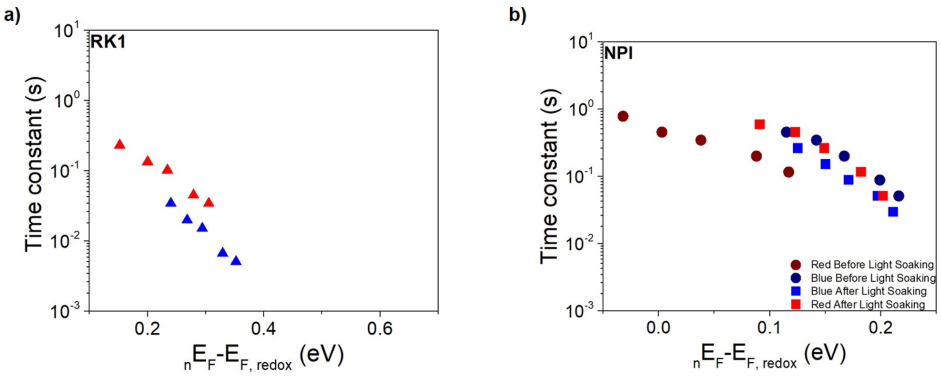

Figure A.11: Time constants obtained from IMPS measurements for an RK1 (a) and an NPI (b) solar cell, with the corrected voltage to account for the difference between the trap occupancy between OC and SC conditions as described in the main text.

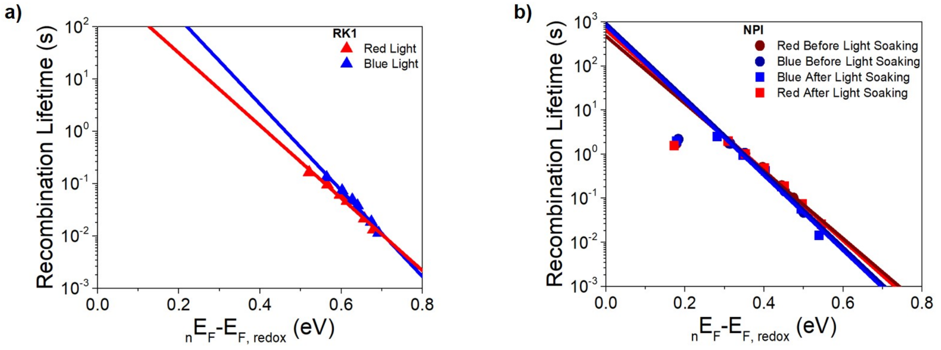

Figure A.12: Recombination lifetime vs. corrected voltage obtained from the EIS measurements (points) and extrapolated to short circuit conditions (lines) of (a) an RK1 and (b) a deactivated and activated NPI-based solar cell.

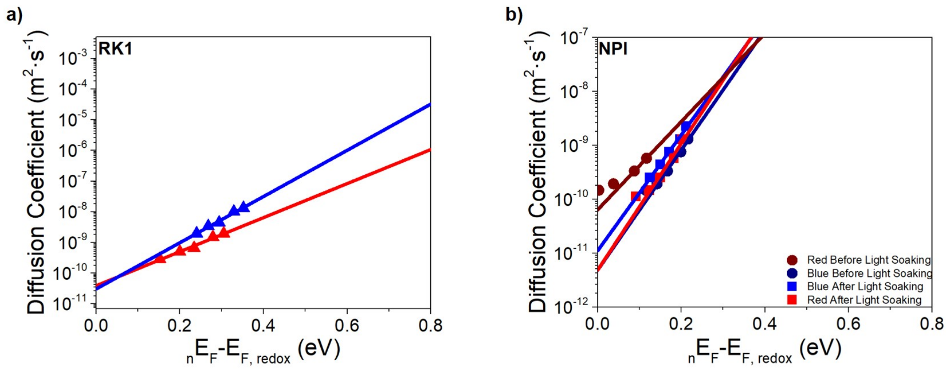

Figure A.13: Diffusion coefficient vs. corrected voltage calculated from the IMPS time constants for an RK1 (a) and a deactivated and activated NPI (b) solar cell using equation 2.57, and extrapolated to short circuit conditions (trend lines).

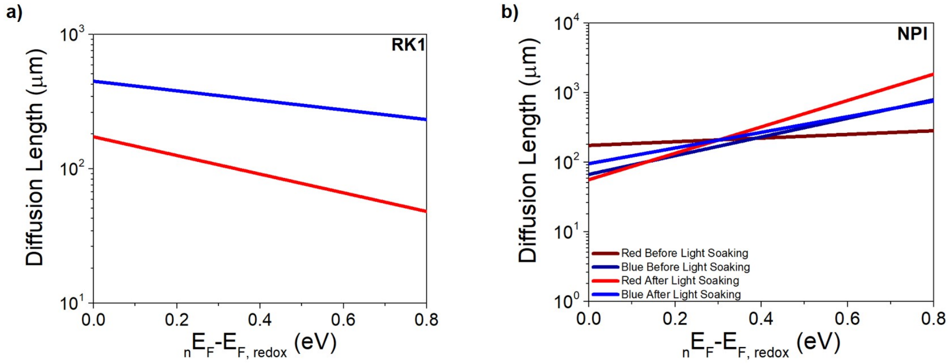

Figure A.14: Diffusion length vs. corrected voltage for an RK1 (a) and a deactivated and activated NPI (b) solar cell calculated by multiplying the trendlines obtained in Figure A.12 and Figure A.13 according to Equation 3.32.

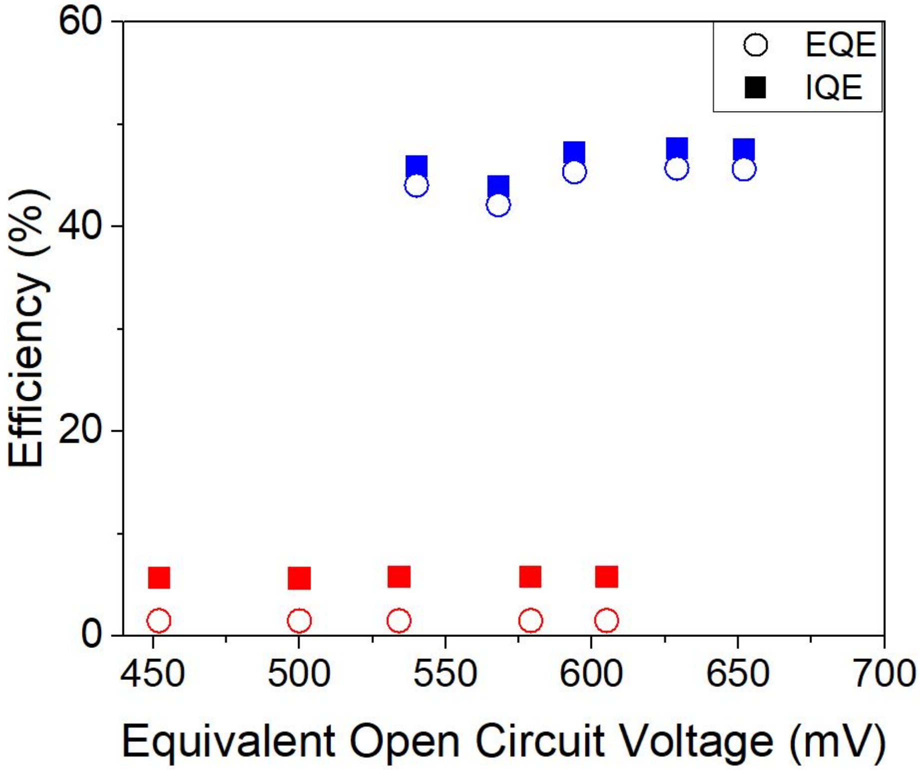

Figure A.15: External (hollow symbols) and internal (solid symbols) quantum efficiency vs. equivalent V_{OC} obtained from IMPS measurements at SC under blue and red monochromatic illumination for an RK1 DSSC.

Appendix B

Internal quantum efficiency and time signals from intensity-modulated photocurrent spectra of perovskite solar cells

B.1 Fabrication of methylammonium lead iodide perovskite ($MAPbI_3$) perovskite solar cell devices

PSCs devices were fabricated on FTO-coated glass (Pilkington-TEC15) patterned by laser etching. Prior to use, the substrates were cleaned using Hellmanex® solution and rinsed with deionized water and ethanol. Thereupon, they were ultrasonicated in 2-propanol and dried using compressed air. The TiO_2 blocking layer was deposited onto the substrates by spray pyrolisis at 450ºC, using a titanium diisopropoxide bis(acetylacetonate) solution (75% in 2-propanol, Sigma Aldrich) diluted in ethanol (1:14, v/v), with oxygen as carrier gas. The TiO_2 compact layer was then kept at 450ºC for 30 min to form the anatase phase. The TiO_2 mesoporous layer was deposited on top of the TiO_2 compact layer by spin coating at 2000 rpm for 10 s using a commercial TiO_2 paste (Dyesol, 18NR-T) diluted in ethanol (1:5, weight ratio). The TiO_2 mesoporous layer was heated at 500ºC for 30 min.

A pure methylammonium lead iodide solution was prepared to be deposited by spin coating under environmental conditions. The perovskite precursor solution was obtained by adjusting DMSO proportion as a function of water vapor pressure in the air (1.5 kPa), 50 μL of the perovskite precursor solution were spin-coated in a one-step setup at 4000 rpm for 50 s. DMF is selectively washed with non-polar diethyl ether during this step just before the white solid begins to crystallize in the substrate. Spiro-OMeTAD was deposited as hole selective material by dissolving 72.3 mg in 1 mL of chlorobenzene as well as 17.5 μL of a lithium bis (trifluoromethylsulphonyl)imide (LiTFSI) stock solution (520 mg of LiTFSI in 1mL of acetonitrile), and 28.8 μL of 4-tert-butylpyridine (TBP). The Spiro-OMeTAD (50 μL) was spin-coated at 4000 rpm for 30 s. Finally, 60 nm of gold was deposited as a metallic contact by thermal evaporation under vacuum level between $1 \cdot 10^{-6}$ and $1 \cdot 10^{-5}$ torr with an active area of 0.32 cm^2. All the deposition processes were carried outside a glovebox under environmental conditions.

B.2 Fabrication of dye sensitized solar cells devices

The cleaning of the working electrode followed a process similar to the one described for the fabrication of PSCs. Then, a TiO_2 nanoparticles film of 12 μm thick was deposited by screen-printing technique with an active area of 0.16 cm^2. In particular, this mesoporous layer consisted of 8 μm of 20 nm TiO_2 nanoparticles (18NR-T, Dyesol) and a layer of 4μm of 400 nm TiO_2 particles (18NR-AO, Dyesol). After that, the electrode was annealed at 500º C for 30 min. The heated electrode was immersed in a solution of $TiCl_4$ (40 mM) at 70º C for 30 min and annealed again at 500º C for 30 min. The

TiO_2 electrode was dyed in an N719 solution overnight. The dye solution was composed of N719 (0.3 mM) and chenodeoxycholic acid (0.3 mM) in ethanol.

The counter-electrode was made by spreading a Platisol solution into a conducting glass substrate (Pilkington-TEC8), followed by heating at 400° C for 15 min. The working and counter-electrodes were sandwiched together using a thin thermoplastic frame. Electrolytes of varying viscosity were prepared by using different ratio of ACN and room temperature ionic-liquid (RTIL) as solvents. The ionic liquid used was 1-Buthyl-1-Methylpyrrolidinium bis(trifluoromethane sulfonyl)imide (Pyr), and the redox pair chosen was the iodide/iodine. The composition and concentration of every electrolyte are shown in Table B.1. Finally, the device was filled with electrolyte through a hole previously made in the back of a platinized counter-electrode. The hole was sealed with the thermoplastic polymer and a cover slide glass.

Table B.1: Composition of the electrolytes for the DSSCs studied in this work. I_2: Iodine, BMII:1-butyl-3-methylimidalozliumiodide, LiI: Lithium iodide, TBP: 4-tertbutylpiridine, GuSCN: Guanidine thiocyanate, ACN: Acetonitrile, Pyr: 1-Buthyl-1-Methylpyrrolidinium bis(trifluoromethanesulfonyl)imide. RTIL means room temperature ionic-liquid.

Device	**Solvent(V/V %)**	**Solutes**
Pyr (75%)	25:75 (ACN/Pyr)	0.03 M I_2 + 1 M BMII + 0.05 M LiI + 0.5 M TBP + 0.1 M GuSCN
Pyr (100%)	100 (Pyr)	
ACN	100 (ACN)	

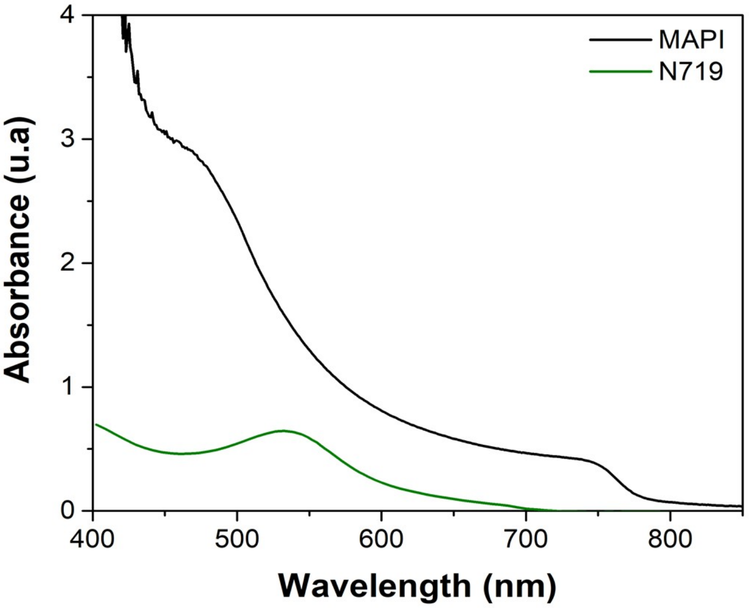

Figure B.1: Optical absorption of $MAPbI_3$ PSC and N719 DSSC. The data was obtained after subtracting the absorption of the underlying TiO_2 layers, which are used as blank (reference) sample in the measurements.

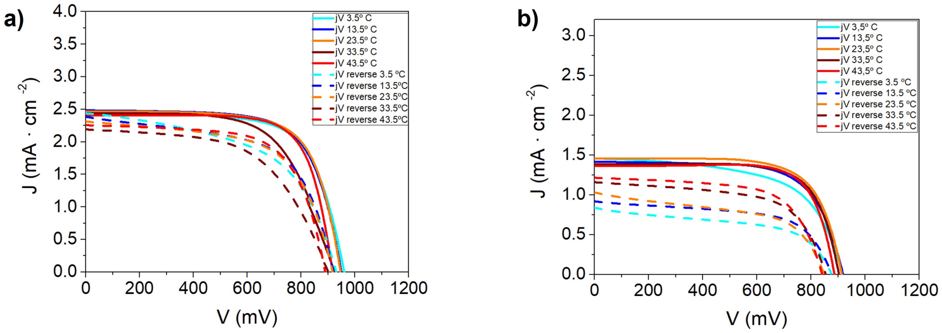

Figure B.2: *JV* curves of $MAPbI_3$ PSCs as obtained with blue (a) and red (b) illumination. The illumination intensities were 2.64 and 2.58 $mA \cdot cm^{-2}$, respectively.

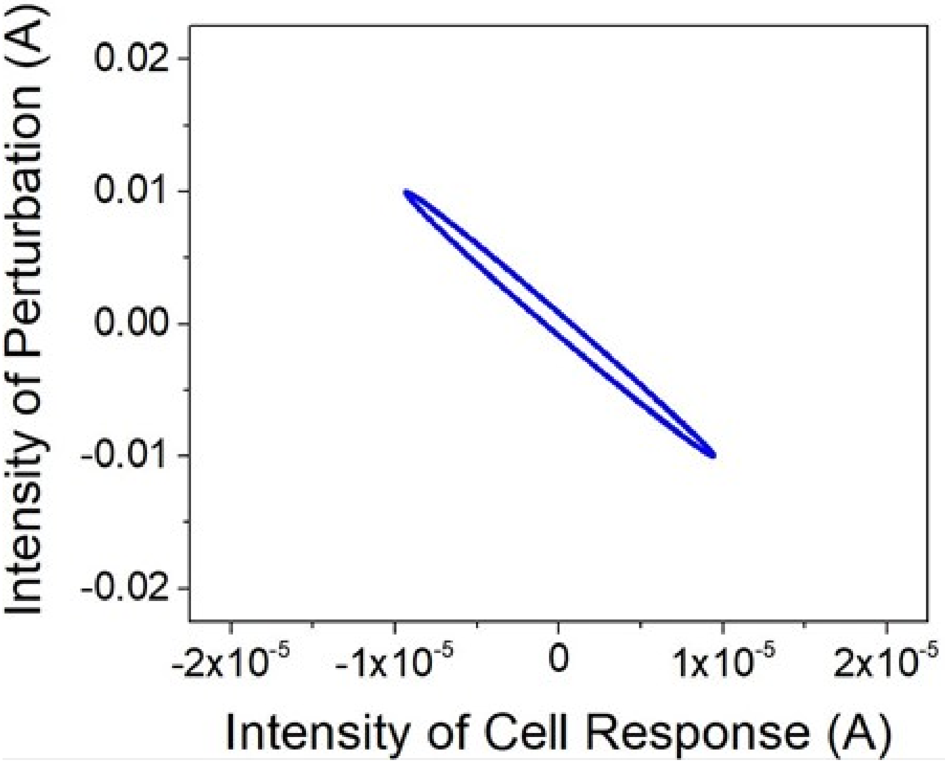

Figure B.3: Lissajous plot at 0.1 Hz of the IMPS measurement of the $MAPbI_3$ solar cell with blue light.

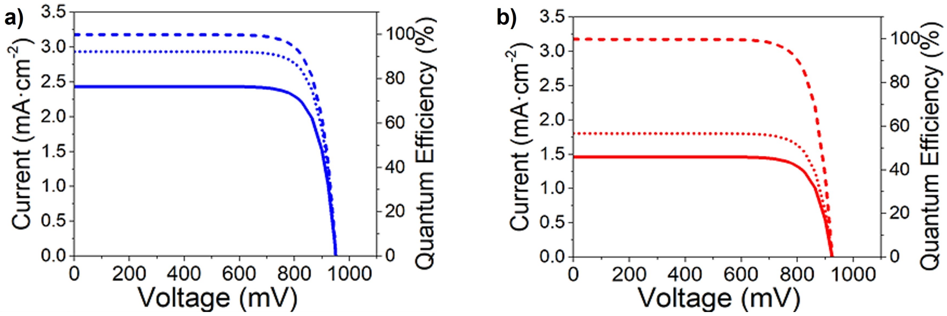

Figure B.4: *JV* curves (solid lines), EQE (dotted lines) and IQE (dashed lines) of $MAPbI_3$ solar cells with blue (a) and red (b) illumination as predicted by the single layer DD model for the experimental parameters in Figure B.2 and τ_n and τ_p set to 90 ns, electron and hole diffusion coefficients of 5 $cm^2 \cdot s^{-1}$, a density of states of $4 \cdot 10^{24}$ m^{-3}, a bandgap of 1.55 eV and a relative permittivity of 24.1.

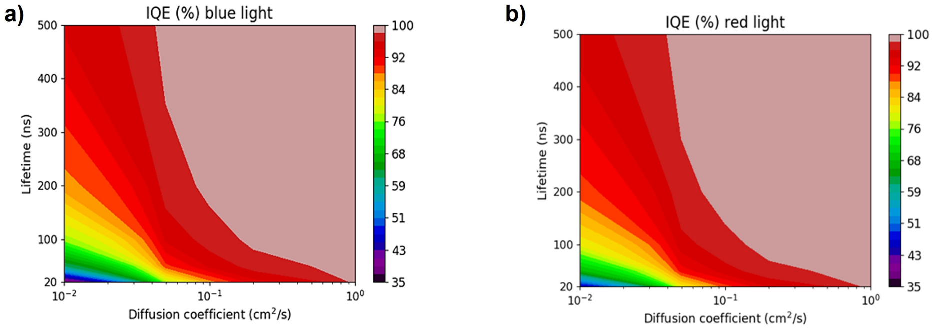

Figure B.5: Theoretical IQE for $MAPbI_3$ based solar cells as predicted by the DD model for a set of diffusion coefficients and lifetimes with blue (a) and red (b) illumination.

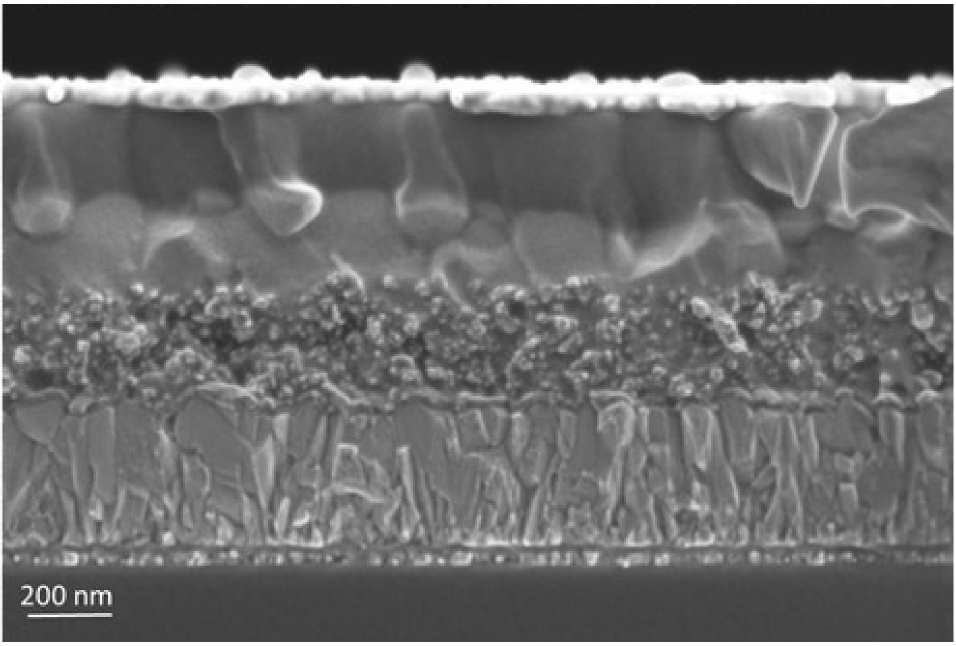

Figure B.6: Cross-sectional image of a PSC fabricated with the experimental protocol described above obtained by scanning electron microscopy (SEM).

Table B.2: α values and power law exponents (N) of the mid-frequency IMPS time constants in DSSCs of different electrolytes compositions and PSC. A test of an ionic liquid electrolyte DSSC with a mesoporous TiO_2 layer of the same thickness as the PSC is also included in the data.

Device	α **(blue)**	α(red)	N (blue)	N (red)
Pyr (75%)	0.86	0.87	0.33	0.68
Pyr(100%)	0.91	0.87	0.17	0.68
ACN	0.76	0.86	0.24	0.49
Ultrathin TiO_2	0.78		0.33	
$MAPbI_3$	0.61	0.66	0.21	0.35

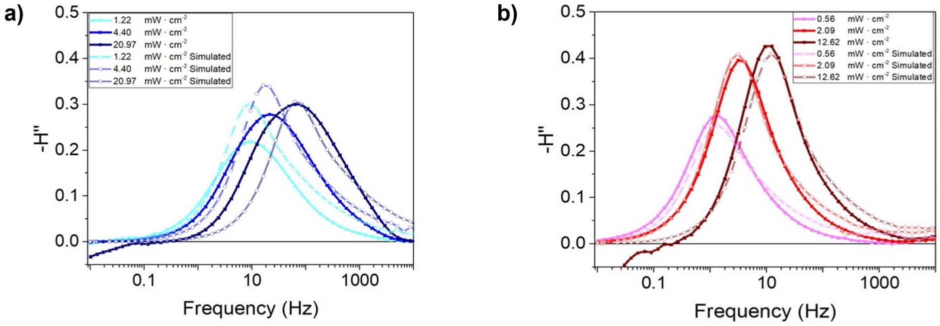

Figure B.7: Experimental and simulated Cole-Cole plots of the IMPS spectra of ACN based electrolyte DSSC with blue (a) and red (b) illumination. Simulations were run with the linearized version of a diffusion-recombination model for electrons in the TiO_2 mesoporous layer. The adjusted diffusion lengths in the simulation were, for increasing light intensities as indicated, 14.8, 15.9 and 18.7 μm in the blue and 10, 14 and 16.3 μm in the red.

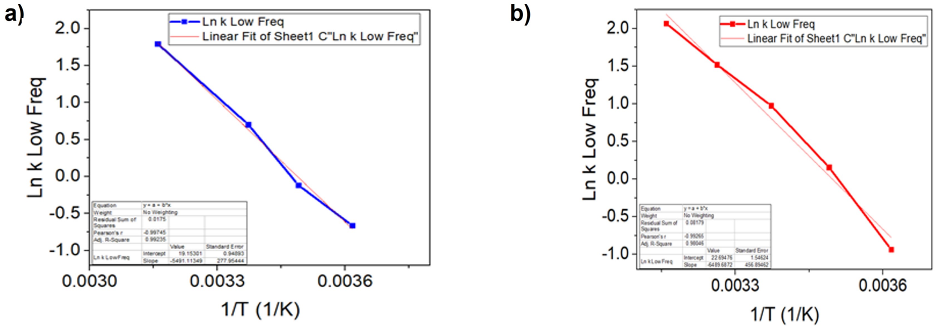

Figure B.8: Arrhenius plots of the LF time constants extracted from the IMPS experiments at different temperatures under blue (a) and red (b) illumination.

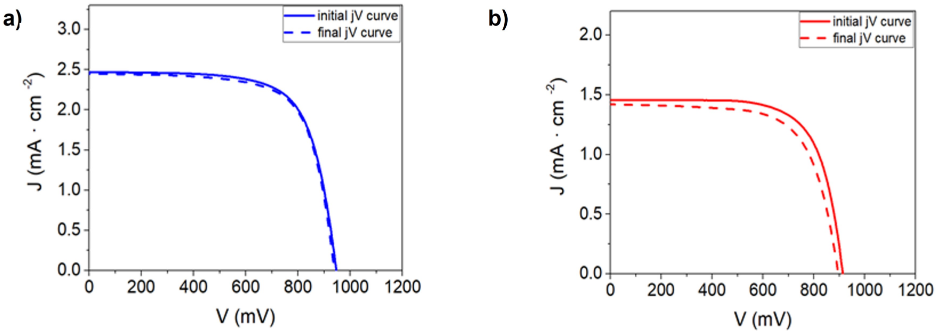

Figure B.9: Monochromatic *JV* curves before and after the small-perturbation experiments.

Appendix C

Identification of recombination losses and charge collection efficiency in a perovskite solar cell by comparing impedance response to a drift-diffusion model

Table C.1: Parameter set used in the DD simulations for regular cell configuration with no surface recombination, in which ε_0 denotes the permittivity of free space.

Parameter	**Value**	**Justification**
Temperature (T)	298 K	Standard conditions
Incident photon flux (F_{ph})	5 - 1000 W·m^{-2}	It is adjusted to give the desired Voc with the 1 sun equivalent as upper limit
Perovskite layer (MAPbI$_3$)		
Width (d)	$3{\cdot}10^{-7}$ m	Direct measurement on similar devices. Ref.[1]
Permittivity (ε_p)	24.1 ε_0	Ref.[2]
Absorption coefficient at 465 nm (α_{abs})	$6.5{\cdot}10^{6}$ m^{-1}	Direct measurement on similar devices
Conduction band minimun (E_C)	(-) 3.8 eV	Intermediate value between Ref.[3] and[4]
Valence band maximum (E_V)	(-) 5.4 eV	Ref.[3]
Electron difusion coefficient (D_n)	$5{\cdot}10^{-5}$ m^{2}s^{-1}	Gives a *CCE* of 100%[1,5] with the bulk electron pseudolifetime used to approximate the V_{OC} of the experimental *JV* curve. Value very close to the reported ($2.05{\cdot}10^{-5}$ m^2) by Wehrenfennig *et al*[6].
Hole diffusion coefficient (D_p)	$5{\cdot}10^{-5}$ m^{2}s^{-1}	Similar value to the perovskite electron diffusion coefficient.
Conduction band density of states (g_c)	$8.1{\cdot}10^{24}$ m^{-3}	Ref.[7]
Valence band density of states (g_v)	$5{\cdot}8{\cdot}10^{24}$ m^{-3}	Ref.[7]
Mean density of anion vacancies (N_0)	$1{\cdot}6{\cdot}10^{25}$ m^{-3}	Ref.[8]
Diffusion coefficient for anions (D_{ion})	10^{-16}m^{2}s^{-1}	Ref.[9]

Recombination parameters

Electron pseudolifetime for bulk SRH (τ_n)	$9{\cdot}10^{-7}$ s	Chosen to match an approximate V_{OC} of 1 V under the 1 sun equivalent illumination. Very close to the value of 7.36 $\cdot\, 10^{-}-7$ reported by Zhou *et al*[10].
Hole pseudolifetime for bulk SRH (τ_p)	$3{\cdot}10^{-9}$ s	Two orders of magnitude smaller than the electron pseudolifetime, therefore this parameter does not affect the calculations when the perovskite is p-type.
Bimolecular recombination parameter, β_{bim}	$9.4{\cdot}\ 10^{-16}$ m^3s^{-1}	Ref.[6]

Electron transport layer (TiO_2)

Work function (E_{FE})	(-) 4.0 eV	Ref.[4]
Effective doping density (d_E)	$1.1{\cdot}10^{26}m^{-3}$	Ref.[10–12]
Width (b_E)	$1{\cdot}10^{-7}$ m	Direct measurement on similar devices
Permittivity (ε_E)	20 ε_0	Ref.[13]
Electron diffusion coefficient (D_E)	$5.14{\cdot}10^{-7}$ m^2s^{-1}	Ref.[4]

Hole transport layer (Spiro-OMeTAD)

Work function (E_{FH})	(-) 5.22 eV	Ref.[4]
Effective doping density (d_H)	$1.1{\cdot}10^{26}m^{-3}$	Similar value to the effective doping density of ETL.
Width (b_H)	$3{\cdot}10^{-7}$ m	Direct measurement on similar devices
Permittivity (ε_H)	3 ε_0	Ref.[4]
Hole diffusion coefficient (D_H)	$2.57{\cdot}10^{-9}$ m^2s^{-1}	Ref.[14]

Table C.2: Parameters changed in the DD simulations in order to fit the experimental data included in this *Chapter* (only parameters which are different from Table C.1 are indicated).

Parameter	**Original Value**	**Modified value**
Perovskite layer ($MAPbI_3$)		
Conduction band minimun (E_C)	(-) 3.8 eV	(-) 3.7 eV
Electron diffusion coefficient (D_n)	$5{\cdot}10^{-5}$ m^2s^{-1}	$8{\cdot}10^{-6}$ m^2s^{-1}
Hole diffusion coefficient (D_p)	$5{\cdot}10^{-5}$ m^2s^{-1}	$8{\cdot}10^{-6}$ m^2s^{-1}
Conduction band density of states (g_c)	$8.1{\cdot}10^{24}$ m^{-3}	$8.1{\cdot}10^{25}$ m^{-3}
Valence band density of states (g_v)	$5.8{\cdot}10^{24}$ m^{-3}	$5.8{\cdot}10^{25}$ m^{-3}
Mean density of anion vacancies (N_0)	$1.6{\cdot}10^{25}$ m^{-3}	$1.6{\cdot}10^{26}$ m^{-3}
Diffusion coefficient for anions (D_{ion})	$10^{-16}m^2s^{-1}$	$3{\cdot}10^{-17}m^2s^{-1}$
Recombination parameters		
Electron pseudolifetime for SRH (τ_n)	$9{\cdot}10^{-7}$ s	$2{\cdot}10^{-7}$ s
Electron recombination velocity at ETL (v_{nE})	0	$10^5 ms^{-1}$
Hole recombination velocity at ETL (v_{pE})	0	20 m s^{-1}
Electron recombination velocity at HTL (v_{nH})	0	7.5 m s^{-1}
Hole recombination velocity at HTL (v_{pH})	0	$10^5 ms^{-1}$

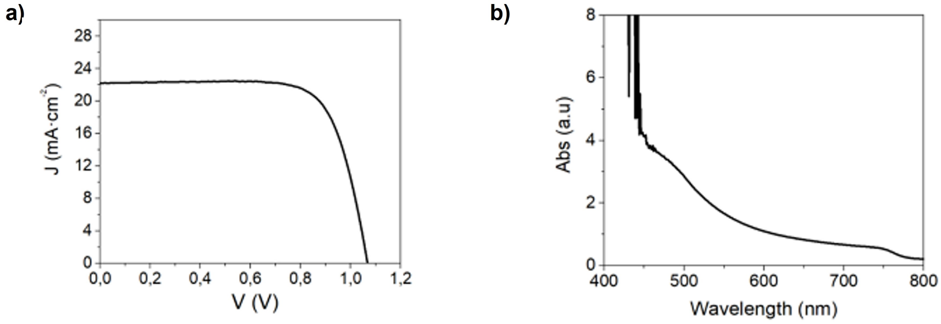

Figure C.1: (a) Experimental *JV* curve at one sun (1000 W·m^{-2}) AM1.5G illumination for PSCs with regular configuration (TiO_2/$MAPbI_3$/Spiro-OMeTAD), (b) absorption spectrum of the same device measured at transmittance mode.

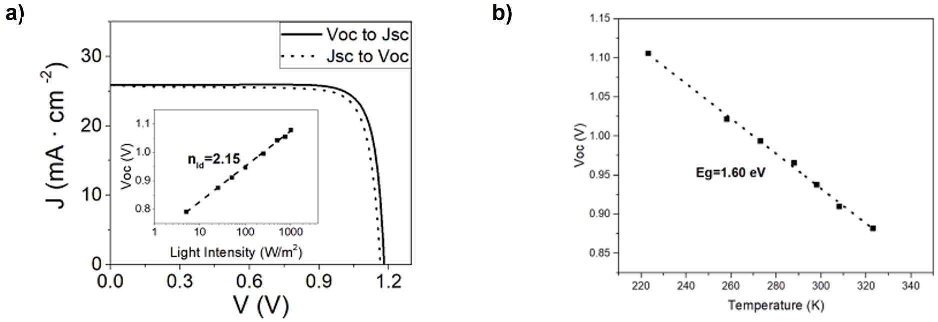

Figure C.2: (a) Validation of *JV* curve as at one sun (1000 W·m^{-2}) AM1.5G illumination for PSC with regular configuration as obtained by DD simulation. The inset shows the dependence of the V_{OC} with respect to illumination and the apparent ideality factor. (b) DD numerical prediction of temperature dependence of the V_{OC}. Simulations run for the standard parameters of Table C.1 in this *Appendix*.

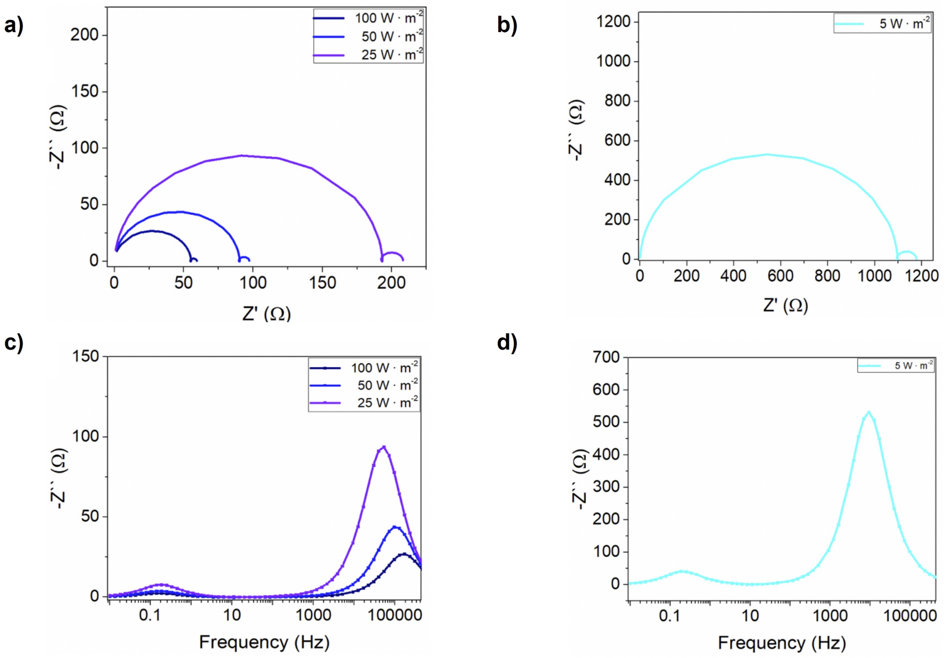

Figure C.3: Simulated impedance spectra at OC and variable ilumination intensity for PSCs with regular configuration using the parameters indicated in Table C.1.

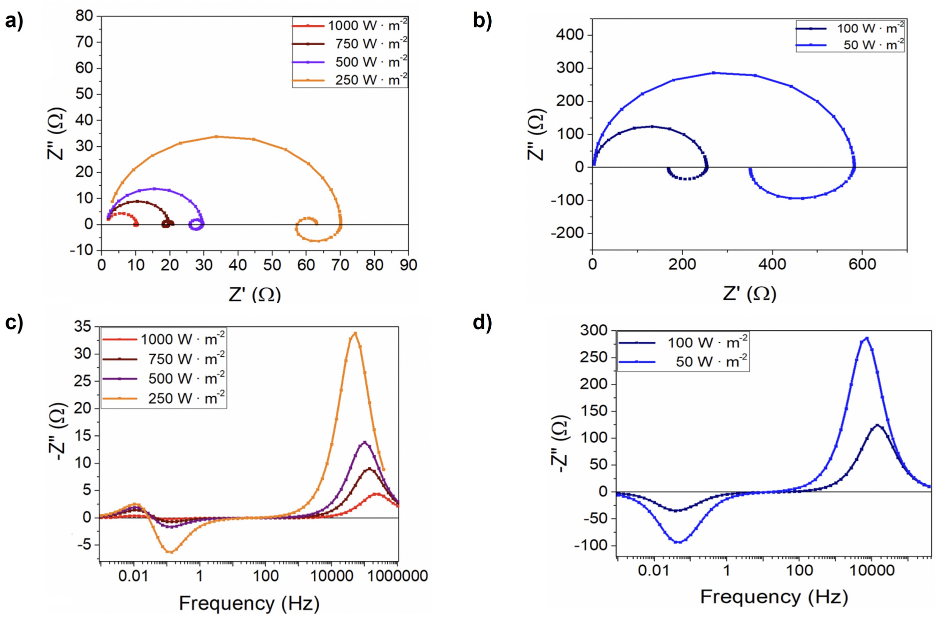

Figure C.4: Simulated impedance spectra at OC and variable illumination intensity for PSCs with inverted configuration. Parameters taken from Ref.[15].

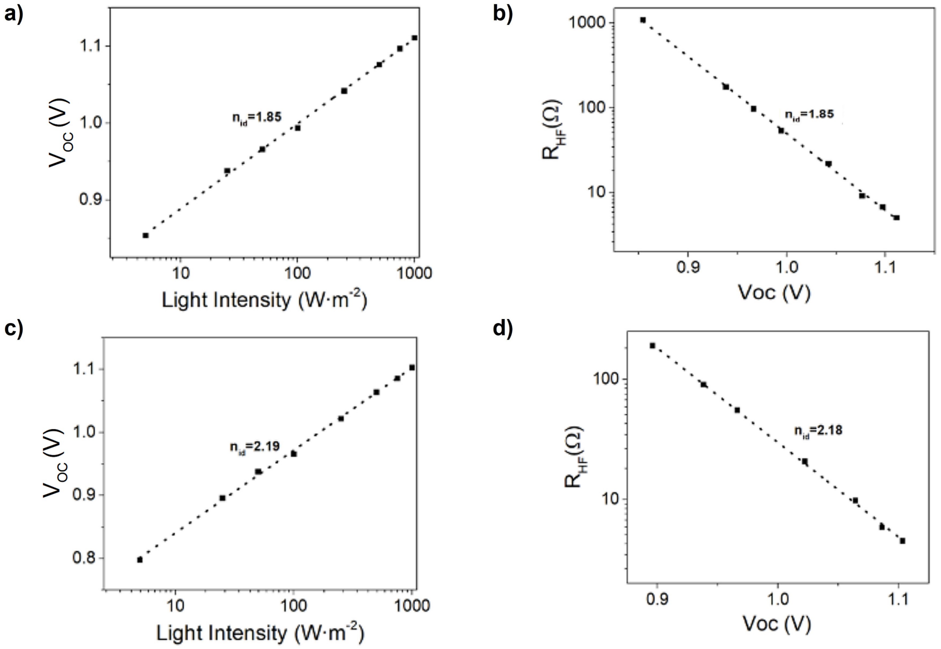

Figure C.5: DD numerical prediction of the ideality factor from V_{OC} *versus* ln(I) (a) and (c) and high frequency resistance *versus* V_{OC} (b) and (d) for two different values of the density of anion vacancies. (10^{25} m^{-3}) (a) and (b) and $1.8{\cdot}10^{25}$ m^{-3}.

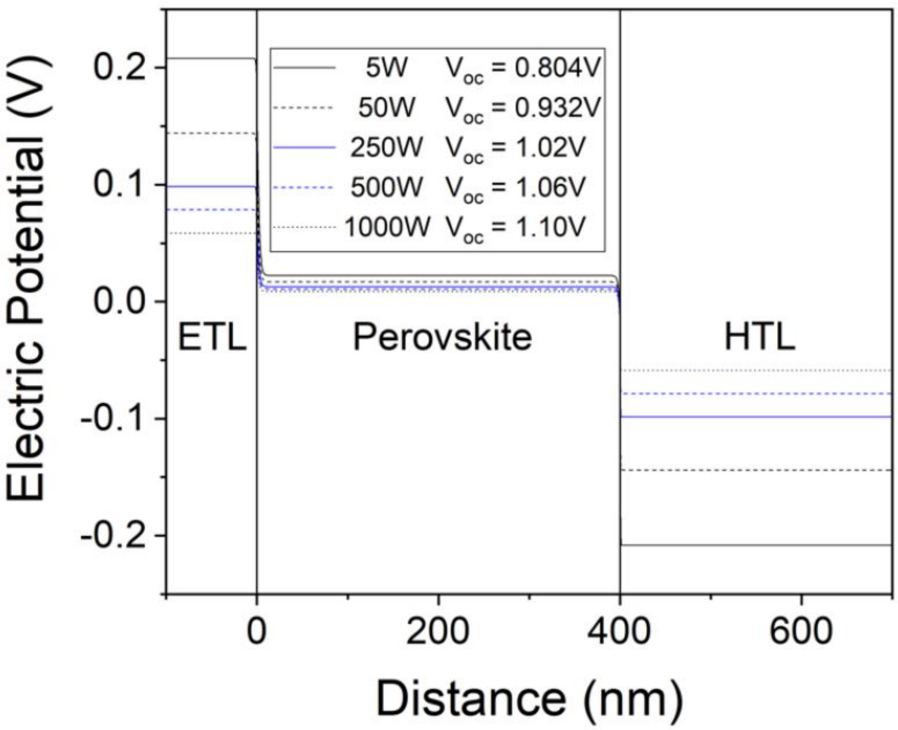

Figure C.6: Steady state electric potentials across the cell at different OCVs with the standard parameter set (Table C.1).

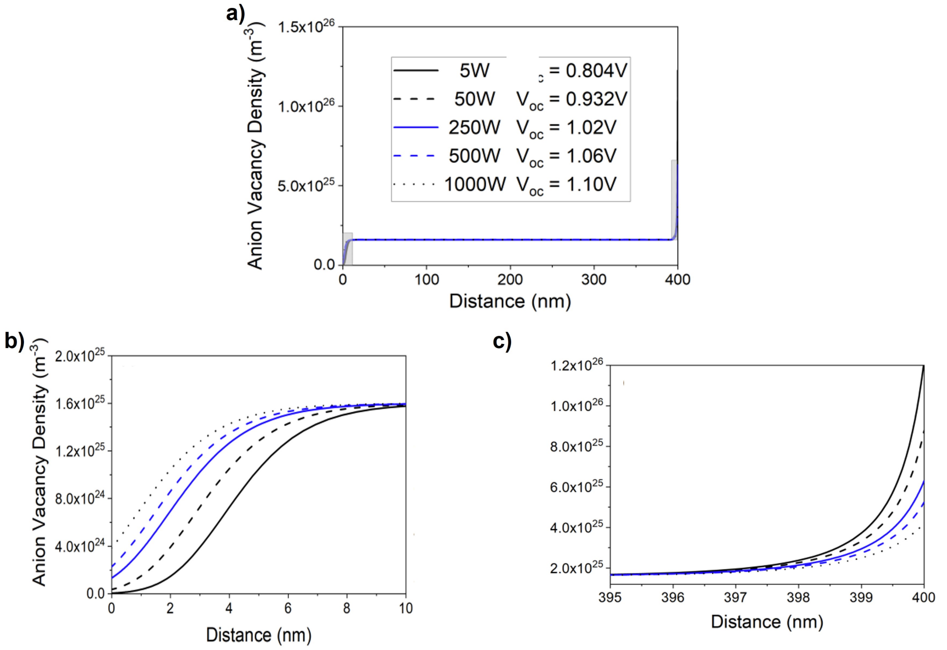

Figure C.7: (a) Steady state anion vacancy densities at different OCVs with the standard parameter set (Table C.1). Zoomed images of the shaded Debye layers are shown in the vicinity of the ETL (b) and near the HTL (c).

Bibliography

[1] L. Contreras-Bernal, S. Ramos-Terrón, A. Riquelme, P. P. Boix, J. Idígoras, I. Mora-Seró, and J. A. Anta, “Impedance analysis of perovskite solar cells: a case study,” *Journal of Materials Chemistry A*, vol. 7, no. 19, pp. 12191–12200, 2019-05.

[2] J. M. Frost, K. T. Butler, and A. Walsh, “Molecular ferroelectric contributions to anomalous hysteresis in hybrid perovskite solar cells,” *APL Materials*, vol. 2, no. 8, p. 081506, 2014-08.

[3] P. Schulz, E. Edri, S. Kirmayer, G. Hodes, D. Cahen, and A. Kahn, “Interface energetics in organo-metal halide perovskite-based photovoltaic cells,” *Energy & Environmental Science*, vol. 7, no. 4, pp. 1377–1381, 2014-03.

[4] S. van Reenen, M. Kemerink, and H. J. Snaith, “Modeling anomalous hysteresis in perovskite solar cells,” *The Journal of Physical Chemistry Letters*, vol. 6, no. 19, pp. 3808–3814, 2015.

[5] I. Zarazua, J. Bisquert, and G. Garcia-Belmonte, “Light-induced space-charge accumulation zone as photovoltaic mechanism in perovskite solar cells,” *The Journal of Physical Chemistry Letters*, pp. 525–528, 2016.

[6] C. Wehrenfennig, G. E. Eperon, M. B. Johnston, H. J. Snaith, and L. M. Herz, “High charge carrier mobilities and lifetimes in organolead trihalide perovskites,” *Advanced Materials*, vol. 26, no. 10, pp. 1584–1589, 2014-03.

[7] F. Brivio, K. T. Butler, A. Walsh, and M. van Schilfgaarde, “Relativistic quasiparticle self-consistent electronic structure of hybrid halide perovskite photovoltaic absorbers,” *Physical Review B*, vol. 89, no. 15, p. 155204, 2014-04.

[8] A. Walsh, D. O. Scanlon, S. Chen, X. G. Gong, and S.-H. Wei, “Self-regulation mechanism for charged point defects in hybrid halide perovskites,” *Angewandte Chemie (International Ed. in English)*, vol. 54, no. 6, pp. 1791–1794, 2015-02.

[9] C. Eames, J. M. Frost, P. R. F. Barnes, B. C. O'Regan, A. Walsh, and M. S. Islam, "Ionic transport in hybrid lead iodide perovskite solar cells," *Nature Communications*, vol. 6, p. 7497, 2015-06.

[10] Y. Zhou and A. Gray-Weale, "A numerical model for charge transport and energy conversion of perovskite solar cells," *Physical Chemistry Chemical Physics*, vol. 18, no. 6, pp. 4476–4486, 2016-02.

[11] I. Abayev, A. Zaban, V. G. Kytin, A. A. Danilin, G. Garcia-Belmonte, and J. Bisquert, "Properties of the electronic density of states in TiO2 nanoparticles surrounded with aqueous electrolyte," *Journal of Solid State Electrochemistry*, vol. 11, no. 5, pp. 647–653, 2007.

[12] H. Tang, K. Prasad, R. Sanjinès, P. E. Schmid, and F. Lévy, "Electrical and optical properties of TiO2 anatase thin films," *Journal of Applied Physics*, vol. 75, pp. 2042–2047, 1994-02.

[13] A. Guerrero, E. J. Juarez-Perez, J. Bisquert, I. Mora-Sero, and G. Garcia-Belmonte, "Electrical field profile and doping in planar lead halide perovskite solar cells," *Applied Physics Letters*, vol. 105, no. 13, p. 133902, 2014-09.

[14] T. Leijtens, J. Lim, J. Teuscher, T. Park, and H. J. Snaith, "Charge density dependent mobility of organic hole-transporters and mesoporous TiO2 determined by transient mobility spectroscopy: Implications to dye-sensitized and organic solar cells," *Advanced Materials*, vol. 25, no. 23, pp. 3227–3233, 2013.

[15] M. T. Neukom, A. Schiller, S. Züfle, E. Knapp, J. Ávila, D. Pérez-del Rey, C. Dreessen, K. P. Zanoni, M. Sessolo, H. J. Bolink, and B. Ruhstaller, "Consistent device simulation model describing perovskite solar cells in steady-state, transient, and frequency domain," *ACS Applied Materials & Interfaces*, vol. 11, no. 26, pp. 23320–23328, 2019-07.

Appendix D

Illumination intensity dependence of the recombination mechanism in mixed perovskite solar cells

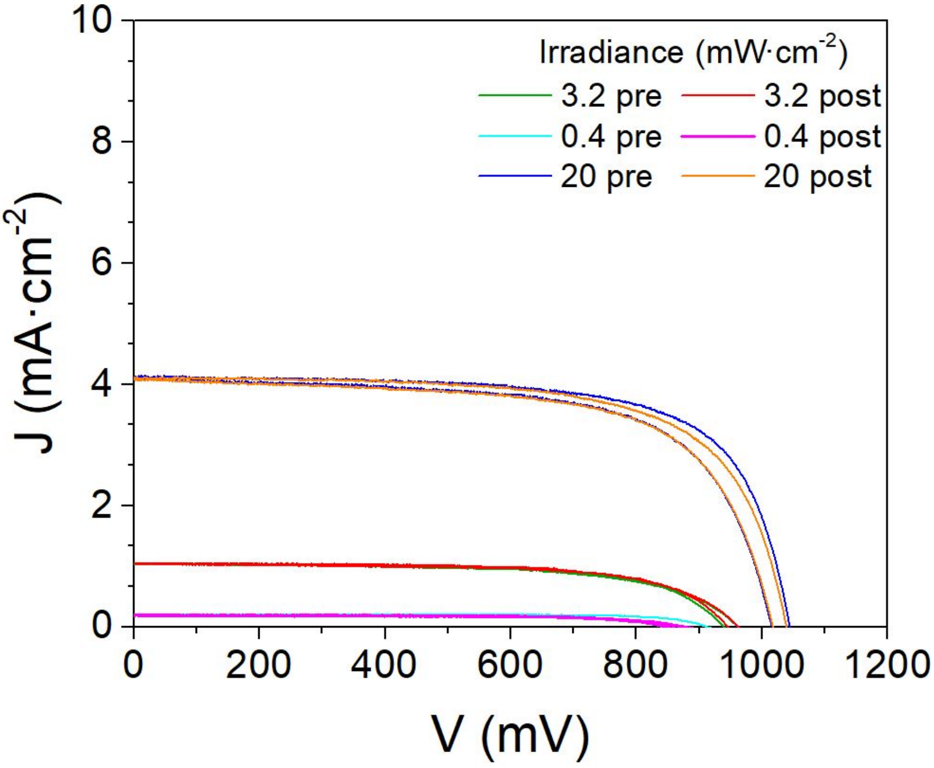

Figure D.1: *JV* curves at various illumination intensities, both before (pre) and after (post) the EIS measurements. The scan rate is 0.05 V·s^{-1}.

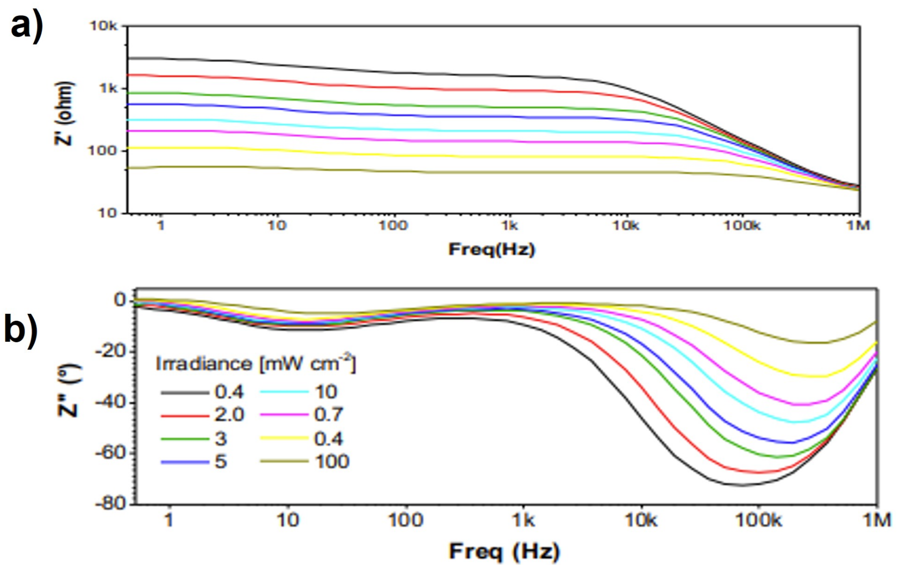

Figure D.2: Bode plots registered measured at OC at different irradiance values.

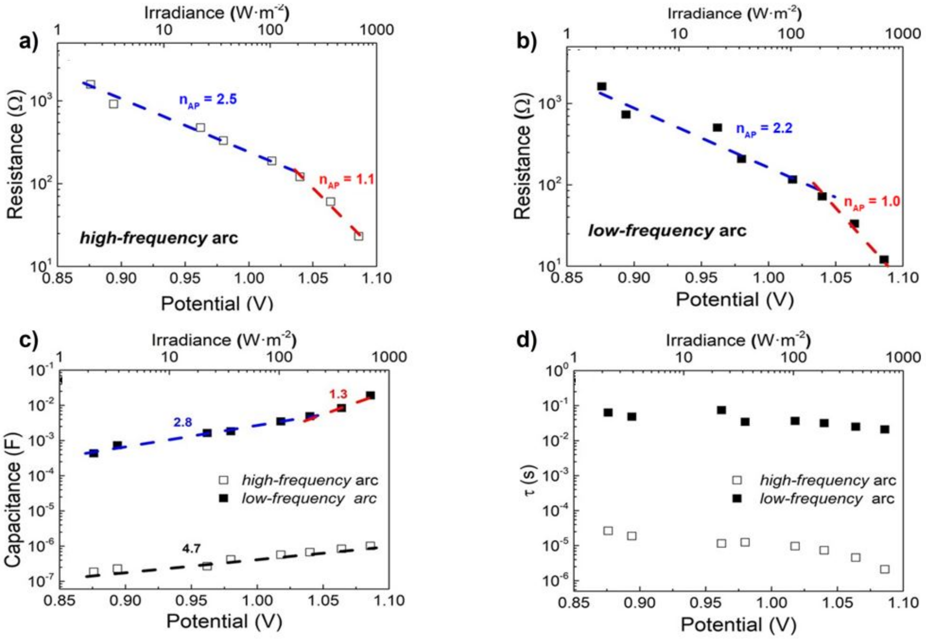

Figure D.3: (a) R_{HF} dependence on V_{OC} and (b) V_{OC} dependence on irradiance for three measured devices, showing the change of behaviour for the two illumination regimes.

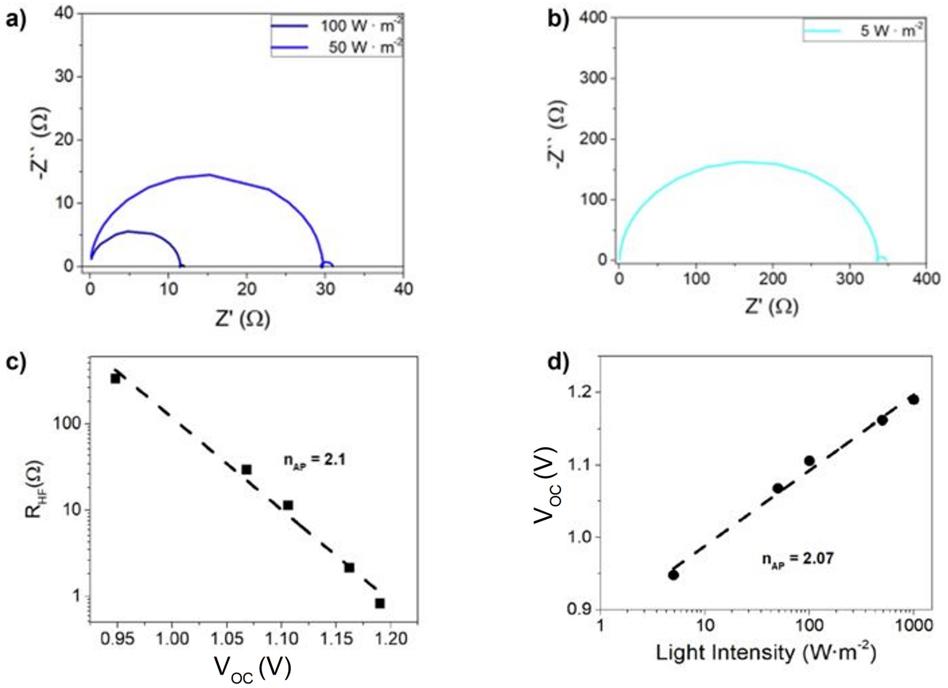

Figure D.4: (a) and (b) DD simulated EIS at OC when the bulk SRH recombination with an electron of $9{\cdot}10^{-7}$ s is the only recombination mechanism (other than bimolecular radiative recombination). (c) DD simulated R_{HF} as a function of V_{OC}. (d) V_{OC} as a function of light intensity. Simulation parameters were similar to the used in *Chapter* 6.

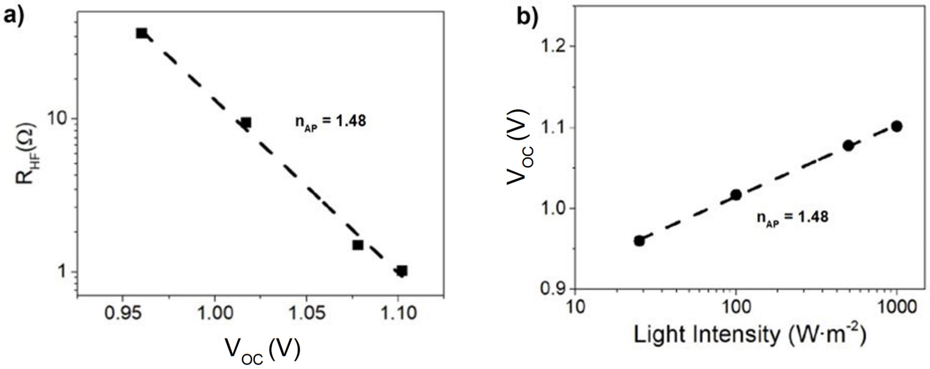

Figure D.5: (a) DD simulated R_{HF} as a function of V_{OC}. (b) V_{OC} as a function of light intensity. Simulation parameters are similar to the used as standard parameters in *Chapter* 6, including surface recombination with 20 and 10 $m \cdot s^{-1}$ at the TiO_2 and the Spiro-OMeTAD interfaces, respectively.

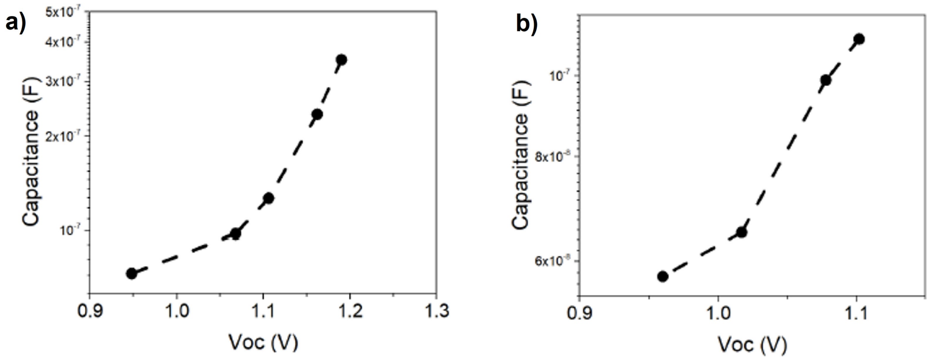

Figure D.6: C_{HF} dependence on V_{OC} as predicted by the DD model without (a) and with (b) surface recombination.

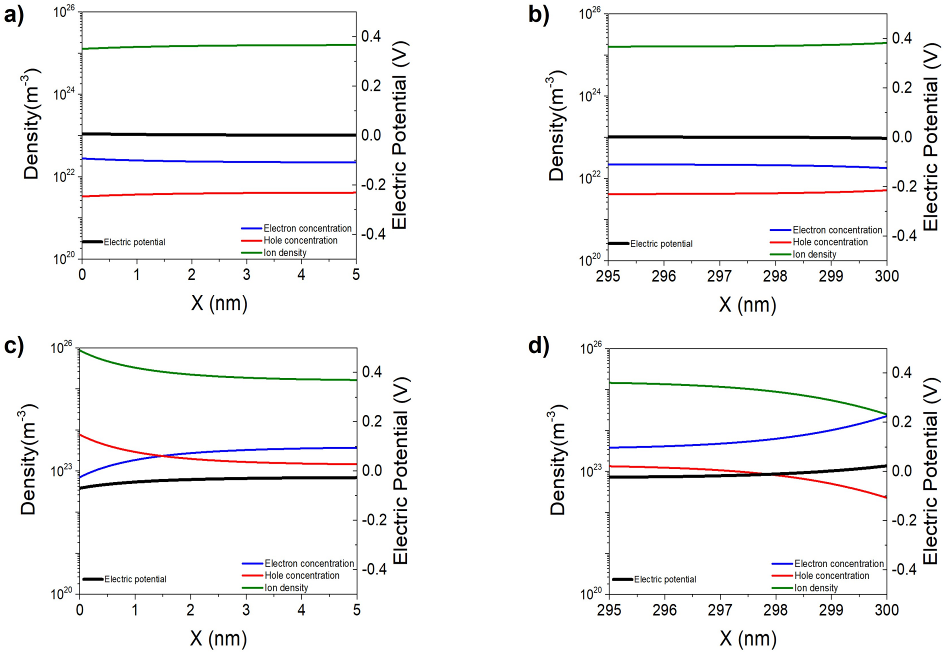

Figure D.7: Electric potential, electronic carriers and ion densities as predicted by DD simulations in the vicinity of the TiO_2 (a) and (c) and Spiro-OMeTAD (b) and (d) interfaces at low (a) and (b) and high (c) and (d) irradiances. Simulation parameters used are those described as standard parameters set in *Chapter* 6. (Ion vacancy density of $1.6{\cdot}10^{25}$ m^{-3}).

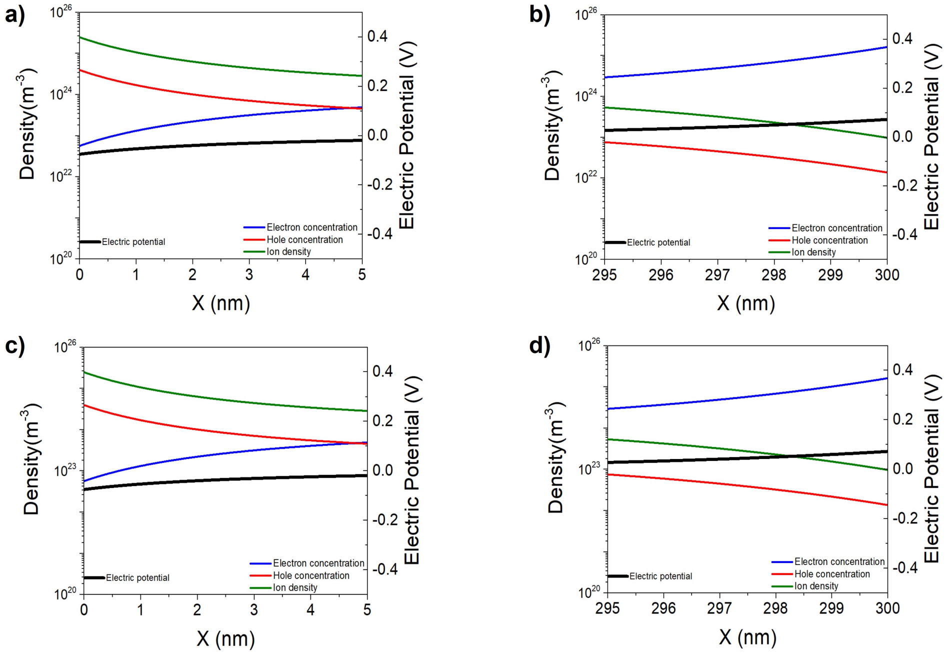

Figure D.8: Electric potential, electronic carriers and ion densities as predicted by DD simulations in the vicinity of the TiO_2 (a) and (c) and Spiro-OMeTAD (b) and (d) interfaces at low (a) and (b) and high (c) and (d) irradiances. Ion vacancy density was set 10 times lower compared to the used in Figure D.7.

Appendix E

Understanding equivalent circuits in perovskite solar cells. Insights from drift-diffusion simulation

Table E.1: SRH Recombination pseudolifetimes for electrons and holes for the simulated spectra with pure SRH recombination.

Parameter	**Value**	**Literature reference or justification**
Electron pseudolifetime for SRH (τ_n)	$9 \cdot 10^{-8}$ s	Chosen to match an approximate V$_{OC}$ of 1 V under the 1 sun equivalent illumination
Hole pseudolifetime for SRH (τ_p)	$3 \cdot 10^{-9}$ s	Two orders of magnitude smaller than the electron pseudolifetime, therefore this parameter does not affect the calculations when the perovskite is p-type (i.e. when there is a greater density of holes than electrons in the perovskite layer).

Table E.2: Surface Recombination velocities for electrons and holes at the ETL and the HTL for the simulated spectra with pure surface recombination.

Parameter	**Value**	**Literature reference or justification**
Electron recombination velocity at ETL (v_{nE})	10^5 m·s^{-1}	Make the electrons disappear as soon as they reach the ETL, simulating the injection into the selective contact
Hole recombination velocity at ETL (v_{pE})	50 m·s^{-1}	Recombination velocity to reach a similar V$_{OC}$ under 1 sun equivalent illumination to the obtained with pure SRH recombination. Slightly faster than v_{nH} to reproduce the differences on how selective both contacts are.
Electron recombination velocity at HTL (v_{nH})	0.5 m·s^{-1}	Recombination velocity to reach a similar V$_{OC}$ under 1 sun equivalent illumination to the obtained with pure SRH recombination. Slightly slower than v_{pH} to reproduce the differences on how selective both contacts are.
Hole recombination velocity at HTL (v_{pH})	10^5 m·s^{-1}	Make the holes disappear as soon as they reach the HTL, simulating the injection into the selective contact

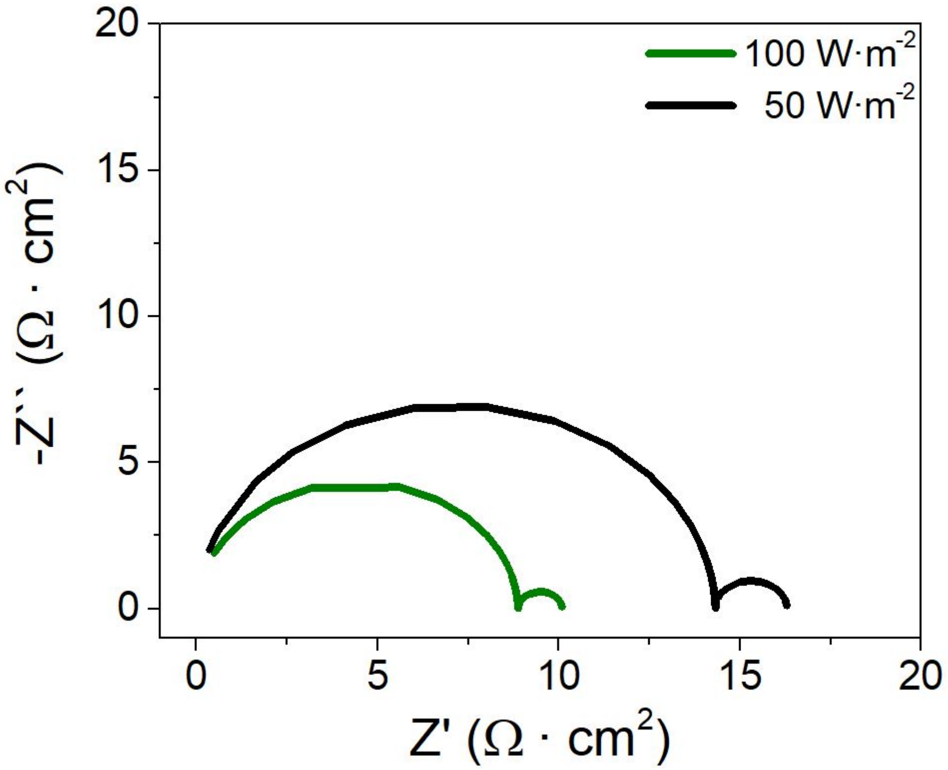

Figure E.1: Simulated impedance spectra at V_{OC} under 100 W·m^{-2} and 50 W·m^{-2} of 465 nm monochromatic illumination using the standard parameters of *Chapter* 6 and surface recombination of Table E.2.

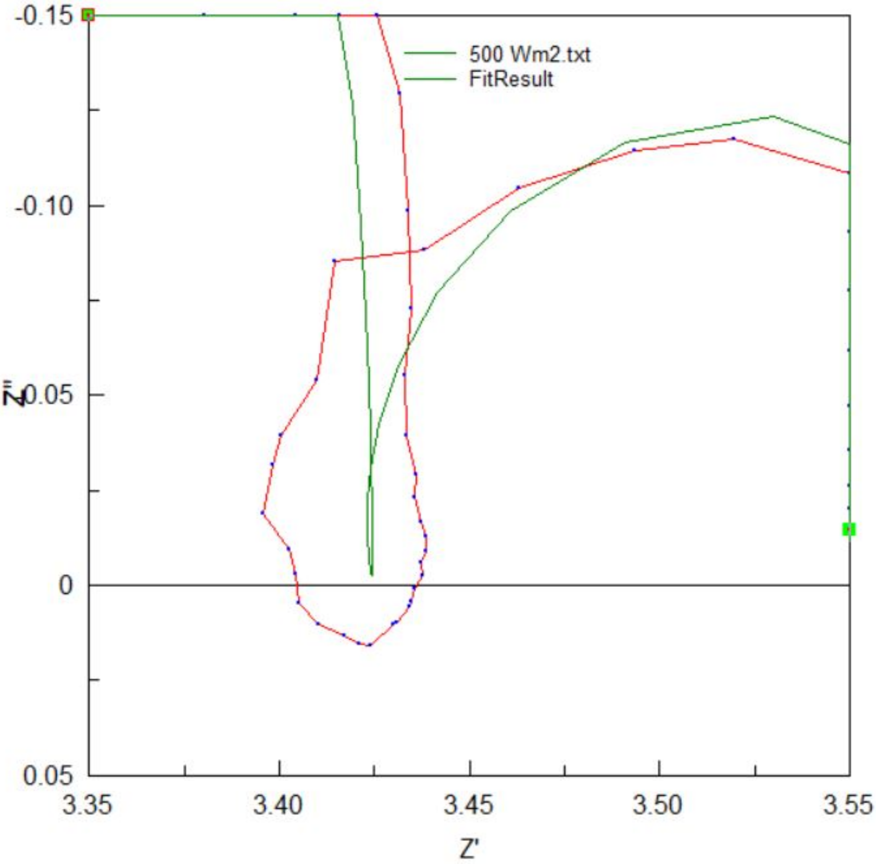

Figure E.2: Zoom in of the fit result (green line) reproducing the loop observed for pure SRH recombination simulations (red line) using the parallel equivalent circuit.

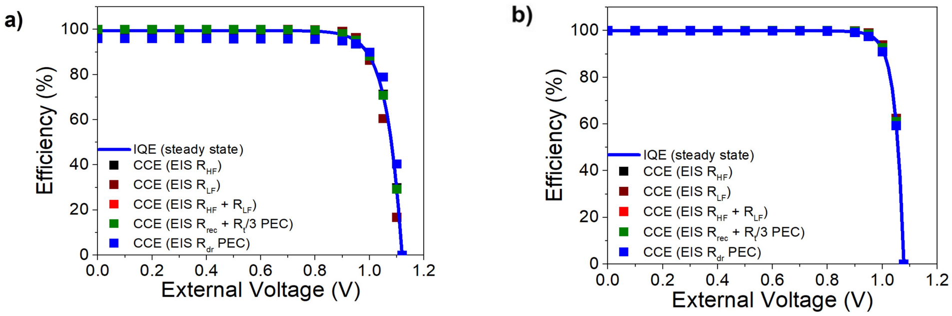

Figure E.3: Charge collection efficiency obtained from applying Eq.6.5 to the resistances extracted for pure SRH recombination (a) and the pure surface recombination (b) scenarios, compared to the *IQE* calculated using Eq.3.9 with the *JV* curve resulting with a $0.01\ \mathrm{mV{\cdot}s^{-1}}$ scan rate using the standard parameters of *Chapter* 6.

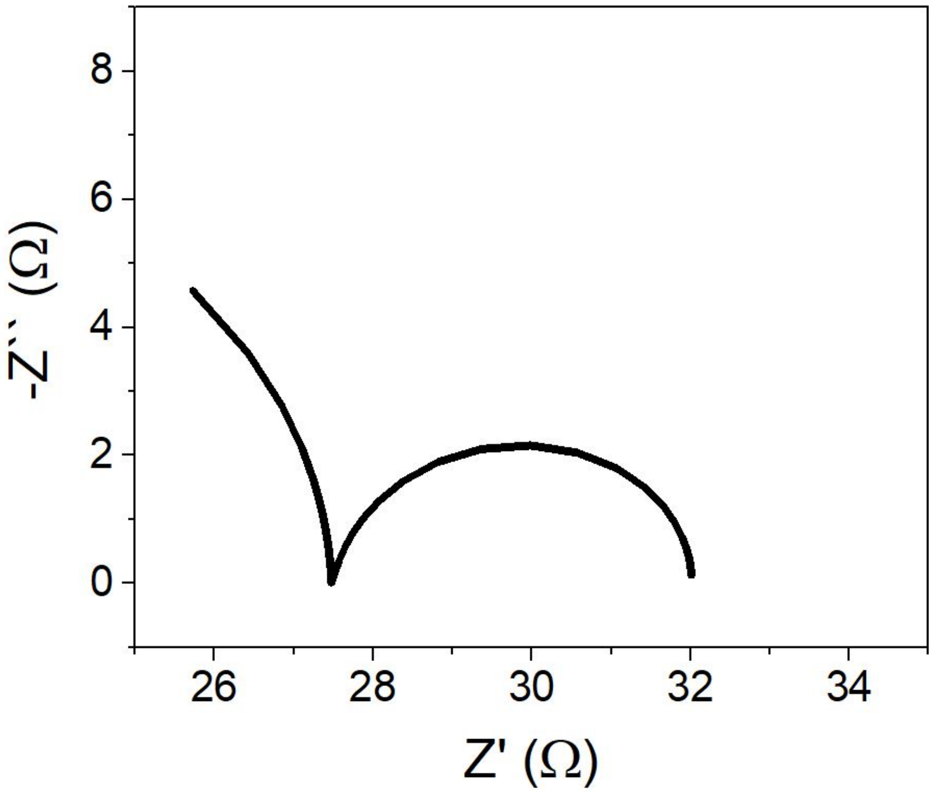

Figure E.4: Simulated impedance spectra at V_{OC} under 100 W·m^{-2} of 465 nm monochromatic illumination using the parameters for experimental fit of *Chapter* 6.

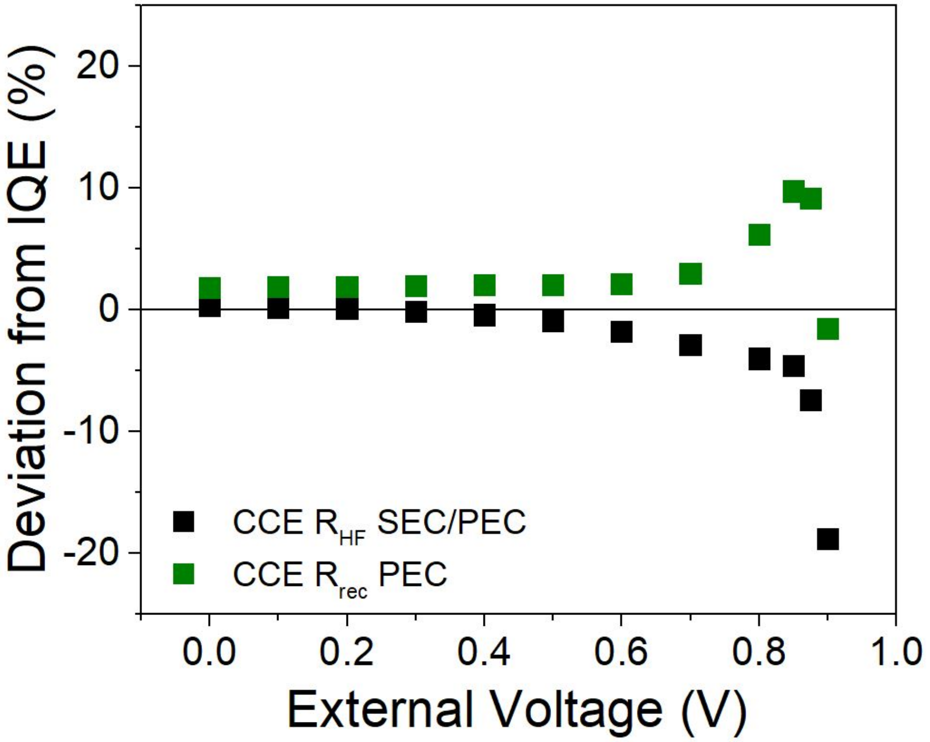

Figure E.5: Deviation between the CCE values obtained from R_{HF} and R_{rec} in Figure 8.6 compared to the steady state JV curve.

Appendix F

Inverted hysteresis in n-i-p and p-i-n perovskite solar cells

F.1 Device Fabrication

Although some of the devices were fabricated following the procedure described in *Chapter 5* (see *Appendix* B) to confirm the universality of the behaviour described in this *Chapter*, most devices were fabricated following the procedure employed in a previous work[1]. All chemicals were purchased from Sigma-Aldrich unless stated otherwise. [6,6]-Phenyl-C_{61}-butyric acid methyl ester (PCBM) was purchased from Ossila (Sheffield, United Kingdom).

TEC-15 fluorine-doped tin oxide (FTO) glass was employed as the substrate. A small strip of the FTO layer was removed by employing zinc powder and a 2 M solution of hydrochloric acid (HCl). The substrates were rinsed with deionized water and sequentially sonicated at 40ºC for 15 min with 2% Hellmanex detergent, water, acetone, ethanol, and isopropanol. The substrates were then dried to air and treated by Ozone irradiation (UV/Ozone ProCleaner Bioforce Nanosciences) for 30 minutes prior to the deposition of the layers. To study the influence of selective contacts on the degree of hysteresis and the universality of the findings in this *Chapter*, the following material compositions were studied:

Spin-coated NiO$_x$

A 0.2 M solution of nickel acetate tetrahydrate in 2-methoxy ethanol was prepared. After complete dissolution, a small volume of ethanolamine was dropped into the solution (12 μL of ethanolamine per mL of the nickel acetate solution) and stirred until it became homogeneous. The solution was filtered through a PTFE syringe filter (45 μm). 100 μL of the prepared solution were spin-coated over each substrate at 3000 rpm for 30 seconds. After spin coating, a small strip of the NiO$_x$ layer was removed with 2-methoxy ethanol, where the cathode contact will eventually be deposited. The substrates were placed on a hot plate at 500ºC for 30 min.

Spray NiO$_x$

The precursor solution was a 5 mM solution of nickel acetylacetonate in acetonitrile deposited by a chromatography sprayer and a manual pump. The substrates were preheated at 450ºC, and the NiO$_x$ layer was sprayed every 30 seconds for 30 cycles. After the deposition, the substrates remained in the hot plate for 30 minutes at 450ºC.

Mesoporous NiO$_x$

This layer was deposited on top of the planar NiO$_x$ layer. The precursor solution was prepared from a commercial paste of NiO$_x$ distributed by Solaronix (Aubonne, Switzerland) diluted in ethanol (12 wt. %). The paste was spin-coated at 3000 rpm for 30 seconds, annealed on a hot plate at 200ºC for 10 minutes, and transferred to a furnace at 450ºC for 30 minutes.

Mesoporous TiO$_2$ (air)

The procedure for depositing the ETL and the HTL was similar to the described in *Chapter* 5 (see *Appendix* B).

Mesoporous TiO_2 (glove box)

The deposit of the TiO_2 layers was similar to described in *Appendix* B. The HTL was deposited from a 0.59 mol/L spiro-OMeTAD solution in chlorobenzene with 28.8 μL of tertbutyl-pyridine per mL of precursor solution and 17.5 μL of bis(trifluoromethane)sulfonamide lithium salt (Li-TFSI) solution (520 mg/mL of acetonitrile) per mL of the precursor solution. The solution was spin-coated on top of the perovskite layer at 4000 rpm for 30 s.

The perovskite layer was similar in all the devices included in this *Chapter*. A 1.25 M solution of MAI and PbI_2 in a 4:1 v/v mixture of DMF/DMSO. The solution was filtered through a PTFE syringe filter 45 μm. Perovskite deposition was performed in a glove box under nitrogen atmosphere (except for the devices named as Mesoporous TiO_2 (air) see *Appendix* B for more details). The perovskite solution was spin-coated over the substrates at 4000 rpm for 30 seconds. 200 μL of ethyl acetate were dropped as antisolvent exactly 7 seconds after the start of the spin-coating of the perovskite layer. The perovskite films were then placed on a hot plate at 100ºC for 10 minutes and left to cool down for two additional minutes. For the p-i-n, the ETL was deposited from 100 μL of a 22 mM solution of PCBM in chlorobenzene, which was spin-coated on top of the perovskite layer at 3000 rpm for 30 seconds and let to dry. Finally, 100 μL of a 1.4 mM solution of bathocuproine (BCP) in ethanol was spin-coated on top of the PCBM layer at 6000 rpm for 30 seconds and let to dry. The metallic contacts for the p-i-n devices were deposited via silver evaporation in a high-vacuum physical vapor deposition chamber (Nano PVD, Moorfield nanotechnology, Cheshire, United Kingdom) under pressure below $1.5 \cdot 10^{-5}$ mbar. For the metallic contact deposition in n-i-p device, the procedure was similar to the one described in *Appendix* B.

In the study on the influence of crystallinity, the perovskite layer underwent an additional process before the deposition of the PCBM and BCP layer. This additional process was also employed to study the influence of preconditioning/illumination. A 1.25 M solution of MAI in DMSO was prepared. After the deposition of the perovskite layer and the subsequent heat treatment, a small piece of a microscope slide (1.0 x 0.5 cm^{-2}) was placed in the middle of the hotplate (and between the perovskite samples), as shown in Figure F.1 and 5 μL of the MAI solution were placed on top of it. The cells and the microscope slide were covered with a large glass petri dish (12 cm diameter, 2 cm depth), and the films were left for 10 min at 100ºC. Once the treatment was over, the cells were completed according to the procedure previously described.

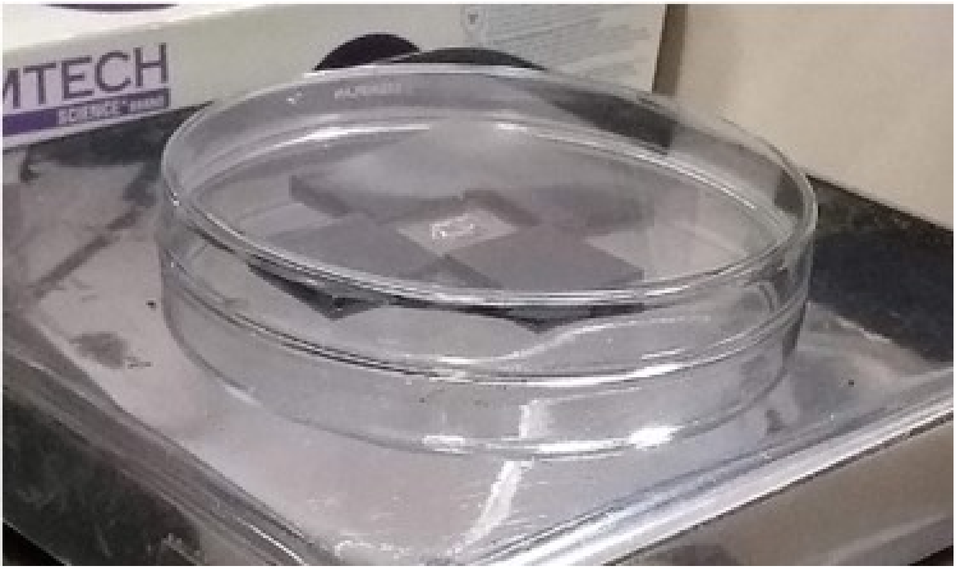

Figure F.1: Arrangement of perovskite films for solvent annealing. The microscope slide with 5 μL of 1.25 M MAI in DMSO is located at the center of the films.

Parameter	**Value**	**Justification**
Temperature (T)	298 K	Standard conditions
Incident photon flux (F_{ph})	$8.5\cdot10^{16}$	Similar to the experimental light intensity using the blue LED
Perovskite layer ($\mathbf{MAPbI_3}$)		
Width (d)	$3\cdot10^{-7}$ m	Direct measurement on similar devices
Permittivity (ε_p)	24.1 ε_0	Ref.[2]
Absorption coefficient at 465 nm (α_{abs})	$6\cdot10^{6}$ m^{-1}	Direct measurement on similar devices
Conduction band minimun (E_C)	(-) 3.8 eV	Intermediate value between Ref.[3] and[4] giving an optical bandgap of 1.6 eV
Valence band maximum (E_V)	(-) 5.4 eV	Ref.[3]
Electron difusion coefficient (D_n)	$1.7\cdot10^{-5}$ $\mathrm{m^2s^{-1}}$	Gives a *CCE* of 100%[5,6] with the bulk electron pseudolifetime used to approximate the V_{OC} of the experimental *JV* curve. Value very close to the reported ($2.05\cdot10^{-5}$ m^2) by Wehrenfennig et al[7].)
Hole diffusion coefficient (D_p)	$1.7\cdot10^{-5}$ $\mathrm{m^2s^{-1}}$	Similar value to the perovskite electron diffusion coefficient.
Conduction band density of states (g_c)	$8.1\cdot10^{24}$ m^{-3}	Ref.[8]
Valence band density of states (g_v)	$5\cdot8\cdot10^{24}$ m^{-3}	Ref.[8]
Mean density of anion vacancies (N_0)	$1.6\cdot\cdot10^{25}$ m^{-3}	Ref.[9]
Diffusion coefficient for anions (D_{ion})	$10^{-18}\mathrm{m^2s^{-1}}$	Ref.[10]

Table F.1: Parameter set used in the DD simulations for inverted cell configuration with no surface recombination, in which ε_0 denotes the permittivity of free space.

Recombination parameters

Electron pseudolifetime for bulk SRH (τ_n)	$3 \cdot 10^{-9}$ s	Two orders of magnitude smaller than the electron pseudolifetime, therefore this parameter does not affect the calculations when the perovskite is n-type.
Hole pseudolifetime for bulk SRH (τ_p)	$3 \cdot 10^{-5}$ s	Chosen to reproduce the observed behaviour of experimental measurements.
Bimolecular recombination parameter, (β_{bim})	$9.4 \cdot 10^{-16}$ m^{3}s^{-1}	Ref.[7]

Electron transport layer (PCBM)

Work function (E_{FE})	(-) 3.9 eV	Ref.[4]
Effective doping density (d_E)	$1.1 \cdot 10^{27}$m^{-3}	Ref.[11] high enough to produce high FF and V_{OC}
Width (b_E)	$1 \cdot 10^{-7}$ m	Direct measurement on similar devices
Permittivity (ε_E)	$3.5\ \varepsilon_0$	Ref.[12]
Electron diffusion coefficient (D_E)	$2.5 \cdot 10^{-7}$ m^{2}s^{-1}	Ref.[13]

Hole transport layer (NiO$_x$)

Work function (E_{FH})	(-) 5.4 eV	Ref.[13]
Effective doping density (d_H)	$1.1 \cdot 10^{27}$m^{-3}	Similar value to the effective doping density of ETL.
Width (b_H)	$2 \cdot 10^{-7}$ m	Direct measurement on similar devices
Permittivity (ε_H)	$11.9\ \varepsilon_0$	Ref.[12]
Hole diffusion coefficient (D_H)	$1 \cdot 10^{-11}$ m^{2}s^{-1}	Ref.[14]

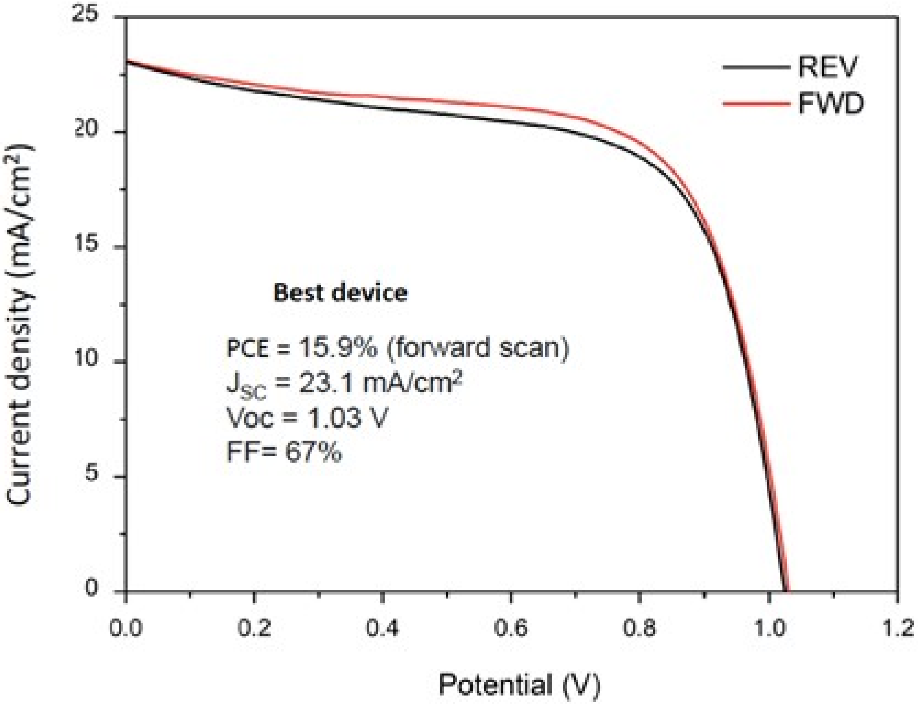

Figure F.2: *JV* curve for the champion device with p-i-n configuration using only planar NiO_x

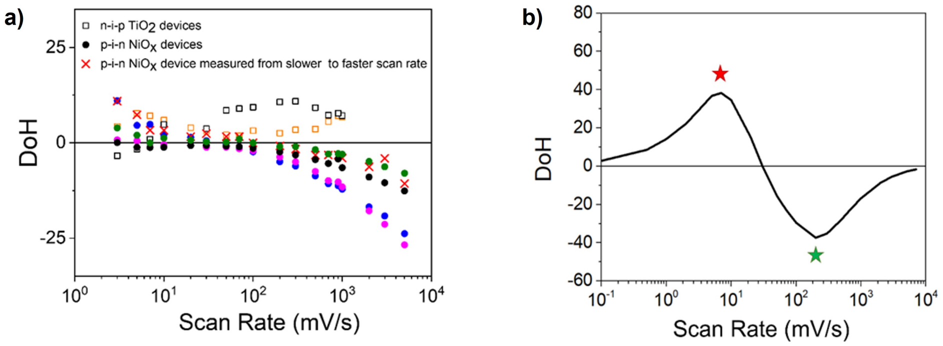

Figure F.3: DoH (%) versus scan rate (mV·s^{-1}) under blue LED illumination (465 nm) and a preconditioning bias of 1.2 V for 20 s. This Figure compares p-i-n PSCs with PCBM as ETL and HTLs of spin coated NiO$_x$ (red circles), spray coated NiO$_x$ (yellow circles), mesoporous NiO$_x$ (green circles) with an n-i-p PSC with spiro-OMeTAD HTL and mesoporous TiO$_2$ ETL (black circles).

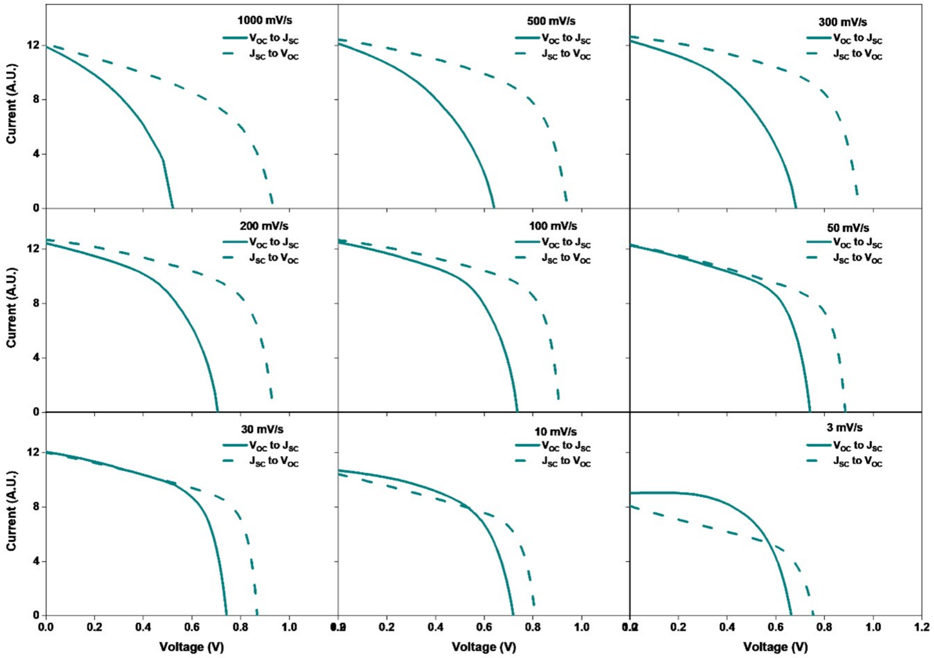

Figure F.4: *JV* curves of a p-i-n PSC with sprayed NiO$_x$ as HTL and PCBM as ETL under blue LED illumination.

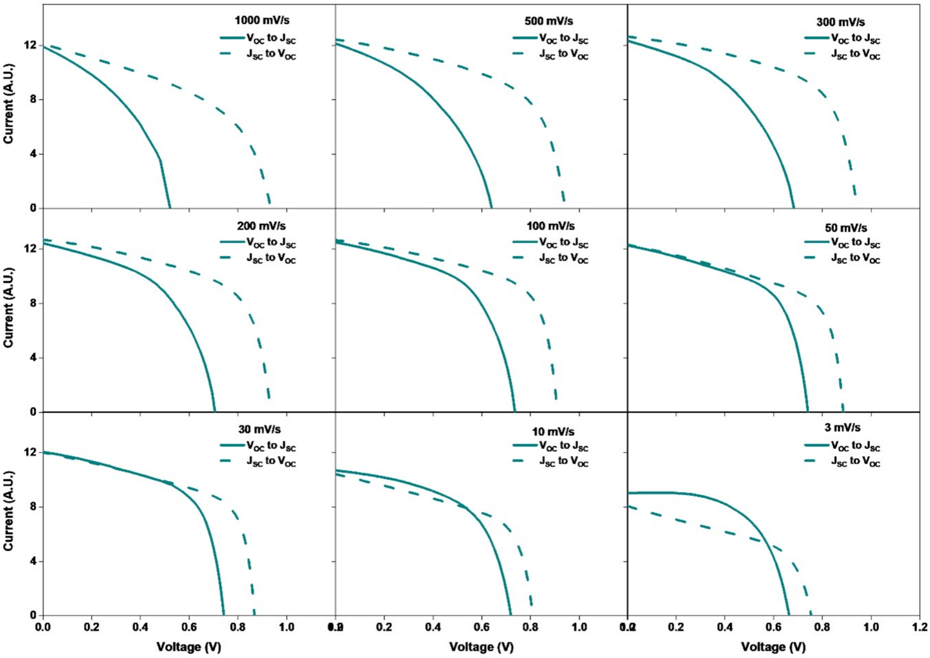

Figure F.5: *JV* parameter for solvent annealed samples under 1 sun illumination. (a) J_{SC} (mA·cm^{-2}), (b) V_{OC} (V), (c) FF, (d) PCE (%) versus preconditioning potentials of 1200, 600, 0, -100, 1200 mV. Closed (open) symbols are for reverse (forward) scans. The second 1200 mV potential is the final measurement, allowing for comparison with the first one to discard the presence of degradation.

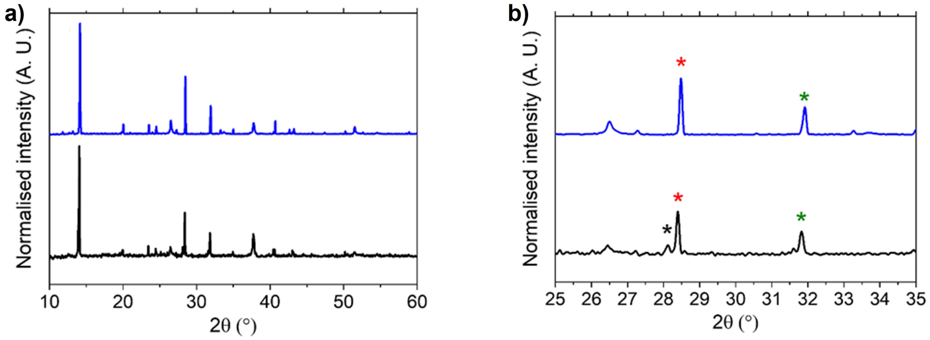

Figure F.6: (a) XRD comparison between perovskite films with (blue line) and without (black line) solvent annealing, showing that the main peak at 14.2º (110) does not change position regardless of the solvent annealing treatment. In (b) main peaks of the tetragonal phase are shown by red stars (004 peak at 28.11º), and black stars (220 peak at 28.36º). The corresponding peak from the FTO substrate is shown by the green stars at 31.8º.

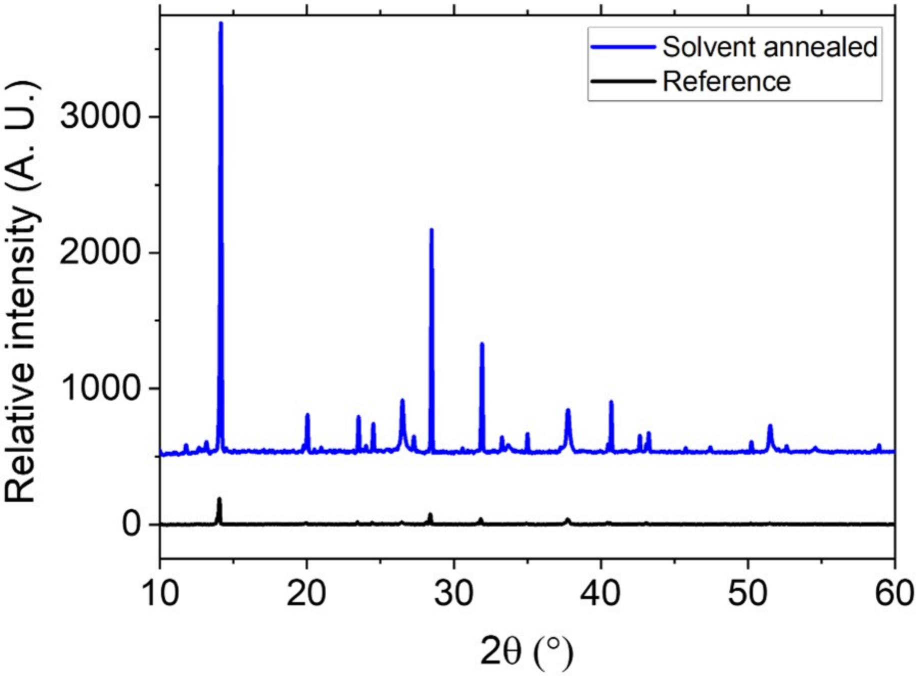

Figure F.7: XRD comparison between perovskite films with (blue) and without (black) solvent annealing treatment. These intensities have not been normalised. The small peaks under 14.2º might indicate the formation of superficial PbI_2 as a result of the solvent annealing process.

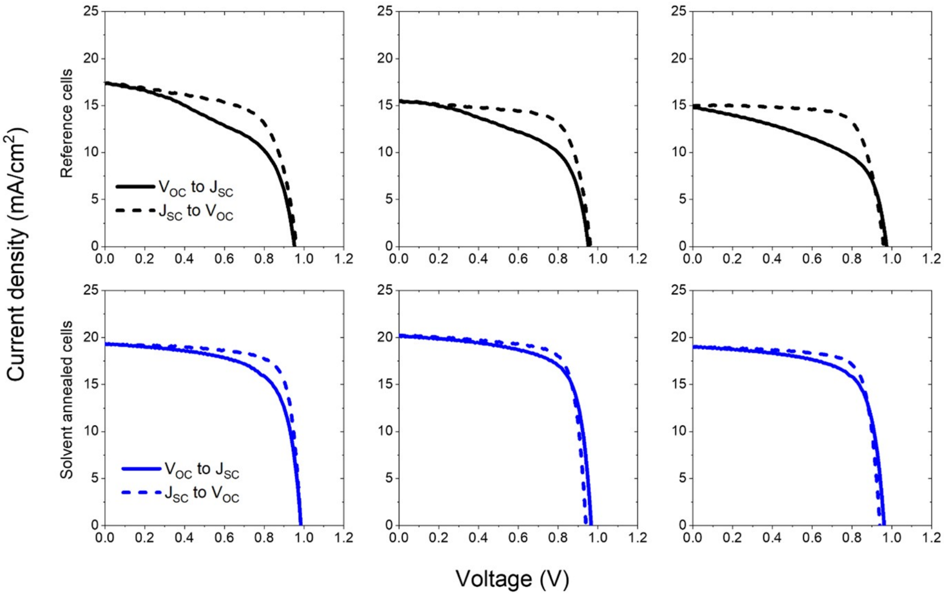

Figure F.8: Comparison of *JV* curves of 3 reference cells (top row, black lines) and 3 solvent annealed cells (blue) under one sun illumination and 100 mV·s^{-1} scan rate. All PSCs have a p-i-n architecture, coated NiO$_x$ acting as HTL, MAPbI$_3$ perovskite layer and a PCBM ETL.

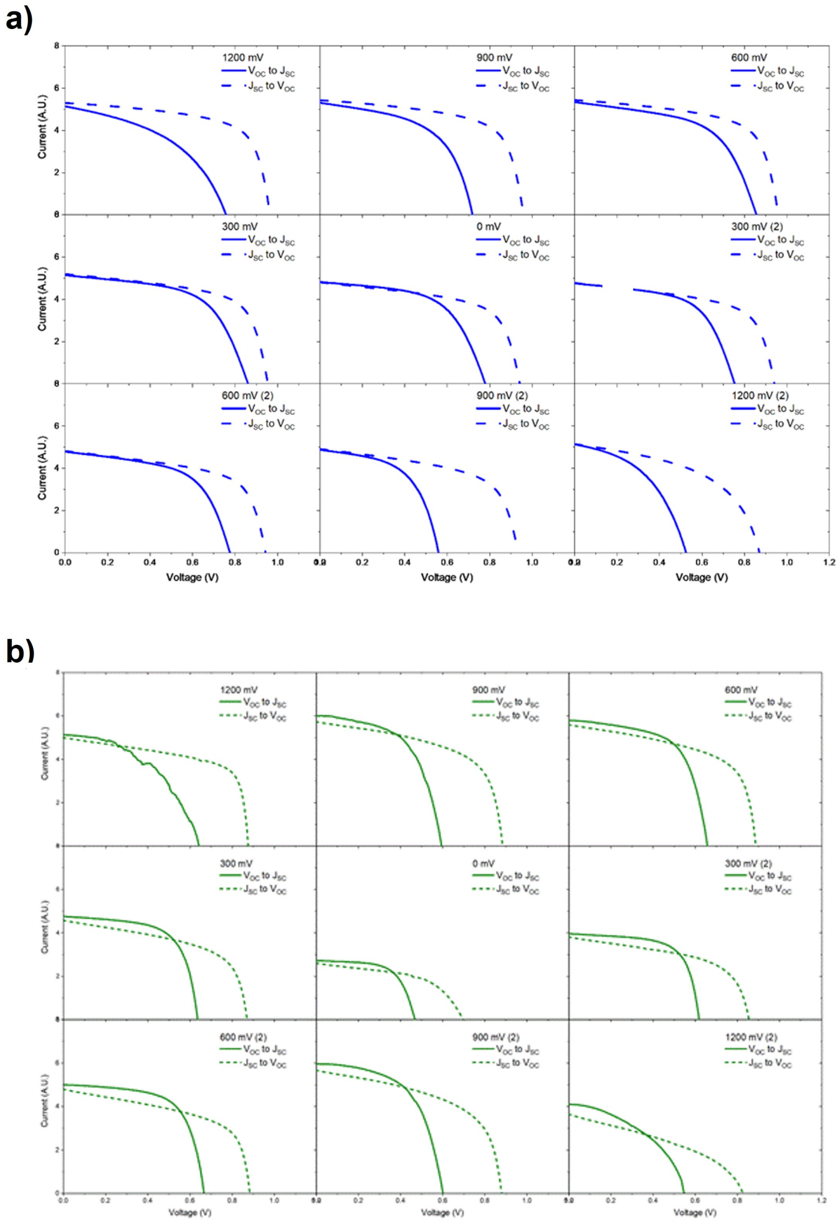

Figure F.9: Influence of preconditioning on *JV* curves under blue LED illumination of the p-i-n cells shown in Figure 9.4b in *Chapter* 9. Top 9 pannels correspond to cell “a” and bottom 9 panels correspond to cell “b”. The scan rate was 100 mV·s^{-1}. Solid lines (dashed lines) are for a reverse (forward) scan. The pre-bias voltages in mV are 1200, 900, 600 (top row), 300, 0, 300 (middle row), 600, 900, 1200 (bottom row).

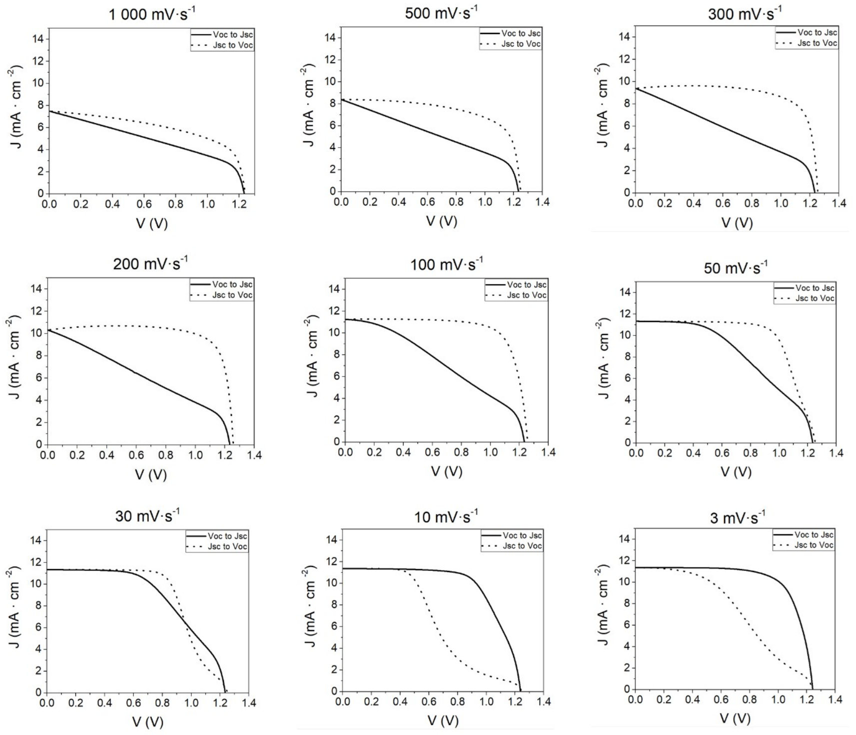

Figure F.10: DD Simulated *JV* curves for the *DoH* results shown in Figure 9.2 in *Chapter* 9, using the parameters included in Table F.1.

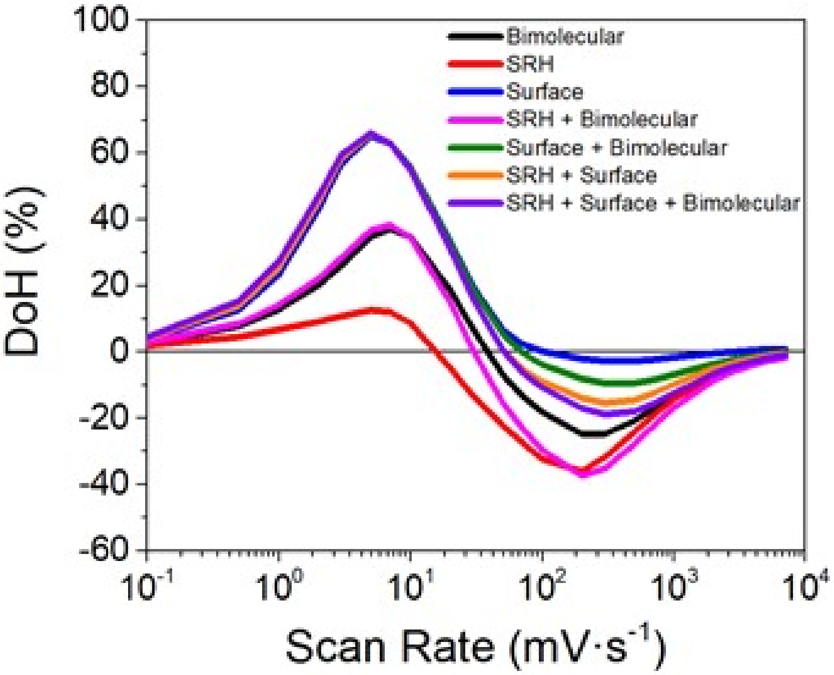

Figure F.11: DD DoH (%) versus scan rate (mV$\cdot$s^{-1}) under blue LED illumination (465 nm) and a preconditioning bias of 1.2 V for 20 s, for different choices of the recombination mechanism.

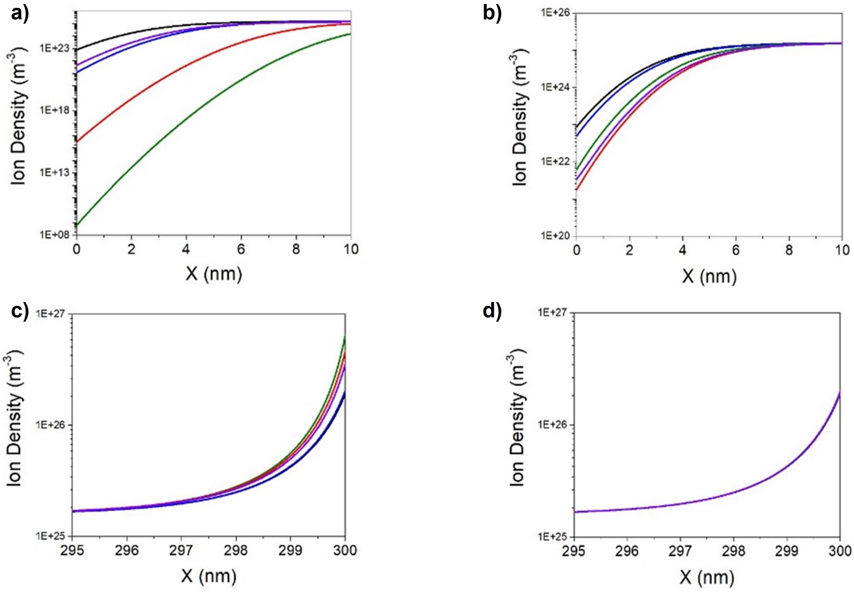

Figure F.12: Snapshots of mobile ion density N_0 (m^{-3} versus distance from ETL/perovskite interface x (nm). (a) and (b) represent to the vicinity of the ETL and (c) and (d) are close to HTL. (a) and (c) correspond to DoH$_{max}$ and (b) and (d) to DoH$_{min}$. The profiles are for $V = V_{OC}$ (black at start of reverse scan and purple at end of forward scan), $V = V_{MP}$ reached during reverse (blue) and forward (red), and $V = 0$ (green). 40 s preconditioning bias is implemented at V_{OC}. These results are for the p-i-n architecture shown in Figure 9.1 in *Chapter* 9.

Bibliography

[1] R. García-Rodríguez, D. Ferdani, S. Pering, P. J. Baker, and P. J. Cameron, “Influence of bromide content on iodide migration in inverted MAPb(i 1-x br x) 3 perovskite solar cells,” *Journal of Materials Chemistry A*, vol. 7, no. 39, pp. 22604–22614, 2019.

[2] J. M. Frost, K. T. Butler, and A. Walsh, “Molecular ferroelectric contributions to anomalous hysteresis in hybrid perovskite solar cells,” *APL Materials*, vol. 2, no. 8, p. 081506, 2014.

[3] P. Schulz, E. Edri, S. Kirmayer, G. Hodes, D. Cahen, and A. Kahn, “Interface energetics in organo-metal halide perovskite-based photovoltaic cells,” *Energy & Environmental Science*, vol. 7, no. 4, pp. 1377–1381, 2014.

[4] S. van Reenen, M. Kemerink, and H. J. Snaith, “Modeling anomalous hysteresis in perovskite solar cells,” *The Journal of Physical Chemistry Letters*, vol. 6, no. 19, pp. 3808–3814, 2015.

[5] L. Contreras-Bernal, S. Ramos-Terrón, A. Riquelme, P. P. Boix, J. Idígoras, I. Mora-Seró, and J. A. Anta, “Impedance analysis of perovskite solar cells: a case study,” *Journal of Materials Chemistry A*, vol. 7, no. 19, pp. 12191–12200, 2019.

[6] I. Zarazua, J. Bisquert, and G. Garcia-Belmonte, “Light-induced space-charge accumulation zone as photovoltaic mechanism in perovskite solar cells,” *The Journal of Physical Chemistry Letters*, pp. 525–528, 2016.

[7] C. Wehrenfennig, G. E. Eperon, M. B. Johnston, H. J. Snaith, and L. M. Herz, “High charge carrier mobilities and lifetimes in organolead trihalide perovskites,” *Advanced Materials*, vol. 26, no. 10, pp. 1584–1589, 2014.

[8] F. Brivio, K. T. Butler, A. Walsh, and M. van Schilfgaarde, “Relativistic quasiparticle self-consistent electronic structure of hybrid halide perovskite photovoltaic absorbers,” *Physical Review B*, vol. 89, no. 15, p. 155204, 2014.

[9] A. Walsh, D. O. Scanlon, S. Chen, X. G. Gong, and S.-H. Wei, “Self-regulation mechanism for charged point defects in hybrid halide perovskites,” *Angewandte Chemie (International Ed. in English)*, vol. 54, no. 6, pp. 1791–1794, 2015.

[10] C. Eames, J. M. Frost, P. R. F. Barnes, B. C. O’Regan, A. Walsh, and M. S. Islam, “Ionic transport in hybrid lead iodide perovskite solar cells,” *Nature Communications*, vol. 6, p. 7497, 2015.

[11] I. Abayev, A. Zaban, V. G. Kytin, A. A. Danilin, G. Garcia-Belmonte, and J. Bisquert, “Properties of the electronic density of states in TiO2 nanoparticles surrounded with aqueous electrolyte,” *Journal of Solid State Electrochemistry*, vol. 11, no. 5, pp. 647–653, 2007.

[12] A. Guerrero, E. J. Juarez-Perez, J. Bisquert, I. Mora-Sero, and G. Garcia-Belmonte, “Electrical field profile and doping in planar lead halide perovskite solar cells,” *Applied Physics Letters*, vol. 105, no. 13, p. 133902, 2014.

[13] J.-Y. Jeng, K.-C. Chen, T.-Y. Chiang, P.-Y. Lin, T.-D. Tsai, Y.-C. Chang, T.-F. Guo, P. Chen, T.-C. Wen, and Y.-J. Hsu, “Nickel oxide electrode interlayer in CH3 NH3 PbI3 perovskite/PCBM planar-heterojunction hybrid solar cells,” *Advanced Materials (Deerfield Beach, Fla.)*, vol. 26, pp. 4107–4113, June 2014.

[14] F. Odobel, L. Le Pleux, Y. Pellegrin, and E. Blart, “New photovoltaic devices based on the sensitization of p-type semiconductors: Challenges and opportunities,” *Accounts of Chemical Research*, vol. 43, no. 8, pp. 1063–1071, 2010.